JOURNAL OF THE MYANMAR ACADEMY OF ARTS AND SCIENCE

Physics, Mathematics, Computer Studies

Journal of the Myanmar Academy of Arts and Science, 2026, **Vol. XXIII, No.2**

Published in August, 2026, Physics, Mathematics, Computer Studies

Myanmar Academy of Arts and Science

Edition

2026, August, 280 Copies

Published by

Dr Maung Kyaw (00322) Vice-President,

Myanmar Academy of Arts and Science

ISSN 2520-0186

LCCN 2003-323143

Printed by

U Tin Soe (00171), Manager

Universities Press, Yangon, Myanmar

FOREWORD

On 26 February 2026, the Myanmar Academy of Arts and Science (MAAS) was reconstituted to accelerate the implementation of four different strategies:

(a) encouraging universities and colleges to engage in more research activities
(b) organizing domestic and international research conferences
(c) publishing research journals and proceedings, and
(d) fostering research collaboration among local and international universities

Since the year 2001, the MAAS has been making every effort to fulfil these important functions in collaboration with universities and colleges across the country. As a result, the MAAS has published research papers in 23 volumes on diverse academic disciplines in the Journal of the Myanmar Academy of Arts and Science. It is a great honor to say that the 24th research conference was successfully held at the University of Yangon on 9–11 March 2024. The theme of this conference is *'Research and Innovation for Peace, Prosperity and Sustainability'*. A total of 369 research papers presented by both faculty and postgraduates at the conference have been published in Volume XXIII as follows:

Vol. XXIII, No. 1A	Chemistry
Vol. XXIII, No. 1B	Chemistry, Industrial Chemistry
Vol. XXIII, No. 2	Physics, Mathematics and Computer Studies
Vol. XXIII, No. 3	Zoology, Marine Science, Environment and Water Studies
Vol. XXIII, No. 4	Botany, Geology
Vol. XXIII, No. 5	English, History, Philosophy, Geography, Psychology, International Relations, Oriental Studies
Vol. XXIII, No. 6	Myanmar
Vol. XXIII, No. 7	Law, Library and Information Studies, Archaeology, Anthropology, Language and Linguistics
Vol. XXIII, No. 8	Applied Statistics, Management Studies, Statistics, Commerce, Economics, Journalism and Tourism
Vol. XXIII, No. 9A	Educational Theory and Management, Curriculum and Methodology
Vol. XXIII, No. 9B	Educational Psychology

I firmly believe that the empirical research findings from these papers will provide practical assistance for research candidates and those who are interested in research work. I am also hopeful that these findings will significantly contribute to the well-being of the community at large as well as the State's socio-economic development.

On behalf of the members of the MAAS, I would like to offer my special gratitude and thanks to those who have contributed their research papers to this journal. I also do appreciate the editing work done by senior professors and scholars of high standing as well as the members of the MAAS Editorial Board. Finally, my heartfelt thanks go to the members of the Publication Committee and the Department of Higher Education for their great dedication to the success of this journal.

Dr. Soe Win
President
Myanmar Academy of Arts and Science

Journal of the Myanmar Academy of Arts and Science

Vol. XXIII. No.2

Contents

Section (i) Physics

Section (ii) Mathematics

Section (iii) Computer Studies

APPLYING VARIATION PRINCIPLE TO 3D QUANTUM HARMONIC OSCILLATOR SYSTEM*

Myat Kay Khaing[1], Nyein Wint Lwin[2]

Abstract

Quantum system with 3D harmonic oscillator well is one of the few problems in quantum mechanics that can be solved analytically. In this work, variational principle is applied to calculate eigenvalues and eigenstates of 3D harmonic oscillator system. The trial wave function is chosen as a linear superposition of Gaussian basis function of the form $r^{m_i}e^{-\frac{r^2}{b_i^2}}$. To validate the variational results, a numerical approach known as Numerov method is also used to calculate energy values and wave functions. The calculated values are further compared with analytical solutions. The results demonstrate that for a basis size of twelve, the energy values for low-lying states up to N = 15 agree very well with the analytical results, making this work suitable for applications to low-lying energy states.

Keywords: 3D harmonic oscillator, variational principle, Numerov method

Introduction

Variational principle, one of the famous approximation methods in quantum mechanics, states that for a quantum system represented by any trial wave function $|\psi\rangle$ with Hamiltonian H, the true ground state energy is less than or equal to the expectation value of the Hamiltonian with respect to trial wave function. Therefore, for a system of known Hamiltonian, it is useful to determine the upper bound energy eigenvalue. Mathematically, it can be expressed as follows.

$$E_0 \leq \frac{\langle\psi|H|\psi\rangle}{\langle\psi|\psi\rangle}$$

where $\langle\psi|H|\psi\rangle$ is the expectation value of the Hamiltonian with respect to trial wave function. According to the principle, true ground state energy is achieved only when trial wave function exactly matches true ground state wave function.

Variational principle is often applied in determining ground state energy. But it could also be extended to higher energy states which is also known as generalized Rayleigh– Ritz method [Yasuyuki S, 1998)]. In mathematical form, it could be expressed as follows.

$$E_n \leq \frac{\langle\psi_n|H|\psi_n\rangle}{\langle\psi_n|\psi_n\rangle}, (n = 0, 2, 3, \ldots)$$

To apply variational principle in practical calculation, trial wave function is initially constructed with adjustable parameters which are later varied to minimize energy value. Trial wave function could take any form or any function, but it must satisfy properties of a well-behaved wave function such as square-integrability and convergence at infinity.

---

* First Prize (2024)

[1] Department of Physics, University of Mandalay

[2] Department of Physics, University of Mandalay

In this work, gaussian basis which is in the form of $r^{m_i}e^{-\frac{r^2}{b_i^2}}$ is chosen as trial basis state. Here, m_i and b_i are known as variational parameters. The parameter b_i is linked to gaussian fall off distance. It determines how far the spatial extent of a gaussian is. Larger b_i represents broader gaussian distribution and smaller b_i results in narrow gaussian width with rapid decay. Therefore, b_i is important parameter in controlling the width of the gaussian basis function. For second parameter m_i, as the value is increased, the peak of the gaussian distribution moves toward larger value of r. The value of m_i determines the peak position of the gaussian basis along the radial axis. The higher m_i value, the more gaussian distribution is translated away from the origin.

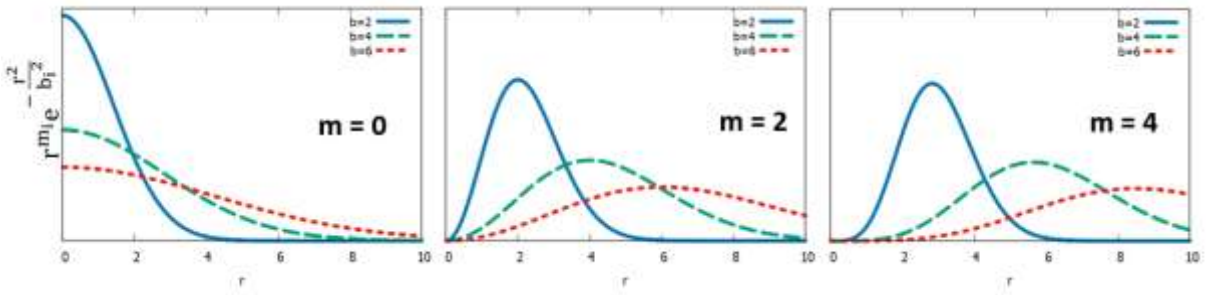

Figure 1. Basis states for various m_i and b_i values

Our trial wave function which is linear combination of chosen gaussian can now be written as $R(r) = \sum_{i=1}^{n} c_i r^{m_i} e^{-\frac{r^2}{b_i^2}}$. Here, n is the number of basis states, c_i is the expansion coefficient in the linear combination of the basis states. It quantifies the contribution of each basis state to the overall wavefunction.

Numerov method, which is also applied in this work, is a mathematical tool which can be used to solve second order differential equation of the form:

$$\frac{d^2y}{dx^2} = g(x)y(x) + s(x)$$

Schrodinger equation which can be written as $\frac{d^2\psi}{dr^2} + k^2(r)\psi = 0$, is an example of such equation and can be solved by using Numerov method. In this equation, the value of k which contains energy value reflects the curvature of the wave function. Setting the energy higher than the actual value gives wave function in higher nodes. On contrary, lower energy value results in equal or fewer number of nodes. By counting the number of nodes and comparing with desired number, one can estimate the energy eigenvalue of a quantum system.

In essence, variational principle gives theoretical framework to get a better estimation of wave function. Whereas, Numerov method is a numerical technique used to solve second order differential equation.

Numerical Calculations for 3D Harmonic Oscillator

Harmonic oscillator potential well is central potential which is expressed as $V(r) = \frac{1}{2}m\omega^2 r^2$. In this work, using natural units, Hamiltonian operator of harmonic oscillator potential can be written as follows.

$$H = -\frac{1}{2}\frac{d^2}{dr^2} + \frac{l(l+1)}{2r^2} + \frac{1}{2}r^2$$

For central potential, which depends only on radial distance, wave function can be written as $\psi(r,\theta,\phi) = R(r)Y_{lm}(\theta,\phi) = \frac{U(r)}{r}Y_{lm}(\theta,\phi)$. Our trial wave function for radial part is already chosen as $R(r) = \sum_{i=1}^{n} c_i r^{m_i} e^{-\frac{r^2}{b_i^2}}$. Accordingly, new basis can be written as $u_i(r) = r^{m_i+1} e^{-\frac{r^2}{b_i^2}}$ and new wave function U(r) is a linear combination of these new 'n' number of basis states.

By solving generalized eigenvalue equation which is in matrix form of $Hc = ESc$ [Yasuyuki S, 1998], energy eigenvalues, E and wave function U(r) can be calculated. Here, H is Hamiltonian operator whose matrix element is given by $\langle u_i(r)|H|u_j(r)\rangle$, S is overlap matrix with matrix elements given by $\langle u_i(r)|u_j(r)\rangle$ which reduces to identity matrix for orthonormal basis states, c is a n-dimensional column vector with i^{th} component corresponding to c_i and E is energy eigenvalue. By adjusting parameters in the chosen basis, lower energy values can be obtained. According to the variational principle, the lower energy eigenvalues, the closer our trial wave function is to the true wave function.

Algorithm for applying variational principle

1. Staring with one single basis state, parameter values of m_1 and b_1 are initialized.
2. Overlap matrix elements and Hamiltonian matrix elements are calculated. The use of gaussian basis simplifies computation of matrix elements.
3. Generalized eigenvalue equation $Hc = ESc$, in matrix form, is solved by using DGGEV subroutine under LAPACK library [Joshua I, 2018]. This step provides energy eigenvalue E and corresponding expansion coefficient c_i.
4. The parameter b_1 is updated to minimize energy eigenvalue. It is found that choosing b_1 value of 1.41 gives optimal ground state energy value in the calculation.
5. Once optimal parameter b_1 is determined, the number of basis states is increased with m_i assigned as i-1 for each additional term. Adding higher values of m_i corresponds to shift of Gaussian peak away from the origin. The number of basis states is increased until energy convergence criterion is satisfied
6. The wave function corresponding to the calculated energy eigenvalue is calculated and normalized.

For the Numerov calculation, the second order differential equation in the form of radial equation for central potential, $\left(-\frac{1}{2}\frac{d^2}{dr^2} + \frac{l(l+1)}{2r^2} + \frac{1}{2}r^2\right)U(r) = EU(r)$ is solved [Nouredine Z, 2009]. Different values of l correspond to different effective potential wells. To solve this second order differential equation, recursion relations known as Numerov forward and Numerov backward calculations are employed to determine the wave function at successive points. For second order differential equation of the form $\frac{d^2U(r)}{dr^2} + k^2(r)U(r) = 0$, Numerov forward and Numerov backward relations can be expressed as follows respectively.

$$U(r+h) = \frac{2\left[1 - \frac{5}{12}h^2k(r)^2\right]U(r) - \left[1 + \frac{1}{12}h^2k(r-h)^2\right]U(r-h)}{1 + \frac{1}{12}h^2k^2(x+h)}$$

$$U(r-h) = \frac{2\left[1 - \frac{5}{12}h^2k(r)^2\right]U(r) - \left[1 + \frac{1}{12}h^2k(r+h)^2\right]U(r+h)}{1 + \frac{1}{12}h^2k^2(x+h)}$$

The above two equations indicate that the value of the wave function at a given point can be determined from its values at two successive neighboring points separated by a small radial step size 'h'. To achieve high-order accuracy, the value of h must be chosen sufficiently small. To initialize the wave function, the asymptotic forms are applied: near the origin $U(r) \sim r^{l+1}$ and at large distances, $U(r) \sim e^{-k^2(r)}$ correspondingly.

In the calculation, the number of nodes obtained from the Numerov method is counted and compared with expected number of nodes for a given state. By evaluating the difference in number of nodes, trial energy value is updated iteratively by using bisection method.

Algorithm for applying Numerov Method

1. Start with trial energy value E which is taken as top of the well in the program.
2. Numerov forward recursion relation is used to calculate wave function at each radial point and number of nodes is counted.
3. Calculated number of nodes is compared with expected number of nodes. If calculated number of nodes exceeds the desired number, trial energy is too high and upper bound of the energy bracket is updated. If the computed number of nodes is smaller, the trial energy is low and lower bound is updated. The Bi-section method is applied iteratively to refine energy values until energy convergence criterion is satisfied.
4. Once the desired energy value is obtained, Numerov backward recursion is applied. At the classical turning point, wave function values calculated by using Numerov backward and forward recursion relations are matched to ensure wave function continuity.
5. The resulting wave function is then normalized.

Result and Discussion

Some low-lying energy eigenvalues and eigen states for different n and l quantum numbers calculated by using variational method and the Numerov method are presented in the tables. Additionally, analytical results are also provided. Calculated energy eigenstates are for l = 0, 1, 2, and 3 and for each l value first four low lying energy values are presented.

Eigenvalue analysis

For the variational method, calculated eigenvalues by using basis number of four, eight and twelve are compared. With basis size of four and eight, very low level eigen states agree well with the analytical results. However, as energy levels become higher, discrepancy becomes significantly larger. As the basis size is increased to twelve, this discrepancy is significantly reduced, and results are in much closer agreement with the analytical values. For comparison, energy values calculated by using Numerov method are also included in the tables.

Table 1. Calculated energy values by using variational principle, Numerov method and analytical result for l = 0

n	l	Energy values by using variational method of different basis states			Energy values by using Numerov method	Analytical result $(N + 1\frac{1}{2})$ N = 2n + 1
		4 basis states	8 basis states	12 basis states		
0	0	1.5000	1.5000	1.5000	0.5000	0.5000
1	0	3.5000	3.5000	3.5000	3.5000	3.5000
2	0	5.5330	5.5000	5.5000	5.5000	5.5000
3	0	11.0791	7.5000	7.5000	7.5000	7.5000

Table 2. Calculated energy values by using variational principle, Numerov method and analytical result for l = 1

n	l	Energy values by using variational method of different basis states			Energy values by using Numerov method	Analytical result $(N + 1\frac{1}{2})$ N = 2n + 1
		4 basis states	8 basis states	12 basis states		
0	1	2.5000	2.5000	2.5000	2.5000	2.5000
1	1	4.5000	4.5000	4.5000	4.5000	4.5000
2	1	7.0537	6.5000	6.5000	6.5000	6.5000
3	1	34.8303	8.5000	8.5000	8.5000	8.5000

Table 3. Calculated energy values by using variational principle, Numerov method and analytical result for l = 2

n	l	Energy values by using variational method of different basis states			Energy values by using Numerov method	Analytical result $(N + 1\frac{1}{2})$ N = 2n + 1
		4 basis states	8 basis states	12 basis states		
0	2	3.5000	3.5000	3.5000	3.5000	3.5000
1	2	5.5320	3.5000	5.5000	5.5000	5.5000
2	2	10.5275	7.5000	7.5000	7.5000	7.5000
3	2	83.8682	9.5012	9.5000	9.5000	9.5000

Table 4. Calculated energy values by using variational principle, Numerov method and analytical result for l = 3

n	l	Energy values by using variational method of different basis states			Energy values by using Numerov method	Analytical result $(N + 1\frac{1}{2})$ N = 2n + 1
		4 basis states	8 basis states	12 basis states		
0	3	4.5000	4.5000	4.5000	4.5000	4.5000
1	3	6.8507	6.5000	6.5000	6.5000	6.5000
2	3	16.2851	8.5000	8.5000	8.5000	8.5000
3	3	157.6074	10.5275	10.5000	10.5000	10.5000

Eigen state analysis

Calculated wave functions by using variational principle with basis size of twelve, Numerov method and analytical solutions of the first six low lying energy states are illustrated in the graphs. The green thick line, dark dashed line and pink line correspond to variational result, Numerov result and analytical results correspondingly. Since variational results in this work produce low lying energy values very well, calculated eigen states yield strong agreement with analytical results. The calculated wave functions are shown in the following graphs.

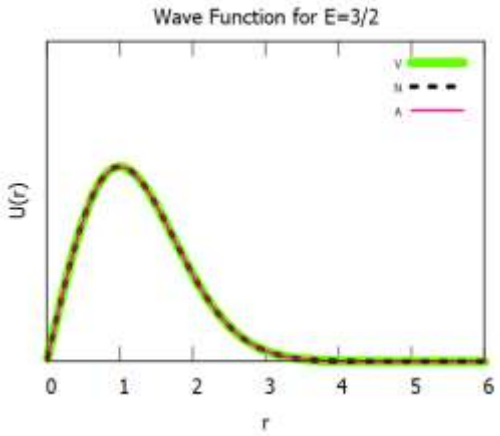

Figure 2. Wave function for N = 0 (n = 0, l = 0)

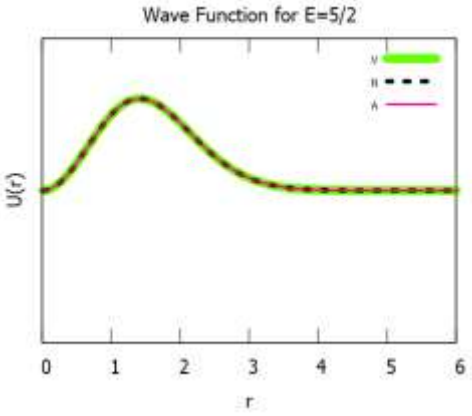

Figure 3. Wave function for N = 1 (n = 0, l = 1)

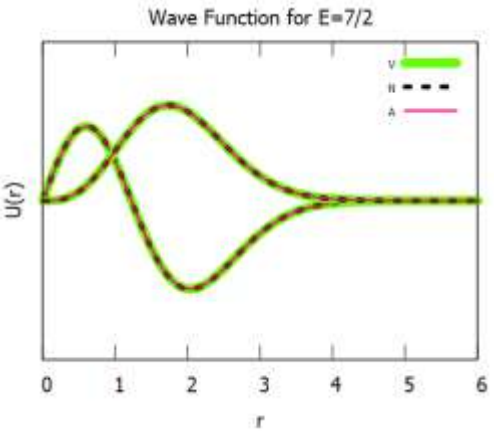

Figure 4. Wave function for N = 2 (n = 0, l = 2 and n = 1, l = 0)

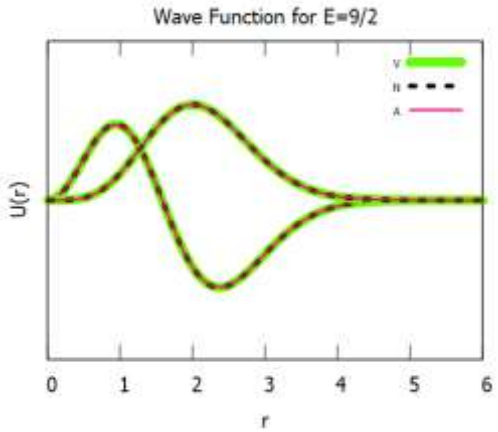

Figure 5. Wave function for N = 3 (n = 1, l = 1 and n = 0, l = 3)

Energy discrepancy of variation result

By using chosen trial wave function with twelve number of basis states, higher energy level states are also calculated and the discrepancy values with analytical results are presented. From the following graphs it could be seen that at low lying levels up to N = 15, variational calculation with chosen gaussian basis of twelve states could produce energy values quite well. But as the system goes to higher levels than N = 15, the discrepancy value begins to be significant and appears to be increasing as the energy levels get higher.

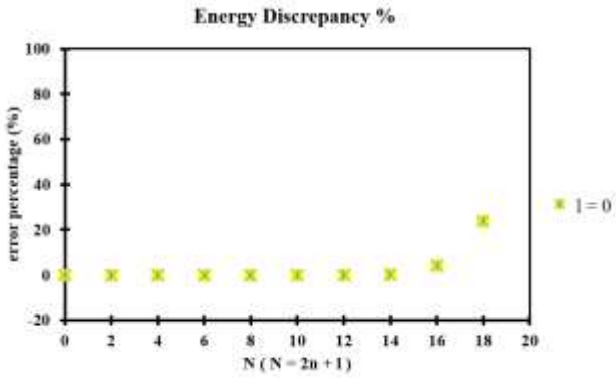

Figure 6. Energy discrepancy for various N values of fixed l = 0

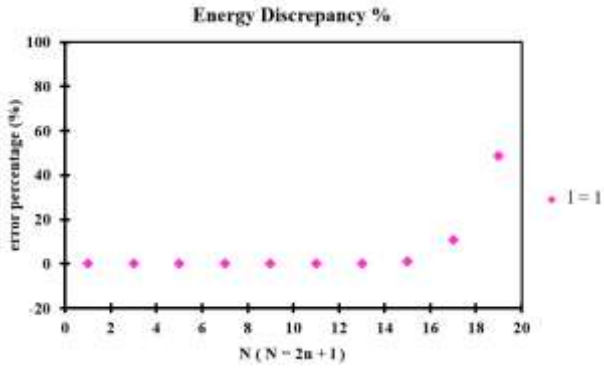

Figure 7. Energy discrepancy for various N values of fixed l = 1

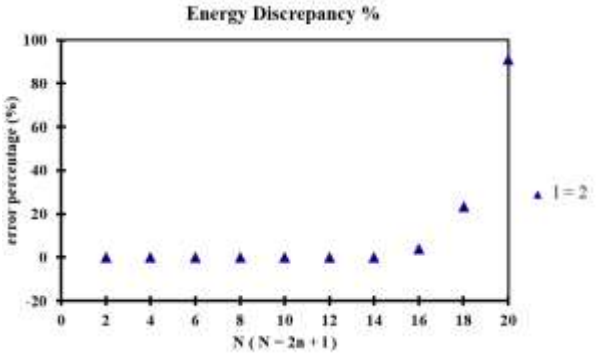

Figure 8. Energy discrepancy for various N values of fixed l = 2

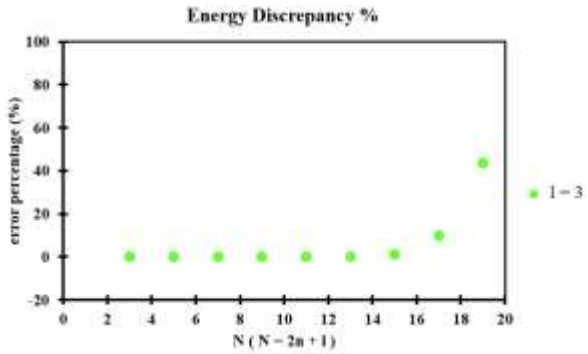

Figure 9. Energy discrepancy for various N values of fixed l = 3

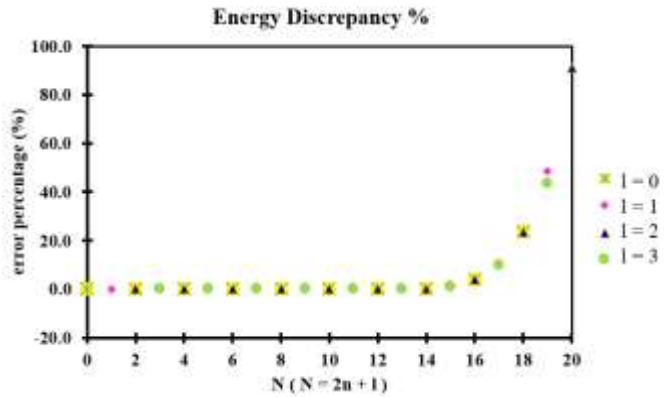

Figure 10. Energy discrepancy for various N values of l = 0, 1, 2 and 3

Conclusion

In this work, low lying energy levels of 3D quantum harmonic oscillator are calculated by using both variational principle and Numerov method. The results are compared with corresponding analytical solutions. For variational calculation, taking linear combination of gaussian basis as trial wave function demonstrated that a basis size of twelve is sufficient to accurately reproduce the low-lying levels of this system up to N = 15. The variational parameters chosen in this work are b_i = 1.41 and m_i starts from 0 to 11. The energy values computed by using Numerov method showed good agreement with analytical results for all considered states. Wave functions of first six low lying energy levels are also plotted, comparing the results obtained from variational method with Numerov method and analytical results. Since the variational results provide similar energy eigenvalues as analytical results, the wave functions appear to coincide.

Acknowledgements

My sincere gratitude is dedicated to everyone who gave me useful advice and feedback in this work.

References

Joshua, I., & W. Jingbo (2018) *Computational Quantum Mechanics.* Springer

Nouredine, Z., (2009) *Quantum Mechanical Concepts and Applications.* John Wiley & Sons

Yasuyuki, S., & V. Kalman, (1998) *Stochastic Variational Approach to Quantum-Mechanical Few-Body Problmes.* Springer

OPTICAL FEATURES OF NANOFIBROUS SCAFFOLDS COMPRISING ZINC STANNATE, FABRICATED THROUGH ELECTROSPINNING*

Hlaing Darli Soe[1], Zin Min Myat[2], Zin Min Tun[3], Yin Maung Maung[4]

Abstract

This study employed a sol-gel method to prepare zinc stannate nanopowder using zinc and tin chloride. Subsequently, zinc stannate nanofibers were synthesized on fluorine-doped tin oxide (FTO) glass substrates through an aqueous solution of zinc stannate and polyvinyl alcohol (PVA) using electrospinning. Natural dyes extracted from barks (Caesalpinia pulcherrima, Prunus domestica, Tamarindus indica, Pterocarpus macrocarpus) were utilized as photosensitizers in dye-sensitized solar cells (DSSCs). The natural dye solutions and zinc stannate nanofibers' optical properties, including absorption wavelengths and energy band gaps, were analyzed using Ultraviolet-Visible (UV-Vis) spectroscopy for DSSC photoelectrodes. The study observed significant variations in absorption wavelengths and energy band gaps. This environmentally friendly and cost-effective approach aims to enhance the efficiency and durability of zinc stannate nanomaterials for energy generation.

Keywords: Zinc Stannate Nanofibers, Sol-gel Method, Electrospinning Method, and UV-Vis.

Introduction

Increasing energy conversion efficiency is a great challenge to overcome in the market entrance of DSSCs. To realize this objective, modifications have been made to the components of the DSSC, as well as to their manufacturing processes. Several methods have been used for producing nanofibers, including electrospinning, melt or solution blowing, phase separation, self-assembly, and template synthesis (M. Afshari, et al.,2017). The electrospinning performance is an option to increase the efficiency of DSSCs, because the resultant nanofibers increase the contact area, garnering a greater absorption of solar energy. Electrospinning is the technique that uses a strong electric field to produce polymer nanofibers from a polymer solution or polymer melt (F. Huang, et al., 2012). In this work, a summary of the components of DSSCs is made, as well as its process. A brief review of the electrospinning technique and its usage in the manufacture of DSSC is discussed, presenting an updated comparison of electrospun compounds and their efficiency, and providing the basis for the progress in the manufacture and design of DSSCs. In the DSSCs study, nanofibers play a major role in obtaining maximum efficiency. Moreover, the nanofibers prepared via electrospinning have a high surface area-to-volume ratio, high porosity, and a unique web structure that are crucial to energy conversion and storage (X. Shi, et al.,2015). General DSSCs have a dye nanofibers coating sandwiched between two conducting glass plates in the existence of an electrolyte. The nanofibers have shown great potential for DSSC applications. This is because the electrospun nanofibers have excellent electrical conductivity and a large surface area to volume ratio, which permits improved penetration of viscous polymer gel electrolytes and provides a higher specific surface area than nanoparticles. It has been shown that replacing nanoparticulates with one-dimensional nanoarchitectures can improve charge transport by reducing the scattering of free electrons from the grain boundaries of the interconnected nanoparticles. As one-dimensional nanostructures provide a more direct pathway for charge collection, we can expect that electron transport in nanofibers would be significantly faster than in nanoparticles (N. Canever, et al.,2017). Several different shapes and sizes of micron and nanoscale fibers can be fabricated from various classes of polymers. Electrospinning offers a straightforward way to produce long polymer fibers with

---

* Second Prize (2024)

[1] Department of Physics, Pathein University
[2] Department of Physics, West Yangon University
[3] Department of Physics, West Yangon University
[4] Department of Physics, University of Yangon

diameters in the range of 40– 2000 nm (S. Ramakrishna, et al.,1996). The basic components of DSSCs primarily consist of transparent conducting oxide glass substrates, dye, photoanode, electrolytes, and counter electrodes (S. N. Karthick, et al.,1996). Potoanode plays two roles in dye adsorption and electron transport media. Photoanode is grown on the surface of Transparent Conducting Oxide (TCO), and mesoporous semiconductor metal-oxide nanoparticles (R. Qohhar, et al.,2020). In the photoanode of a DSSC, morphology, and structure play a very important role in the performance of electron transport Several studies have been carried out for the development of photoanodes with materials with one-dimensional morphology. Therefore, nanofiber compounds are a very promising option for use in DSSC (J. G. López-Covarrubias, et al.,2020). The photoanode contains a metal oxide semiconductor deposited on the surface of a transparent conductive oxide substrate. The transparent conductive oxide allows the collection and transfer of electrons to an external circuit. A high electron transport rate is required to reduce the electron-hole recombination rate and enhance conversion efficiency (L. T. Yan, et al.,2012). Usually, fluoride-doped tin oxide is used as the transparent conductive oxide; this is due to its excellent electrical conductivity, optical transparency, and 75% transmittance. The dye sensitizer in the DSSC is responsible for absorbing the light generated from the electron current through photoexcitation and is thus fixed to the photoanode. The role of the photoanode material itself is very crucial in achieving higher light harvesting, proper dye loading, uninterrupted electron transport or diffusion, ultrafast injection of photoelectron, and lowering the recombination reactions (P. P. Das et al.,2016).

Materials and Methods

Sample Preparation of zinc stannate nanopowders

Materials

In this research, Zinc Stannate, PVA, and distilled water were used as the starting materials to produce zinc stannate nanofibers, and distilled water was used as the dissolving solvent.

Methods

The synthesis method consisted of two steps: (1) The preparation of zinc stannate nanopowders was synthesized by the sol-gel technique, and (2) zinc stannate nanofibers were fabricated using the electrospinning method.

Cleaning Process of FTO Glasses

Fluorine-doped tin oxide glasses were used as transparent substrates, and the glass slides were cleaned as follows.

(1) Firstly, the FTO glass slides were cleaned with distilled water.
(2) They were taken and immersed in ethanol for 15 minutes and dried.
(3) And then, they were immersed in acetone for 15 minutes and dried.

Eventually, clean FTO glass slides were obtained. The space of (1cm×1cm) of FTO glass was used for the coated area, and the other area was masked by using a tape spacer, and they were ready to use for the photoelectrode.

Preparation of Natural Dye Extraction

In this research, samples were collected from the stem barks of Caesalpinia pulcherrima (Peacock Flower Tree), Prunus Domestica (Plum Tree), Tamarindus indica (Tamarind Tree), and P. macrocarpus (Padauk Tree). The natural dye solution from four different barks of the plants was extracted as sensitizers for dye-sensitized solar cells by using a simple and easy solvent extraction method. The obtained samples were washed with water to remove dust particles and then dried at room temperature in the dark for one week in the laboratory. The dried samples were chopped into small pieces. Dye solutions were extracted from different barks using ethanol

as the extraction solvent. Then, 50 g of small pieces of bark samples were mixed with 70 ml of ethanol at room temperature. The mixtures were annealed at 80 °C for 45 min until the mixtures showed homogeneity in color. The solutions were carefully filtered with filter papers, and then the resulting filtrate was used as a natural dye sensitizer. All dye solutions were stored in the dark. Figure 1 describes the step-by-step preparation of four different dye solutions from bark samples.

Weighing **Mixed with solvents**

Annealing at low temperature

Filtering dye solutions

Figure 1 Step-by-step preparation of four different dye solutions from bark samples

Preparation of Zinc Stannate Nanofiber Electrode

In this research work, the photoanodes of zinc stannate nanofiber were prepared by using the Electrospinning method. The zinc stannate nanofiber was coated onto the FTO glass substrates by using the electrospinning method. Firstly, the viscosity is used to obtain the nanofibers. The solution used to produce nanofibers was prepared with PVA. Fibers were produced using five types of zinc stannate nanopowder at different temperatures. Zinc stannate nanopowder and solution are mixed and added to the beaker, and then stirred with a magnetic stirrer. The mixture was first heated at 80ºC with constant stirring until a transparent homogeneous polymer solution was formed. The electrospun Zn_2SnO_4/PVA nanofiber membranes were prepared using the electrospinning system. Then it was allowed to cool down to room temperature and was transferred to a syringe pump connected to a needle. A high voltage of 2.5 kV was applied between the tip of the needle and the grounded drum collector, which were fixed 8 cm apart. The PVA nanofibers were deposited onto a glass substrate, which was attached to the drum collector by an aluminum foil. The nanofiber membrane is deposited on the glass substrate. The zinc stannate nanofibers coated film was heated at 100℃ for 45 minutes and annealed at 450℃ for 1 hour. After annealing, the film was cooled down at room temperature, and a zinc stannate nanofiber photoelectrode was obtained. Then, the zinc stannate nanofiber photoelectrode was immersed in a dye solution for 24 hours, and the optical properties of the zinc stannate nanofiber photoanode were examined by Ultraviolet-Visible Spectroscopy.

Washed with distilled water

Immersed in ethanol (15 min)

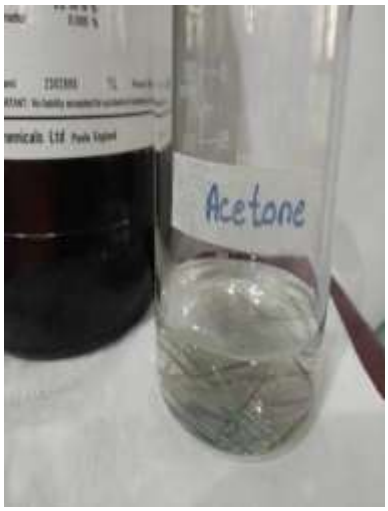

Immersed in acetone (15 min)

Figure 2 Cleaning process of FTO Glasses and checking conductive side

(a) Electrospinning process **(b) As prepared electrospun nanofibers on FTO**

Figure 3(a, b) Preparation of Zinc Stannate nanofiber photoanodes

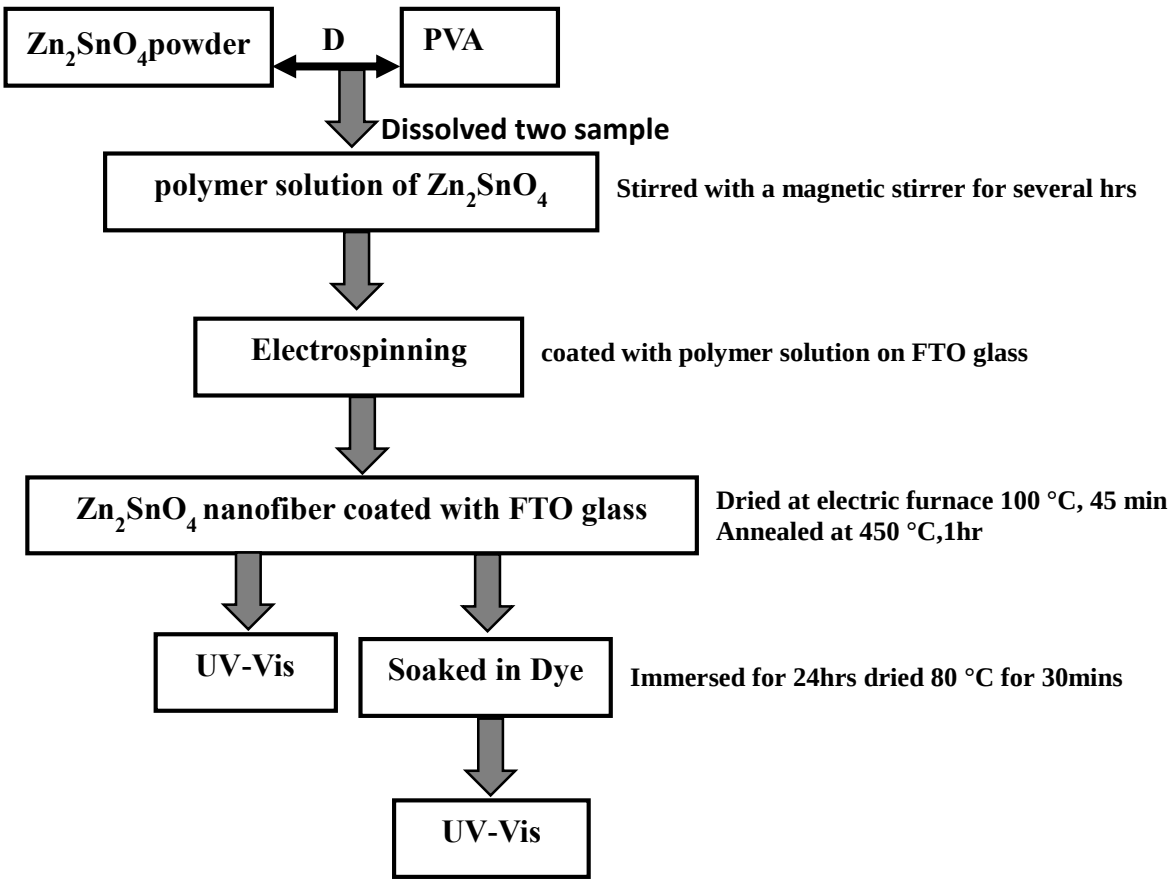

Figure 4 Block diagram of the preparation of Zinc Stannate nanofiber photoanode

Results and Discussion

UV-Vis Analysis of Zinc Stannate Nanofiber Photoanodes

The optical absorption property of the electrospun Zn_2SnO_4 nanofibers on FTO substrates was investigated using UV-Vis spectroscopy. Figure 5(a-e) showed the energy bandgaps using Tauc's electrospun Zn_2SnO_4 nanofiber photoanodes equation. The estimated energy bandgaps for Zn_2SnO_4 nanofiber photoanodes were 3.50 eV, 3.20 eV, 3.18 eV, 3.17 eV, and 3.14 eV for different temperatures, respectively. The energy bandgap of Zn_2SnO_4 nanoparticles ranges from 3.25 eV to 3.65 eV (D. L. Young et al.,2002; H. Zhu et al.,2016). But, in this study, the energy bandgaps of Zn_2SnO_4 nanofibers were narrowed from 3.50 eV to 3.14 eV due to the heat treatment, phase changes (powders to nanofibers), and incorporation of excess Zn into Zn_2SnO_4 crystal (M. A. Alpuche-Aviles et al.,2009). Although the optical absorption property of Zn_2SnO_4 remains controversial, the observed energy bandgap values of the electrospun Zn_2SnO_4 nanofibers photoanodes agreed well with previous reports. Table 1 listed the observed energy bandgaps and referenced energy band gaps.

Table 1. Observed energy bandgaps and referenced energy bandgaps

Samples	Temperatures	E_g (this study)	E_g (references)
Zn_2SnO_4 nanofibers	500 ºC	3.50 eV	3.25 – 3.67 eV [11,12]
	600 ºC	3.20 eV	
	700 ºC	3.18 eV	
	800 ºC	3.17 eV	
	900 ºC	3.14 eV	

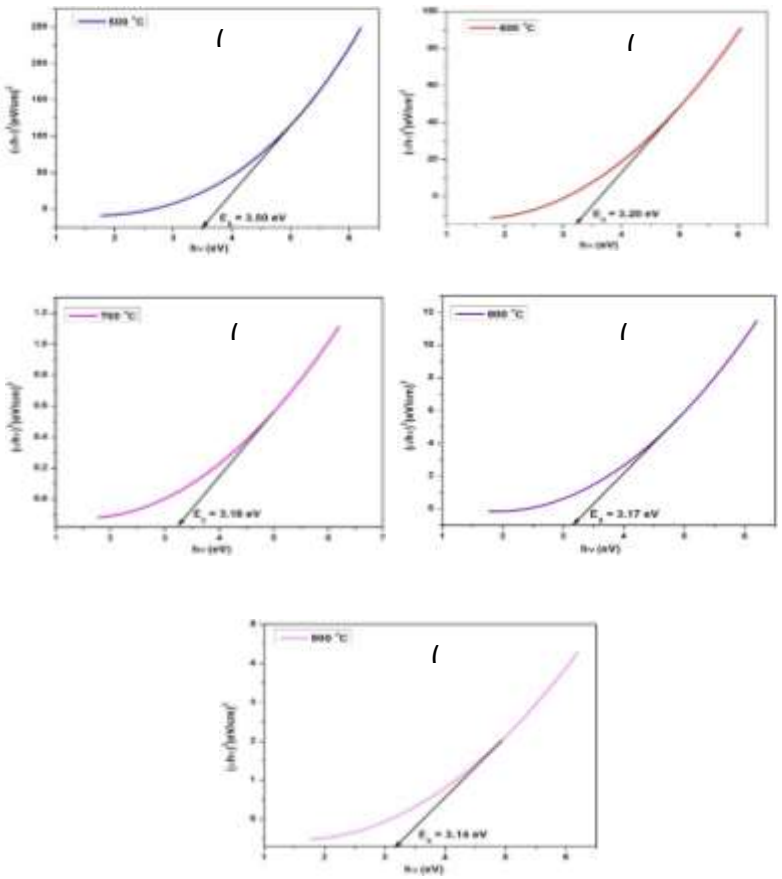

Figure 5(a-e). UV-Vis analysis of electrospun Zn_2SnO_4

UV-Vis Analysis of Dye-soaked Zinc Stannate Nanofiber Photoanodes

The energy bandgaps of natural dyes with ethanol solvent were 2.05 eV for Padauk, 2.83 eV for Peacock flower, 2.91 eV for Plum, and 2.56 eV for Tamarind trees, respectively. In this study, these natural dye sensitizers were adsorbed on zinc stannate nanofiber photoanodes, and the optical properties of dyes-soaked nanofiber photoanodes were investigated using UV-Vis spectroscopy. Figures 6(a-e), 7(a-e), 8(a-e), and 9(a-e) showed the energy bandgaps of dyes-soaked nanofiber photoanodes. According to the results, the energy bandgaps of dye-soaked zinc stannate nanofiber photoanodes were well matched with the standard energy bandgap values of zinc stannate. Although some of the samples had wider energy bandgap values, most were suitable for the usage of dye-sensitized solar cell applications. The energy bandgap values of all dye-soaked nanofiber photoanodes were tabulated in Table 2.

Table 2. Energy bandgaps comparison between dyes and dye-soaked photoanodes

Dyes	Zn_2SnO_4	E_g (dyes)	E_g (dye-soaked photoanodes)
Padauk	500 ºC	2.05 eV	3.19 eV
	600 ºC		3.15 eV
	700 ºC		3.33 eV
	800 ºC		3.27 eV
	900 ºC		3.74 eV
Peacock	500 ºC	2.83 eV	3.73 eV
	600 ºC		3.89 eV
	700 ºC		3.32 eV
	800 ºC		3.48 eV
	900 ºC		3.74 eV
Plum	500 ºC	2.91 eV	3.16 eV
	600 ºC		3.23 eV
	700 ºC		3.09 eV
	800 ºC		3.08 eV
	900 ºC		2.95 eV
Tamarind	500 ºC	2.56 eV	3.08 eV
	600 ºC		3.06 eV
	700 ºC		3.14 eV
	800 ºC		2.94 eV
	900 ºC		3.01 eV

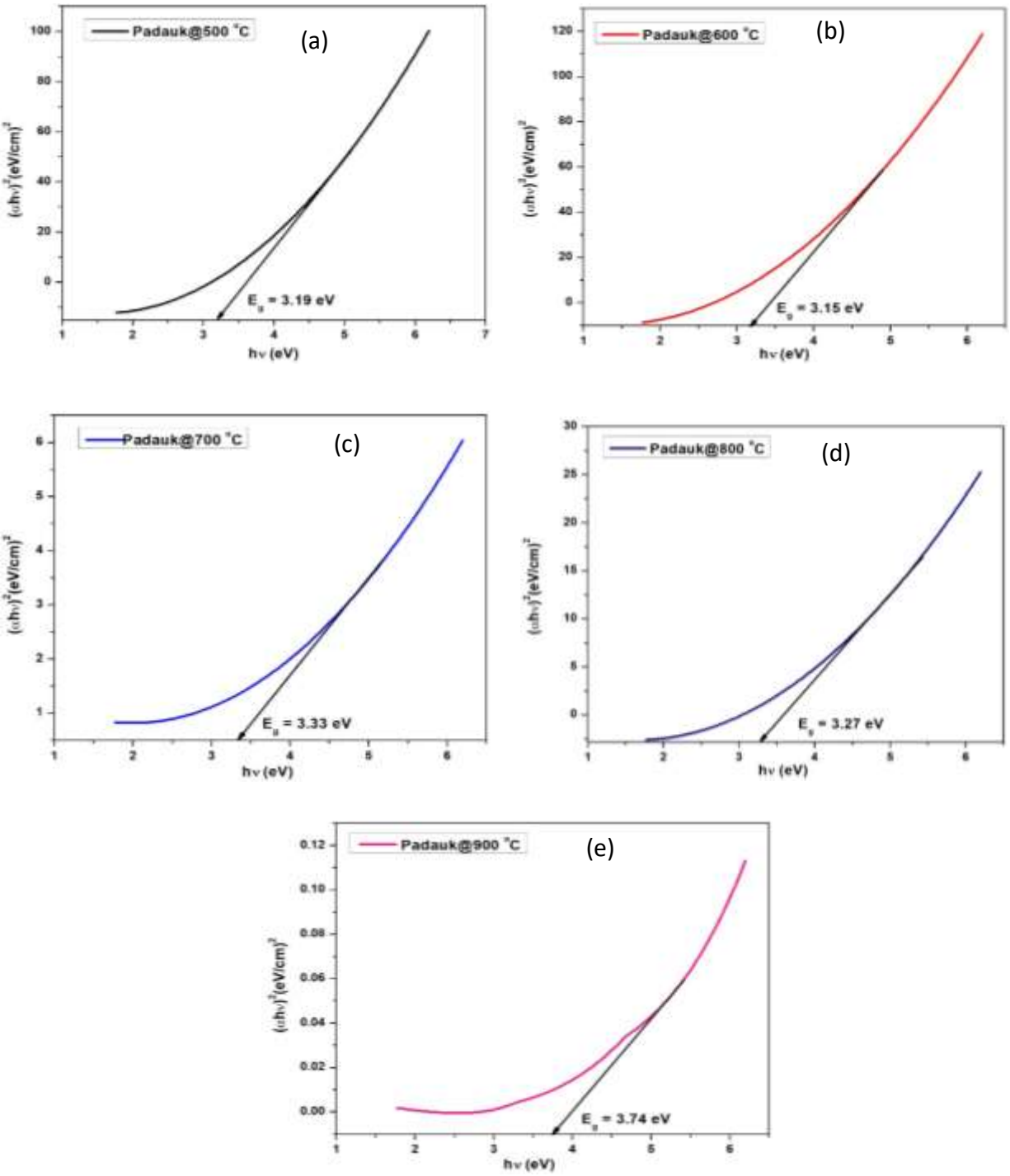

Figure 6(a-e). Energy bandgaps for Padauk dye-soaked nanofiber photoanodes

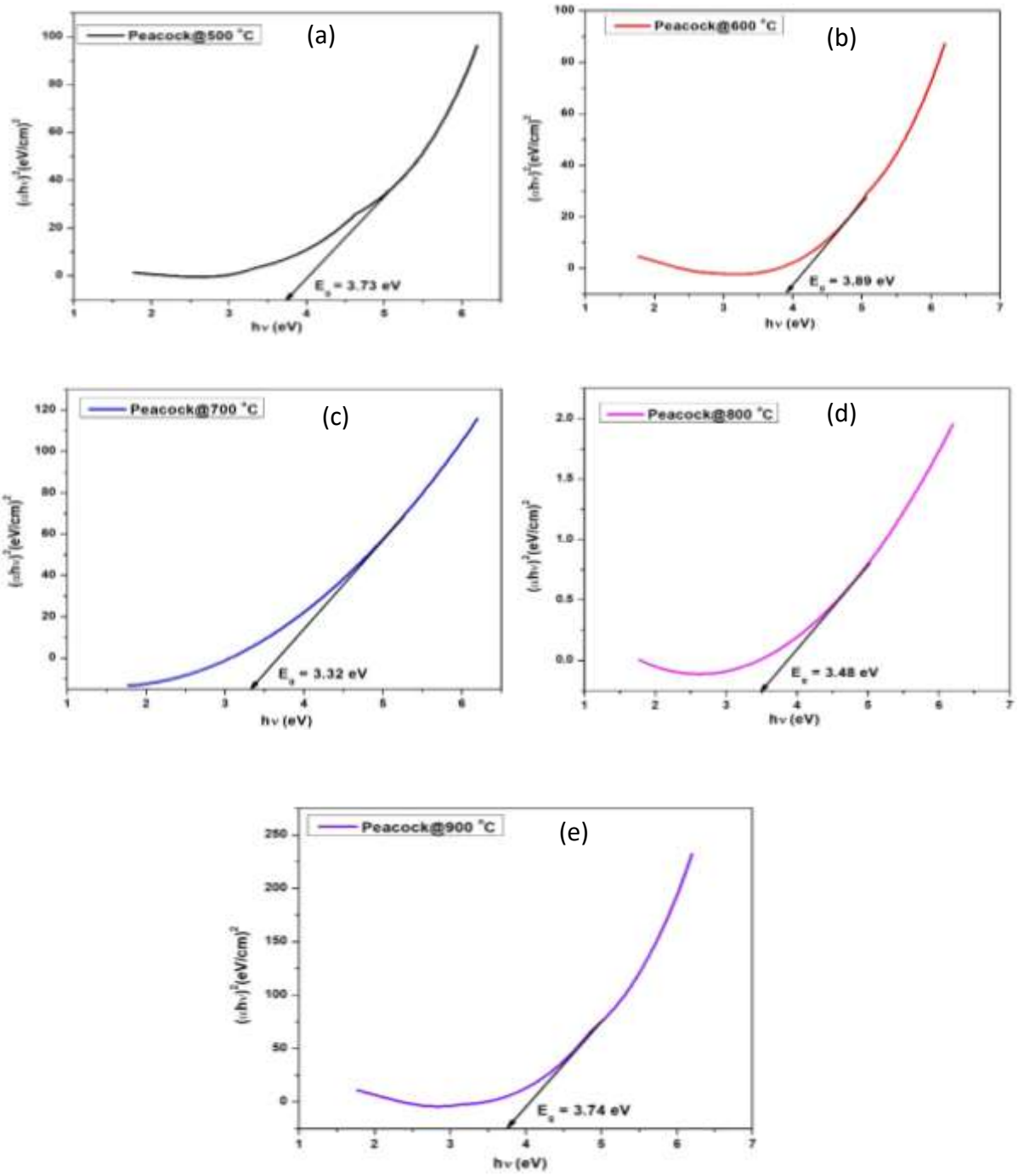

Figure 7(a-e). Energy bandgaps for Peacock flower dye-soaked nanofiber photoanodes

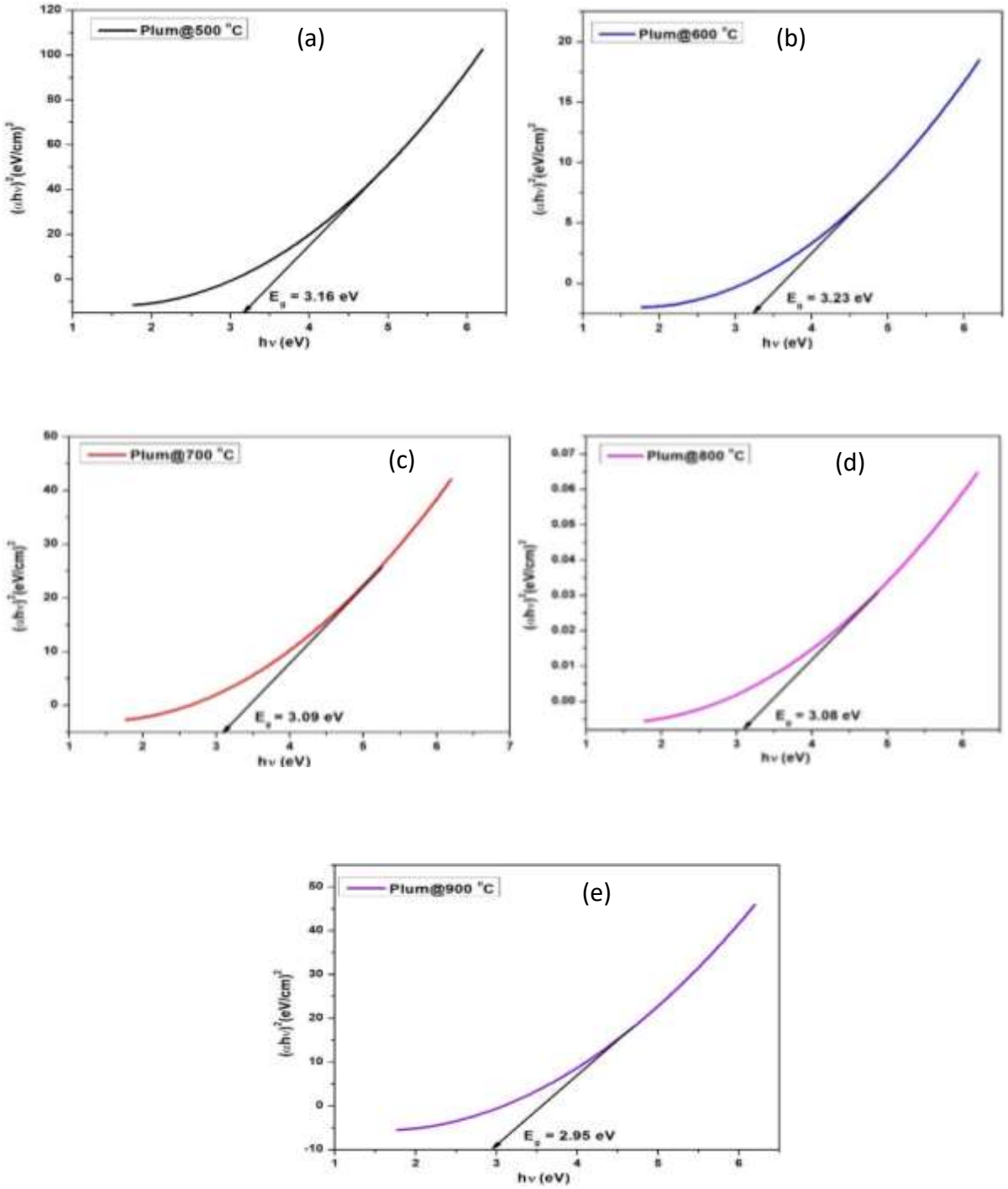

Figure 8(a-e). Energy bandgaps for Plum dye-soaked nanofiber photoanodes

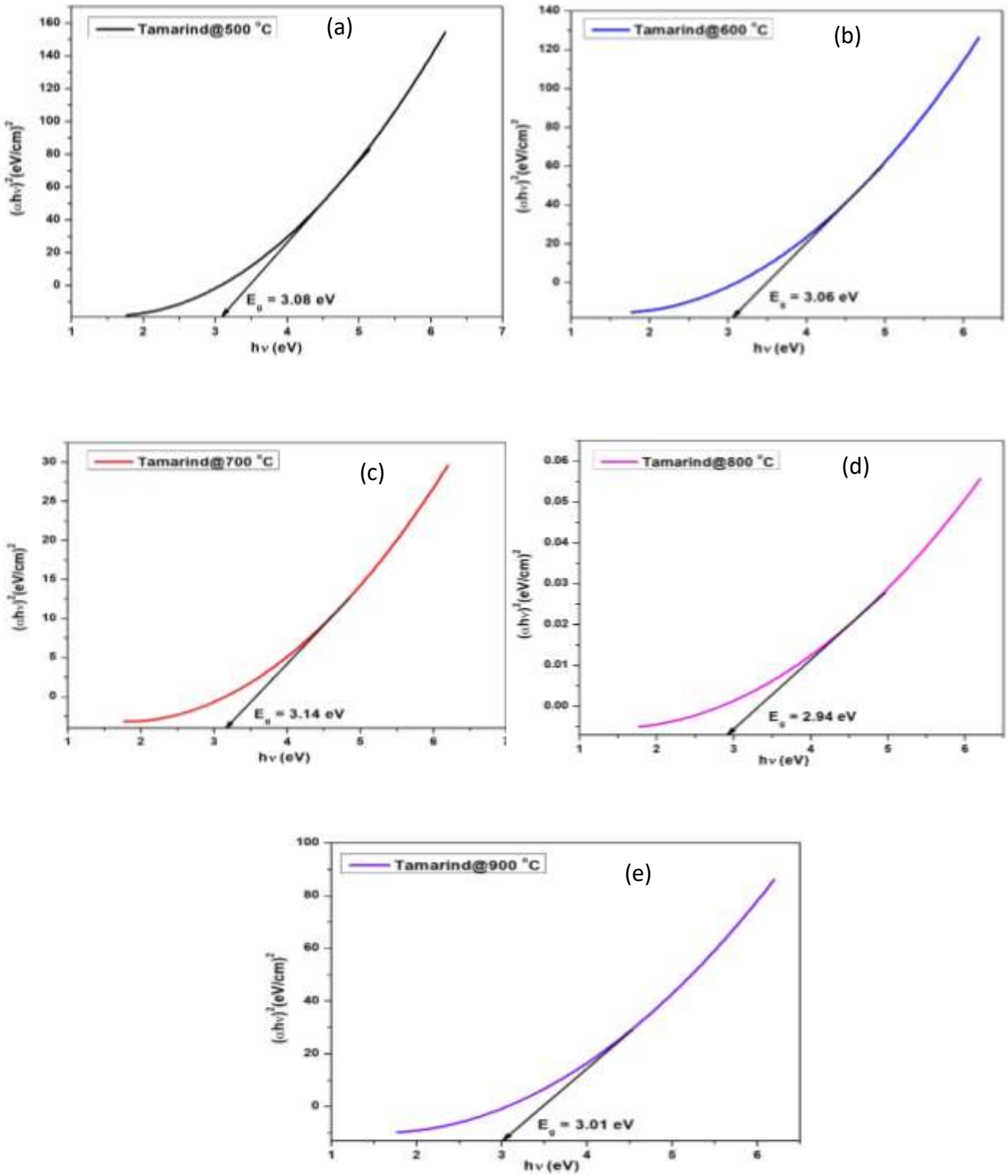

Figure 9(a-e). Energy bandgaps for Tamarind dye-soaked nanofiber photoanodes

Conclusion

Zinc stannate (Zn_2SnO_4) nanofibers exhibited decreasing optical band gap energies with rising temperatures: 3.50 eV at 500 ˚C, 3.20 eV at 600 ˚C, 3.18 eV at 700 ˚C, 3.17 eV at 800 ˚C, and 3.14 eV at 900 ˚C. These values align with optimal zinc stannate band gaps (3.2 - 3.7 eV). Dyes attached to Zn_2SnO_4 fibers showed absorption in the visible region (400 nm to 700 nm). Dye-sensitized solar cells (DSSCs) utilizing four tree bark natural dyes demonstrated solar

energy conversion potential. UV-Vis spectroscopy studied the optical properties of dye solutions, revealing that higher dye concentration correlated with increased photon absorption. Four bark dye solutions had band gap energies of 2.05 eV, 2.83 eV, 2.91 eV, and 2.56 eV for ethanol solvents. Testing Zn_2SnO_4 nanofibers before and after dye soaking confirmed their applicability in DSSCs, with the Peacock dye showing particular promise for light absorption and charge-carrier transport. Extracted dyes proved effective, showcasing their potential for environmentally friendly, low-cost applications in light energy harvesting.

Acknowledgments

I would like to express my sincere thanks to Professor Dr Yin Maung Maung, Professor and Head of the Department of Physics, University of Yangon, for his kind encouragement, guidance, and permission to perform this research work. I would like to thank Professor Dr Ye Chan, Professor and Head, Universities Research Center, University of Yangon, and Professor Dr Cho Cho Thet Department of Physics, University of Yangon, for their kind advice and suggestions for this research. I am deeply grateful to Dr Zin Min Myat, Associate Professor, Department of Physics, University of West Yangon, for her valuable guidance, helpful advice, and encouragement throughout this research work.

References

D. L. Young, H. Moutinho, Y. Yan and T. J. Coutts, J. Appl. Phys., 2002, 92, 310

F. Huang, Q. Wei, and Y. Cai, Surface functionalization of polymer nanofibers. Woodhead Publishing Limited, 2012. doi: 10.1533/9780857095640.1.92.

H. Zhu, D. Yang, G. Yu, H. Zhang, D. Jin and K. Yao, J. Phys. Chem. B, 2006, 110, 7631

J. G. López-Covarrubias, L. Soto-Muñoz, A. L. Iglesias, and L. J. Villarreal-Gómez, "Electrospun nanofibers applied to dye solar sensitive cells: A review," Materials (Basel)., vol. 12, no. 19, pp. 1–18, 2019, doi: 10.3390/ma12193190.

L. T. Yan et al., "Photoanode of dye-sensitized solar cells based on a ZnO/TiO2 composite film," Int. J. Photoenergy, vol. 2012, pp. 1–5, 2012, doi: 10.1155/2012/613969.

M. Afshari, "Introduction," Electrospun Nanofibers, pp. 1–8, 2017, doi: 10.1016/B978-0-08-100907-9.00001-5.

M. A. Alpuche-Aviles and Y. Wu, J. Am. Chem. Soc., 2009, 131, 3216

N. Canever, F. Hughson, T. J. Macdonald, and T. Nann, "Electrospinning of photocatalytic electrodes for dye-sensitized solar cells," J. Vis. Exp., vol. 2017, no. 124, pp. 1–7, 2017, doi: 10.3791/55309.

P. P. Das, A. Roy, and P. Sujatha Devi, "Zn2SnO4 as an Alternative Photoanode for Dye Sensitized Solar Cells: Current Status and Future Scope," Trans. Indian Ceram. Soc., vol. 75, no. 3, pp. 147–154, 2016, doi: 10.1080/0371750X.2016.1228482.

R. Qohhar, E. Supriyanto, Sujito, A. T. Nugroho, and A. Subekti, "Photoanode nanostructure optimization in dye-sensitized solar cell," AIP Conf. Proc., vol. 2278, 2020, doi: 10.1063/5.0015224.

S. Ramakrishna et al., "Chapter 1 - Introduction," Nanotechnology, vol. 7, no. 3, pp. 1–21, 1996, [Online]. Available:http://stacks.iop.org/0957-4484/7/i=3/a=009?key=crossref.b62a3c509c723c5a2561f1e 345fc 1706

S. N. Karthick, K. V. Hemalatha, S. K. Balasingam, F. Manik Clinton, S. Akshaya, and H. J. Kim, "Dye-sensitized solar cells: History, components, configuration, and working principle," Interfacial Eng. Funct. Mater. Dye. Sol. Cells, pp. 1–16, 2019, doi: 10.1002/9781119557401.ch1.

X. Shi, W. Zhou, D. Ma, Q. Ma, and D. Bridges, "Review Article Electrospinning of Nanofibers and Their Applications for Electrospinning of Nanofibers and Their Applications for," vol. 2015, no. May, 2015, doi: 10.1155/2015/140716.

GREEN SYNTHESIS OF SILVER NANOPARTICLES FROM *CENTELLA ASIATICA* (L.) LEAF EXTRACT AND THEIR ANTIMICROBIAL ACTIVITY*

Zaw Min Tun[1], Zin Min Myat[2]

Abstract

Silver nanoparticles (AgNPs) exhibit unique properties due to their size, distribution, and morphology, which contribute to their prominence in the expanding domain of nanotechnology. In this research, leaf extract from *Centella asiatica* L. was used to synthesize silver nanoparticles utilizing a green synthesis. The synthesized nanoparticles were characterized using a variety of experimental techniques, such as X-ray Diffraction (XRD), Scanning Electron Microscopy (SEM), Fourier Transform Infrared Spectroscopy (FTIR), and UV-Vis Spectroscopy. The resulting silver nanoparticles were evaluated for their antimicrobial activity against six microorganisms: *Aspergillus flavous, Bacillus subtilis, Candida albicons, Escherichia coli, Klebsiella pneumonia, and Pseudomonas flurorescens*. This research leads to comprehensive and valuable results, due to their primary physicochemical characteristics and some of their potential medical uses.

Keywords: Green synthesis, XRD, SEM, FTIR, UV-Vis and Antimicrobial activity

Introduction

Nowadays, silver nanoparticles (AgNPs) have attracted a great deal of attention due to the excellent physicochemical properties and consequently their significance range of application in the fields of physics, chemistry, materials science, renewable energies, environmental remediation and biomedicine (Jamil Ahmed, et al. 2015). Silver nanoparticles exhibits good conductivity, high chemical stability, catalytic activity and antimicrobial activities (Song et al. 2009). In medicine, silver nanoparticles have widely applications including skin ointments and creams to avoid infection of burns and open wounds, resistance against microbes, drug delivery, antibiotics and immune chromatography, tissue/tumour image, anticancer activities and identification of pathogens in clinical specimens (Durán et al. 2005). Nanoparticles can be synthesized using many strategies including chemical reduction, physical vapor condensation and biological approaches. But physical and chemicals used are toxic, flammable and lead to non-ecofriendly (Verma et al. 2016). Biological method of nanoparticles synthesis using microorganisms, enzymes and plant or plant extract have advantages over other methods, because these approaches are cost-effective, one step in nature, environment friendly, cleaner synthesis route and often results in more stable materials (Logeswari et al. 2015). Plant extracts are rich bio-reducing agents that can reduce silver ions to silver nanoparticles. In the present research, the silver nanoparticles were synthesized by the reduction of $AgNO_3$ solution using medicinal plant *Centella asiatica*. *Centella asiatica* (L.) Urban., (Family Apiaceae), commonly known as Asiatic pennywort or gotu kola, is a well-known herb that has been used in both medicinal and culinary practices of many countries. It contains vitamins especially vitamin B, vitamin C, vitamin G and some amino acids etc. This plant was recommended for the treatment of various skin conditions such as leprosy, lupus, asthma, ulcers, wound healing, diarrhea, memory improvement, disease of the female genitourinary tract, antibacterial, antifungal, and anti-cancer (Chatterjee TK et al.1992). Some basic principles of "green synthesis" can be explained by several components like minimization of waste, reduction of pollution and the use of safer (or nontoxic) solvent as well as renewable feedstock.

---

* Third Prize (2024)

[1] Department of Physics, Dagon University

[2] Department of Physics, University of West Yangon

Experimental Procedures

Preparation of *Centella asiatica* (L.) Leaf Extract

Fresh leaves of *Centella asiatica* L. were collected from the Dagon University Campus. Firstly, 20 g of leaves were properly washed in both tap water and distilled water. Next, they were crushed and ground with a pestle and mortar by adding distilled water dropwise. After mixing the paste with 150 ml of distilled water, it was heated on a hot plate at 80 ˚C for 15 minutes. Then, it is set to cool down, and the extract solution is filtered by filter paper until no debris is present.

Synthesis of Silver Nanoparticles

Silver nitrate ($AgNO_3$) was analytically pure and used straight out of the container without any additional processing. First, 1mM of silver nitrate solution were dissolved in 100 ml of distilled water and stirred for 15 minutes. Then, these solutions were mixed with two separate volumes of leaf extract solution (10 ml and 30 ml) at 60 ˚C, 70 ˚C, and 80˚C for 15 minutes. During stirring, the yellowish color of the solution gradually changed to dark brown upon the addition of the leaf extract. The silver solution was considered ready once the dark brown color change was observed and the time recorded at 80˚C. The mixture solution was then centrifuged and washed three times with deionized water to remove the by-product. Finally, the silver nanoparticles were formed when these precipitated particles were heat treated at 300˚C for 1 h. Figure 1 showed the synthesis procedure of green synthesis of silver nanoparticles.

(a) leaves

(b) Leaf extract solution

(c) Silver nitrate solution

(d) Silver solution

(e) Silver nanoparticles

Figure 1. Synthesis procedure of green synthesis of silver nanoparticles

Characterization Techniques

The green synthesized silver nanoparticles will be characterized by XRD, SEM, FTIR and UV-Vis spectroscopy for structural, morphological, chemical and optical properties. The antimicrobial activity will be studied with these silver nanoparticles using *Centella asiatica* (L.) leaf extract.

Results and Discussion

XRD Analysis of Silver Nanoparticles from Centella asiatica (L.) Leaf Extract

The silver nanoparticles were obtained by green synthesis and XRD technique was used to examine the phase analysis, particle structure and crystallographic investigation and lattice parameters. Sample was scanned from 10˚ to 80˚ in diffraction angle 2θ with a step-size of 0.02˚. The XRD profiles of silver nanoparticles synthesized from different leaf extract concentrations (10 ml and 30 ml) at 300˚C are shown in Figure 2. As observed, the peaks at 2θ values of 38.1°, 44.4°, 64.5°, and 77° correspond to the (111), (200), (220), and (311) crystal planes, respectively, according to JCPDS No. 04–0783. According to the XRD pattern, the growth direction of silver nanoparticles was mostly in the (111) plane. A few additional peaks (especially at 35.25° and 40.21°) were appeared, which are weaker than the silver peaks. These peaks are due to the crystallization of organic compounds that are responsible for covering and stabilizing silver nanoparticles. A similar result has been reported in the investigation of silver nanoparticles synthesized by the green method (Kumar et al. 2009). The crystallite size was calculated from the XRD peak broadening of the (111), (200), (220) and (311) peaks using Scherrer's formula. The average crystallite sizes of silver particles were in the range of 55.05 nm for 10 ml of extract solution and 54.33 nm for 30 ml **o**f extract solution.

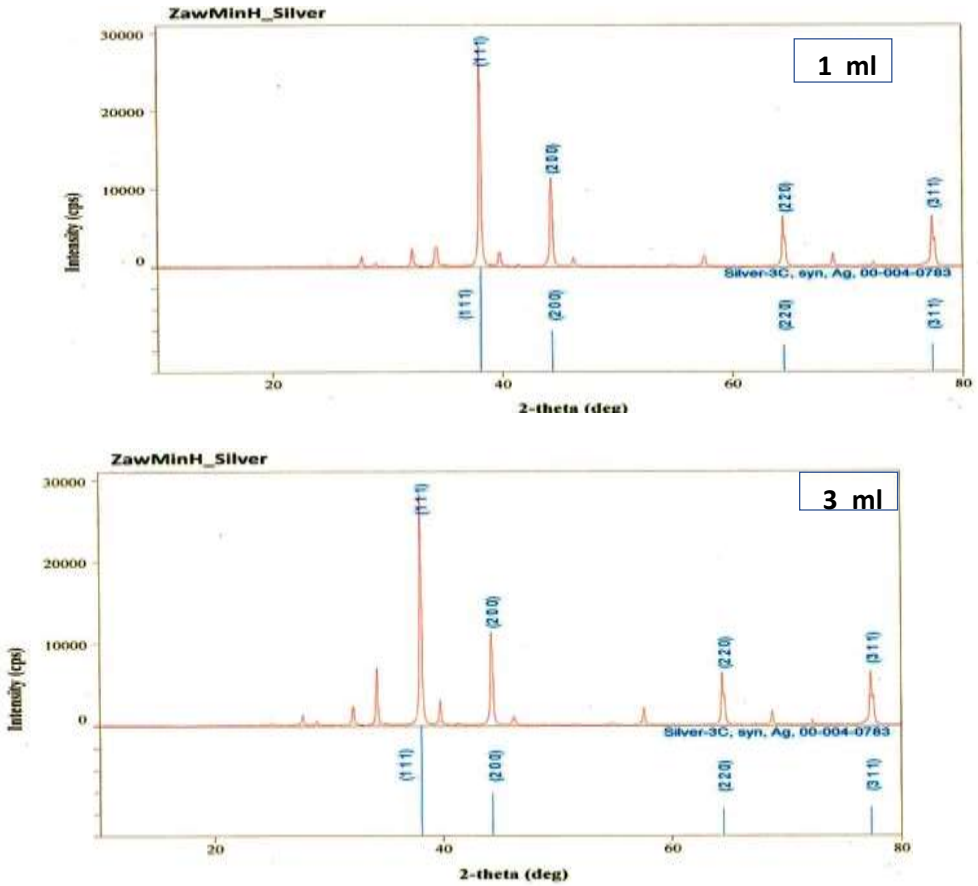

Figure 2. XRD pattern of silver nanoparticles with different leaf extract concentrations

SEM Analysis of Silver Nanoparticles from *Centella asiatica* L. Leaf Extract

The microstructural properties of silver nanoparticles synthesized using the green synthesis method was examined by scanning electron microscopy (SEM). Figure 3 shows the SEM images of silver nanoparticles synthesized with 10 ml and 30 ml leaf extract solutions. The grain sizes were calculated by using image J software. For the 10 ml extract solution, the

average grain size of the silver nanoparticles was calculated to be 46.30 nm. The nanoparticles exhibited a relatively uniform distribution, though some larger particles were present. The overall morphology showed slight roughness, with pores scattered throughout. In contrast, the nanoparticles synthesized with the 30 ml extract solution exhibited a smaller average grain size of 30.98 nm**.** The nanoparticles displayed a more uniform size distribution, with fewer pores and a denser, smoother structure compared to the 10 ml extract solution. No visible cracks were observed, indicating enhanced structural stability. These results suggest that increasing the leaf extract concentration leads to a reduction in both grain size and pore size**,** resulting in more uniform nanoparticles with improved structural integrity.

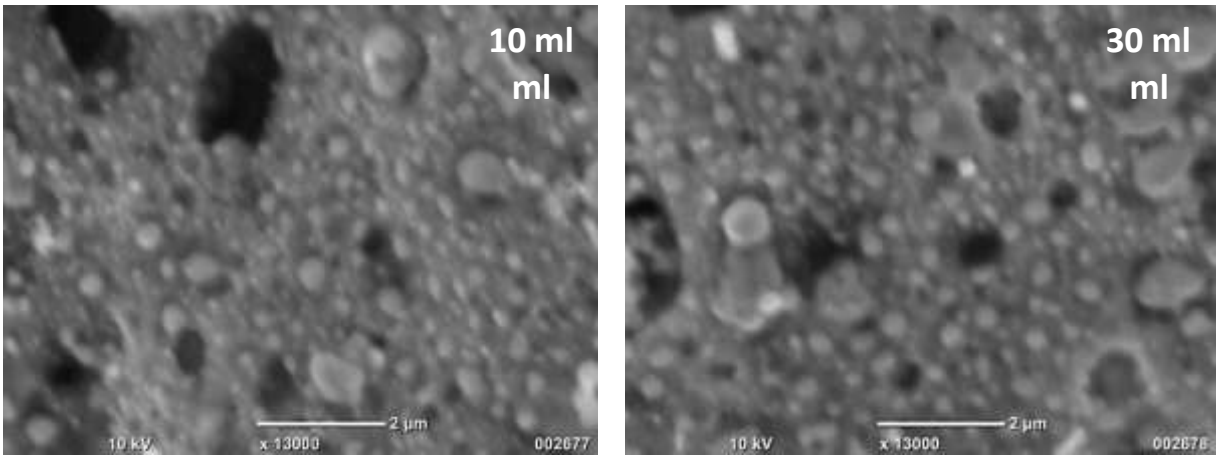

Figure 3. SEM image of silver nanoparticles with different leaf extract concentrations

FTIR Analysis of Silver Nanoparticles from *Centella asiatica* (L.) Leaf Extract

Fourier Transform Infrared Spectroscopy (FTIR) is important tool to characterize the molecular orientation in the condition of material transition, detecting functional groups and characterizing covalent bonding information. The FTIR spectra of silver nanoparticles in case both of 10 ml and 30 ml leaf extract solution were shown in Figure 4. According to FTIR analysis, the prominent bands of absorbance were observed at around 3270.93 cm^{-1}, 3210.69 cm^{-1}, 2920.82 cm^{-1}, 2116.99 cm^{-1}, 1551.02 cm^{-1}, 1552.05 cm^{-1}, 1375.25 cm^{-1},1304.14 cm^{-1}, 1270.75 cm^{-1}, 1242.27 cm^{-1}, 1030.07 cm^{-1}, 1027.96 cm^{-1} and 1024.15 cm^{-1} for silver nanoparticles (10 ml extract solution) and silver nanoparticles (30 ml extract solution) respectively. The peak in the range of above these values were assigned as –OH stretching in alcohols with strong hydrogen bond, C=O bond of the carbonyl group and the stretching variations of amides, N-O stretching, C-O stretching of alcohol and phenol, C= C groups or from aromatic rings and alkyne bonds respectively. The presence of these peak values confirmed that the silver nanoparticles were converted by plant secondary metabolites with functional groups such as ketone, aldehyde, carboxylic acid and proteins. The presence of these groups is due to the stability of the silver nanoparticles.

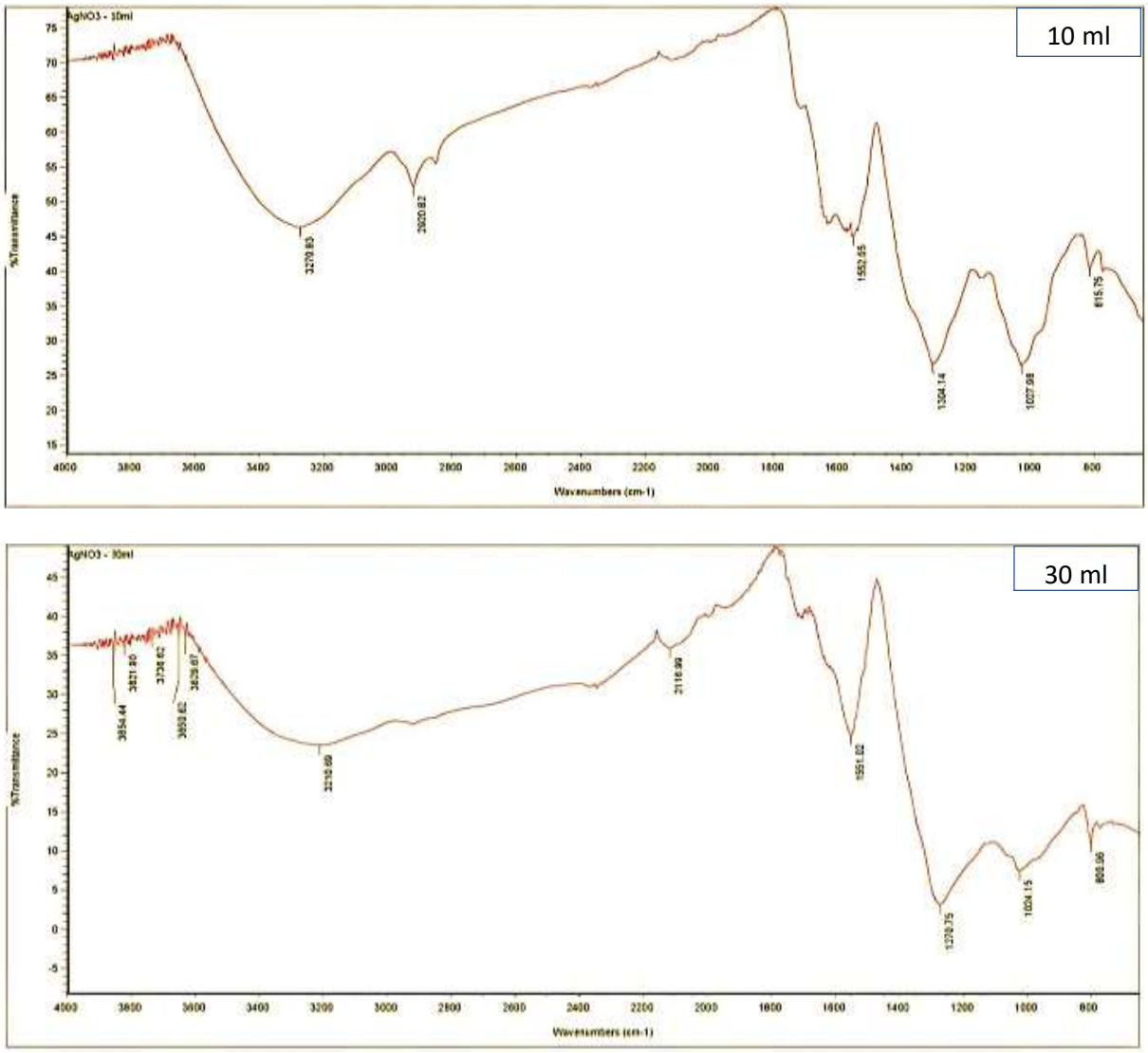

Figure 4. FTIR spectrum of silver nanoparticles with different leaf extract concentrations **UV-Vis Analysis of Silver Nanoparticles from *Centella asiatica* (L.) Leaf Extract**

The optical absorption spectra for a range of samples of silver nanoparticles with different *Centella asiatica* L. leaf extract concentration was obtained in UV/ VIS/ NIR region (up to1100 nm) using a SHIMADZU U-1800 UV/ VIS Double Beam Spectrophotometer. The absorption spectra of silver nanoparticles with different *Centella asiatica* L. leaf extract concentration were shown in Figure 5. As the different leaf extracts were added to aqueous silver nitrate solution, the colour of the solution changed from faint light to yellowish brown to reddish brown and finally to colloidal brown indicating silver nanoparticles formation. The colour change is due to the Surface Plasmon Resonance phenomenon. From different literatures, it was found that the silver nanoparticles show SPR peak at around (350 nm – 550 nm). In this result, the dominant sharp band of silver nanoparticles was observed around 392 nm in case of 10 ml extract solution whereas the band for 30 ml extract solution was found around 430 nm. This blue shift in the 30 mL extract solution indicates the formation of smaller nanoparticles, as the SPR peak shifts to a lower wavelength with decreasing particle size (Zielińska et al. 2009). Additionally, the intensity of absorption peak increases with increasing more extract solution. It was observed that the silver nanoparticles were dispersed in the aqueous solution with no evidence for aggregation in UV-Vis absorption spectrum.

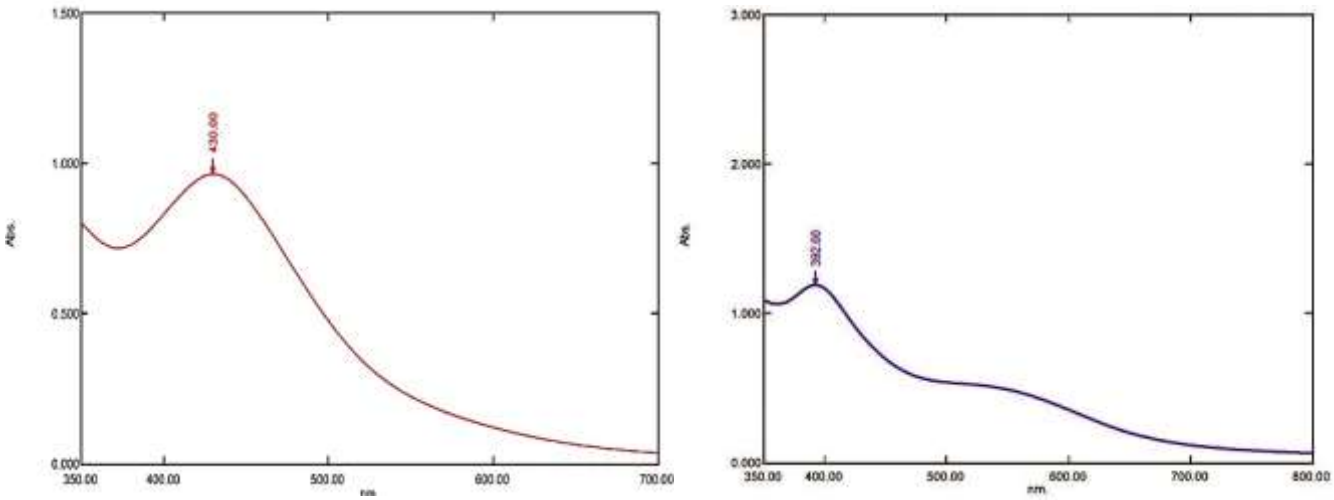

Figure 5. Absorption spectrum of silver nanoparticles with different leaf extract concentrations

Antimicrobial activity of microorganisms by paper disc diffusion assay

Isolated bacterial strains grown on nutrient agar were inoculated into 50 ml conical flasks containing 10 ml of sterile growth medium. Then, they were incubated for 72 hours at 30 °C on a reciprocal shaker starting at 200 rpm. In this research, test organisms were *Aspergillus flavous, Bacillus subtilis, Candida albicons, Escherichia coli, Pseudomonas flurorescens, Klebsiella pneumonia.* The assay medium was mixed with 0.3 ml of test organisms and then transferred into plates. After solidification, test plates were covered with paper discs that had been impregnated with broth samples. The plates were then incubated at 30 °C for 24 to 36 hours. After for 24-36 hours, the test discs' surrounding "inhibitory zones" or clear zones indicate the presence of bioactive substances that prevent test organism growth. Table 1 and Figure 6 display the widths of the inhibition zones that appeared. According to experimental results, the enhanced antimicrobial activity observed in AgNPs synthesized with a higher extract concentration is attributed to their smaller particle size, which leads to increased surface area, improved bacterial interaction, and greater silver ion release. Smaller nanoparticles maintain closer contact with bacterial membranes, facilitating deeper penetration into microbial cells and enhancing their reactivity with biomolecules, leading to increased antimicrobial effectiveness.

Table 1. Inhibitory zones of silver nanoparticles with two different volume of leaf extract solution

No	Test organisms	Inhibition zones (mm)		Diseases
		10 ml extract solution	30ml extract solution	
1	*Aspergillus flavous*	8	8	Aspergillosis, Allergic reactions
2	*Bacillus subtilis*	14	28	Food poisoning, Gastroenteritis
3	*Candida albicons*	12	16	Yeast infections, Oral thrush
4	*Escherichia coli*	12	16	Urinary tract infections, Diarrhea
5	*Klebsiella pneumonia*	12	28	Pneumonia, Urinary tract infection
6	*Pseudomonas flurorescens*	8	8	Skin infections, Respiratory infections

Control media without bacteria	Zone of inhibation (10ml extract solution)	Zone of inhibation (30ml extract solution)

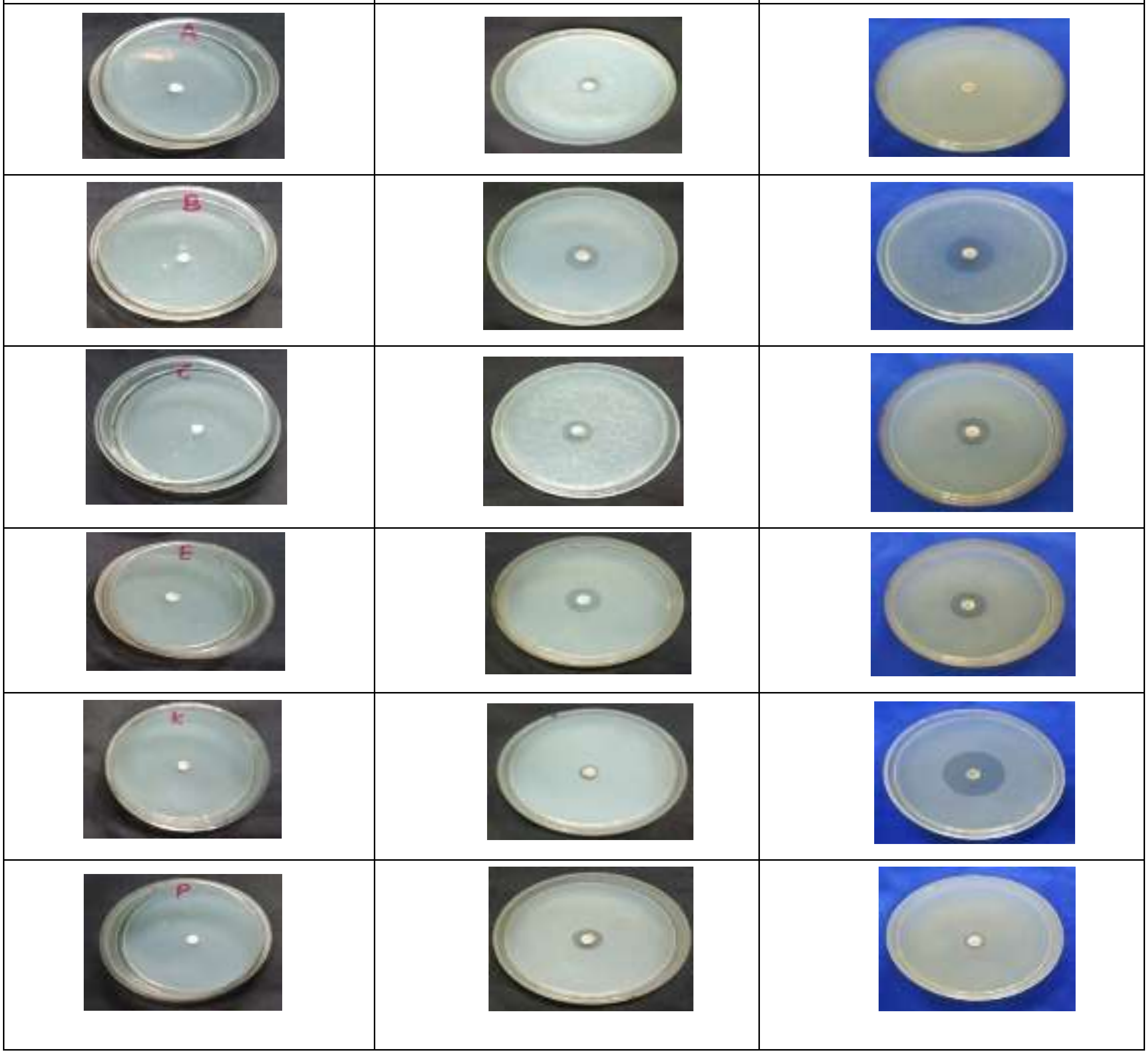

Figure 6. Comparing control and inhibitory zones against *Aspergillus flavous, Bacillus subtilis, Candida albicons, Escherichia coli, Klebsiella pneumonia, Pseudomonas flurorescens* of silver nanoparticles

Conclusion

In conclusion, the synthesis of silver nanoparticles using the leaf extract of *Centella asiatica* L. has been successfully demonstrated. XRD results showed that the average crystallite sizes of AgNPs were 55.05 nm for a 30 ml extract solution and 54.33 nm for a 10 ml extract solution in a cubic structure. According to the SEM data, the average particle sizes were found to be 30.98 nm and 46.30 nm with spherical shapes. The smaller particle size of 30.98 nm was observed with the larger extract volume, suggesting that a higher extract concentration leads to the formation of smaller nanoparticles. FTIR confirmed that plant compounds were involved in reducing and stabilizing the nanoparticles. According to UVVis analysis, there were no signs of aggregation, and the silver nanoparticles were evenly distributed throughout the aqueous solution. This indicates that the plant compounds prevented particle clumping, leading to a uniform distribution of nanoparticles in solution. Importantly, the antimicrobial results demonstrated that AgNPs synthesized with the 30 mL extract solution exhibited significantly enhanced antibacterial activity, ascribed to their smaller particle size and increased surface area, which promote stronger interactions with microbial cell membranes. From a technological

perspective, these silver nanoparticles have promising applications in the biomedical field. This simple synthesis method offers several advantages, including cost-effectiveness and compatibility with medical and pharmaceutical applications, particularly in wound healing, antimicrobial coatings, and pharmaceutical formulations.

Acknowledgements

I would like to sincerely thank Professor Dr U Win, Head of the Department of Physics, Dagon University for his encouragement to conduct this research and his kind permission to carry out this research work.

References

Chatterjee, T. K., Chakraborty, A., Pathak, M., and S. G. E., (1992) "Effect of plant extract Centella asiatica (Linn.) on cold restraint stress ulcer in rats" Indian Journal of Experimental Biology, vol. 29, pp. 1293014.

Durán, N., Marcato, P. D., Alves, O. L., De Souza, G. I. H., and Esposito, E., (2005) "Mechanistic aspects of biosynthesis and usage of silver nanoparticles by several Fusarium oxysporum strains" Journal of Nanobiotechnology, vol. 3, pp. 1-7.

Kumar, V., and Yadav, S. K., (2009) "Plant-mediated synthesis and usage of silver and gold nanoparticles and their applications" Journal of Chemical Technology and Biotechnology, vol. 84, no. 2, pp. 151-157.

Logeswari, P., Silambarasan, S., and Abraham, J., (2015) "Synthesis and usage of silver nanoparticles using plant extracts and analysis of their antimicrobial property" Journal of Saudi Chemical Society, vol. 19, no. 3, pp. 311-317.

Muhammad Jamil Ahmed, Ghulam Murtaza, Ansar Mehmood, and T. M. B., (2015) "Green synthesis and antibacterial activity of silver nanoparticles using leaves extract of Skimmia laureola" Materials Letters, vol. 153, pp. 10-13.

Song, J. Y., and Kim, B. S., (2009) "Rapid biological synthesis and usage of silver nanoparticles using plant leaf extracts" Bioprocess and Biosystems Engineering, vol. 32, no. 1, pp. 79-84.

Verma, A., and Mehata, M. S., (2016) "Controllable synthesis and usage of silver nanoparticles using Neem leaves and their antimicrobial activity" Journal of Radiation Research and Applied Sciences, vol. 9, no. 1, pp. 109-115.

Zielińska, A., Skwarek, E., Zaleska, A., Gazda, M., and Hupka, J., (2009) "Preparation and usage of silver nanoparticles with controlled particle size" Procedia Chemistry, vol. 1, no. 2, pp. 1560-1566.

ELECTRICAL PROPERTIES OF REDUCED GRAPHENE OXIDE-CONDUCTIVE COPOLYMER COMPOSITE FILMS*

Wint Nandar Soe[1], Than Than Htwe[2], Nyunt Win[3] and Cho Cho Thet[4]

Abstract

Conductive composites include any composite having significant electrical conductivity. An electrically conductive filler such as carbon-based materials like graphene when added to insufficient quantities of a polymeric resin, a conductive composite is formed. This research focus on the preparation of the conductive polymer using the organic copolymer and the inorganic particles. Copolymer P(Py-co-FPy) films were prepared by chemical copolymerization of pyrrole (Py) and pyrrole -2carboxaldehyde (FPy) in the trifluoroacetic acid (TFA) catalyst and chloroform ($CHCl_3$) solvent. As the inorganic component, reduced graphene oxide (rGO) was synthesized by chemical reduction method. In preparation of P(Py-co-FPy)-rGO composite films the different grams of rGO powders are incorporated into the copolymer matrices by ex-situ chemical copolymerization through spin coating technique. The structural and electrical properties of copolymer and composite films were characterized by Fourier transform infrared spectroscopy (FTIR) and the conductivities of the composite films are increased with the concentration of inorganic particles. It is found that the conductivities of P(Py-co-FPy)-rGO (0.3 g) composite film are greater than those of pure copolymer P(Py-co-FPy) film.

Keywords: copolymer, composite film, conductivity, four probe method, rGO, sheet resistivity

Introduction

Recently, lightweight conductive composite materials with high electrical conductivity have been focused in many applications including battery components, electrodes, electromagnetic interference shields and circuitry components. Conductive composites include any composite having significant electrical conductivity. The conductivity of the composites depends on the filler contents. The electrical conductivity of the composites can be changed by several orders of magnitude by small variation of the filler content (Qu et al., 2018). Thus, the conductivity of the composites can be controlled by varying the volume fraction of the conductive filler for the various applications. The values of electrical conductivity of polymers are between 10-14 and 10-17 Scm-1. The composite materials must have an electrical conductivity in the range between 10-12 and 10-2 Scm-1 for the conductive applications (Alemour et al., 2019).

The electrical conductivity of conductive composites depends on filler type, shape, size, and filler dispersion and distribution in the composite. The conductive filler type has an important effect on the electrical conductivity of the composite. Carbon based materials such as graphite and graphene can be used as conductive filler (Mohammad et al., 2022; Kumar et al., 2017). In addition, the electrical conductivity of each material is different and thus, the electrical conductivity of the composite will be different depending on each filler type used.

Conducting polymers (CPs) are regarded as promising pseudo-capacitive materials because of their large specific capacitance and the characterization of many active sites. Most commonly used polymers are polyaniline (PANI), polypyrrole (PPy), polythiophene (PTh) and poly 3,4-ethyl-enedioxythiophene (PEDOT). Besides, various doping types of conducting polymers are used in supercapacitor as electrode materials. The lifecycles CPs are shorter than those of carbon-based materials. Conducting polymers are significant electrode materials for pseudocapacitors due to their high capacity, improved conductivity, ease of synthesis, and low

---

* Special Award (2024)

[1] Department of Physics, University of Yangon
[2] Department of Physics, Yenanchaung University
[3] Department of Physics, Pathein University
[4] Department of Physics, University of Yangon

cost. These polymers are often composited with other materials such as carbon nanotubes or metal oxides in order to further enhance their electrochemical properties. This hybrid approach can improve the overall performance of supercapacitors, including their capacitance, cycle life, and energy density. The materials for electrolyte and electrode are crucial in supercapacitors.

Carbon-based electrode materials are frequently used in supercapacitors because of high surface area, good electrical conductivity, chemical stability, versatility and costeffectiveness. These properties are contributed to the high-power density, long cycle life and overall efficiency of supercapacitors. Among the carbon derivatives materials for supercapacitors, reduced graphene oxide (rGO) has garnered considerable interest due to its superior properties including strong mechanical stability, superior electrical conductivity, and large surface area. rGO is a suitable surface area compared to graphene oxide (GO) since it can enhance its ability to store charge which in turn improve the capacitance and overall performance of supercapacitors. rGO generally shows better electrochemical stability, making it more reliable for long-term applications in energy storage devices. In this work, the electrical properties of reduced graphene oxide composited with copolymer film is investigated by four probe method for the application of supercapacitors.

Experimental Details

Preparation of P (Py-co-FPy) Copolymer Films

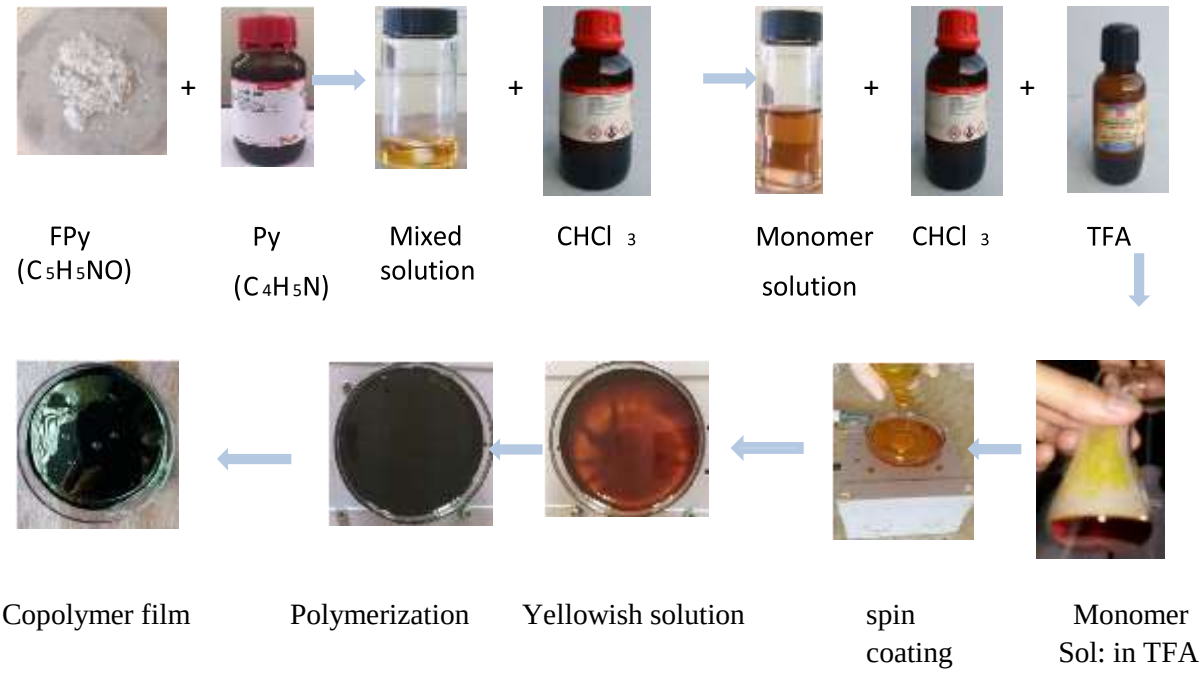

Figure 1 Preparation of P (Py-co-FPy) copolymer film

Copolymer solution is prepared by 207 μL of pyrrole (C4H5N) and 286 mg of pyrrole2-carboxaldehyde (C5H5NO) in 2 mL of chloroform (CHCl3) (Hoshina and Kobayashi, 2012). Then, they were stirred at the room temperature (RT) for 1h in order to form homogeneous monomer brown solution. Then, the mixture containing of 2 mL of CHCl3 and 1 mL of trifluoroacetic acid (TFA) are added to the monomer solution. As a result, the color of the solvent immediately changes from transparent brown to yellowish red. Then, the mixed solution is spin-coated onto the 9 cm diameter of the Petri dish at 25 rpm by using a homemade spin coater. The spin coating process is carried out for 2:30 h at room temperature to be completed polymerization process. Finally, a metallic greenish copolymer film was casted into 11 the Petri dish as shown in

Figure 1. After that, the film was washed by distilled water until all residuals of reaction in the film is completely removed. Then, the film was washed again with acetone and dried in a vacuum desiccator for 24 h. This film was chemically doped by iodine (I2) by before FTIR and four probe measurements.

Preparation of P (Py-co-FPy) – rGO Conductive Composite Films

Composite films were prepared by ex-situ polymerization method. Firstly, different weight of rGO powders including 0.1, 0.15, 0.2, 0.3 g were mixed with the monomer solution. The mixture solution was stirred for several days until to become the well dissolved solution. Then, the mixed solvent of 2 mL CHCl3 and 1 mL TFA are added to the homogeneous solution. Then, the solutions were spin-coated onto the Petri dishes. After that, the films were washed by distilled water until all residuals of reaction in the film is completely removed. Then, the films were washed again with acetone and dried in a vacuum desiccator for 24 h. Finally, composite films were successfully obtained as presented in Figure 2. All films were doped by iodine (I2) before four probe measurement.

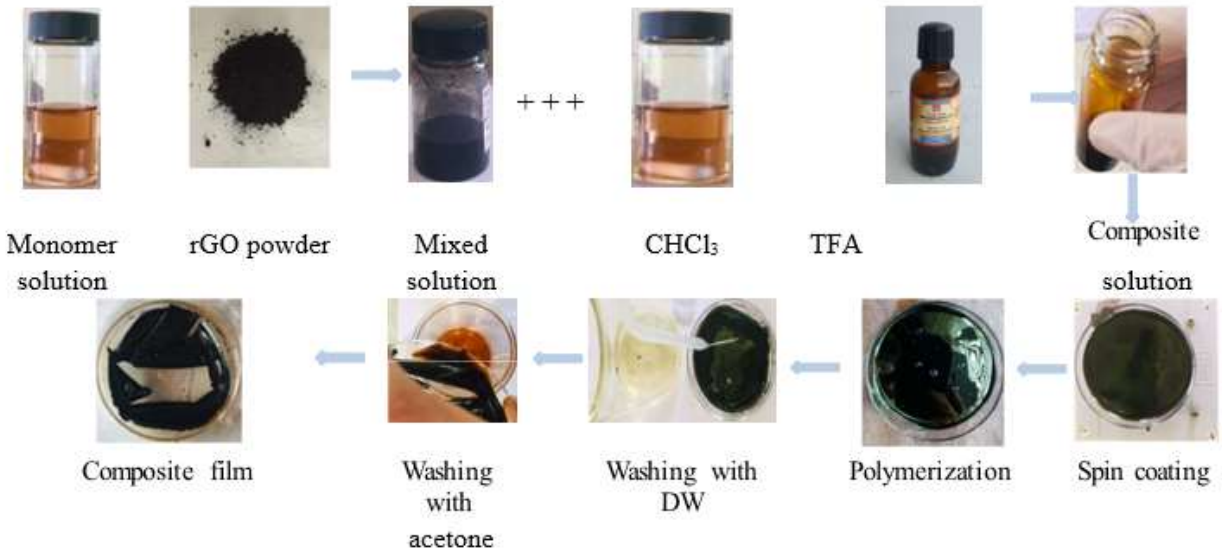

Figure 2 Preparation of composite film

Results and Discussion

FTIR analysis is carried in order to study the compound identification of pure and composite films. FTIR spectra of the films before and after iodine doped are shown in Figure 3. Before I2 doping, the peaks at 3361.88, 3384.27, 3366.68, 3380.28, 3398.67 cm-1 are due to the O-H stretching vibration. The peak of C = N stretching is occurred at 1658.64, 1653.84, 1645.05, 1655.44, 1661.04 cm-1 respectively. The peak for C-F bond at 1476.95, 1487.33, 1477.13, 1481.77 cm-1. The peaks at 799.82, 710.26, 789.43, 792.63, 797.42 cm-1 are C-H bonding. The peaks at 1174.06,1176.45, 1180.45, 1177.25, 1176.45 cm-1 are related to the C-O stretching of amine group. After I2 doping, the peaks observed at 3341.09, 3343.49, 12 3359.48 cm-1 are assigned to O-H stretching vibration. The peaks of C=C stretching at found at 1661.04 cm-1and the absorption bands at1587.47, 1595.47 cm-1 are vibration mode of the N-H bending (Yang et al., 2007). The peaks at 794.22, 697.47, 797.42 cm-1 are aromatic C=C bending. The peaks at 1121.28, 1128.48, 1134.87 cm-1 can be related to C-O stretching (Factors, I.R.). One more additional peak within 600 – 480 cm−1 regions are due to the presence of iodine which is corresponded to aliphatic C–I stretch. Thus, iodine atoms are incorporated into backbone of

copolymers.

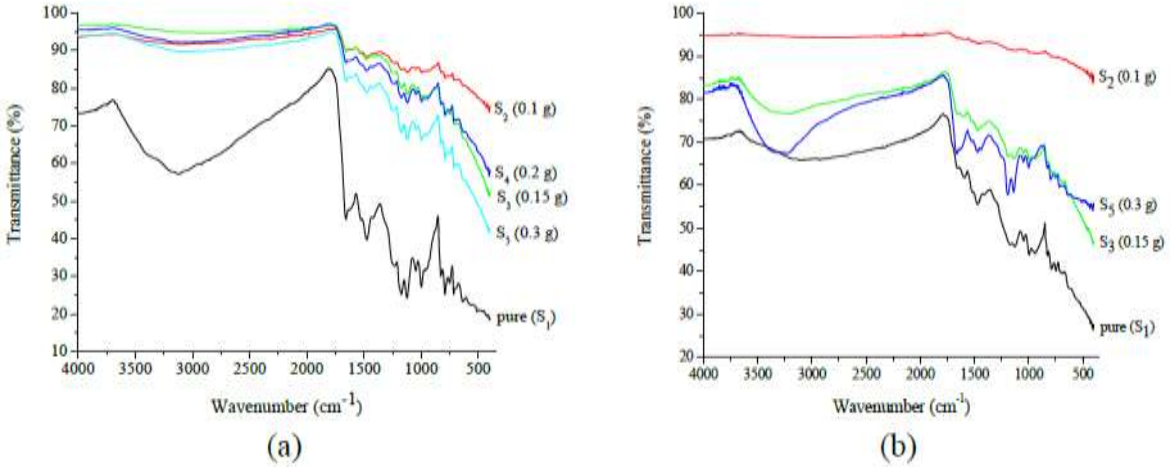

Figure 3 FTIR spectra of films (a) before and (b) after iodine doping

Figure 5 shows the structure of the composite film was further studied by X-ray diffraction (XRD). In the case of rGO an intense broad peaks at 24.64˚and 26.40˚which are very close to reduced graphene oxide's peak and its interlayer distance were 0.36 Å and 0.34 Å. The XRD pattern of copolymer shows figure diffraction peaks extending around 15 - 24˚. The diffraction peak of the composite, the diffraction pattern of rGO with 2θ = 26.50˚. The peak confirm the presence of rGO in the composite. On the other hand, the peak 2θ = 20.7˚confirm the presence of polymer (Bejjanki and Puttapati,2023).

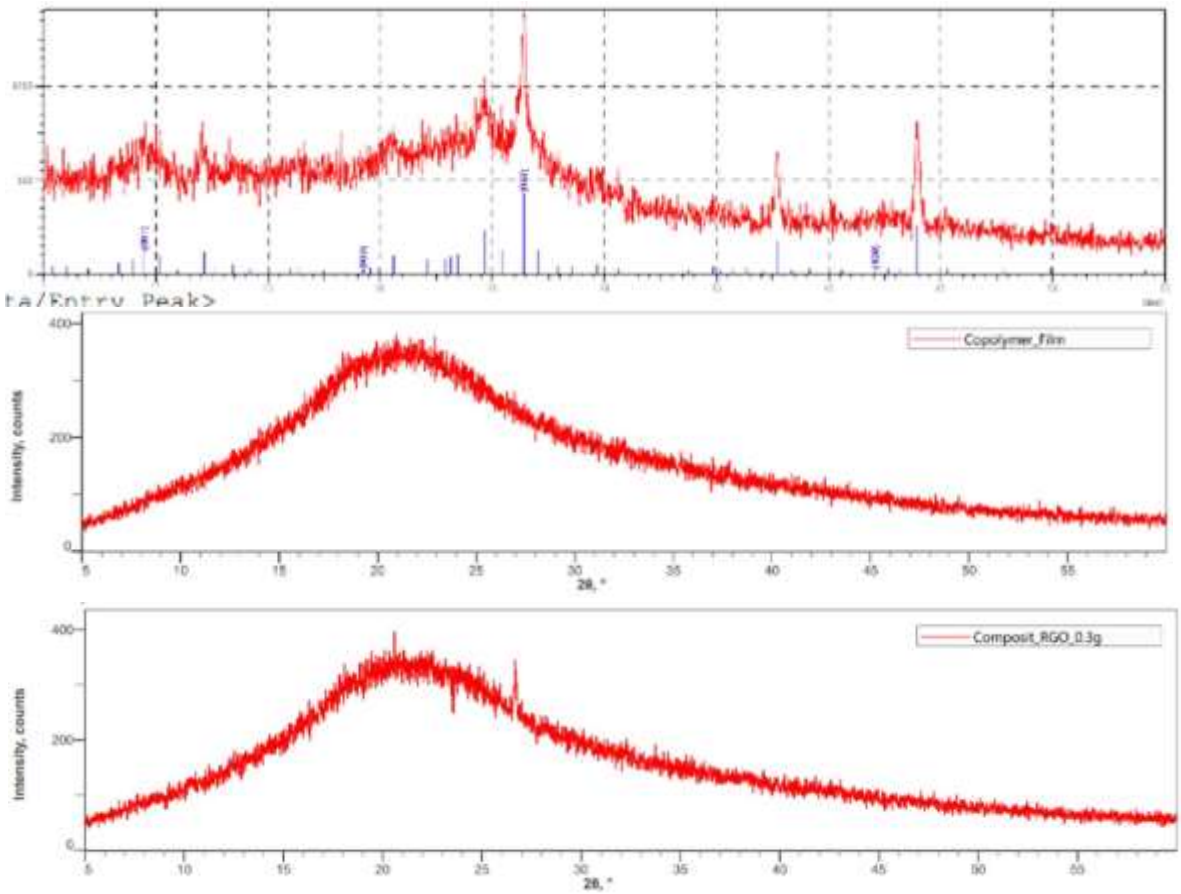

Figure 4. (a) XRD spectrum of rGO powder, XRD spectra of films (b) pure copolymer film and (c) composite film

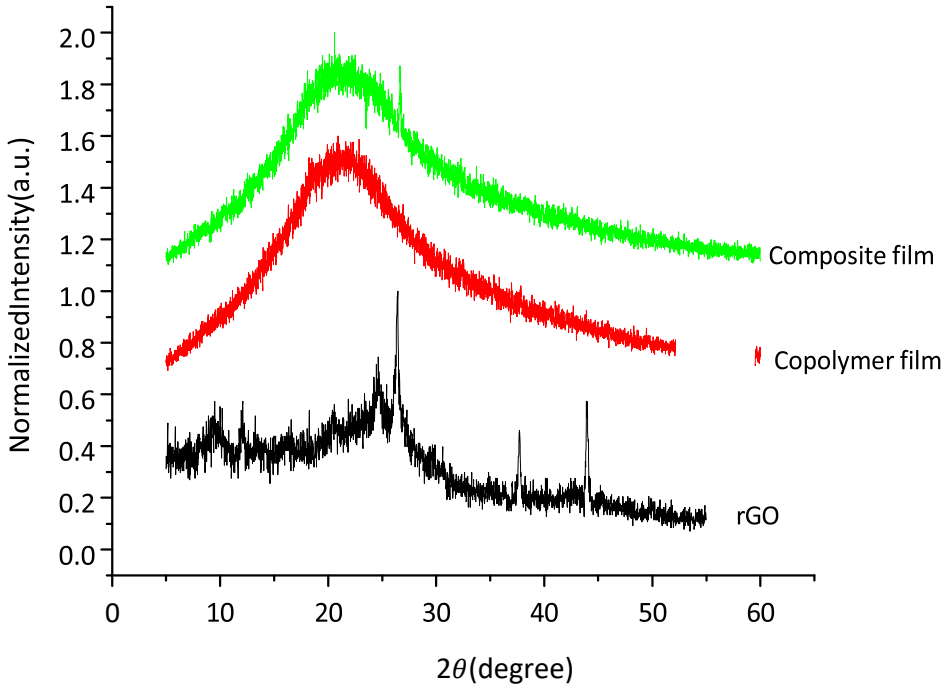

Figure 5. XRD spectra of the films

Figure 6 shows the graph of sheet resistivity and electrical conductivities of the films depending on different of rGO content (0.1 g, 0.15 g, 0.2 g, 0.3 g). The conductivity of the pure copolymer showed the lowest value. It was found out that the highest conductivity was obtained for the films composited with 0.3 g of rGO powder among the four samples. As shown in the graph, the conductivities of the films were increased with an increasing weight of rGO powder. The increase in electrical conductivity with the increasing concentration of rGO are due to the combination rGO in the copolymer matrix which gives rises to the conduction of charge carriers. The enhancement in concentration of charge carriers are tended to increase the doping of rGO in copolymer backbone. This can be explained that the delocalization effect which is associated with doping process and that produces polarons and /or bipolaron in the composite structure which in turn enhance the conductivity. Table 1 shows the values of sheet resistivity and conductivities of pure and composite films at different rGO content. The compared graph between sheet resistivity and conductivity is illustrated in Figure 7.

Table 1. Sheet resistivity and conductivities of pure copolymer and P(Py-co-FPy)-rGO composite films

Sample	rGO content (g)	Thickness (d) (mm)	V/I	Sheet resistivity (ρ) (kΩ cm)	Conductivity (σ) (Scm^{-1})
S1	0	1.73	7936663	1.522	0.657×10^{-3}
S2	0.1	1.32	3541418	0.872	1.147×10^{-3}
S3	0.15	0.30	472909	0.715	1.399×10^{-3}
S4	0.2	0.11	1347376	0.619	1.616×10^{-3}
S5	0.3	0.55	94593	0.262	3.817×10^{-3}

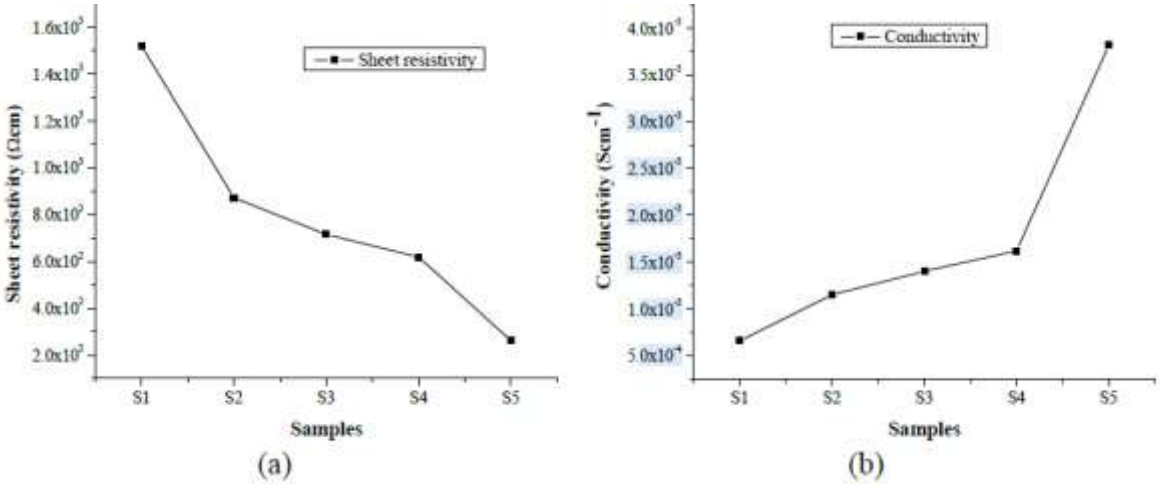

Figure 6 Graph of (a) sheet resistivity and (b) electrical conductivity of the films depending on different gram of rGO

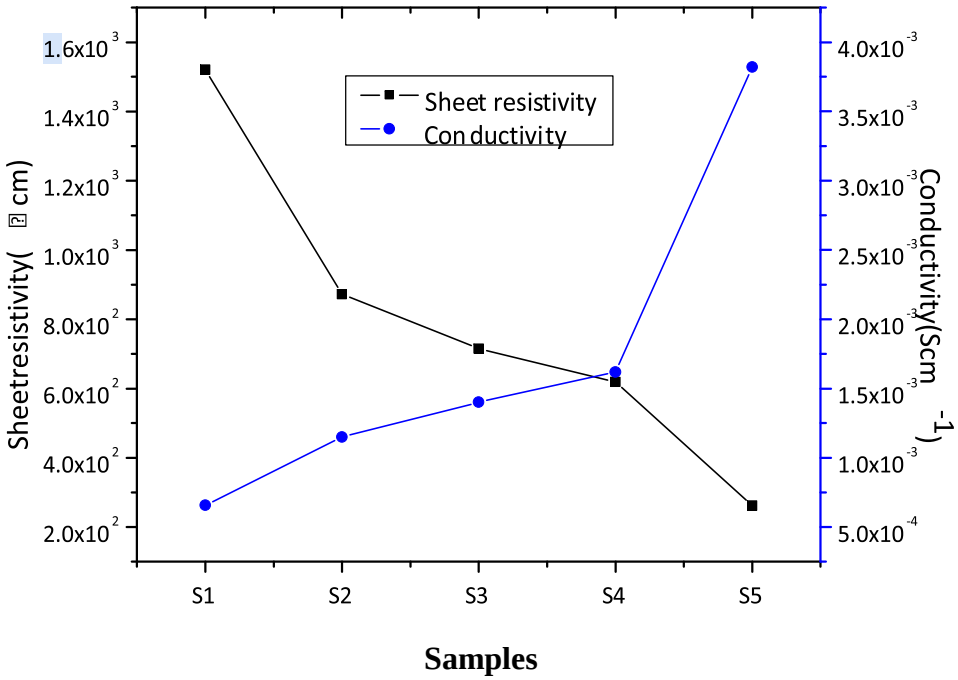

Figure 7. Compared graph of sheet resistances and conductivities of pure copolymer and composite films

Conclusions

In summary, the conductive copolymer film and composite films are prepared by exsitu chemical copolymerization process through spin coating method. The DC electrical properties of copolymer (PPy-2FPy) and composite films P (Py-co-FPy)-rGO are systemically investigated by four probe method. It is found out that the values of conductivity of the composite films are enhanced with increasing concentration of inorganic rGO particles. Besides, it is remarkable to note that the conductivities of P (Py-co-FPy)-rGO (0.3 g) composite film is higher than P (Py-co-FPy)-rGO (0.1, 0.15, and 0.2 g) composite films within the investigation rGO content. FTIR spectra of film proved that formation of conjugated chemical structure is in their copolymer film. It means that, rGO particles combined very well in the copolymer matrix in order to integrate the

composite film and performed in the enhancing of charge carriers which in turn improve the electrical conductivities of composite films. Therefore, the research finding can be used in conductive applications such as electrostatic dissipation and shielding.

Acknowledgements

We would like to acknowledge to U Htain Linn, Rector, Nationalities Youth Resource Development Degree College (Yangon), for his encouragement and allowing us to participate in this event. Our special thanks go to Dr Yin Maung Maung, Professor and Head of Department of Physics, for his kind permission to contribute this work and excellent discussion

References

Alemour, B., Badran, O. And Hassan, M.R. (2019) 'A Review of Using Conductive Composite Materials in Solving Lightening Strike and Ice Accumulation Problems in Aviation', Journal of Aerospace Technology and Management, 11, Pp. 1–23. Available at: Https://Doi.Org/10.5028/Jatm.V11.1022.

Bejjanki, D. And Puttapati, S.K. (2023) 'Easy Synthesis of Nio-Mn2O3@Reduced Graphene Oxide Ternary Composite as Electrode Material for Supercapacitor Application', Journal of Electronic Materials, 52(7), Pp. 4729–4737. Available At: Https://Doi.Org/10.1007/S11664-023-10436-4.

Factors, I.R. (No Date) 'No Title'.

Hoshina, Y. And Kobayashi, T. (2012) 'Electrically Conductive Films Made of Pyrrole-Formyl Pyrrole By Straightforward Chemical Copolymerization', Ind. Eng. Chem. Res., Vol.51, Pp.5961-5966,

Kumar, P. Et Al. (2017) 'An Asymmetric Electrically Conducting Self-Aligned Graphene/Polymer Composite Thin Film for Efficient Electromagnetic Interference Shielding', AIP Advances, 7(1). Available At: Https://Doi.Org/10.1063/1.4973535.

Mohammad, H., Stepashkin, A.A. And Tcherdyntsev, V. V. (2022) 'Effect of Graphite Filler Type on the Thermal Conductivity and Mechanical Behavior of Polysulfone-Based Composites', Polymers, 14(3). Available At: Https://Doi.Org/10.3390/Polym14030399.

Qu, M., Nilsson, F. And Schubert, D.W. (2018) 'Effect of Filler Orientation On the Electrical Conductivity of Carbon Fiber/PMMA Composites', Fibers, 6(1), Pp. 1–10. Available At: Https://Doi.Org/10.3390/Fib6010003.

Yang, L. Et Al. (2007) 'Ultra Fine Carbon Nitride Nanocrystals Synthesized by Laser Ablation in Liquid Solution', Journal of Nanoparticle Research, 9(6), Pp. 1181–1185. Available At: Https://Doi.Org/10.1007/S11051-006-91924.

INVESTIGATING THE ROLE OF SnO_2/ZnO BILAYER FILMS AS ELECTRON TRANSPORT LAYERS IN PEROVSKITE SOLAR CELLS

Nan Htet Htet Oo[1], Zin Min Myat[2], Zin Min Tun[3], Yin Maung Maung[4]

Abstract

This study focuses on the structural, chemical, and optical properties of SnO_2/ZnO films, prepared through sol-gel and spin-coating techniques on FTO-coated glass substrates. The research employs X-ray Diffraction (XRD) for crystalline structure analysis, Fourier Transform Infrared Spectroscopy (FTIR) for material verification, and UV-Vis spectroscopy to examine optical properties and energy band gaps. The presented approach demonstrates an efficient and cost-effective method for producing approving SnO_2/ZnO ETLs in perovskite-based quantum dot solar cells.

Keywords: SnO_2 /ZnO, ETL, XRD, FTIR, UV and perovskite solar cell

Introduction

The perovskite solar cells (PSCs) have recently gained major attention as potentially useful photovoltaic technology due to their ever-increasing power-conversion efficiency (PCE). The efficiency of PSCs depends strongly on the type of materials selected as the electron transport layer (ETL). Material selection is the foundation of all engineering applications and designs. This selection process can be defined by application requirements, possible materials, physical principles, and selection (M. Karolus, et al.,2023). In the past few years, SnO_2 is an important n-type wide-energy-gap semiconductor (Eg = 3.64 eV, 330 K) which has a wide range of applications such as in solid-state gas sensors, transparent conducting electrodes (Chopra, K.L., Major, S., et al.,1983), rechargeable Li batteries (Peng, Z., Shi, Z., Liu, M., et al,2000), and optical electronic devices (Aoki, A., Sasakura, H.: et al.,1970). During the past decade, SnO_2 nanostructures have been one of the most important oxide nanostructures due to their properties and potential applications. Many processes have been developed to the synthesis of SnO_2 nanostructures, e.g., spray pyrolysis (Paraguay-Delgado, F., et al.,2005) hydrothermal methods, evaporating tin grains in air (Duan, J., Yang, S., ei al.,2005), chemical vapor deposition, thermal evaporation of oxide powders, rapid oxidation of elemental tin, the sol–gel method, etc. The sol-gel method is one of the most promising because it is relatively simple process that enables straight-forward control of thin film properties. Kim et al. reported that films prepared using sol gel methods were suitable for device applications. The Controlling the size and shape of nanostructures can affect their electrical and optical properties (Cheng, B., Russell, J.M., ei al.,2004). The sol-gel method has many advantages over hybrid organic-organic materials that do not exist in nature (Liu, Y., Koep, E., Liu, M.: ei al.,2006). In addition, it is a low-cost and large-area processing technique. In this study, SnO2 films were prepared by Sol-Gel Spin Coating Method (SGSC) with SnCl2.2H2O (Dai, Z.R., Gole, J.L., ei al.,2002). Most high-performance PSCs are fabricated using the spin-coating method, which has better control over film thickness, quality, and machinability of the substrates, as well as dynamic spinning, hot-casting, anti-solvent annealing, Other methods such as gas and vacuum-quenching, facile spin-coating techniques, etc., are likely to be used to fabricate high-quality perovskite films (. Tin oxide is one of the best metal oxide materials for use as an electron transport layer (ETL) in PSCs. Among all the candidates, SnO2 stands out as one of the best candidates for ETL due to its wide optical band gap (3.6–4.0 eV), deep bandgap, high electron-to-electron (V-10) s-1), long carrier diffusion length, excellent chemical stability, and ease of preparation (via solution processing) at

[1] Department of Physics, University of Yangon
[2] Department of Physics, West Yangon University
[3] Department of Physics, West Yangon University
[4] Department of Physics, University of Yangon

low temperatures (Pourfayaz, F., et al.,2005). Due to its solution processing, SnO2 offers low production cost, flexibility, It can bring advantages such as easy scaling, and additive manufacturing processes (20.0.0). However, ZnO is a promising candidate due to its high transparency, suitable energy band structure, and high electron mobility. The influence of ZnO structures with different weight percentages on photovoltaic performance was investigated. The choice of SnO2 /ZnO is related to the low temperature required for their synthesis and their properties, in particular, Lamfred. F.C. Raghuwanshi, ei al.,2015).

Materials and Methods

Experimental Procedure of Tin Oxide (SnO_2) Films

Starting materials such as tin chloride dihydrates ($SnCl_2.2H_2O$) and ethanol (CH_3CH_2OH) were of analytical grade and used without further purification. The methods used in this research work were sol-gel and spin coating. The tin oxide films were prepared using $SnCl_2.2H_2O$ and ethanol by sol-gel method. In a typical experiment, different molar concentration of (0.01M-0.05M) of $SnCl_2.2H_2O$ was dissolved with 40 ml of ethanol under magnetic stirring at 1000 rpm for 5 h to form a homogeneous solution at room temperature. The experiment was prepared five times for five different molar concentrations and then, the stirring temperature was improved at 70 º C for 2 h to form a sol-gel. Afterward, the sol-gel solution was kept overnight at room temperature. Then the precursor solutions were coated onto the fluorine doped tin oxide (FTO) glass substrates by direct spin coating method. Before coating, firstly, the 1 cm × 1 cm FTO glass substrates were cleaned with distilled water and dried at room temperature and then, they were also immersed in a solution of ethanol and acetone for 15 min respectively and dried at room temperature. The cleaning glass substrates were tested the conducting layers with digital meter. The precursor solution of five different molarities was spin coated on a glass substrate at 3000 rpm for 30 s. After spin coating, glass substrates were dried at 100º C for 30 min. the prepared films were annealed at 500º C for 1 h respectively. The block diagram of preparation of tin oxide films were shown in figure 1. Figure 2 (a-d) showed the photos of preparation of tin oxide (SnO_2) films.

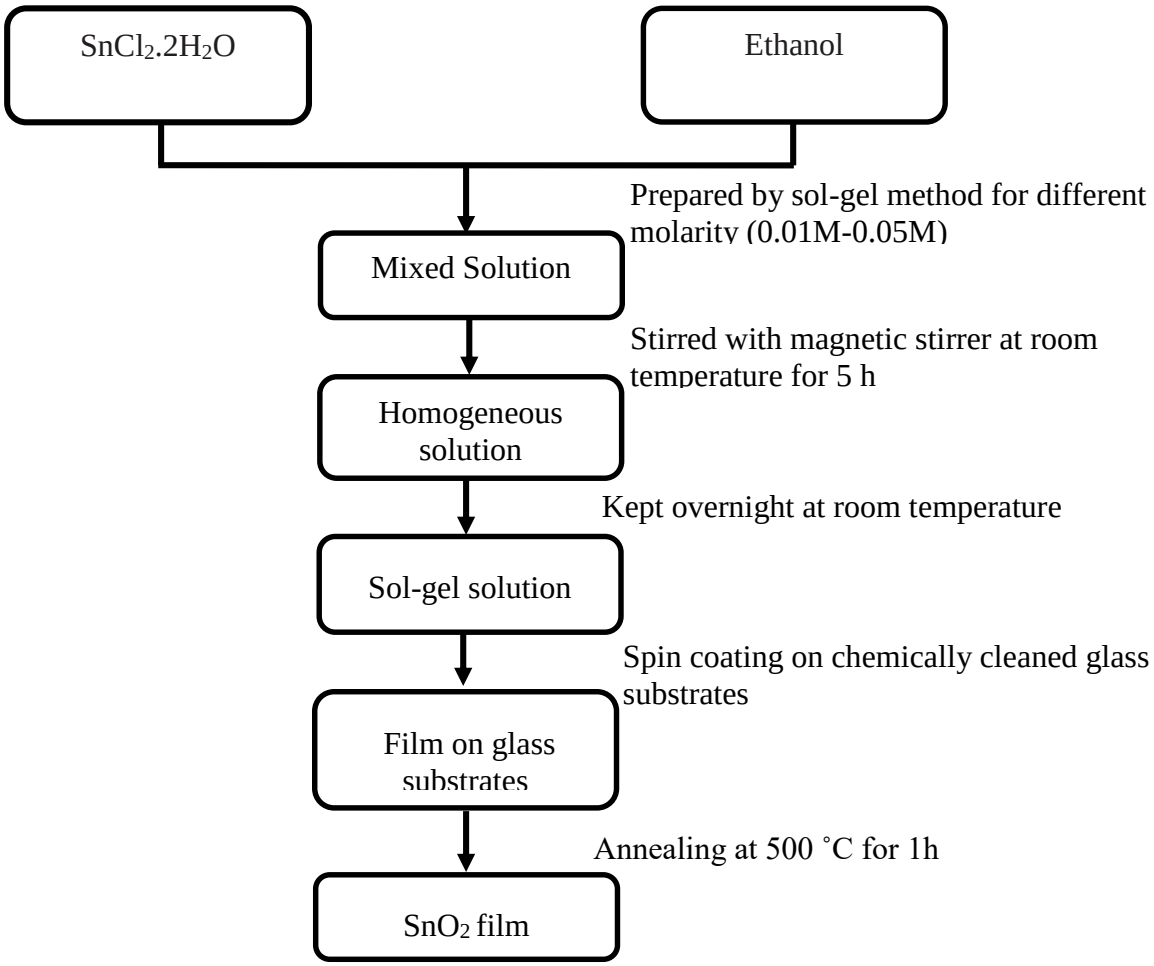

Figure 1 The block diagram of preparation of tin oxide film

Figure 2 (a) Stirring process

Figure 2 (b) Sol-gel solution

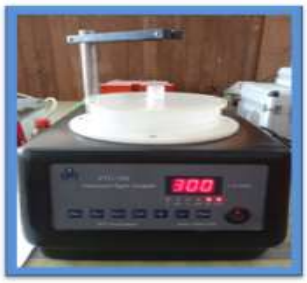

Figure 2 (c) Spin coating process

Figure 2 (d) Annealing process

Synthesized Method of ZnO and Device Fabrication of FTO/SnO_2/ZnO Films

Zinc Oxide nanostructure was synthesized by using sol-gel method. Firstly 20.83 g of $ZnCl_2.4H_2O$ and 4g of Sodium Hydroxide (NaOH) were weighted using a weighting balance. Then 100 ml of deionized water was measured by a measuring cylinder two times. After that, 20.83 g of $ZnCl_2.4H_2O$ was dissolved with a 100 ml of deionized water and 4 g of Sodium Hydroxide (NaOH) was dissolved in a 100 ml of deionized water. The solutions were stirred with a magnetic stirrer for 15 minutes each. After well mixed, sodium hydroxide solution was poured to the solution containing $ZnCl_2.4H_2O$ with a constant stirring by magnetic stirrer at 80ºC for 3 hours. After the reaction, white color sol-gel was formed. Then this solution was spin coated on the FTO/ SnO_2 glass substrates at 3000 rpm for 30 s. After that, FTO/SnO_2/ZnO glass substrates were dried at 100 ºC for 30 min. These prepared films were annealed at 500 ºC for 1 h. Finally, the fabrication of SnO_2/ZnO bilayers as electron transporting layers in perovskite solar cells was successfully observed. Figure 3 showed the block diagram of experimental procedure of ZnO and device fabrication FTO/SnO_2/ZnO films. The structural, function group and the vibrational energy of the molecules of the sample were examined by X-ray diffraction (XRD) and Fourier Transform Infrared Spectroscopy measurements. UV-Vis spectroscopy was used for measurement of optical properties of FTO/SnO_2/ZnO films.

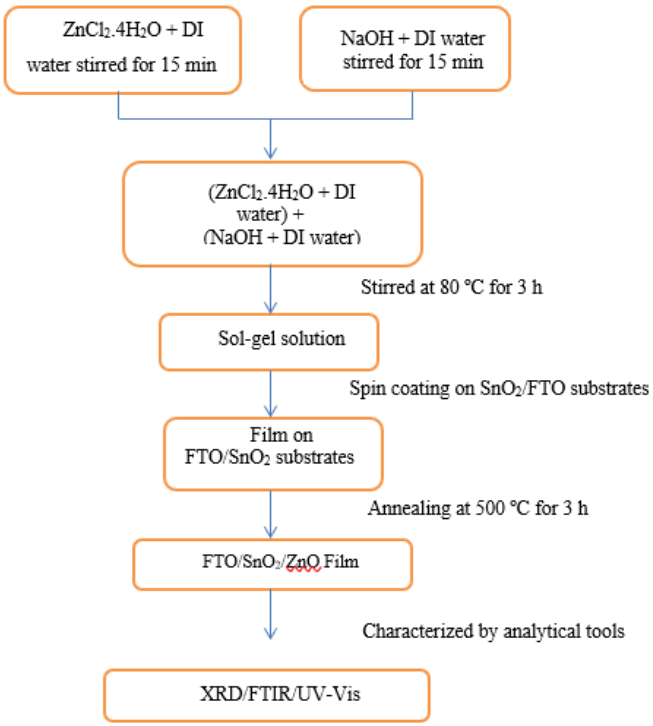

Figure 3 Experimental procedures of ZnO and Device Fabrication FTO/ SnO_2/ZnO films

Results and Discussion

XRD Analysis of SnO_2/ZnO Films

The structural properties of sol-gel synthesized SnO_2/ZnO films were determined by using XRD method. According to XRD results, the distinct peaks at 2θ values of 20.98º and 37.76º, which were assigned to indices (110) and (200) crystal planes. They can be indexed as a tetragonal crystal structure of SnO_2 by matching with the Joint Committee on Powder Diffraction Standard (JCPDS) card number 00-046-1088. The diffraction peaks at 2θ = 25.12º, 28.92º, 32.82º, 43.98º, 64.34º and 67.10º correspond to the crystalline planes (101), (100), (102), (103)

and (201) respectively. These results were in good agreement with of hexagonal crystal structure ZnO phases according to the JCPDS card number 00-065-0725. The XRD analysis revealed that all of the characteristic peas in these spectra were the evidence of the coexistence of both tetragonal SnO_2 and hexagonal ZnO crystal structures in the samples (K. Wongsaprom, A. Winyayong, S. Maensiri, 2018). The sharp and narrow peaks in all spectra implied that the samples have high crystallinity degrees. These XRD spectra indicated that the SnO_2/ZnO films were successfully synthesized using sol-gel method. The XRD pattern comparison of SnO_2/ZnO films with different molar ratios was shown in figure 4. Table (1-5) listed the structural properties and average crystallite sizes of SnO_2/ZnO films with different ratios. According to these results, the average crystallite sizes were decrease with increasing molar ratios.

Table 1. Structural properties and average crystallite sizes of SnO_2/ZnO films (S-1)

(hkl)	2θ (deg)	FWHM (deg)	Crystallite size (nm)
(110)	20.98	0.57353	14.08
(101)	28.92	0.15292	53.64
(200)	37.76	0.24967	33.62
(102)	43.98	0.26078	32.84
(103)	64.34	0.33955	27.63
Average crystallite size			32.36

Table 2. Structural properties and average crystallite sizes of SnO_2/ZnO films (S-2)

(hkl)	2θ (deg)	FWHM (deg)	Crystallite size (nm)
(110)	20.98	0.5385	15.01
(101)	28.92	0.25959	31.59
(200)	37.76	0.25526	32.88
(102)	43.98	0.26887	31.86
(103)	64.34	0.20830	45.04
Average crystallite size			31.27

Table 3. Structural properties and average crystallite sizes of SnO_2/ZnO films (S-3)

(hkl)	2θ (deg)	FWHM (deg)	Crystallite size (nm)
(110)	20.98	0.58812	13.73
(101)	32.78	0.21856	37.88
(200)	37.74	0.25407	33.03
(102)	43.98	0.2493	34.36
(103)	64.34	0.32317	29.03
(201)	67.14	0.24508	38.89
Average crystallite size			31.15

Table 4. Structural properties and average crystallite sizes of SnO_2/ZnO films (S-4)

(hkl)	2θ (deg)	FWHM (deg)	Crystallite size (nm)
(110)	20.98	0.58334	13.84
(101)	25.12	1.02822	7.914
(100)	32.82	0.23081	35.87
(200)	37.76	0.26234	31.99
(102)	43.98	0.25125	34.09
(103)	64.34	0.30314	30.95
(201)	67.1	0.20903	45.59
Average crystallite size			28.61

Table 5. Structural properties and average crystallite sizes of SnO_2/ZnO films (S-5)

(hkl)	2θ (deg)	FWHM (deg)	Crystallite size (nm)
(110)	20.98	0.55183	14.63
(101)	28.92	0.25759	31.84
(200)	37.76	0.24872	33.75
(102)	43.98	0.26108	32.81
(103)	64.34	0.36817	25.48
Average crystallite size			27.70

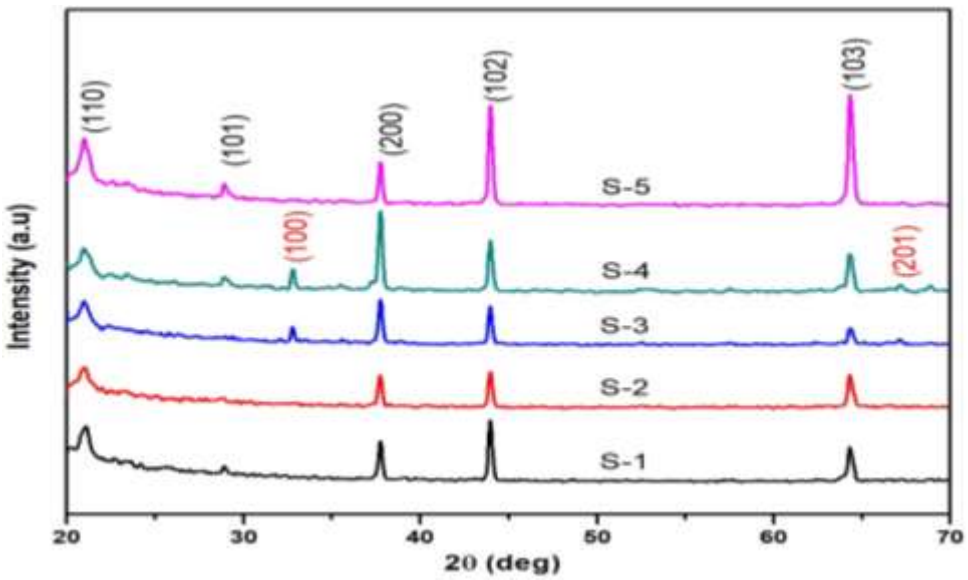

Figure 4 Comparison of XRD patterns of SnO_2/ZnO films

FTIR Analysis of SnO_2/ZnO Films

The functional groups of the sol-gel synthesized SnO_2/ZnO films investigated using FTIR spectroscopy. The spectra of SnO_2/ZnO films have strong and broad bands at ~3360 cm^{-1} peak that are related to O-H stretching of water molecules adsorbed on the surface of the synthesized materials. Similarly, another strong band at ~1630 cm^{-1} peaks assigned to O-H bending vibration of hydroxyl group. The weak bands observed at ~2000-2500 cm^{-1} were C ≡ C stretching vibration of alkyne. The finger prints region of metal oxygen bond showed the characteristic absorption bands in the wave number region 400 cm^{-1} to 800 cm^{-1} (L. Motelica, O. Oprea, B. Vasile, et al.,2023). In this study, the absorption peaks of O-Sn-O stretching vibration were observed at ~649-689 cm^{-1} and the absorption peaks of Zn-O stretching vibration were observed at ~437-465 cm^{-1} respectively (Z. Khatoon, H. Fouad, H. K. Seo, et al.,2020). The comparison of FTIR spectra for SnO_2/ZnO films with different molar ratios was shown in figure 5.

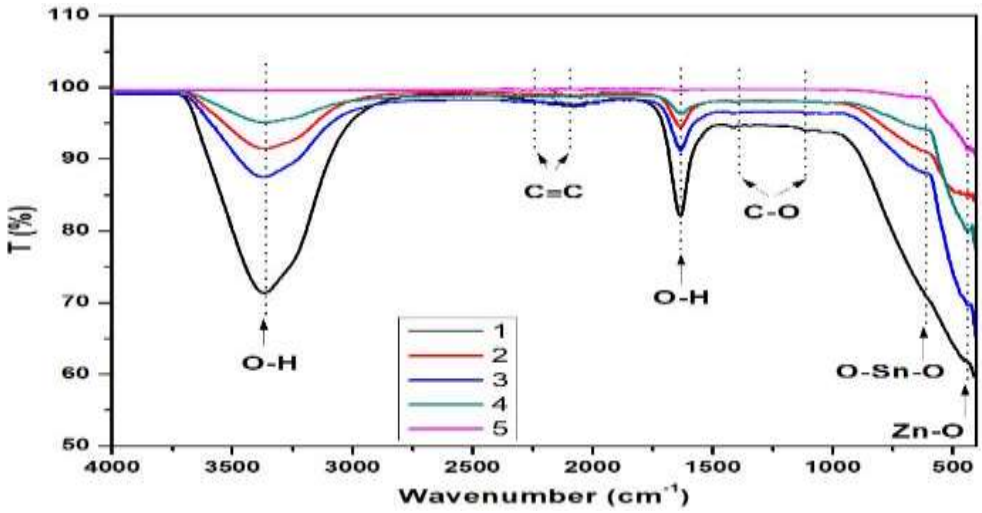

Figure 5. Comparison of FTIR spectra for SnO_2/ZnO films with different molar ratios

UV-Vis Analysis of SnO_2/ZnO Films

The UV-Vis spectra of all films were obtained on UV-Vis spectrometer in the range of 200 nm -700 nm. Figure 6 (a-e) showed that the UV-Vis absorption spectra of SnO_2/ZnO electron transport layer (ETL) films with different molar concentrations. It was found that the maximum absorption of wavelength obtained by coating onto FTO is in the ultraviolet region. The wavelength ranges of spectrum laid between 200 nm to 400 nm. There are different methods to obtain the optical band gap of the thin films. Here, the Tauc's plot method is used to obtain the band gap of the SnO_2 films with different molar concentrations. The $(\alpha h\upsilon)^2$ and $h\upsilon$ characteristic curve of SnO_2/ZnO ETL films with different molar concentrations were listed in Table 6. On the characteristic curve, the extrapolating the straight line onto horizontal axis ($(\alpha h\upsilon)^2 = 0$), give the values of band gap and the obtained films had the direct band gap of 3.44 eV, 3.47 eV, 3.53 eV, 3.55 eV and 3.58 eV with different molar concentrations respectively.

Table 6 Observed energy bandgaps and referenced energy bandgaps

Samples	E_g (for 2 layers) (This study)	E_g (for SnO_2 only) (previous study)	References
S-1	3.44 eV	3.95 eV	3.2-3.6 eV
S-2	3.47 eV	3.93 eV	
S-3	3.53 eV	3.93 eV	
S-4	3.55 eV	3.94 eV	
S-5	3.58 eV	3.97 eV	

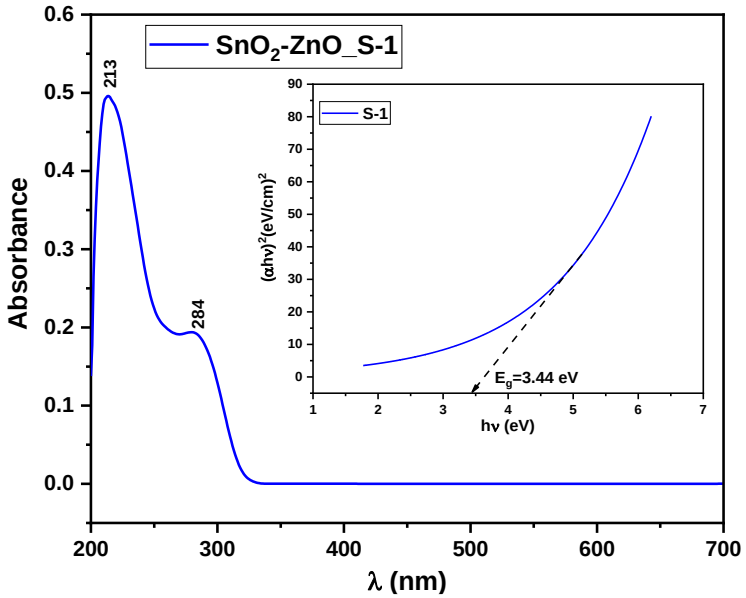

Figure 6 (a) UV-Vis absorption spectrum and energy band gap of SnO_2/ZnO film (S-1)

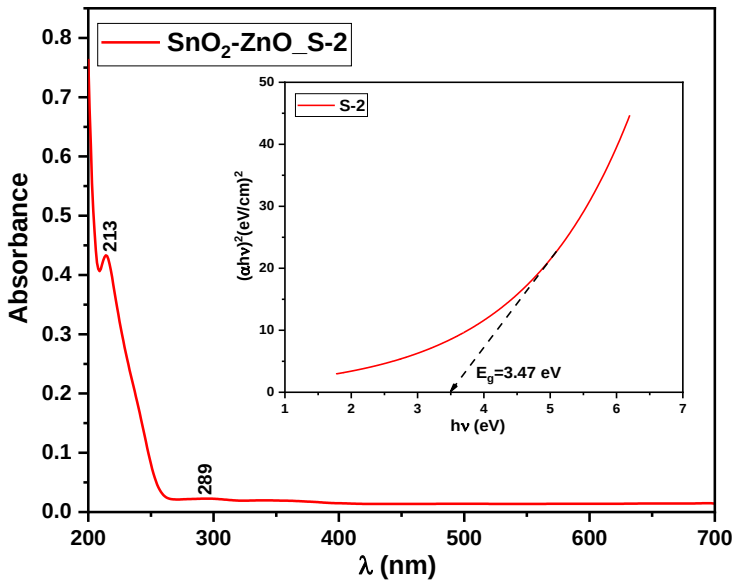

Figure 6 (b) UV-Vis absorption spectrum and energy band gap of SnO_2/ZnO film (S-2)

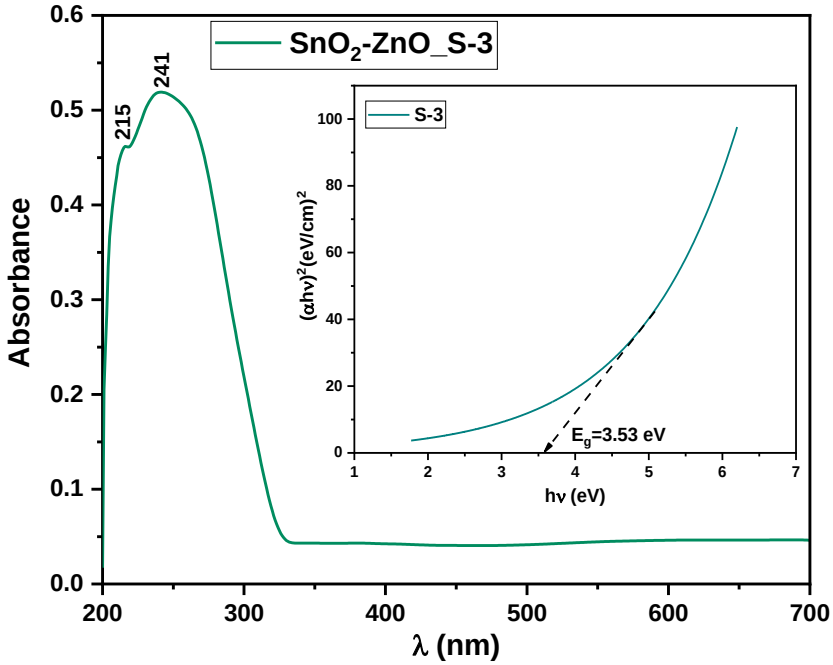

Figure 6 (c) UV-Vis absorption spectrum and energy band gap of SnO_2/ZnO film (S-3)

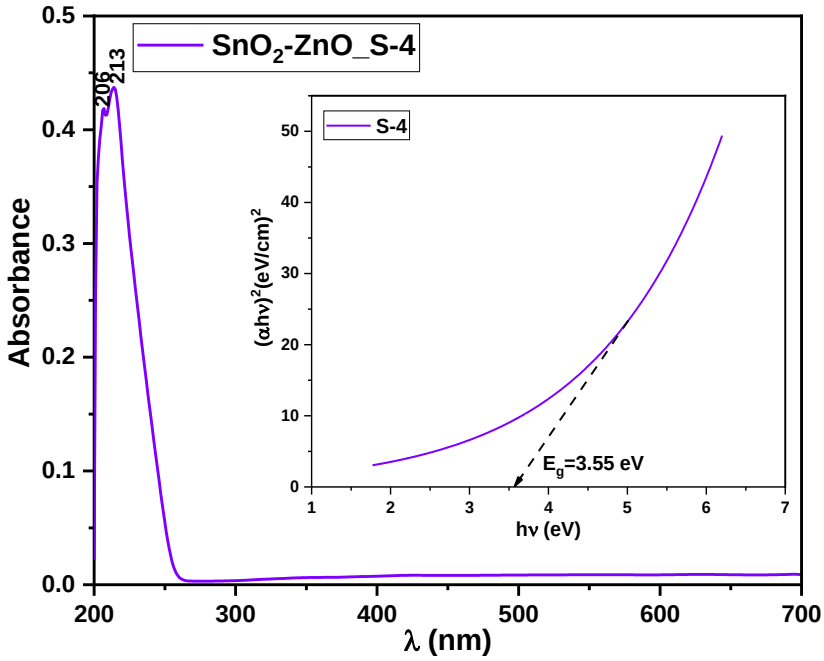

Figure 6 (d) UV-Vis absorption spectrum and energy band gap of SnO_2/ZnO film (S-4)

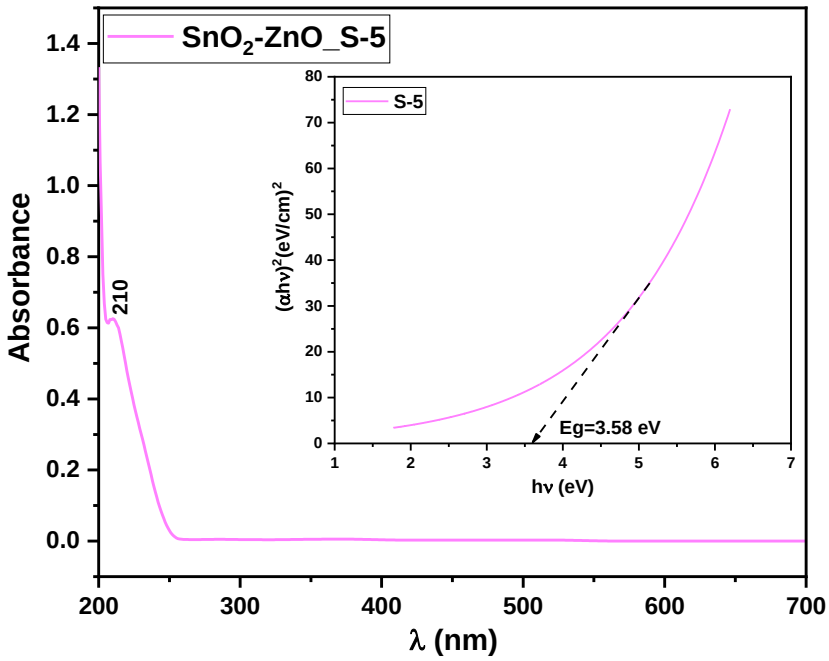

Figure 6 (e) UV-Vis absorption spectrum and energy band gap of SnO_2/ZnO film (S-5)

Conclusions

The suitable synthesis of SnO_2/ZnO films through sol-gel spin coating at varying molar ratios was examined by XRD analysis, indicating the presence of both SnO_2 and ZnO structures with distinct crystalline patterns. The XRD results further indicated a reduction in grain size with increased molar concentration. FTIR analysis highlighted specific absorption peaks, including O-Sn-O (~649-689 cm-1) and Zn-O (~437-465 cm-1), providing insights into the chemical bonding within the deposited films. UV-Vis results indicated energy band gap values closely aligned with reported values (3.2-3.6 eV) (S. Dániel, S. Tamas, D. Imre, et al., 2009). These findings collectively suggest the potential of SnO_2/ZnO layers as effective electron transport layers (ETL) in perovskite solar cells, thereby enhancing overall performance.

Acknowledgments

We wish to express our deepest gratitude to Dr Tin Maung Tun, Rector, University of Yangon, for his encouragement to submit this paper. We are very grateful to Professor Dr Yin Maung Maung, Head of Department of Physics, University of Yangon, for his kind encouragement. We would like to express our sincere thanks to Dr Ye Chan, Professor and Head, Universities' Research Center, and Professor Dr Cho Cho Thet, Department of Physics, University of Yangon, for their valuable advice to this paper.

References

Aoki, A., Sasakura, H.: Tin oxide thin film transistors. Japan J. Appl. Phys. 9,582,1970.

Chopra, K.L., Major, S., Pandya, D.K.: Transparent conductors–a status review. Thin Solid Films 102, 1, 1983.

Cheng, B., Russell, J.M., Shi, W., Zhang, L., Samulski, E.T.: Large-scale, solution phase growth of single-crystalline SnO2 nanorods. J. Am. Chem. Soc. 126, 5972, 2004.

Du, F., Guo, Z., Li, G.: Hydrothermal synthesis of SnO2 hollow microspheres. Mater. Lett. 59, 2563, 2005.

Duan, J., Yang, S., Liu, H., Gong, J., Huang, H., Zhao, X., Zhang, R., Du, Y.: Single crystal SnO2 zigzag nanobelts. J. Am. Chem. Soc. 127, 6180, 2005.

Dai, Z.R., Gole, J.L., Stout, J.D., Wang, Z.L.: Tin oxide nanowires, nanoribbons, and nanotubes. J. Phys. Chem. B 106, 1274, 2002.

Fujihara, S., Maeda, T., Ohgi, H., Hosono, E., Imai, H., Kim, S.: Hydrothermal routes to prepare nanocrystalline mesoporous SnO2 having high thermal stability. Langmuir 20, 6476, 2004.

G. Lamdhade, F.C. Raghuwanshi, R.M. Agrawal, V.M. Balkhande, T. Shripathi, "SnO_2 Nanoparticles Synthesis Via Liquid-Phase Co-Precipitation Technique," *Adv. Mater. Lett*. 6, 738–742, 2015.

Hu, J.Q., Ma, X.L., Shang, N.G., Xie, Z.Y., Wong, N.B., Lee, C.S., Lee, S.T.: Large scale rapid oxidation synthesis of SnO2 nanoribbons. J. Phys. Chem. B 106, 3823, 2002.

K. Wongsaprom, A. Winyayong, S. Maensiri, "Synthesis and room-temperature ferromagnetism in flower-like SnO_2 nanostructures," *J. Phys. Conf. Ser*. 1144, 012042, 2018.

Liu, Y., Koep, E., Liu, M.: A highly sensitive and fast-responding SnO2 sensor fabricated by combustion chemical vapor deposition. Chem Mater 17, 3997, 2006.

L. Motelica, O. Oprea, B. Vasile and A. Ficai, "Antibacterial activity of solvothermal obtained ZnO nanoparticles with different morphology and photocatalytic activity against a dye mixture," *Int.J.Mol.Sci*.245677, 2023.

M-G. Kim, M. G. Kanatzidis, A. Facchetti, and T. J. Marks, Nature Materials 10, 2002.

Perovskite, S. Cell, and M. Karolus, "Hybrid Mesoporous TiO 2 /ZnO Electron Transport Layer for Efficient Perovskite Solar Cell," 2023.

Peng, Z., Shi, Z., Liu, M.: Mesoporous Sn–TiO2 composite electrodes for lithium batteries. Chem. Commun. 21, 25, 2000.

Paraguay-Delgado, F., Antúnez-Flores, W., Miki-Yoshida, M., Aguilar-Elguezabal, A., Santiago, P., Diaz, R., Ascencio, J.A.: Structural analysis and growing mechanisms for long SnO2 nanorods synthesized by spray pyrolysis. Nanotechnology 16, 688, 2005.

Pourfayaz, F., Khodadadi, A., Mortazavi, Y., Mohajerzadeh, S.S.: SnO2 sensor selective to ethanol in presence of CO, LPG and CH4. Sensors Actuators B 108, 172, 2005.

P.A. Luque, O. Nava, C.A. Soto-Robles, M.J. Chinchillas-Chinchillas, H.E. Garrafa-Galvez, Y.A. Baez-Lopez, K.P. Valdez-Núñez, A.R. Vilchis-Nestor, A. Castro-Beltrán, "Improved photocatalytic efficiency of SnO2 nanoparticles through green synthesis," *Optik*, 206, 164299, 2020.

S. Chen, Z. Sun, L. Zhang, H. Xie, "Photodegradation of Gas Phase Benzene by SnO_2 Nanoparticles by Direct Hole Oxidation Mechanism," *Catalysts*, 10, 117, 2020.

S. Dániel, S. Tamas, D. Imre, "Optical properties of zinc peroxide and zinc oxide multilayer nanohybrid films," *Appl. Surf. Sci*, 255, 6953−6962, 2009.

W. Zhou, Y. Y. Liu, Y. Z. Yang, P. Wu, "Band Gap Engineering of SnO2 by Epitaxial Strain: Experimental and Theoretical Investigations," *J. Phys. Chem. C*, 118, 6448−6453, 2014.

Z. Khatoon, H. Fouad, H. K. Seo, et al, "Sensing biomarkers of lung cancer feasibility study of doped SnO_2 nanomaterial for electronic nose towards sensing biomarkers of lung cancer," *J.Mater.Sci.:Mater. Electron*.3115751–63, 2020.

DESIGN ON FDM BASED 3D PRINTING SYSTEM FOR INDUSTRIAL APPLICATIONS

Kyaw Kyaw[1], May Zin Nyein[2], Hnin Yu Khaing[3]

Abstract

This research work focus on the modelling and construction of fused deposition method (FDM) based 3D printing system, specifically focusing on optimizing the structural design and hot end thermal analysis for FDM 3D printers. The study explores strategies aimed at maximizing the accuracy and resolution of the 3D printed objects. By acknowledging the specific constraints and potentials in FDM 3D printing, researcher can better tailor their designs for FDM printing, thus enhancing outcomes. This research work emphasizes the importance of considering the capabilities and restrictions of the manufacturing method when it comes to the design process. In this research study, all the electronic and mechanical parts are successfully built and fully functional, the Cartesian coordinate positioning-based 3D printing machine printed 3d models with desired accuracy level. In terms of current regulation in Ramps controller, it was observed that the current regulator achieved the required output current to control motors such as stepper motors and heating elements, which was to simply control the current flowing on phase winding, even when facing input voltage ripple. In its real implementation, however, it was observed current spikes that might lead to motor overall life cycle reduction.

Keywords: FDM, 3D Printing, Accuracy, Resolution, thermal Analysis

Introduction

Nowadays, 3D printing has become very popular. 3D printing technology is currently applied to many fields like engineering, sciences, medicine and entertainment. 3D printing is becoming increasingly capable and affordable. 3D printing is widely used to prototype the components but also to produce the working products. 3D printing technique also has the ability in realizing flexible designs. The implementation of three-dimensional objects can take place through both subtractive manufacturing process and additive manufacturing process. Generally, the subtractive manufacturing processes are known as traditional. In that process, the 3D objects are obtained by cutting or milling the material from a larger shape. The most utilized technologies of this type are numerically controlled machine drills or laser cutter. On the other hand, the additive manufacturing method allows to create an object through the superposition of several layers of the same material or different materials. Actually, additive manufacturing or 3D printing techniques are categorized according to the procedure the layers are deposited. 3D Printing or additive manufacturing is a process of making a three-dimensional solid object of virtually any shape from a digitally designed model. Successive deposited layers of fused material are laid down to construct a desired object. Metal 3D printing process also greatly reduces material waste since subtracting manufacturing generates metal chips while additive manufacturing uses only what is necessary and lays material down layer by layer [Gianfrano F., *et al*]. 3D printing is a manufacturing method that is recently used to build three dimensional objects by using digital CAD (computer aided design) files. 3D model was created by using (CAD) software like SolidWorks, 3D scanner and Ansys software. The most popular and affordable type of additive manufacturing is known as Fused Deposition Modeling (FDM). These method utilize the extrusion of heated thermoplastic filament to build parts one layer at a time. FDM printers are capable of building parts from (CAD) files, however they must first be converted into a file format that the printer can understand, such as a STL file. The STL files allow the printer to operate how the part must be built layer by layer, ensuring the printer is capable of extruding both the part material and any support material for thin materials parts.

[1] Department of Physics, University of Mandalay
[2] Department of Physics, Ba Maw University
[3] Department of Physics, Mandalay University of Distance Education

Fused Deposition Modelling (FDM) was selected as the printing method for this research work according to its fabrication cost and reliability. In the FDM, the filament was firstly heated until it reached a semi-liquid state and then extruded through a nozzle on a platform or previously printed and deposited layer. This method relies on the thermoplasticity of the material to fuse together during the heating process. The durability of the materials, the stability of mechanical properties, and the suitability of the material for the detailed functional prototype are the main advantages of this printing method [Karel D., *et al*]. The two types of 3D printing devices exist within the field of FDM printing, these are the Cartesian coordinate system and polar coordinate system. All utilized filament extrusion to fabricate objects, however they differed in the depositing ways how they extrude filament, which can lead to numerous differences in print time, print quality, and machine usage.

System Components and Operation

The central processing control unit is implemented with Arduino Mega2560 development board. The linear movement for Cartesian coordinate system was drove with the help of high precision TB6600 stepper motor drivers. The Repetier host software was installed in the PC and the corresponding GCODE of 3D model was send via RS232 serial communication protocol through USB port. The block diagram of the constructed 3D printer is illustrated in Figure 1.

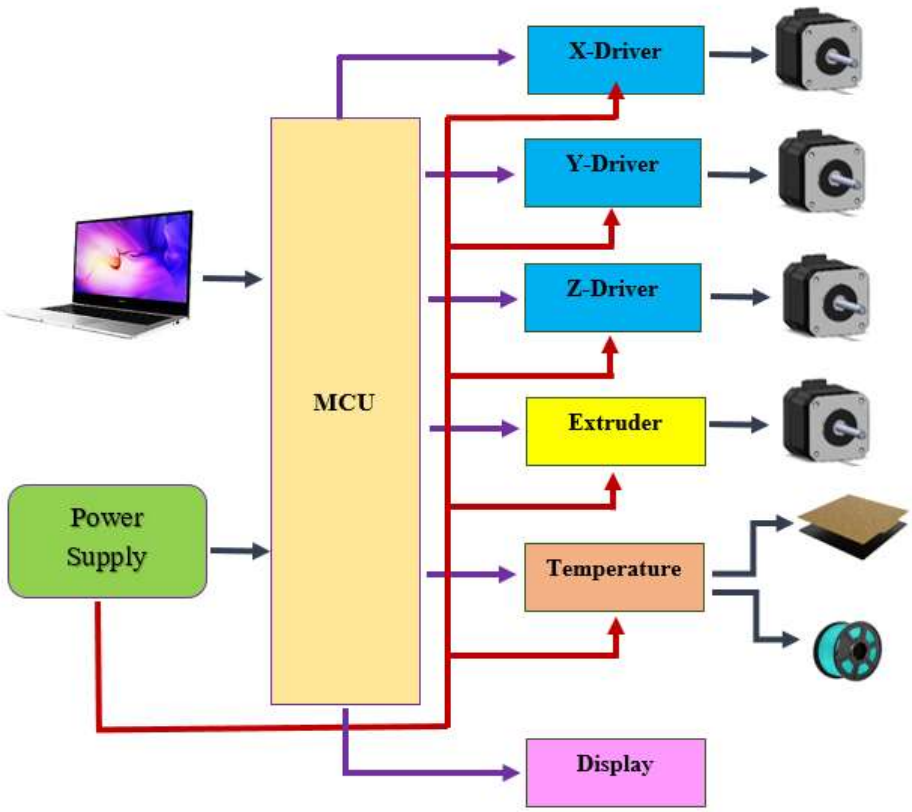

Figure 1. Block diagram of the constructed system.

Hardware Mechanism for 3D Printing System

A 3D printing machine was designed with three Cartesian axes, with 150 mm of length in X axis and 90 mm of length in Y axis and 20 mm of length in Z axis. In this constructed system, three stepper motors with holding torque of 10 kg.m, 8 W of power per phase, 1.8º step angle and positioning precision higher than 95% were conducted as axial motion actuators. The MK8 Extruder was combined as end effector (hot end) with nominal power of 40 W at 12 V, and nominal feed rate of 100 mms^{-1}. The 1045 steel threaded rods were used to convert rotational to

translational mechanic converter for moving end effector. Its pitch had 3 mm per step and threading precision was higher than 95%. The machine's general characteristics are listed in Table 1 and 3D model of printer components are illustrate in Figure 2.

Table 1. The specification of the constructed 3D printing machine

Travel on axis X and Y	150 mm, 90 mm
Travel on axis Z	20 mm
Maximum torque on axis	10 kg.m
Motor wiring	Bipolar
Bipolar motor parameters	L = 0.020 H, R = 4 Ω
Resolution	200 steps per revolution at full step control mode
Driving mode	Half step
Threaded Rod	Trapezoidal, 14 mm diameter, 3mm step
Nut	Polyacetal and Bronze
End effector	MK8 extruder with stepper motor and 0.4 mm nozzle
Mandrel	3.2 mm diameter

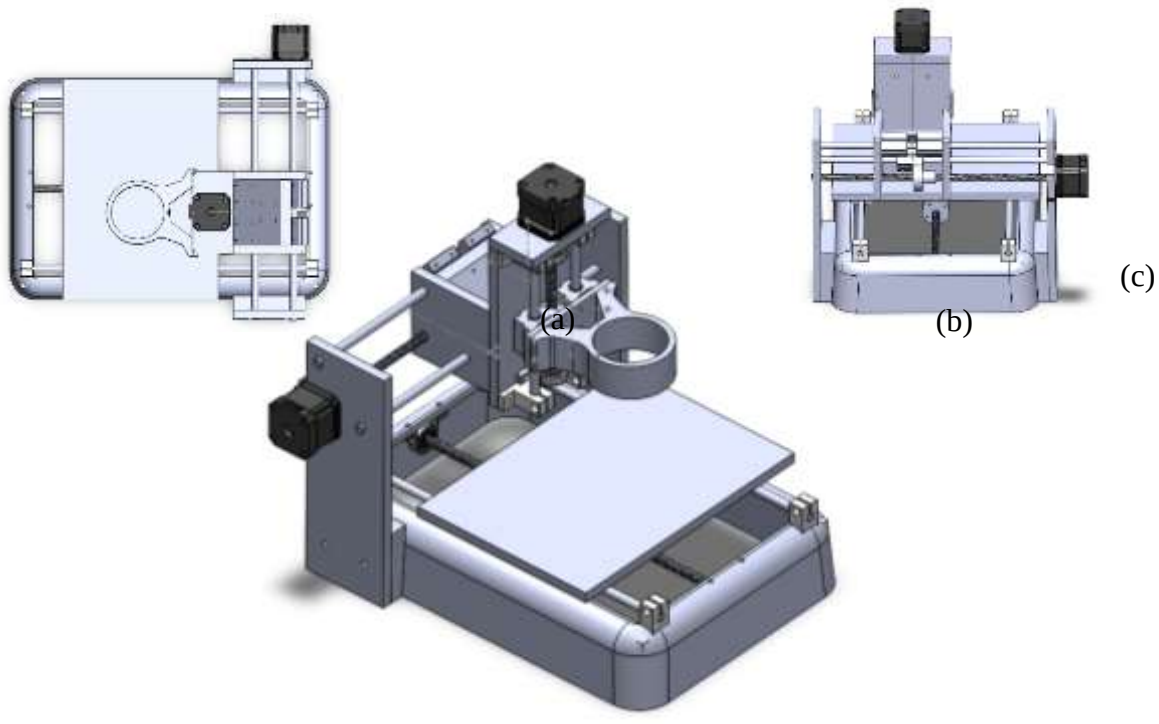

Figure 2. 3D assemble of the 3D printing system, (a) Top view of 3D printer, (b) Back view of 3D printer and (c) Perspective view of 3D printer

Software Interfacing

The software interfacing was based on Arduino firmware and PC printing host software. Repetier Host software was easy to understand for auto and manual control of 3D printing

system. It could not only to display electrical and mechanical variables but also to send GCODE commands and receive commands. It could be implemented as bidirectional interface between 3D printer and the host computer. The communication system followed in a way that the host computer always transmitted the acknowledge signal of the present task being executed by the machine. Therefore, a protocol would have to be developed, allowing the data exchange between the machine and the computer. The program could operate in two operation modes: the manual and the automatic. In the manual mode, the movement coordinates were converted into GCODE and it was sent to the machine to move in predefined discrete steps on each axis. Fused deposition operation was also follow with acquired GCODE related layer height, feed rate and temperature PID control. In the automatic mode, the user would have to load a file containing sliced layer code, such as G and M codes. The program then loads the selected files, decoded commands and sent them to the 3D printing machine. GUI interface of the host software is illustrated in Figure 3.

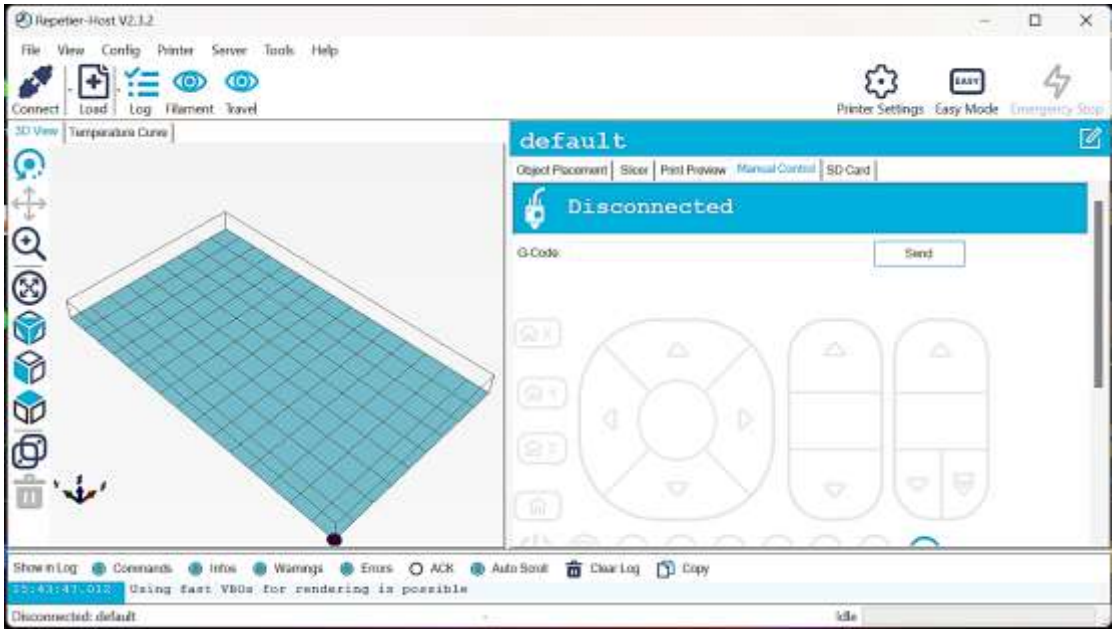

Figure 3. Desktop of the 3D printer control software.

Results and Discussion

After the designing of all the mechanical parameters of the machine, the initial 3D model was developed using the SolidWorks 2020 software. The model was of great relevance for the physical implementation of the machine, allowing the individual design of each component, reducing the possibility of vibration errors. The partial assembly of the machine were also shown in previous figures. Some of the parts of the machine were not meant to be permanent, such as the nut holders, which were presently parts were made with plastic. The printer control software was designed in such a way that it had both user-friendly and informative system. In order to achieve this capability, the software was programmed in Arduino IDE and Repetier host, which provided powerful tools to easily design the program. The software includes the necessary controls for the operation as well as all useful variables for the process in a simple and intuitive way.

Thermal Analysis of the 3D Printing Extruder using SolidWorks

The extrusion head (hot end) had the task of heating the plastic material such as ABS, PLA and PVC, and deposited by means of a nozzle on the heated bed platform. Heat could be transferred in three different ways: conduction, convection and radiation. Finite elements analysis

was used to calculate the thermal effects in the extruder using SolidWorks 2022 software. Finite Element Analysis (FEA) consists of a computer model of the object that is stressed, analyzed to obtain its behavior for specific loading condition. It is used in new product design, and for existing product refinement. Using this method, it is possible to verify if the constructed design would be able to perform to the 3D printing. In case of structural failure, FEA may be used to help to determine the needed design modifications to meet the desired condition. The assembly of the extruder head was modeled in 3D and meshed in finite elements, to perform in the software program the finite elements simulation. The analysis was performed to quantify the heat transmitted from extruder head to the aluminum frame. The operating temperature of the extruder was 243°C for ABS materials. The environmental temperature was set at 25°C. The heat transmission was steady and was transmitted to the aluminum frame by conduction and radiation (convection is neglected because the ABS material was thermos-isolated inside the extruder). After determining and setting all the boundary conditions, the virtual simulation and analysis was performed. For parts mesh creation, the minimum value for triangular distance parameters was set to 0.2 mm. The FEA analysis performed with SolidWorks is shown in Figure 4. The photographs of the constructed 3D printing machine and the printing process are illustrated in Figure 5 and Figure 6.

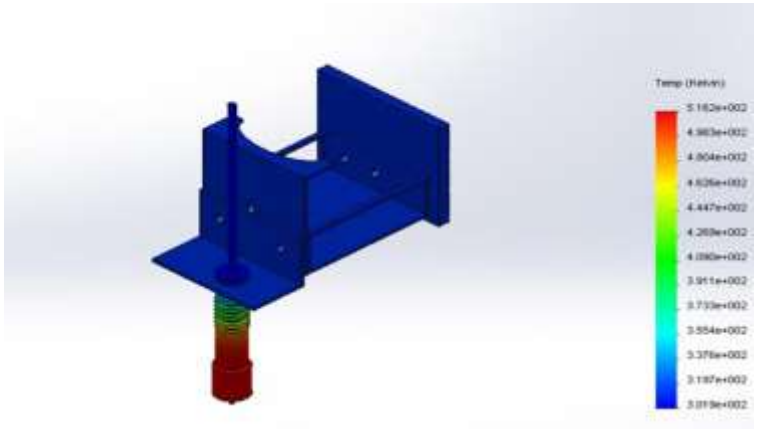

Figure 4. The FEA analysis of 3D printer extruder.

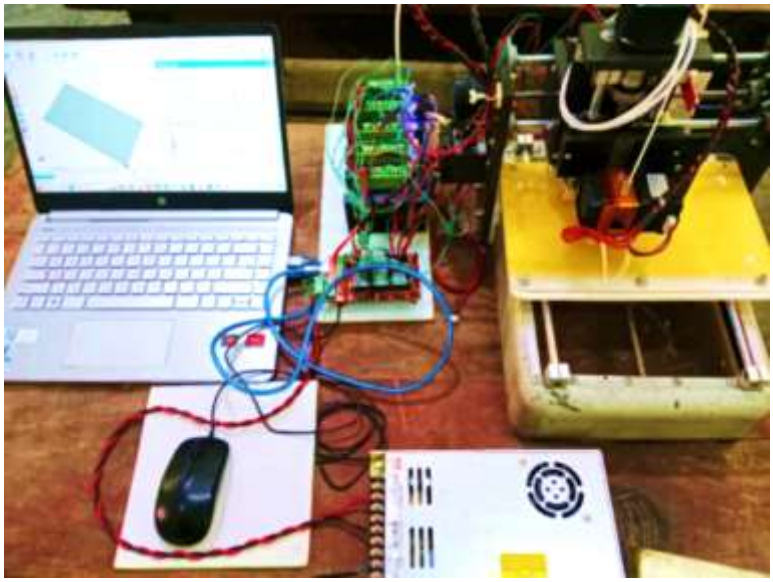

Figure 5. The photograph of the constructed 3D printing system.

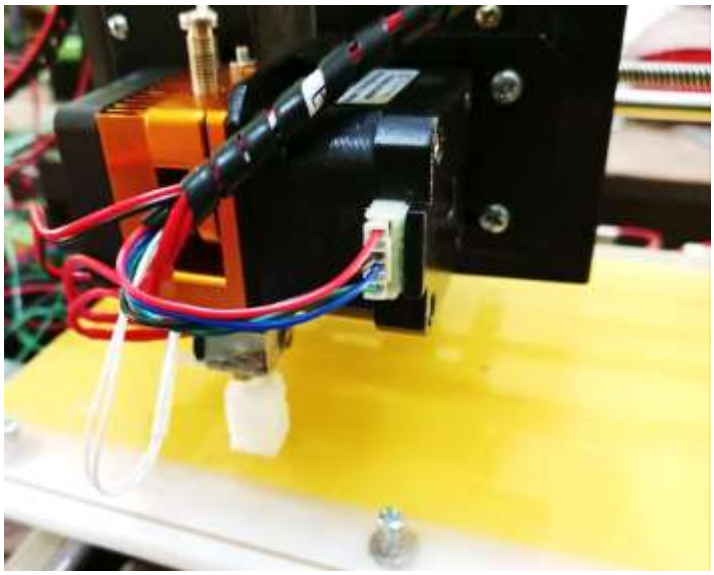

Figure 6. The printing process of the 3D printing system.

Conclusion

The Cartesian coordinate positioning-based 3D printing machine was successfully built with electronic and mechanical parts. In terms of current regulation in Ramps controller, it was observed that the current regulator achieved the required output current to control system components such as stepper motors and heating elements, which was to simply control the current flowing on phase winding, even when facing input voltage with ripple. In its real implementation, it was observed current spikes that might lead to motor overall life cycle reduction. The analysis led to the conclusion that the current spikes were caused by very high switching-off latency and diode latency, lack of coordination on switching the H bridge transistors and measurement interference caused by the currents surge that in its turn are caused by the switching of the load. As solution to these problems, it was suggested that the replacement of the BJT based H bridge by a power MOSFET based H bridge and use of switching diodes even faster than those MBR350 used, and revision of the driver board, considering more carefully the design of the board in what it refers to the current carrying lines.

The extruder head was designed and analyzed to ensure a better heat concentration only in the area of heating block containing the nozzle and heater. It was also needed to avoid as much as possible dissipation of heat to the aluminum frame or to the environment. Furthermore, cooling fan would be used to lowering the temperature of the deposited ABS material passage which improved the flowing of the material, because it is heated only in the area of extrusion, where it is needed.

The FEA thermal analysis confirmed the design requirements, the temperature measured on the nozzle was observed 240 °C and it was equal to the value needed to melt the ABS materials. The temperature value of the extruder thermal insulator part was equal to 40.7 °C. In the FEA analysis, the temperature value of the extruder thermal insulator part was 37 °C. The difference of 3.7 °C is related to the environmental temperature of 25 °C set during the simulation, different from the value measured during the thermographic analysis that was 28.7 °C. This difference of three degrees decreases the difference to 0.7 degrees between the FEA analysis and thermographic analysis. This is a small difference and it can be neglected, because it does not affect and disturb the system for printing with ABS materials.

Acknowledgements

This research work was totally implemented in Electronics lab, Department of Physics, University of Mandalay.

References

Alaa J. A., (2015), "The process and Technologies of 3D Printing", International Journal of Advances in computer science and technology, vol.4 (10), pp.161-163.

Budi H., Robby W., (2021), "Development and Accuracy Test of a Fused Deposition Modeling (FDM) 3D Printing Using H-bot mechanism", Springer, vol.3 (1), pp. 46-53.

Gianfrano F., (2019), "Print on air: FDM 3D Printing without Supports", IEEE access, vol. 19, pp. 350-352.

Joseph F., (2019), "Cartesian, Delta, and Polar 3D Printers: What are they and what's the difference?", Web resource: https://www.JosephF.org,(Accessed date - 15.7.2024).

Karel D., (2017), "3D Model Preparing for Rapid Prototyping by FDM method", 8th Edition, McGraw Hill Press, USA.

Kevin H., "What is a CoreXY 3D printer?", Web resource: https://www.3dtechvalley.com/what-is-a-corexy-3d-printer/, (Accessed date - 3.7.2021).

FABRICATION AND PROFILING OF TIO_2 THIN FILMS VIA LOW-TEMPERATURE SYNTHESIS

Nyo Mar Soe[1], Soe Ko Ko Aung[2] and Yin Maung Maung[3]

Abstract

The focus on low-temperature processed electron transport layers (ETLs) has gained significant attention for the fabrication of flexible perovskite solar cells. In this study, anatase titanium dioxide (TiO_2) nanoparticles were synthesized via a hydrothermal method and applied using the spin-coating technique, with annealing performed at 200 °C. X-ray diffraction analysis confirmed the crystal structures of the TiO_2 film. Additionally, the UV-Vis spectrum revealed a high transmittance exceeding 80%. The energy band gap (3.25 eV) and thickness (542 nm) of the TiO_2 film were determined through Tauc's plot method and Envelope method, respectively. These findings suggest that this straightforward approach to preparing TiO_2 ETLs holds promise for integration into the fabrication of perovskite solar cells.

Keywords*:* Titanium dioxide (TiO_2), Electron Transport Layer (ETL), Spin coating method, Optical properties

Introduction

Solar cells have supplied a solution to the energy crisis and environmental contamination because of their potential to use solar energy (F. Rehman et al., 2023). Solar cells (SCs) can overcome the energy crisis for environmental all over the world. The fabrication of solar cell is completed with a suitable band energy alignment at the interface of two layers through unlike semiconductors. In addition, absorption of light, charge charriers, restriction of recombination loss and quality of selected material support solar cell system (H. Soonmin et al., 2023). First generation solar cells were fundamentals silicon p-n junction semiconductor. Second generation solar cells based on are thin-film technologies, especially based on amorphous silicon (a-Si) and inorganic substances such as copper indium gallium selenide (CIGS) and cadmium telluride (CdTe) with a larger absorption coefficient (B. P. Singh et al., 2021). Third-generation solar cells are dye-sensitized solar cells (DSSCs), perovskite solar cells (PSC), and quantum dot sensitized solar cells (QDSSCs) are being widely discovered and undergoing rapidly development. Their implementation with thin-film technologies could have an enormous impact economical friendly, making solar energy one of the most available and cheapest selection for future energy production (N. Shah et al., 2023).

To date, perovskite solar cells (PSCs) have been enhanced power conversion efficiency (PCE) from 3.8% to 26.1% in 2024. Perovskite Solar Cells will be built electron transport layer (ETL), hole transport layer (HTL), perovskite layer and metal electrode. Among them, electron transport layer is crucial to overcome band alignment issues and improve electron transport. Moreover, ETLs are basically used to increase device performance and stability of perovskite solar cells. Metal oxide semiconductors involved titanium dioxide, zinc oxide, tin oxide, etc. Low temperature processed semiconductor metal oxides, such as cadmium selenide (CdSe), zinc oxide (ZnO) and ternary metal oxides have been explored as a potential contender to replace TiO_2 since TiO_2 must be post-treated at high temperature (Z. Yin, et al., 2022). These devices achieve high power conversion efficiencies (15−22%) but mainly require high-temperature sintering (>450 °C), which is not possible for temperature-sensitive substrates. To overcome these issues, alternative low-temperature (<150 °C) processed carbon-based PSCs will be fabricated to realize high-efficiency TiO_2based efficient perovskite solar cells. Low temperature processed carbon-based perovskite cells (C-PSCs) have gained great attention because of ease of fabrication and

[1] Department of Physics, Yangon University of Distance Education

[2] Department of Physics, University of Mandalay

[3] Department of Physics, University of Yangon

low cost (S. K. K. Aung, et al., 2022). In addition, hydrothermal synthesis method of TiO_2 benefits the ability to create crystalline phase and do not require high temperature calcination (H. G. Hameed et al., 2023). It is less energy consumption and also cost effectiveness.

The present work purposes to identify the crystal structure and the optical properties of anatase TiO_2 films. In addition, energy band gap and thickness of prepared film are calculated by Tauc's plot method and envelope method. The results show that high transmission (above 80%) TiO_2 film at 200 °C which is a suitable electron transport layer in low temperature processed fabrication in perovskite solar cells.

Materials and Methods

Preparation of TiO_2 Thin Film

Firstly, fluorine-doped tin oxide (FTO) pure glass substrates of 1cm × 1cm were created and cleaned with a small amount of detergent and water followed by acetone, ethanol and isopropanol in ultrasonic vibration for 15 mins to remove impurities. After that, the substrates were dried with dryer. Then, 23 ml of acetic acid and 100 ml of distilled water (DW) were combined to get 4 M of acetic acid solution. At the same time, 30 ml of titanium tetraisopropoxide (TTIP) and 100 ml of DW were also mixed to get 1M of titanium tetraisopropoxide solution. Subsequently, 20 ml of acetic acid solution was combined with 100 ml of TTIP solution and the mixture solution was stirred for 1 h. After stirring, the mixture was kept for 24-hours at room temperature. After 24-hours, the mixture was transferred to a Teflon-lined autoclave and dried at 180 °C for 6h in a muffle furnace. And then, the autoclave was cooled down to room temperature. The colloidal solution was coated onto a silicon wafer by using spin coating technique. The structured properties of TiO_2 coated Si wafer were examined by XRD analysis. Furthermore, 200µL of colloidal solution was dropped on the FTO cleaned substrate via 100 µL-1000 µL pipette and spin coated with 3000 rpm for 30 s. Then resultant substrates were annealed at 200 °C on the hot plate for 30 mins. In order to know the optical properties of TiO_2 coated FTO thin film, UV-vis spectroscopy was employed. The schematic diagram of the synthesis of the TiO_2 thin film was shown in Figure 1 and the photograph of the synthesis of TiO_2 thin film was also shown in Figure 2.

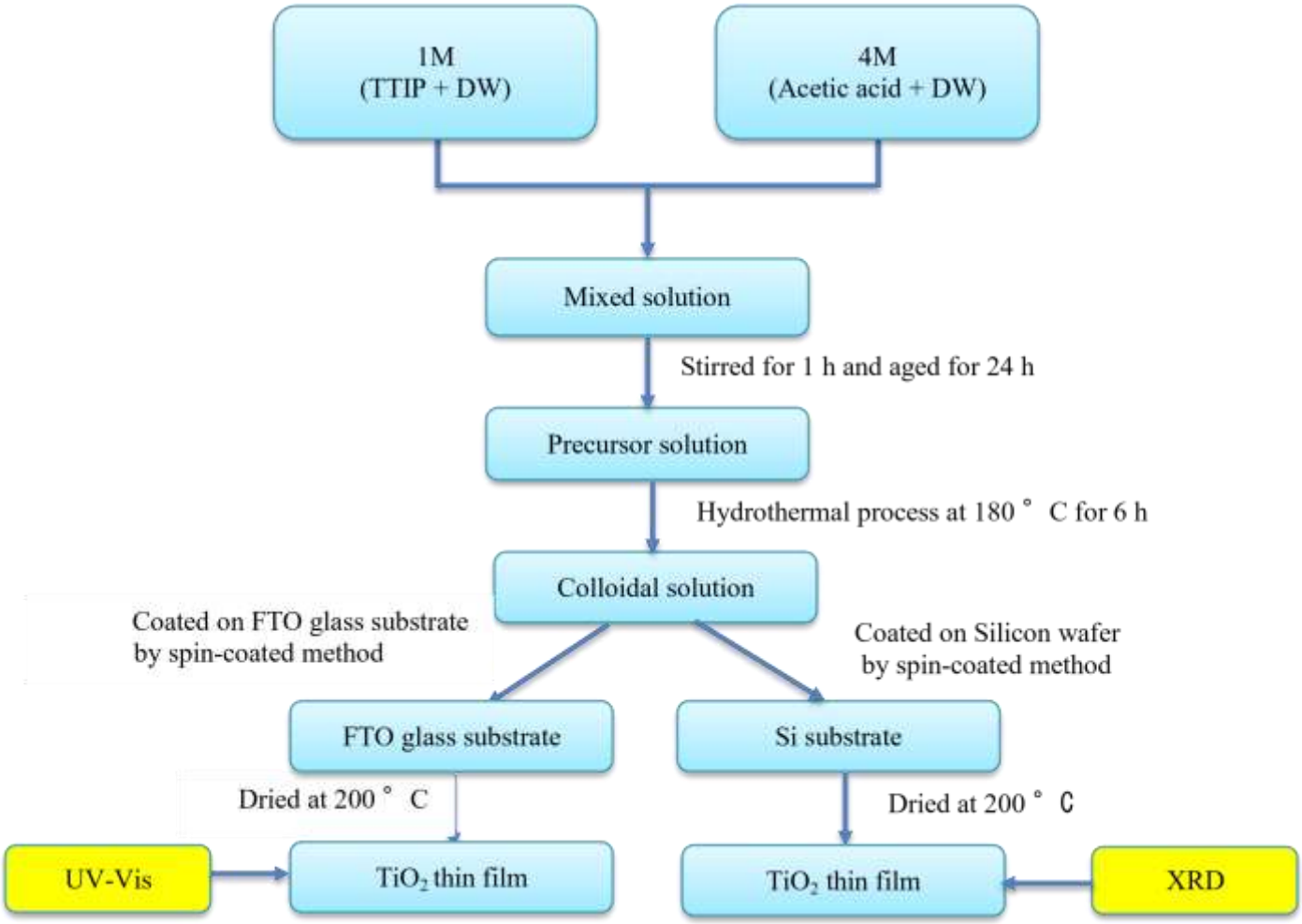

Figure. 1 Schematic diagram of the synthesis of TiO_2 thin film

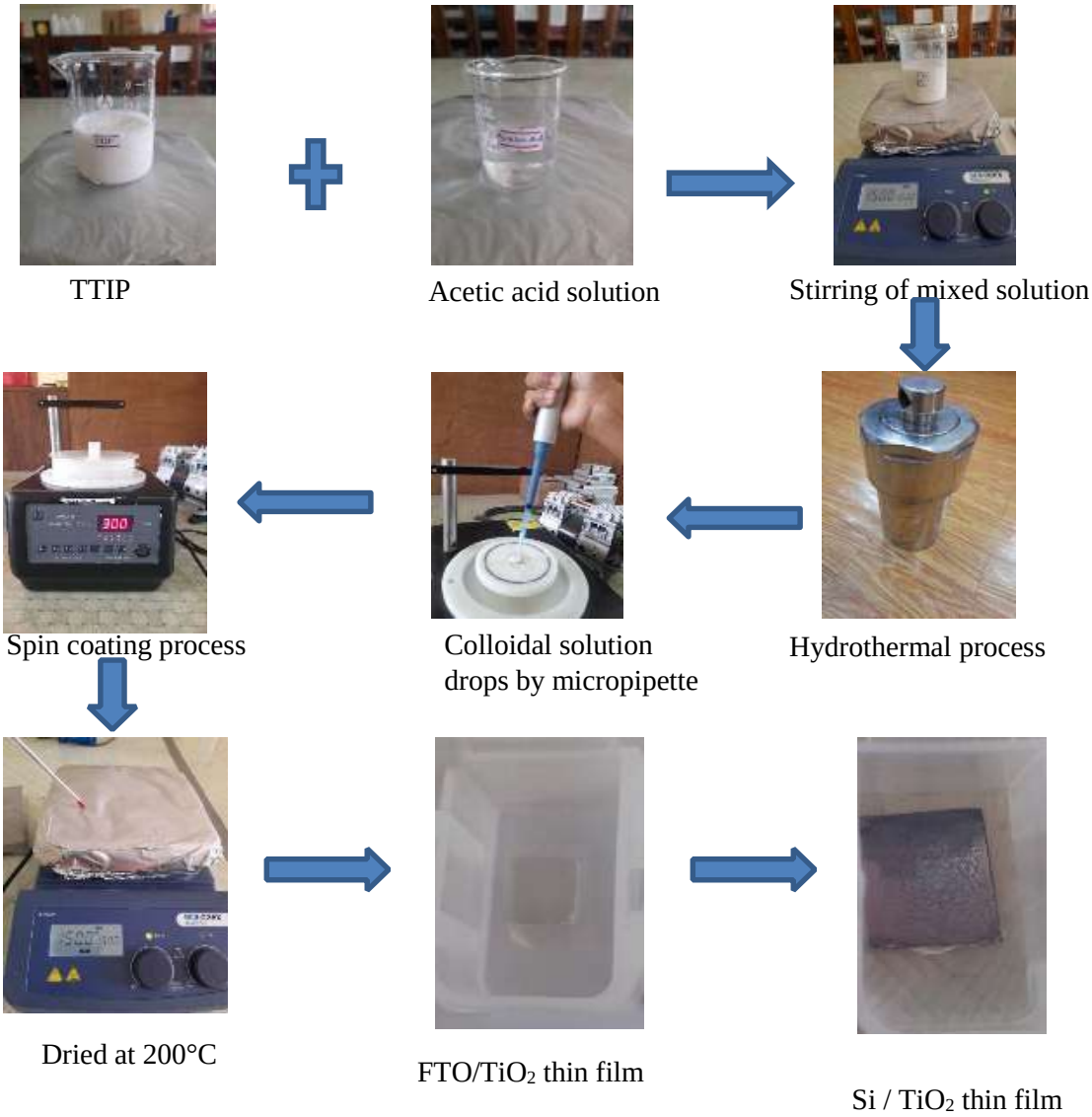

Figure. 2 Photograph of the synthesis of TiO_2 thin film

Characterization techniques

The optical properties of TiO_2 thin film were recorded in the wavelength range between 190 – 1100 nm by using UV-Vis spectrophotometer (Thermo Genesys 10S). The crystal structure of prepared films was measured using SmartLab Rigaku.

Results and Discussion

XRD Analysis of TiO2 Thin Film

The crystal structures of TiO_2 thin film were confirmed by X-ray diffraction (XRD) spectra using Cu-Kα radiation (1.54059 Å) at a scanning range of 10−60° (Rigaku Corporation) seen in Figure 3. The characteristic peaks corresponded well with the JCPDS card (21–1272), inferring an anatase type of TiO_2 was formed. The XRD spectrum revealed prominent diffraction peaks at 24.72° (101), 37.27° (004), 47.43° (200), 53.51° (105), and 54.59° (211), aligning with the anatase phase of TiO_2. Furthermore, the average crystallite size was determined by the Debye-Scherrer equation using the following equation: $D = K\lambda/\beta\cos\theta$, where, λ= wavelength of the incident X-ray beam (1.5405 Å) for CuKα, K = shape factor constant, β = FWHM (full width at half maximum) (radian), θ = diffraction angle (radian) and D = crystallite size (nm) (T.

Theivasanthi, et al., 2023). The average crystallite size of the TiO_2 particle was to be approximately 16.89 nm listed in Table 1.

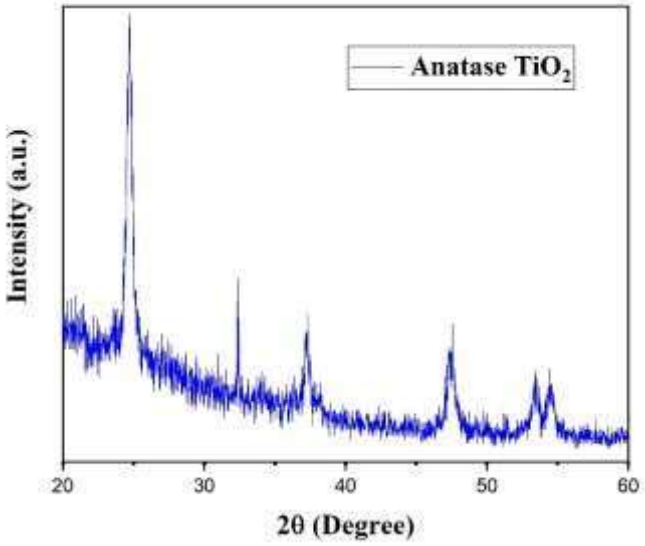

Figure. 3 XRD pattern of TiO_2 thin film

Table 1. Crystallites (grain) size from XRD data using Debye-Scherrer equation.

No.	2θ (degree)	FWHM (degree)	(hkl)	Crystallite size (D) (nm)
1	24.72	0.47	(101)	17.1177
2	37.27	0.39	(004)	21.2792
3	47.43	0.66	(200)	12.9999
4	53.51	0.53	(105)	16.5109
5	54.59	1.53	(211)	16.5905
Average crystallite size				**16.89 nm**

Optical Properties of TiO_2 Thin Film

The UV-Vis spectrum describes that how much a sample component absorption light in the thin film area due to it is scanned through each wavelength in the ultraviolet-visible range of the electromagnetic radiation. The transmission and absorption spectra emerge at each wavelength. Figure 4 showed UV-Vis transmission spectra of TiO_2 coated FTO substrate and bare FTO substrate in the wavelength range 300-900 nm. Transmittance data for FTO /TiO_2 and FTO films were listed in Table 2. It was found that the transmittance spectrum of the TiO_2 coated FTO substrate which is slightly lower than that of the bare FTO substrate.

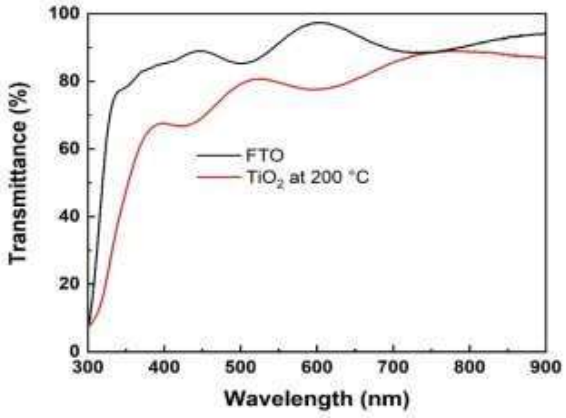

Figure. 4 UV-Vis transmission spectra of TiO_2 thin film

Table 2. Transmittance (%) data for TiO_2 thin film and FTO

Film	Wavelength (nm)			Transmittance (%)		
	1st peak	2nd peak	3rd peak	1st peak	2nd peak	3rd peak
FTO	336	446	601	76	89	**97**
TiO_2	395	520	774	67	81	**89**

Optical Band Gap Calculation

The band gap shows a specific minimum energy for an electron to jump from the valence band to the conduction band (K. M. Reddy, et al., 2003). Optical band energy was determined from the absorption spectrum by applying Tauc's plot equation:$(\alpha\ h\ \nu)^n = A\ (h\ \nu\ E_g)$ where, E_g is the optical band gap and α is the absorption coefficient. The optical energy gap of TiO_2 was observed for indirect transition (n=1/2) and the optical energy gap of FTO was examined for direct transition (n= 2). Then, the plot of deviation of $(\alpha\ h\ \nu)^{1/2}$ for TiO_2 and $(\alpha\ h\ \nu)^2$ were demonstrated in Figure 5. The calculated energy gap for TiO_2 (3.25 eV) was lower than that of FTO (3.75 eV) due to decreased in transmittance corresponding to increase in thickness. Hence, we investigated the thicknesses of FTO/TiO_2 and FTO substrates by using Swanepoel's envelope method. Energy band gap data for FTO/TiO_2 and FTO films were listed in Table 3.

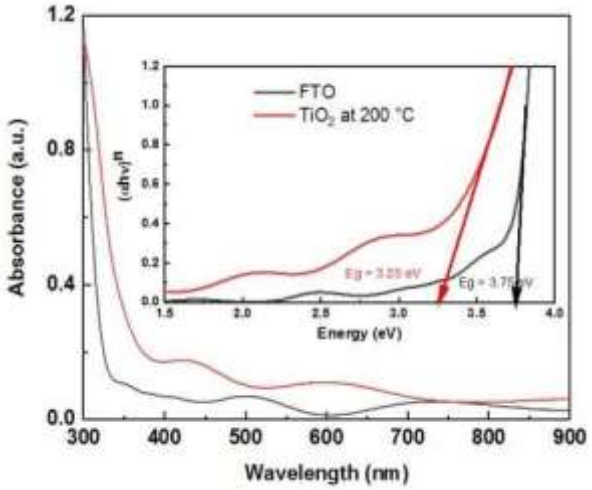

Figure. 5 UV-Vis absorption spectra of TiO_2 thin film

Table 3. Energy band gap data for TiO_2 thin film and FTO

Film	Energy Band Gap (eV)	Thickness (nm)
TiO_2	3.25	542
FTO	3.75	604

Determination of thin film thickness

When the light interference from the two surface of thin film, transmission spectrum of thin film can be observed in the spectral regions of weak and medium absorption. Thickness of TiO_2 thin film can be examined from the interference peaks of the transmission spectrum over the visible region. The estimation of refractive index, n of thin film in weak and medium absorption at each wavelength can be calculated by using upper envelope of the curve, T_M and lower envelope of the curve, T_m in the transmission spectrum, $n = [N + (N^2 - s^2)^{1/2}]^{1/2}$ where, $N = 2s \left(\frac{T_M - T_m}{T_M T_m}\right) + \frac{s^2+1}{2}$, s is the refractive index of the substrate (E. R. Shaaban, et al., 2012). n_1 and n_2 are refractive indices for two adjacent maxima or minima at the wavelengths of λ_1 and λ_2 as well as λ_2 and λ_1. Finally, thickness of films from the transmission spectra can be calculated using the following equation, $d = \frac{\lambda_1 \lambda_2}{2(\lambda_1 n_2 - \lambda_2 n_1)}$. The thickness of TiO_2 thin film (542 nm) was lower than that of FTO film (604) can be seen in Figure 6(a) and (b) determined by envelop method. In these figures, the envelopes pass through tangentially through transmission curve in the range 300-900 nm. The interference fringes were observed in the transmittance spectra for TiO_2 film as deposited on FTO glass substrate annealed at 200°C. This result showed that the roughness is related to the surface fluctuations. The calculated refractive index and thickness values were given in Table 4.

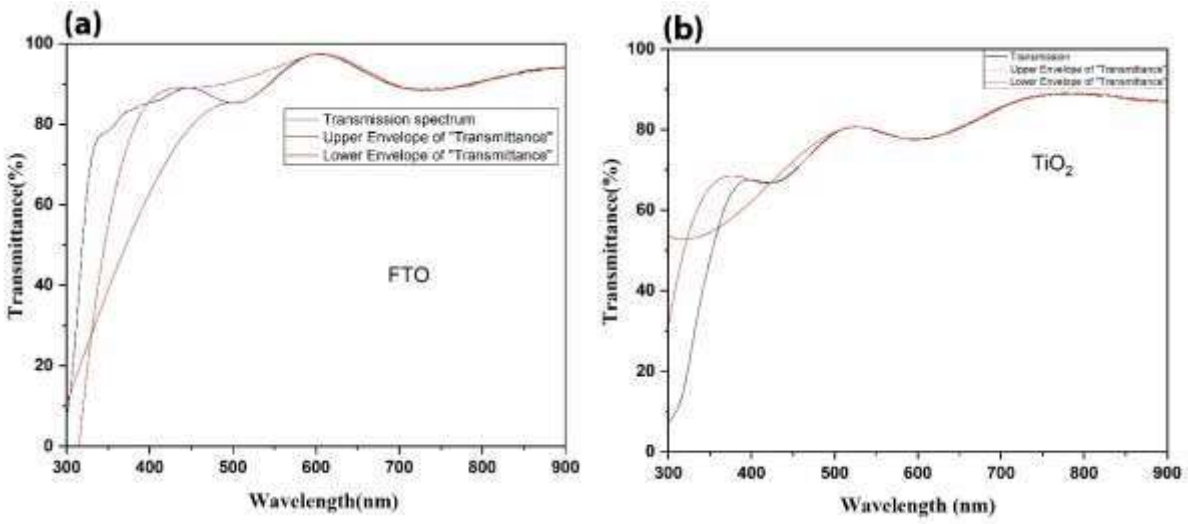

Figure 6. Thicknesses determination of (a) FTO film and (b) TiO_2 film

Table 4. Thickness data for FTO and TiO_2 films

Film	λ_1 (nm)	λ_2 (nm)	Refractive index (n_1)	Refractive index (n_2)	Thickness (d) (nm)
FTO	584	444	1.5101	1.5156	604
TiO_2	507	389	1.5099	1.5168	542

Conclusions

In this study, anatase TiO_2 nanoparticles were synthesized through a hydrothermal route and applied them using the spin-coating method, with annealing performed at 200 °C. The XRD results indicated well-defined characteristic peaks of TiO_2, confirming the formation of an anatase type. The TiO_2 thin film exhibited excellent transmission exceeding 80%, and the UV-Vis spectra revealed an optical bandgap of 3.25 eV. Utilizing Swanepoel's envelope method, we determined the thickness of the TiO_2 film to be 542 nm. This research establishes that the TiO_2 thin film, processed at 200°C, is well-suited as an electron transport layer in perovskite solar cells.

Acknowledgements

I especially thank you to Prof Dr Khin Khin Kyaw, Head of Department of Physics, Yangon University of Distance Education, for her kind permission to contribute of this work. My special thanks go to Prof Dr Hsun Lwin, Department of Physics, Yangon University of Distance Education, for his permission to contribute of this work. I sincerely thank to Prof Dr Cho Cho Thet, Department of Physics, University of Yangon, for giving encouragement of this work. Author thanks to international science programme (ISP), Uppsala University for providing research facilities.

References

B. P. Singh, S. K. Goyal, and P. Kumar, (2021) "Solar pv cell materials and technologies: Analyzing the recent developments," *Mater. Today Proc.*, vol. 43, pp. 2843–2849, doi: 10.1016/j.matpr.2021.01.003.

E.R. Shaaban, I. S. Yahia, and E. G. El-Metwally, (2012) "Validity of swanepoel's method for calculating the optical constants of thick films," *Acta Phys. Pol. A*, vol. 121, no. 3, pp. 628–635, doi: 10.12693/APhysPolA.121.628.

E. Rehman *et al.*, (2023) "Fourth-generation solar cells: a review," *Energy Adv.*, vol. 2, no. 9, pp. 1239–1262, doi: 10.1039/d3ya00179b.

H. G. Hameed and N. A. Abdulrahman, (2023) "Synthesis of TiO2 Nanoparticles by Hydrothermal Method and Characterization of their Antibacterial Activity: Investigation of the Impact of Magnetism on the Photocatalytic Properties of the Nanoparticles," *Phys. Chem. Res.*, vol. 11, no. 4, pp. 771–782, doi: 10.22036/pcr.2022.351688.2137.

H. Soonmin, Hardani, P. Nandi, B. S. Mwankemwa, T. D. Malevu, and M. I. Malik, (2023) "Overview on Different Types of Solar Cells: An Update," *Appl. Sci.*, vol. 13, no. 4, pp. 1–37, doi: 10.3390/app13042051.

K. M. Reddy, S. V. Manorama, and A. R. Reddy, (2003) "Bandgap studies on anatase titanium dioxide nanoparticles," *Mater. Chem. Phys.*, vol. 78, no. 1, pp. 239–245, doi: 10.1016/S0254-0584(02)00343-7.

N. Shah *et al.*, (2023) "A Review of Third Generation Solar Cells," *Processes*, vol. 11, no. 6, doi: 10.3390/pr11061852.

S. K. K. Aung, A. Vijayan, M. Karimipour, T. Seetawan, and G. Boschloo, (2023) "Reduced hysteresis and enhanced air stability of low-temperature processed carbon-based perovskite solar cells by surface modification," *Electrochim. Acta*, vol. 443, p. 141935 doi: 10.1016/j.electacta.2023.141935.

S. Theivasanthi and M. Alagar, (2013) "Titanium dioxide (TiO2) Nanoparticles XRD Analyses: An Insight," 2013, [Online]. Available: http://arxiv.org/abs/1307.1091

Z. Yin, B. Lu, Y. Chen, and C. Guo, (2022) "Advances of Commercial and Biological Materials for Electron Transport Layers in Biological Applications," *Front. Bioeng. Biotechnol.*, vol. 10, no. May, pp. 1–20, 2022, doi: 10.3389/fbioe.2022.900269.

ANALYSIS OF TiO_2/ZnO LAYERS FOR PEROSKITE SOLAR CELLS: EXPLORING CRYSTALLINITY, CHEMICAL PROPERTIES, AND OPTICAL PERFORMANCE

Cherry Moh Moh Than[1], Zin Min Myat[2], Zin Min Tun[3], Yin Maung Maung[4]

Abstract

The electron transport layer (ETL) was designed for perovskite solar cells (PSCs) using a sol-gel spin coating method on FTO glass substrates, including TiO2 and ZnO nanocrystals. Characterization using X-ray Diffraction (XRD) and Fourier Transform Infrared Spectroscopy (FTIR) implied the crystallinity and chemical properties of the FTO/TiO2/ZnO ETL layers. UV-Vis measurements revealed TiO2 absorption within the range of 211 nm-226 nm and ZnO absorption from 302 nm-387 nm. The energy band gap values of TiO_2/ZnO films showed their suitability as an ETL for PSCs. The study suggests that this ETL not only enhances electron transport and interfacial engineering but also holds promise as a light-harvesting layer in PSCs, attributed to its favorable crystalline quality, chemical characteristics, and optical performances.

Keywords: ETL, FTO, TiO2 /ZnO, Perovskite Solar Cells, XRD, FTIR and UV-Vis

Introduction

Since 2009, Lead halide perovskite materials were obtained. There has been a strong focus on solar cells (Sanglee, K, et al.,2022). Perovskite solar cells have rapidly reached a Power Conversion Efficiency (PCE) of 25.5% in the past few years (Drygała, A&Dobrzański, L.A,et al.,2016). Perovskite materials have unique photovoltaic properties, such as strong light absorption and long carrier lifetime. Optimizing the absorber layer and selecting suitable materials as electrodes are also important in improving the PCE. Surface engineering techniques, such as coating a thin layer on the electron transport layer (ETL) or hole transport layer (HTL) or surface modification, can significantly improve the electrical and optical properties, stability, and scalability of solar cells. Many studies have focused on the conventional (n-i-p) structure of PSCs. The electron transport layer (ETL) is a key component of a solar cell. ETLs protect the perovskite layer from direct contact with the transparent oxide and perovskite crystal structure, and play a crucial role in efficient transfer and transport. Among metal oxides, TiO2 can best serve as ETL in planar or mesoporous form. Surface modification of TiO2 has been carried out using different materials such as SnO2 (S. Casaluci, et al.2009), ZnO, MgO (Kojima, K. Teshima, &T. Miyasaka, et al.2009). Typical ETLs are titanium dioxide (2H, zinc) (Szewieczek, 0;. Zuo, C.; Zhang, L, et al.2023) or zinc-tin oxide (G. S. Han, H. S. Chung, et al.2015).In particular, perovskite solar cells with ETL from aged titanium sol revealed significant differences of short circuit current which is 8% higher than their counterpart with ETL from fresh sol (M.M. Tavakoli et al.,2015). Titanium dioxide can be deposited by chemical vapor deposition (G. San Vicente et al..2001) atomic layer deposition or sol-gel method (Liu H., Yang W., Ma Y., Cao Y.,et al., 2002), where the sol-gel is frequently used due to inexpensive, easy processing and high repeatability. Sol-gel method is low cost of necessary materials; TiO_2 is known to be the most widely used because of its mild reaction conditions and high purity and uniformity (Yu J.G.,& M. M. Ba-Abbad,et al.,2012). TiO_2 is an n-type wide bandgap semiconductor and has three crystalline phases, i.e. anatase (tetragonal), rutile (tetragonal), and brookite (orthorhombic) with band gap 3.02 eV (410 nm), 3.20 eV (387 nm) and 2.96 eV (419 nm), respectively. Among these three types, the rutile phase is most stable form while anatase and brookite types are

[1] Department of Physics, Pathein University
[2] Department of Physics, West Yangon University
[3] Department of Physics, West Yangon University
[4] Department of Physics, University of Yangon

metastable and possible to transform to rutile phase under high temperature of about 750°C. Synthesis of anatase, rutile and brookite of TiO_2 particle and thin film from $TiCl_3$ were reported by Leal J L *et al*. (Affa Rozana Abdul Rashid,et al.,2021), Considering ETL as an important part of perovskite-based solar cell we put more emphasis on examination of its impact on perovskite solar cell parameters.

Materials and Methods

Synthesis of Titanium Dioxide Films

In the present research, titanium trichloride ($TiCl_3$), hydrochloric acid (HCl) and ammonium hydroxide (NH_4OH) solutions were used as starting materials. All chemical reagents used in these experiments were of analytical grade, commercially purchase from chemical market used as received without purification. Deionized water (DI) was used as solvent. TiO_2 solution have been firstly prepared by using sol-gel method. Firstly, 20 ml of $TiCl_3$ was dissolved with 100 ml of Deionized (DI) water stirred for about 1hour on the magnetic stirrer. At that time, the color of solution was found to be purple. During stirring, the 40ml of ammonium hydroxide (NH_4OH) solution was added and it was found that the color of solution changed purple to dark black. The solution was stirred continuously about 15 minutes the color change to sky blues. After stirred at 15 minutes the color of this solution was changed to perfectly white. This procedure last totally about five hours. This solution reached the pH value in 10. During stirring, hydrochloric acid (HCl) was poured by using drop by drop in the mixture solution until to get a homogeneous solution and adjust pH levels to reach pH 7. The block diagram of TiO_2 films preparation was shown in Figure 1. Figure 2 showed the change in color of TiO_2 sol gel solution while the adjustment of pH level to reach 7.

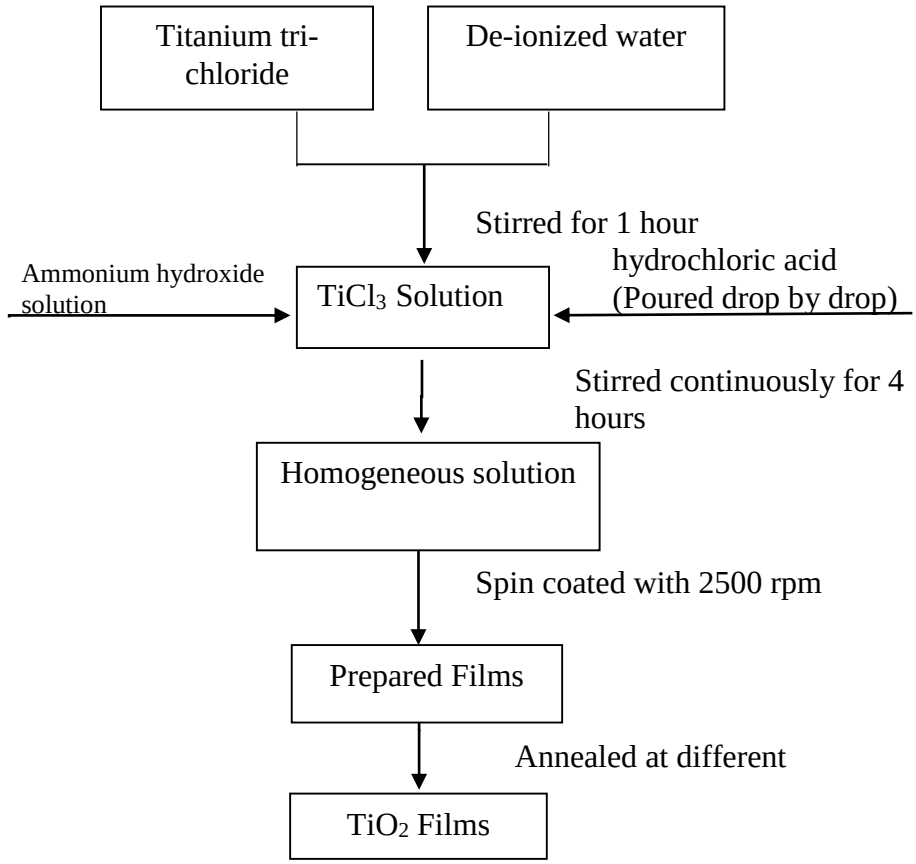

Figure 1 The block diagram of TiO_2 films preparation

Figure 2 Change in color of solution while the adjustment of pH level to reach 7

Synthesis of Zinc Oxide sol-gel solution

They were first agitated by a magnetic stirrer in various containers of 4g NaOH in 100ml DI water and 20.83 g $ZnCl_2.4H_2O$ in 100 ml DI water, and then stirred at room temperature for 15 min on a magnetic stirrer. Finally, the solution containing NaOH was slowly poured into a container of $ZnCl_2.4H_2O$ for three hours at 80°C with a magnetic stirring to obtain ZnO sol-gel solution.

Device Preparation of hybrid TiO_2/ZnO Electron Transport Layer

Firstly, the cutting Fluorine doped Tin Oxide glass substrates with a thickness of 1.1 mm and size of 1x1 cm^2 (11-20Ω) immersed by hydrochloric acid (HCl) and distilled water in the ratios 1:20 for 30 minutes to remove some impurities on the glass substrates. Secondly, these glasses were certainly washed by distilled water and were dried up at room temperature. And then, they were dipped in ethanol about 10 minutes and dried. After this process, these glasses were dipped in acetone for about 15 minutes and finally dried at room temperature. TiO_2 solution was coated on FTO glass substrates through spin coating machine with 2500 rpm for 30 s. After the deposition, the films were dried at 80 °C for 1 hour and allowed to cool slowly at room temperature. The prepared TiO_2 films onto FTO substrates were annealed at 400 °C, 450 °C, 500 °C, 550 °C and 600 °C for 2 hours respectively. Figure 4 showed TiO_2 solution was coated on FTO glass substrates. And then, ZnO solution was coated on the TiO_2 layer on FTO glass samples made at different temperatures by a spin coating machine at 2500 rpm for 30 seconds. The films were dried at 80 °C for 1 hour and cooled slowly to room temperature. The sample Preparation of hybrid TiO_2/ZnO Electron Transport Layer onto FTO glass substrates were annealed for 2 hours respectively shown in figure 3. The structural characterization of the deposited films was carried out by X-ray Diffraction and Functional groups and the vibrational energy of the molecules of sample were examined by Fourier transform Infrared Spectroscopy (FTIR). The optical properties of TiO_2/ZnO films were examined using UV-Vis spectroscopy.

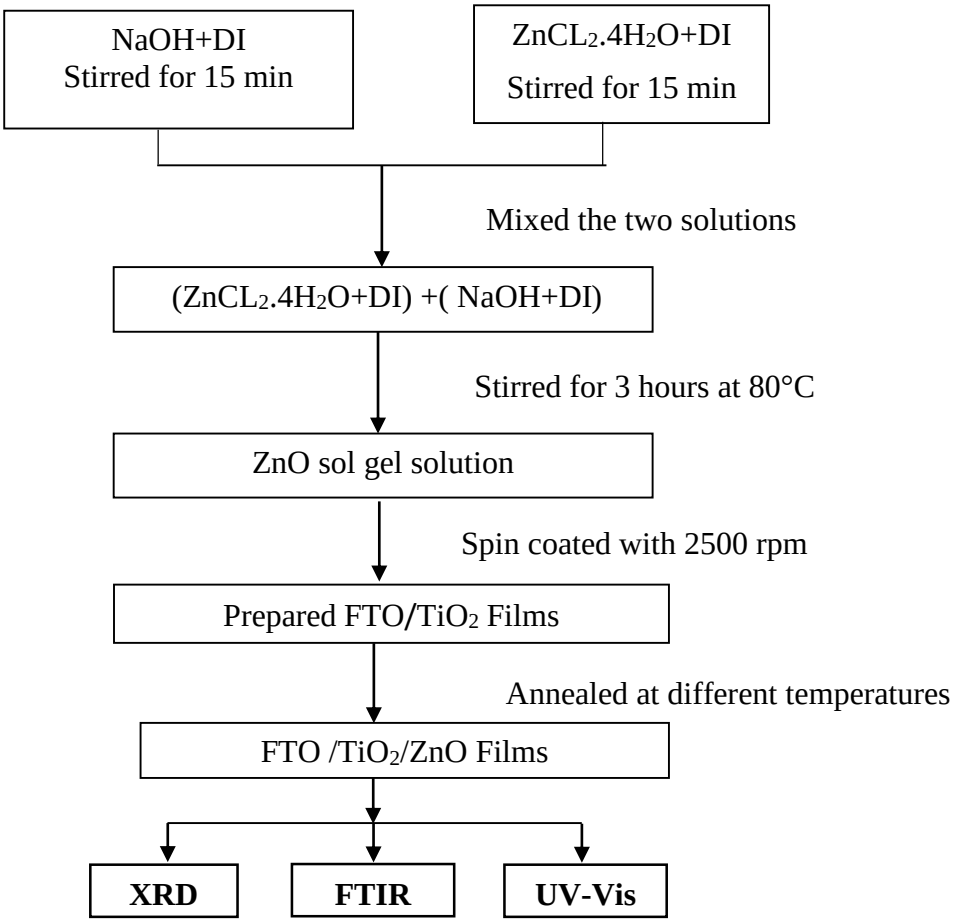

Figure 3 The block diagram of FTO/ TiO_2/ZnO preparation

Results and Discussions

XRD Analysis of TiO_2/ZnO Films

The structural properties of TiO_2/ZnO films were characterized by X-ray diffraction method. The tetragonal brookite phase of TiO_2 peaks were observed at (111), (201), (140) and (133) planes with their respective diffraction angles (2θ). JCPDS card number 00-003-0380 library file confirmed these diffraction peaks. For the ZnO, the distinct peaks were detected at (100), (002), (101) and (102) planes with their respective 2θ values. These results were in good agreement with of hexagonal crystal structure ZnO (Zincite) phases according to the JCPDS card number 00-001-1136. According to the XRD results, there were some minor peaks were also found. This may be the requirements of sample preparation and substrate cleaning process. All the XRD spectra of TiO_2/ZnO films compared in figure 4. The average crystallite sizes of TiO_2/ZnO films were calculated by Debye Scherrer formula. From the calculation results, the average crystallite sizes of TiO_2/ZnO films were 26.71 nm at 400 ^oC, 24.13 nm at 450 ^oC, 23.81 nm at 500 ^oC, 23.72 nm at 550 ^oC and 23.32 nm at 600 ^oC respectively. Table 1 tabulated the structural properties of TiO_2/ZnO films at different process temperatures. According to the XRD analysis, temperature conditions highly influenced the crystallinity during the thermal oxidation process. Increases oxidation temperature on TiO_2/ZnO films were decreased crystallite sizes.

Table 1. Structural properties of TiO_2/ZnO films at different temperatures

Distinct peaks (hkl)	Average crystallite size (nm)	Assigned structure
(111)	26.71 (400 °C) 24.13 (450 °C) 23.81 (500 °C) 23.72 (550 °C) 23.32 (600 °C)	TiO_2
(100)		ZnO
(002)		ZnO
(101)		ZnO
(201)		TiO_2
(140)		TiO_2
(102)		ZnO
(133)		TiO_2

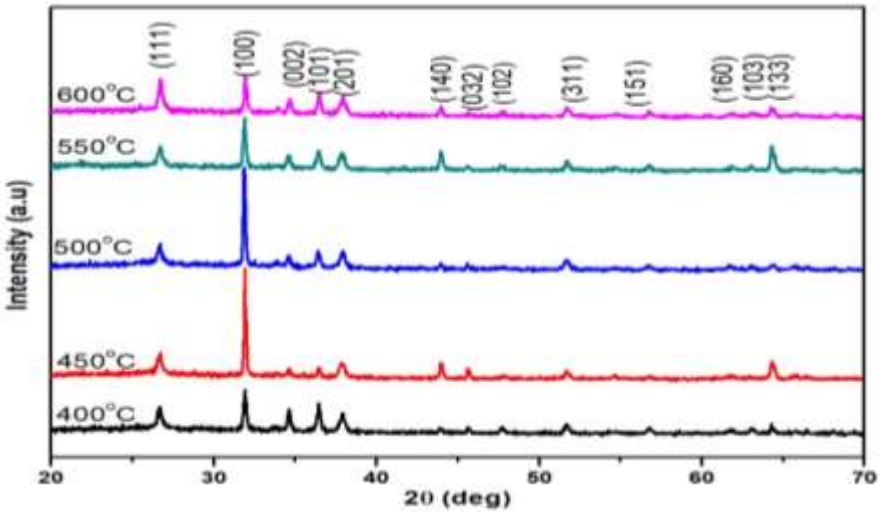

Figure 4 Comparison of XRD spectra for TiO_2/ZnO films at different temperatures

FTIR Analysis of TiO_2/ZnO Films

In this study, the chemical properties of the sol-gel synthesized TiO_2/ZnO films were examined by using FTIR spectroscopy. In these results, the absorption band at ~3368 cm^{-1} is related to O-H stretching vibration and ~1631 cm^{-1} to O-H bending representing the water as moisture. The peaks observed at ~1390 cm^{-1}-1500 cm^{-1} assigned to O-H bending vibration in carboxylic acid. The Ti-O stretching vibrations were detected at the wavenumbers ranges of 621 cm^{-1} -704 cm^{-1} [17]. The absorption peaks of Zn-O were observed at ~443 cm^{-1}- 448 cm^{-1} respectively. The existence of these characteristic bands in FTIR spectra confirms the successful formation of TiO_2 and ZnO. FTIR spectra comparison of TiO_2/ZnO films was shown in figure 5.

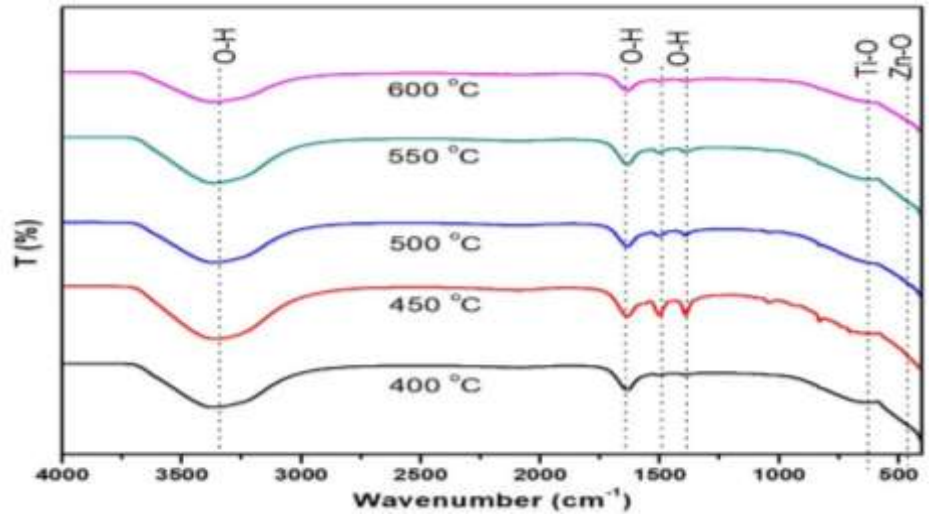

Figure 5 FTIR spectra comparison of TiO_2/ZnO films at different temperatures

UV-Vis Analysis of TiO_2/ZnO Films

The UV-Vis spectra of all TiO_2 films were obtained on Lambda 365 UV-Vis spectrometer in the range of 200 nm -700 nm. Figure 6 (a-e) showed that the UV-Vis absorption spectra with their corresponding energy band gaps of TiO_2/ZnO films at 400 ˚C, 450 ˚C, 500 ˚C, 550 ˚C and 600 ˚C. It was found that the maximum absorption of wavelength obtained by coating onto FTO is in the ultraviolet region. The maximum wavelength ranges of spectrum for all films laid between 200 nm to 400 nm. From the absorption spectra, the wavelength ranges 211 nm-226 nm was TiO_2 absorption and 302 nm-387 nm was ZnO absorption. The alternative method to observe the band gap is Tauc's plot method. On the characteristic curve, the extrapolating the straight line onto horizontal axis ($(\alpha h\upsilon)^2 = 0$) the values of band gap and the obtained films had a direct band gap shown in Table 2.

Table 2. Observed energy bandgaps and referenced energy bandgaps

Samples	**E_g (TiO_2/ZnO) (This study)**	**E_g (for TiO_2 only) (previous study)**	**References**
400 ºC	2.31 eV	3.94 eV	3.3-3.8 eV [18]
450 ºC	2.45 eV	3.92 eV	
500 ºC	3.50 eV	3.77 eV	
550 ºC	3.51 eV	3.74 eV	
600 ºC	3.86 eV	3.62 eV	

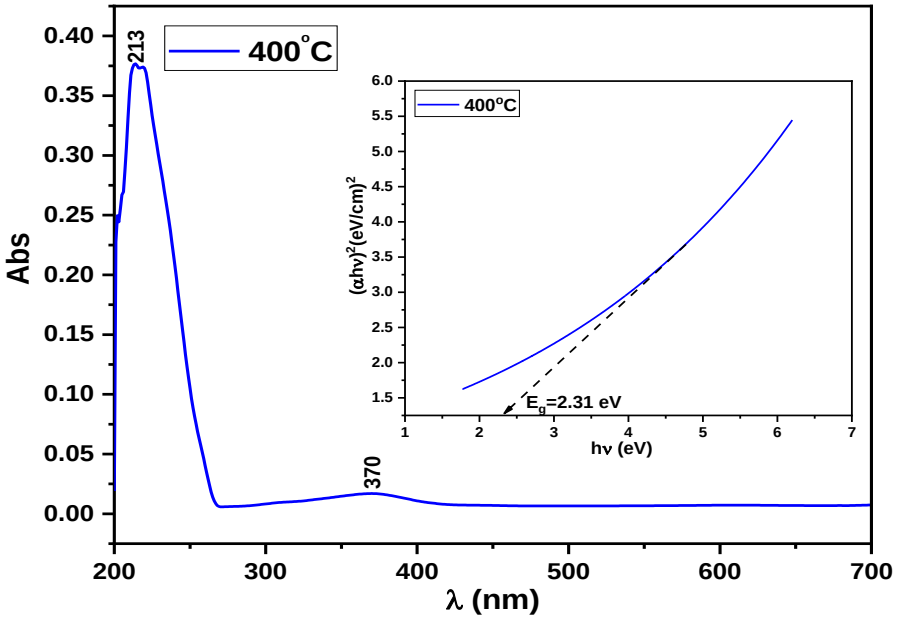

Figure 6(a) UV-Vis absorption spectrum and energy band gap of TiO_2/ZnO film (400 °C)

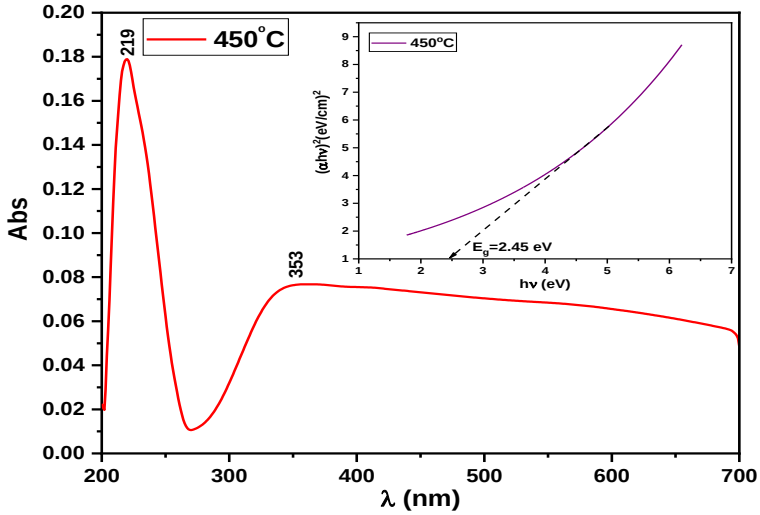

Figure 6(b) UV-Vis absorption spectrum and energy band gap of TiO_2/ZnO film (450 °C)

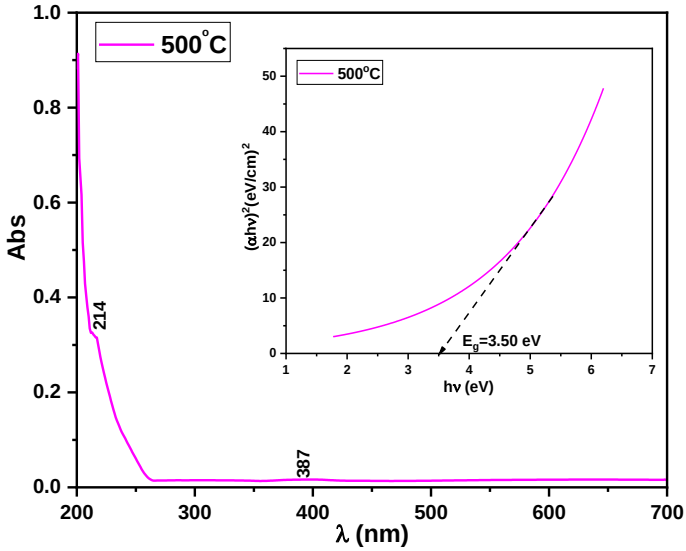

Figure 6(c) UV-Vis absorption spectrum and energy band gap of TiO_2/ZnO film (500 °C)

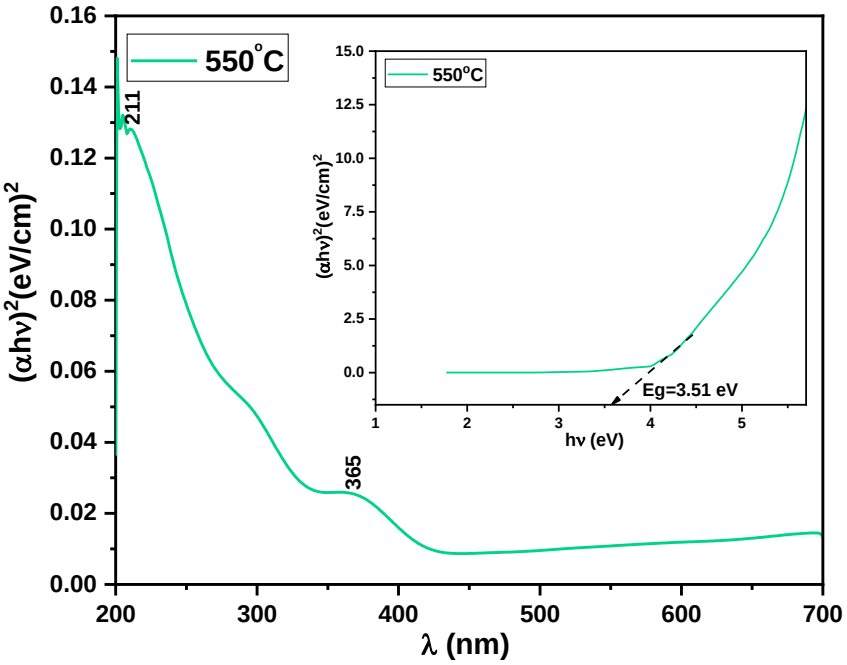

Figure 6(d) UV-Vis absorption spectrum and energy band gap of TiO_2/ZnO film (550 °C)

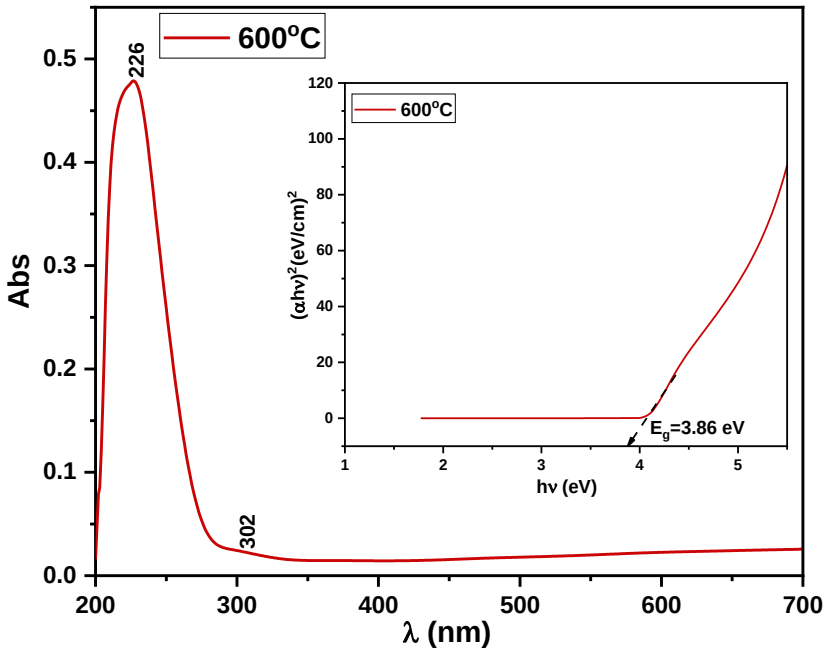

Figure 6(e) UV-Vis absorption spectrum and energy band gap of TiO_2/ZnO film (600 °C)

Conclusion

This study employed a sol-gel method to craft TiO_2/ZnO films at temperatures ranging from 400 °C to 600 °C. XRD and FTIR spectroscopy investigated the structural and chemical properties of FTO/TiO2/ZnO films, indicating temperature-dependent effects on crystallinity. XRD data resulted in a predominant alignment with TiO_2 and ZnO structures, with decreasing crystallite sizes at higher temperatures. FTIR analysis highlighted shifts in functional groups, including peaks indicating Ti-O and Zn-O bonds. UV-Vis spectrometry showcased maximum absorption in the ultraviolet region after coating onto FTO, and the energy band gap values

suggested suitability for use as an electron transport layer in perovskite solar cells. These findings spotlight the importance of optimized electron transport and crystalline quality for systematic perovskite layer growth.

Acknowledgments

We wish to express our deepest gratitude to Dr. Than Tun, Rector, of Pathein University for his encouragement to submit this paper. Further, we sincerely thank to Dr Khaing Lae Win and Dr Moe Moe Aye Pro-Rectors, Pathein University, for their valuable suggestions. We especially thank Dr Aye Ngwe Professor and Head, Department of Physics, Pathein University for his valuable guidance and helpful advice in carrying out this work.

References

Affa Rozana Abdul Rashid, Hani Khaliesah Tazri, "Optical Properties of ZnO, TiO2 and ZnO: TiO_2 Composite Films," *Nano Hybrids and Composites*, Vol- 31,25-33, February 2021.

Drygała, A. "Influence of TiO2 film thickness on photovoltaic properties of dye-sensitized solar cells," *IOP Conf. Ser. Earth Environ. Sci.* 642, 012001, 2021.

Drygała, A.; Dobrzański, L.A.; Szindler, M.; Prokopowicz, M.P.V.; Pawlyta, M.; Lukaszkowicz, K. "Carbon Nanotubes Counter Electrode for Dye-Sensitized Solar Cells Application," *Arch. Met. Mater.*2016.

G. S. Han, H. S. Chung, B. J. Kim, D. H. Kim, J. W. Lee, B.S. Swain, K. Mahmood, J. S. Yoo, N. G. Park, J. H. Lee, et al., "Retarding charge recombination in perovskite solar cells using ultrathin MgO-coated TiO2 nanoparticulate films," *J. Mater. Chem. A*, vol. 3, no. 17, pp. 9160–9164, 2015.

G. San Vicente et al. "Preparation and characterization of sol-gel TiO antireflective coatings for silicon," *Thin Solid Films*, 2001.

Garcia, V.J.; Pelicano, C.M.; Yanagi, H. "Low temperature-processed ZnO nanorods-TiO2 nanoparticles composite as electron transporting layer for perovskite solar cells," *Thin Solid Films*, 662, 70–75, 2018.

H.; Zuo, C.; Zhang, L.; Zhang, W.; Hao, F.; Yi, C.; Liu, F.; Jin, H.; Ding, L. "Efficient inorganic perovskite solar cells made by drop-coating in ambient air," *Nano Energy*, 2023.

Kojima, K. Teshima, Y. Shirai, and T. Miyasaka, "Organometal halide perovskites as visible-light sensitizers for photovoltaic cells," *J. Am. Chem. Soc.*, vol. 131, no. 17, pp. 6050–6051, 2009.

Liu H., Yang W., Ma Y., Cao Y., Yao J. "Promoted phase transition of titania nanoparticles prepared by a photo-assisted sol-gel method," *New J. Chem.* 26:975–977, 2002.

M. M. Ba-Abbad, A. A. H. Kadhum, A. B. Mohamad, M. S. Takriff and K. Sopian, "Synthesis and catalytic activity of TiO2 nanoparticles for photochemical oxidation of concentrated chlorophenols under direct solar radiation," *Int. J. Electrochem. Sci*,7, 4871-4888, 2012.

M.M. Tavakoli et al. "Fabrication of efficient planar perovskite solar cells using a one-step chemical vapor deposition method," *Sci. Rep*. 2015.

Sanglee, K.; Nukunudompanich, M.; Part, F.; Zafiu, C.; Bello, G.; Ehmoser, E.-K.; Chuangchote, S. "The current state of the art in internal additive materials and quantum dots for improving efficiency and stability against humidity in perovskite solar cells," *Heliyon*, 2022.

S. Casaluci *et al. "*A simple approach for the fabrication of perovskite solar cells in air," *J. Power Sources*, 2015.

Szewieczek, D.; Tyrlik-Held, J.; Lesz, S. "Changes of mechanical properties and fracture morphology of amorphous tapes involved by heat treatment," *J. Mater. Process. Technol*.,109, 190–195, 2001.

Smok, W.; Tański, T.; Drygała, A.; Podwórny, J. "Facile route to prepare hybrid TiO_2-SnO_2 DSSCs," *Appl. Surf. Sci.*, *605*, 154850, 2022.

Wibowo, A.; Marsudi, M.A.; Amal, M.I.; Ananda, M.B.; Stephanie, R.; Ardy, H.; Diguna, L.J. "ZnO nanostructured materials for emerging solar cell applications," *RSC Adv*, 2020.

Yu J.G., Yu J.C. "Low Temperature Solvent Evaporation-induced Crystallization Synthesis of Nanocrystalline TiO_2 Photocatalyst," *Chin. J. Chem*. 21:994–997, 2003.

Yu J.G., Yu J.C., Ho W.K., Jiang Z.T. "Effects of calcination temperature on the photocatalytic activity and photo-induced super-hydrophilicity of mesoporous TiO_2 thin films," *New J. Chem*. 26:607–613, 2002. doi: 10.1039/b200964a.

PREPARATION OF TIN OXIDE THIN FILMS BY CHEMICAL BATH DEPOSITION TECHNIQUE

Yin Myo Khaing[1], Pyae Pyae Win[2], Chit Su Aung[3], Aye Moe Thae[4], Soe Ko Ko Aung[5]

Abstract

To improve the performance of the perovskite solar cells (PSCs), the bottom Electron Transport Layer (ETL) is plays a critical role in extracting and transporting the photo-generated electrons as well as blocking holes to reduce charge recombination. In the present work, SnO_2 thin films were prepared by chemical bath deposition method. The optical properties and surface properties of resulted films were characterized by using UV-vis spectrophotometry and water contact angle measurements. The optical band gap of SnO_2-CBD (180℃) and SnO_2-CBD (500 ℃) are found to be 3.42 eV and 3.88 eV respectively. Excellent transmittance of SnO_2-CBD (180 ℃) film showed over 90 % than that of SnO_2CBD annealed at 500 ℃. Hydrophobic properties of the surface are closely related to the crystalline behavior of the SnO2 films at 180 ℃ confirmed by Water Contact Angle measurement.

Keywords: Chemical bath deposition, thin films, SnO_2, Energy Gaps, Transmittance

Introduction

Perovskite solar cell (PSCs) have rapidly popular in photovoltaic field due to its high efficiency, easy fabrication and low cost. The power conversion efficiency (PCE) of PSCs swiftly raised from ≈ 3.8% in 2009 to 26.7% in 2023 due to their remarkable photovoltaic properties (Liu et al., 2023). Basic structure of perovskite solar cell consists of transparent conductive oxide (TCO), electron transport layer (ETL), perovskite absorber layer, hole transport layer (HTL) and the electrode.

Currently, numerous n type metal oxide such as TiO_2, SnO_2 and TiO_2 have been explored as ETLs fabricated in PSCs. Low-temperature processed semiconductor metal oxides, such as zinc oxide (ZnO), cadmium selenide (CdSe) and ternary metal oxides have been explored as a prospective contender to replace TiO_2 since it must be post-treated at high temperature (Sugapriya et al., 2013). Among them, the interests of SnO_2 thin film in fabrication of ETL are composed of the primary factors such as appropriate energy matching, high optical transparency, good electron mobility and high electrical conductivity, which can enhance the efficiency, stability due to reduce the recombination loss (Xiong et al., 2018).

In order to obtain SnO_2 thin films, has been many different methods such as hydrothermal method, spray-coating, spin-coating, blading coating, slot-die coating, physical vapor deposition, chemical bath deposition and atomic layer deposition have been commonly operated (Hoang Huy & Bark, 2023). Different preparation methods for ETL exhibit different morphologies which influencing the performance of solar cells. The optical properties of thin films depend on film thickness, deposition method, surface properties and substrate temperature (Park & Zhu, 2022).

Thanks to chemical bath deposition method has advantages such as low cost of production, low temperature processing, easy to handle and large area deposition.

In the present work, SnO_2 thin films has been prepared by chemical bath deposition method. Optical properties of SnO_2 film showed the highest transmittance at 180 ℃ than that of

[1] Department of Physics, Mandalar University
[2] Department of Physics, University of Mandalay
[3] Department of Physics, University of Mandalay
[4] Department of Physics, University of Mandalay
[5] Department of Physics, University of Mandalay

500 ℃ fabricated in ambient air. Energy gap was increased with increasing temperature from 3.42 to 3.88 eV. Morphology of SnO_2 annealed at 180 ℃ showed relatively close to hydrophobic nature measured by water contact angle measurement. It may be attributed to improve morphology due to compact and thin SnO_2 layer was formed. Hence, low temperature processed SnO_2 films prepared by Chemical Bath Deposition Method are potential candidate for efficient electron transport layer for perovskite solar cells.

Materials and Method

Materials

Urea (CH_4N2O, ACS reagent, 99.0%), Tin (II) chloride dihydrate ($SnCl_2.2H_2O$, ACS reagent, 98%) and Deionized water were purchased by Sigma Aldrich. Concentrated hydrochloric acid (37 %HCl) and Sodium Hydroxide were bought by Aladdin Scientific. FTO conductive glasses (TEC7 Glass Plates 2.2 100mm x 100mm) were purchased by Great Cell Solar, Austria.

Preparation of SnO_2 Thin Films at 180℃ by Chemical Bath Deposition Method

In this procedure, SnO_2 thin films were fabricated for low temperature using chemical bath deposition method (Bu et al., 2018). In this method, 625 mg of urea (CH_4N_2O) was firstly dissolved into 50 ml of deionized water, followed by the addition of 625 µl hydrochloric acid. Finally, 137 mg of tin (II) chloride dihydrate power ($SnCl_2.2H_2O$) was dissolved in the solution at a concentration of 0.012 M and then stored in fridge for 3 days before use. The ascleaned FTO glass was soaked into the diluted $SnCl_2.2H_2O$ solution (0.012M) by chemical bath deposition and then annealing 70℃ at 2h. SnO_2 thin films washed by deionized water and dried. The films were annealing at 180℃ on the hot plate for 1h. The preparation steps of SnO2 via CBD method at 180 °C were showed in Figure 1.

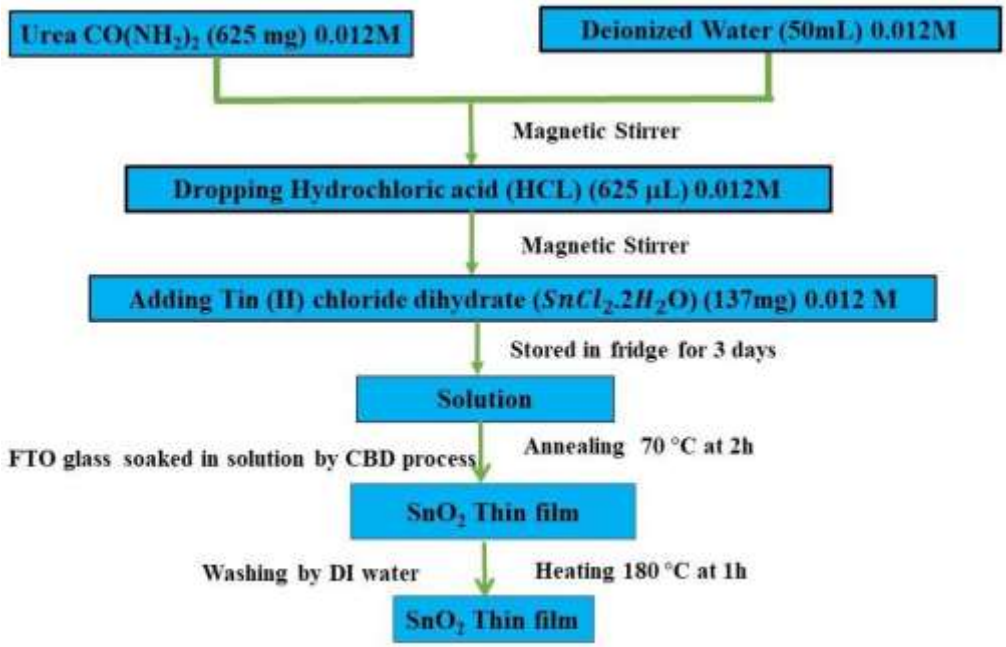

Figure 1. Preparation steps of SnO2-CBD thin film at 180 °C

Preparation of SnO_2 Thin Films at 500 ℃ by Chemical Bath Deposition Method

In this procedure, SnO_2 thin films were prepared for high temperature by using chemical bath deposition method (Rahman et al., 2021). In this method, 113 mg of tin (II) chloride dihydrate ($SnCl_2.2H_2O$) was dissolved into 200ml of deionized water and 60 mg of urea (CH_4N_2O) was dissolved into 15ml of deionized water. These two solutions were mixed together and stirring 30 minutes and 1M of sodium hydroxide (NaOH) was added drop wise to the solution until the PH value reached at 12, stirring the solution. The cleaned FTO glass immersed in solution at room temperature for 24 h by chemical bath deposition and then annealed at 50℃ at 1h. SnO2 thin films were washed with deionized water and dried as a twice. The films were annealed at 500℃ for 2h. The preparation steps of SnO_2 via CBD method at 500 °C were showed in Figure 2.

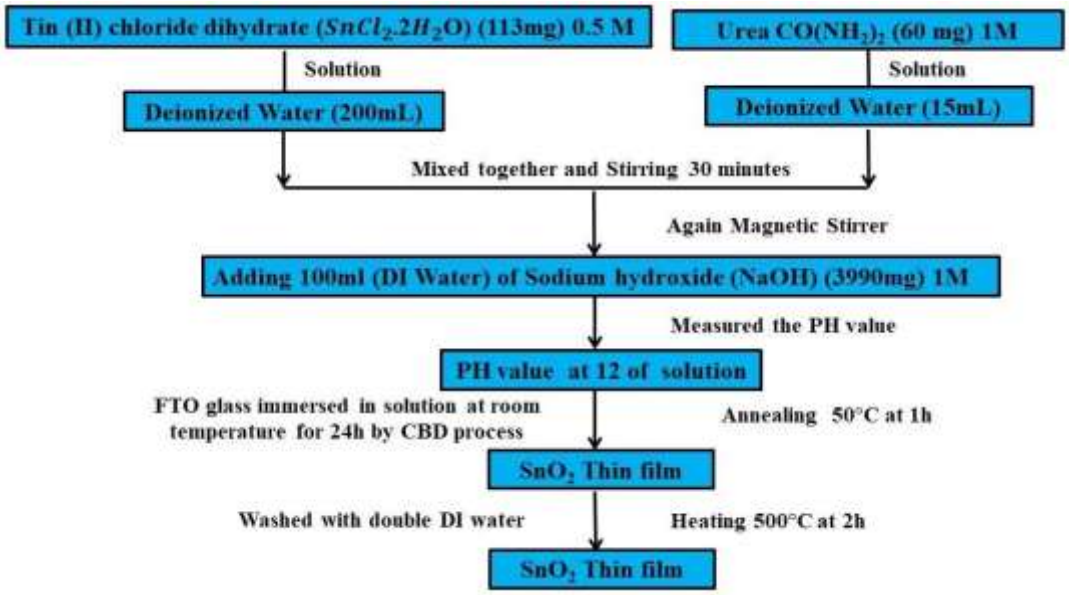

Figure 2. Preparation steps of SnO_2-CBD thin film at 500 °C

Characterization

The SnO_2-CBD thin films were characterized using a UV-vis spectrophotometry (Genesys 10S UV-vis) at wavelength range from 200 to 900 nm, with spectral resolution of 0.1 nm. In addition, the SnO_2-CBD thin films were investigated using a Contact Angle Goniometer (L2004A1, Ossila).

Results and Discussion

Optical Properties and Band Gap Energy of SnO2 Thin Films

The optical absorption and transmission spectra of SnO_2 thin films were measured between 200 nm to 800 nm by UV- vis spectrophotometry. The UV-Vis spectra for SnO_2 thin films using different temperature were shown in figure (1), (2), (3) and (4). SnO_2-CBD (180 °C) film exhibits highest transmittance than rigid glass substrate which has high roughness surface also leads to light scattering increasing the path of the incident light and leading to a higher probability of photon absorption. SnO_2-CBD annealed at 500°C film exhibits lower transmittance and higher band gap than low temperature (180°C) annealed film. It may be attributed the presence of cracks in high-temperature growth. In order to find out, the optical band gap energy of rigid glass substrate (FTO) and SnO_2 thin films were investigated from Tauc's plot equation, $(\alpha h\nu)^n = A\ (h\nu - E_g)$, where α is absorption coefficient, $h\nu$ is the energy of absorbed photons, A is the proportionality constant and Eg is the band gap of the material. The exponent 'n' inspects the

transition type of the material. The value of n is 2 for direct transition of SnO_2 thin films. Figure 2 and figure 4 shows the plot of the $(\alpha h\nu)^2$ versus energy (eV) graph. The value of the band gap energy for FTO, SnO_2 film at 180℃ and SnO2 film at 500℃ were found 3.89 eV, 3.42 eV and 3.88 eV.

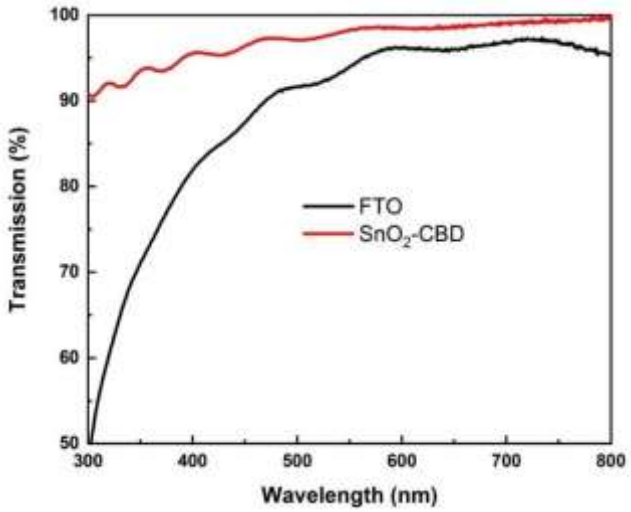

Figure 3. UV-Vis transmission spectra of FTO substrate and SnO_2 films at 180 ℃

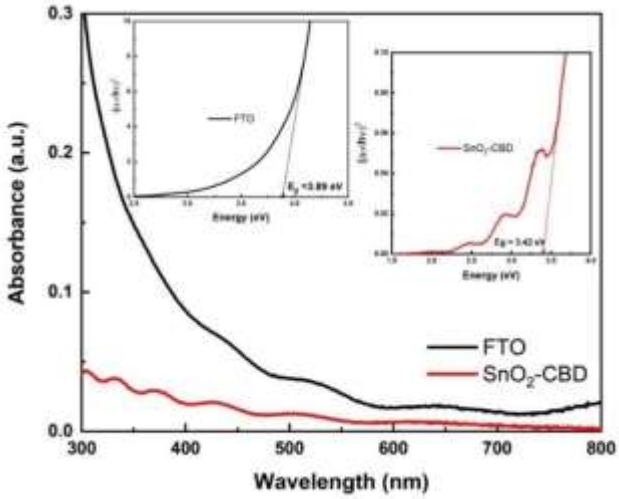

Figure 4. UV-Vis absorption spectra under temperature at 180 ℃ of SnO_2 thin films. Zoom images showed energy gaps of FTO and SnO_2 films.

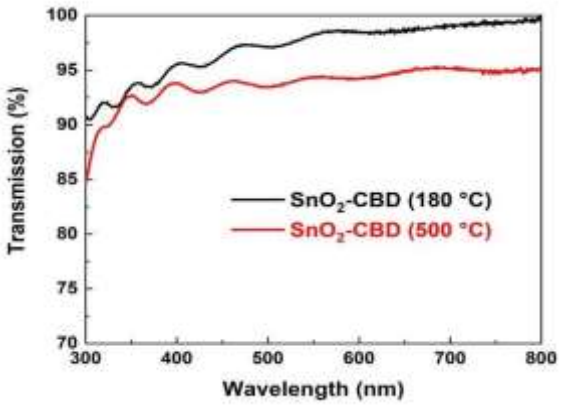

Figure 5. Transmission spectra of SnO_2 thin films at 180 ℃ and 500 °C

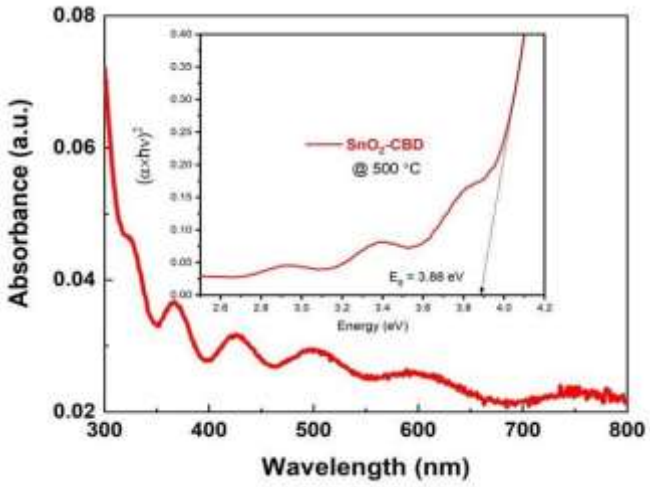

Figure 6. UV-Vis absorption spectrum of SnO_2 thin films at 500 °C. Zoom image showed a energy gap of SnO_2 at 500 °C

Water Contact Angle Measurement of SnO_2 Thin Films

The water contact angle (WCA) is the angle formed between a water droplet and a solid surface. The water contact angle of less than 90° and greater than 90°, the surface was determined hydrophilic and hydrophobic. The SnO_2-CBD at 180 °C film shows an average contact angle of 69.89° shown in Figure 6, which is higher than pure FTO film which has an average contact angle of 44.74° as shown in Figure 5. WCA confirm that smooth surface (SnO_2) may contribute to reducing the formation of large clusters and decreasing defects whereas, pristine fluoride doped tin oxide (FTO) substrate is responsible for reducing surface wettability.

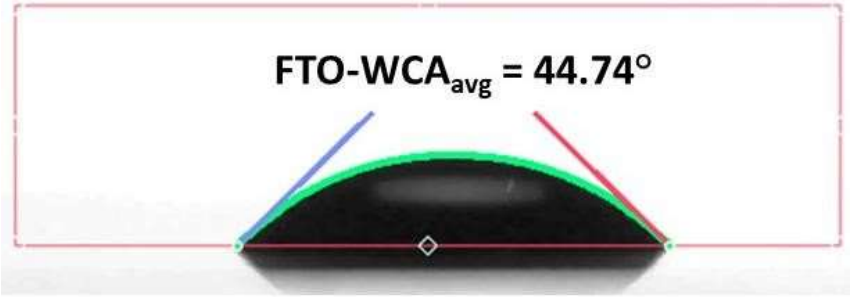

Figure 7. WCA measurement of FTO glass

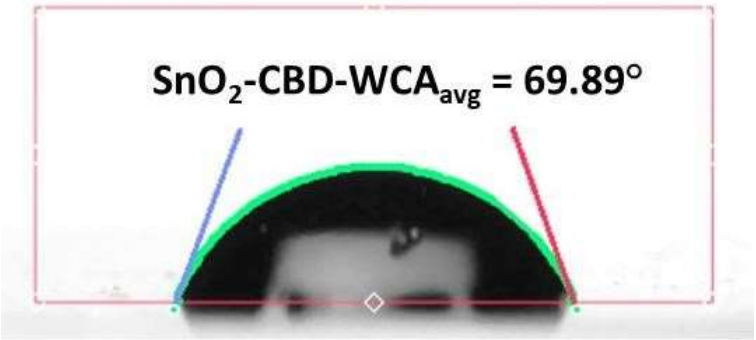

Figure 8. WCA measurement of SnO_2-CBD film at (180°C)

Summary and Conclusion

Excellent transmittance of over 90% of SnO_2 thin films in FTO glasses at 180 ℃ and 500 ℃ were prepared by Chemical Bath Deposition Technique. It was found that higher transmittance and lower energy gap were achieved in low temperature processed SnO_2-CBD film. Hydrophobic property of the surface was closely related to the crystalline behavior of the SnO_2 films at 180 ℃ confirmed by water contact angle measurement. Furthermore, post treatment spin coated technique via CBD will be applied for efficient SnO_2 films.

Acknowledgement

This work was fully funded by International Science Programme (ISP), Uppasala University, Sweden, e-ASIA project and Prof. Fuming Chen (South China Normal University). We Thank Prof. Nyein Wint Lwin, Prof. San Yu Swe and Prof. Khin Than Tint for support research facilities and useful discussion.

References

Bu, T., Li, J., Zheng, F., Chen, W., Wen, X., Ku, Z., Peng, Y., Zhong, J., Cheng, Y. B., & Huang, F. (2018). Universal passivation strategy to slot-die printed SnO 2 for hysteresis-free efficient flexible perovskite solar module. *Nature Communications*, *9*(1), 1–10.

Hoang Huy, V. P., & Bark, C.-W. (2023). Review on Surface Modification of SnO2 Electron Transport Layer for High-Efficiency Perovskite Solar Cells. *Applied Sciences*, *13*(19), 10715.

Liu, S., Biju, V. P., Qi, Y., Chen, W., & Liu, Z. (2023). Recent progress in the development of high-efficiency inverted perovskite solar cells. *NPG Asia Materials*, *15*(1), 27.

Park, S. Y., & Zhu, K. (2022). Advances in SnO2 for Efficient and Stable n–i–p Perovskite Solar Cells. *Advanced Materials*, *34*(27), 1–20.

Rahman, M. T., Ahmed, Z., Islam, M. J., Kamaruzzaman, Khatun, M. T., Gafur, M. A., Bashar, M. S., & Alam, M. M. (2021). Comparative Study of Structural, Optical and Electrical Properties of SnO2 Thin Film Growth via CBD, Drop-Cast and Dip-Coating Methods. *Materials Sciences and Applications*, *12*(12), 578–594.

Sugapriya, S., Sriram, R., & Lakshmi, S. (2013). Effect of annealing on TiO2 nanoparticles. *Optik*, *124*(21), 4971–4975.

Xiong, L., Guo, Y., Wen, J., Liu, H., Yang, G., Qin, P., & Fang, G. (2018). Review on the Application of SnO2 in Perovskite Solar Cells. *Advanced Functional Materials*, *28*(35), 1–19.

DETERMINATION OF BRANCHING RATIO FOR THE RADIOISOTOPES OF ALPHA EMITTERS IN THORIUM DECAY SERIES EVENTS

Chaw Su Myint[1], Aye Moh Moh Myo[2], Khin Than Tint[3]

Abstract

The purpose of this research is to identify the decay branching ratios of five radioisotopes in thorium decay chain from their measured ranges and kinetic energies. Totally 50 thorium decay series events which were detected in nuclear emulsion of plate #5, Module #26 in J-PARC E07 experiment were analyzed. The type of radioisotopes of alpha emitters were identified with measured range and the range in emulsion obtained from empirical formula and Barkas' literature. Moreover, branching ratio for the radioisotopes of alpha emitters in thorium decay series events were obtained from their measured ranges and corresponding kinetic energies. The results are consistent with the results in Barka's literature.

Keywords: alpha particles tracks, thorium series, nuclear emulsion, range, kinetic energy

Introduction

Nuclear emulsion is the key detector for the detection of three-dimensional trajectory of charged particles. Nuclear emulsions gel are composed by seven elements (hydrogen, carbon, nitrogen, oxygen, bromine, silver, iodine) with different densities. Nuclear emulsion plates are fabricated by drying after pouring gel on both sides of base polystyrene film. When a charged particle passing through nuclear emulsion, silver ions (Ag+) contained in AgBr crystal became silver atom (Ag) by the reduction reaction of silver. And then form a small cluster of metallic silver atoms called a latent image which is an invisible image. After development process, the latent image changes into visible image. Fuji GIF emulsion gel was used for E07 emulsion plate detectors production [Hayakawa. S, (2019)], .

Among the three naturally occurring decay series, thorium and uranium decay series can be detected in nuclear emulsion of emulsion-counter hybrid experiment (J-PARC E07 experiment). Since, the time for pouring and development of nuclear emulsion plates took about two years for that experiment, the five alpha particles tracks were observed as the decay chain of thorium series in both sides of emulsion plates. This event can occur if the successive nuclides found are of short life. Five alpha tracks are emitted from ^{228}Th, ^{224}Ra, ^{220}Rn, ^{216}Po and ^{212}Po (or ^{212}Bi) nuclides [Barkas. W. H, (1963)]. The thorium decay series events, totally 50 events, in nuclear emulsion plate of #5 and Mod#26 of E 07 experiment are described in Figure 1.

Materials and Methods

Firstly, Q value and kinetic energy of alpha particles emitted from all decay modes in Thorium Series were calculated by using the following equations (1) and (2).

$$Q = \Delta m \times 931 \text{ MeV} \quad (1)$$

In above equation, $m_{p,}$ m_d and m_α are the masses of parent nuclide, daughter nuclide and alpha particle, respectively. From the conservation of energy and momentum, the kinetic energy

[1] Department of Physics, Mandalay Technological University

[2] Department of Physics, Mandalay University of Distance Education

[3] Department of Physics, University of Mandalay

of emitted alpha particles related to Q value and the mass number A of the original nucleus is calculated by using the following equation.

$$KE_\alpha = \frac{A-4}{A}\ Q \tag{2}$$

Secondly, the range of alpha particles moving in nuclear emulsion for the kinetic energies were deduced from the following equations (equations 3 to 6). For alpha particles, the range in air at normal temperature and pressure is

$$R(mm, air) = exp\left[1.61\sqrt{T(MeV)}\right]\ for\ 1 < T\ \leq 4\ MeV \tag{3}$$

$$R(mm, air)[0.05\ T\ (MeV) + 2.85]\ T^{\frac{3}{2}}(MeV), for\ \ 4 < T \leq 15 \tag{4}$$

Where T = kinetic energy of the particle in MeV.

If the range is known for one material, it can be determined for any other by applying the *Bragg-Kleeman* rule.

$$\frac{R_1}{R_2} = \frac{\rho_2}{\rho_1}\sqrt{\frac{A_1}{A_2}} \tag{5}$$

Where ρ_i and A_i are density and atomic weight of material i. Since, nuclear emulsion gel is composed of eight kinds of element, an effective molecular weight was obtained from the equation

$$\sqrt{A_{ef}} = \left(\sum_{i=1}^{l}\frac{w_i}{\sqrt{A_i}}\right)^{-1} \tag{6}$$

On the other hand, range of alpha particles for corresponding kinetic energies are also obtained from traditionally range-energy formula in emulsion of a particle with charge of Z and mass of *M* in units of the proton mass is expressed as

$$\text{Range } R_{obs} - R_c = \rho\left[\frac{M}{Z^2}\cdot\lambda(\beta) + R_{ext}\right] \tag{7}$$

The range-energy relation in emulsion was written in Fortran code by Prof. Nakazawa, Gifu University, Japan.

The ranges of α-tracks in decay chain were measured with Graphical User Interface tool (GUI) and identified the radioactive isotope by comparing the range of α-tracks obtained by empirical formula and range energy relation based on W.H. Barkas' literature [Chaw Su Myint and Khin Than Tint, (2024)]. Finally, branching ratios were determined.

Results and Discussion

In nuclear emulsion, a member of an alpha-active series as several tracks may be found emerging from a common point. This event can occur if the successive nuclides found are short life. Five alpha tracks are emitted from ^{228}Th, ^{224}Ra, ^{220}Rn, ^{216}Po and ^{212}Po nuclides.

Ranges of α-tracks in thorium decay chain according to their kinetic energies were calculated by using equations 3 to 6 and range energy relation in emulsion based on Barkas' literature (equation 7) are expressed in Table 1.

Table 1. Calculated range of alpha particles in Thorium Decay Series

Decay Mode	Kinetic Energy of Alpha Particle (MeV)	Range of Alpha Particles (μm)	
		Obtained from Empirical Formula	Obtained from Range - Energy Relation (Barkas' literature)
$^{228}_{90}Th \rightarrow {}^{224}_{88}Ra + \alpha$	5.340	23.65	23.48
	5.423	24.68	24.0
$^{224}_{88}Ra \rightarrow {}^{220}_{86}Rn + \alpha$	5.448	24.86	24.17
	5.685	26.60	25.70
$^{220}_{86}Rn \rightarrow {}^{216}_{84}Po + \alpha$	5.747	27.67	26.11
	6.288	31.20	29.79
$^{216}_{84}Po \rightarrow {}^{212}_{82}Pb + \alpha$	5.985	28.88	27.71
	6.778	35.24	33.30
$^{212}_{84}Po \rightarrow {}^{208}_{82}Pb + \alpha$	8.784	50.63	49.37

The image processing (GUI tool) with personal computer and slice pictures taken by microscope was used to measure the range of alpha particles in thorium decay series events. Identifying radioisotopes of alpha emitters in thorium decay series event (one of the fifty events) by comparing measured range and calculated range in emulsion is presented in the following Table 2. Similarly, the other 49 events of thorium decay series events were analyzed as the same manner. The measured ranges of alpha tracks of events were consistent with the range of alpha track obtained from range-energy relation by Barkas.

Table 2. Identifying radioisotopes of alpha emitters in thorium decay series event by comparing measured range and calculated range in emulsion

Event #	Track #	Range of measured alpha tracks (μm) our result	Calculated Range(μm) [Equations 3 to 6]	Range of alpha tracks (μm) [Range-Energy Relation, Barkas]	Identified Radioactive Isotope for sample event
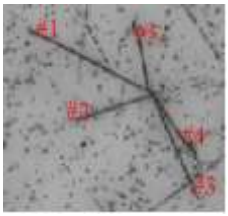 20190328T141648	1	49.91± 0.24	50.63	49.37	^{212}Po
	2	29.64 ± 0.28	29.67	29.79	^{216}Po
	3	32.64 ± 0.23	33.24	33.30	^{220}Rn
	4	24.30± 0.10	24.68	24.00	^{224}Ra
	5	25.73 ± 0.20	26.60	25.70	^{228}Th

The range of alpha particle tracks emitted form five radioactive isotope were grouped according to their kinetic energies. The results for the obtaining alpha decay branching ratios for five alpha particle tracks in thorium decay series from their ranges are described in Table 3. The summarized branching ratios for radioisotopes of alpha emitters in thorium decay events and results from Barkas' literature are presented in Table 4.

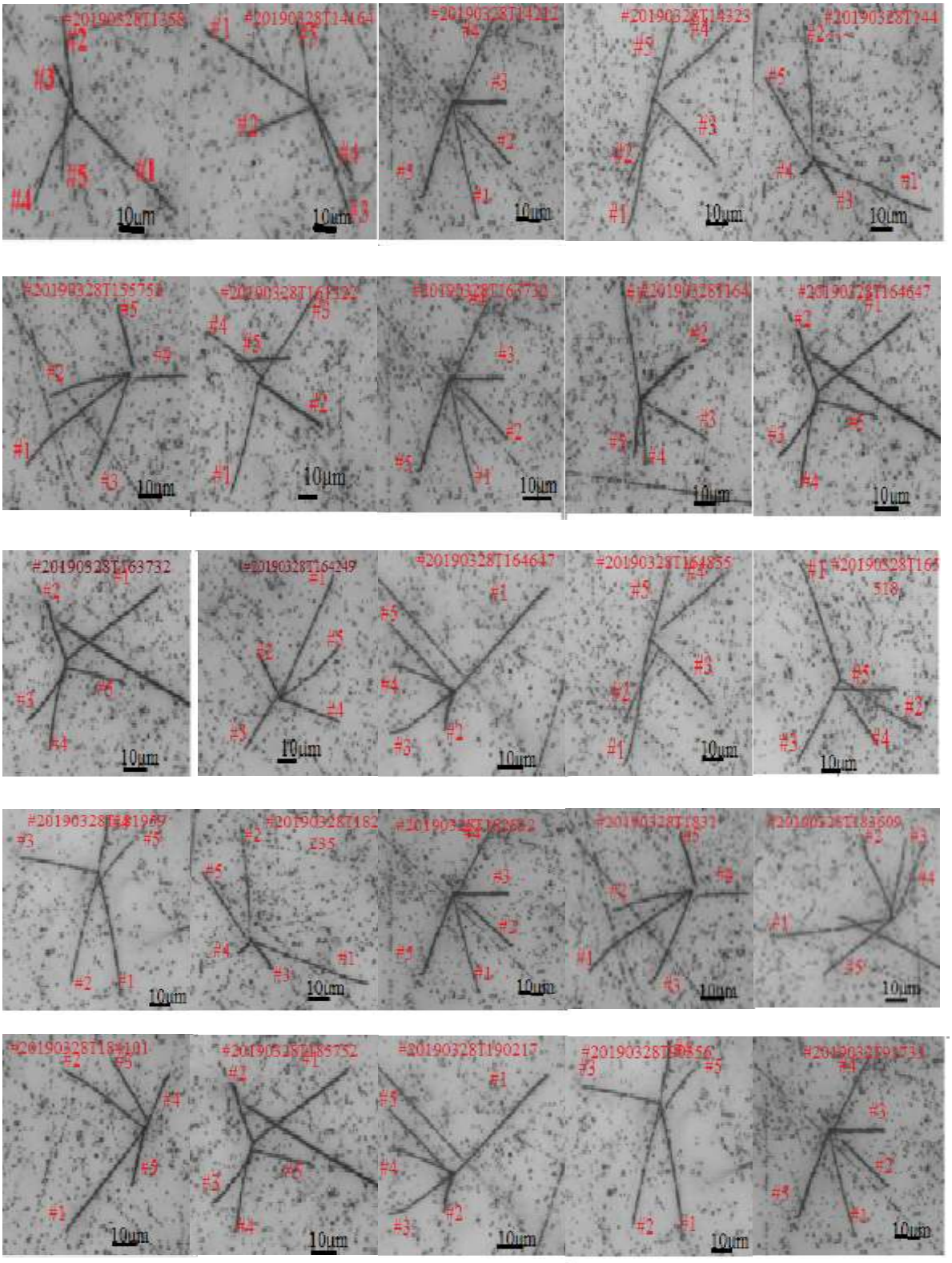

Figure 1. Thorium decay series events in nuclear emulsion plate of E07 experiment

Table 3 Alpha decay branching ratio

Sr No.	Event #	Radioisotopes of alpha emitters and measured range alpha tracks in micro meter								
		^{228}Th		^{224}Ra		^{220}Rn		^{216}Po		^{212}Po
1.	#20190328T135838	23.72± 0.11	-	-	25.92 ± 0.22	27.01 ± 0.90	-	-	32.69± 0.13	48.66± 0.87
2.	#20190328T141648	-	24.30 ± 0.11	-	25.74 ± 0.36	-	29.13± 0.27	-	31.81± 0.59	48.71± 0.89
3.	#20190328T142122	23.71± 0.10	-	24.52 ± 0.10	-	-	29.64± 0.28	-	31.85± 0.57	49.59± 0.82
4.	#20190328T143203	23.75± 0.13	-	24.5 ± 0.12	-	-	28.21± 0.86	-	31.94± 0.85	48.44± 0.33
5.	#20190328T144802	23.78± 0.36	-	-	25.76 ± 0.36	-	29.19± 0.67	-	33.22± 0.67	49.16± 0.68
6.	#20190328T155752	23.86± 0.23	-	24.50 ± 0.11	-	-	28.21± 0.84	-	31.92± 0.83	48.47± 0.35
7.	#20190328T161322	-	24.33 ± 0.36	-	25.75 ± 0.35	-	29.1± 0.39	-	33.22± 0.67	49.16± 0.68
8.	#20190328T163732	-	24.21 ± 0.20	-	25.74 ± 0.33	-	28.12± 0.85	-	32.78 ± 0.22	48.82± 0.44
9.	#20190328T164249	-	23.68 ± 0.69		25.61 ± 0.56	-	28.17± 0.29		32.11± 0.73	48.66± 0.47
10.	#20190328T164647		24.36 ± 0.12		25.67 ± 0.26		28.19± 0.54		32.01± 0.35	49.33± 0.76
11.	#20190328T164855		24.35 ± 0.11		25.61 ± 0.25		28.21± 0.44		32.09 ± 0.34	49.23± 0.77
12.	#20190328T165518		24.36 ± 0.12		25.12 ± 0.68		28.1± 0.90		32.6± 0.96	49.56 ± 0.35
13.	#20190328T180507		24.20 ± 0.13		25.58 ± 0.38		29.45± 0.14		32.17± 0.75	49.11± 0.54
14.	#20190328T180722		24.21 ± 0.13		25.57 ± 0.34		28.25± 0.90		32.20± 0.72	48.58± 0.82
15.	#20190328T181310		24.25 ± 0.12		25.83 ± 0.67		28.81± 0.12		33.01± 0.96	49.1 ± 0.92
16.	#20190328T181959		24.35 ± 0.11		25.81 ± 0.66		29.83± 0.36		32.25 ± 0.61	49.48± 0.64
17.	#20190328T182235	23.67± 0.12			25.71 ± 0.21		29.71 ± 0.26		32.69± 0.78	49.91± 0.24
18.	#20190328T182812		24.20 ± 0.12		25.73 ± 0.20		29.67± 0.31		32.98± 0.63	48.81± 0.68
19.	#20190328T183113	23.70 ± 0.21	-	-	25.74 ± 0.22	-	29.75± 0.29	-	32.78± 0.78	49.86± 0.22
20.	#20190328T183609	23.71 ± 0.11	-		25.13 ± 0.64	-	28.22± 0.83	-	32.68± 0.65	48.77± 0.52
21.	#20190328T184101	-	24.27 ± 0.11	-	25.14 ± 0.56	-	28.83 ± 0.36	-	32.77 ± 0.70	49.82± 0.64

Sr No.	Event #	**Radioisotopes of alpha emitters and measured range alpha tracks in micro meter**								
		^{228}Th		**^{224}Ra**		**^{220}Rn**		**^{216}Po**		**^{212}Po**
22.	#20190328T185752	23.63 ± 0.22	-	-	25.71 ± 0.25	-	29.64± 0.28	-	32.66± 0.68	49.91± 0.27
23.	#20190328T190217	-	24.34 ± 0.13		25.73 ± 0.20	-	29.71± 0.31	-	32.54± 0.48	49.58± 0.18
24.	#20190328T90356	-	24.21 ± 0.22	-	25.74 ± 0.22	-	29.74± 0.38	-	32.51± 0.57	49.85± 0.12
25.	#2019032T191733	23.64 ±0.23	-	-	25.15 ± 0.59	-	28.22± 0.53	-	32.27± 0.21	49.73± 0.24
26.	#20190328T175558		24.30 ± 0.14	-	25.83 ± 0.67	-	28.75± 0.24	-	32.16 ± 0.21	49.48± 0.64
27.	#20190328T180007	23.73 ± 0.11	-	-	25.70 ± 0.23	-	29.53± 0.38	-	32.4± 0.71	49.73± 0.22
28.	#20190328T180152	23.71 ± 0.21	-	-	25.73 ± 0.20	-	29.64± 0.27	-	32.2± 0.24	49.59± 0.37
29.	#20190328T180832	-	24.32 ± 0.17	-	25.74 ± 0.22	-	29.51± 0.38	-	32.27 ± 0.17	49.84± 0.41
30.	#20190328T181058	23.68 ± 0.24	-	-	25.12 ± 0.76	-	28.23± 0.81	-	32.66± 0.68	49.57± 0.24
31.	#20190328T182328		24.18 ± 0.16	-	25.83 ± 0.67	-	28.54± 0.31	-	32.16± 0.21	49.48± 0.64
32.	#20190328T15047	23.85 ± 0.23	-	-	25.68 ± 0.27	-	29.64± 0.29	-	32.41± 0.84	49.57± 0.31
33.	#20190328T182948	-	24.30 ± 0.10	-	25.73 ± 0.14	-	29.53± 0.21	-	32.54± 0.14	49.62± 0.30
34.	#20190328T183324	-	24.21 ± 0.11	-	25.74 ± 0.22	-	29.64± 0.29	-	32.63± 0.68	49.24± 0.51
35.	#20190328T183616	-	24.27 ± 0.12	-	25.81 ± 0.27	-	28.22± 0.83	-	32.71± 0.47	49.84± 0.24
36.	#20190328185502	-	24.27 ± 0.13	-	25.83 ± 0.67	-	28.71± 0.29	-	32.16± 0.23	49.48 ± 0.64
37.	#20190328T190323	23.77± 0.17	-	-	25.71 ± 0.21	-	29.64± 0.30	-	32.60± 0.78	49.69± 0.24
38.	#20190328T190804	-	24.30 ± 0.10	-	25.73 ± 0.20	-	29.71± 0.89	-	32.71±0 . 66	49.71± 0.69
39.	#20190328T191430	-	24.18 ± 0.15	-	25.74 ± 0.22	-	29.64± 0.28	-	32.56± 0.68	49.74± 0.96
40.	#20190328T191740	-	24.21 ± 0.21		25.82 ± 0.28	-	28.22± 0.83	-	32.41 ± 0.42	49.87± 0.24
41.	#20190328T192622	-	24.25 ± 0.22	-	25.83 ± 0.67	-	27.60± 0.25	-	32.16± 0.21	49.48± 0.15
42.	#20190328T193401	-	24.19 ± 0.23	-	25.71 ± 0.21	-	29.64± 0.38	-	32.66± 0.68	49.78± 0.27
43.	#20190328T193858	-	24.27		25.73	-	29.65±	-	32.57±	49.85±

Sr No.	Event #	Radioisotopes of alpha emitters and measured range alpha tracks in micro meter								
		^{228}Th		**^{224}Ra**		**^{220}Rn**		**^{216}Po**		**^{212}Po**
			± 0.10		± 0.20		0.29		0.63	0.24
44.	#20190328T194332	-	24.28 ± 0.11	-	25.74 ± 0.22	-	29.61± 0.28	-	32.66± 0.68	49.65± 0.53
45.	#20190328T194842	-	24.20 ± 0.21	-	25.52 ± 0.68	-	28.22± 0.83	-	32.27± 0.75	49.93± 0.62
46.	#20190328T195025	-	24.17 ± 0.22	23.72 ± 0.11		-	29.83± 0.36	-	32.16± 0.21	49.48± 0.64
47.	#20190328T195657	-	24.20 ± 0.17	-	25.65 ± 0.27	-	29.64± 0.27	-	32.27 ± 0.81	49.69± 0.53
48.	#20190328T200222		24.19 ± 0.22	-	25.73 ± 0.20	-	28.61 ± 0.68	-	32.63± 0.68	49.78± 0.24
49.	#20190328T1204352	-	24.25 ± 0.12	-	25.74 ± 0.22	-	29.28± 0.31	-	32.42± 0.48	49.76± 0.55
50.	#20190328T1205123	-	24.23 ± 0.21	-	25.81 ± 0.27	-	28.22± 0.83	-	32.91± 0.47	49.64± 0.24
	Total events for each range and kinetic energy	15	35	5	45	**1**	**49**	-	**50**	**50**

Table 4 The branching ratios of five radioisotopes in thorium decay series

Radioactive isotopes (Parent)	Half-Life	Kinetic Energy of Emitted Alpha Particles (MeV)	Branching Ratio (%) our result	Branching Ratio(%) Barakas' Literature
^{228}Th	1.910yr	5.340	30	28
		5.423	70	71
^{224}Ra	3.64day	5.448	10	5
		5.685	90	95
^{220}Rn	51.5sec	5.747	2	-
		6.288	98	99+
^{216}Po	0.158sec	5.958	-	-
		6.778	100	100
^{212}Po	3.04×10^{-7}sec	8.784	100	99+

Conclusion

The measured range of alpha particle tracks in each thorium decay series events in nuclear emulsion of plate #5, Mod#26 of E07 experiment are comparable with the ranges obtained from range energy relation in emulsion based on Barkas' literature. The calculated ranges of alpha particles by using empirical formula are a little longer than the measured range. From the measured range of alphas; the types of radioactive isotopes are identified. Moreover, the decay branching ratio of each decay mode is also identified. The branching ratios for the radioisotopes of alpha emitters in thorium decay series events in nuclear emulsion of E07 experiment are quite consistent with the results in Barkas' literature.

Acknowledgement

We wish to express our warmest thanks to Prof. Dr Tin Tun, Rector, University of Mandalay and Pro-Rectors, University of Mandalay for their kind permission for this research work. The author would like to acknowledge Prof. Dr Nyeint Wint Lwin, Head of Department and Prof. Dr San Yu Swe, Department of Physics, University of Mandalay for their kind permission and encourage to carry out this research work. I would like to express my special thanks to Prof. Dr Khin Than Tint, University of Mandalay, for her close supervision and permission to perform this research.

References

Barkas. W. H, (1963), *Nuclear Research Emulsions,* Academic Press, New York and London.

Barkas. W. H., *et.a*l, (1958) "Range-Energy Relation in Emulsion", Nuovo Cimento, vol 8, pp,185-200.

Chaw Su Myint and Khin Than Tint (2024) "Identification of Type of Radioisotopes from Thorium Decay Series Events in Nuclear Emulsion" Mandalay Technological University Journal, vol 10 (accepted).

Hayakawa. S, (2019) "Study of Ξ^- nucleus interaction by measurement of twin hypernuclei with hybrid emulsion method", D. Sc Thesis, Department of Physics, Osaka University (unpublished).

Heckman et.al, 1960, "Range and Energy-Loss Process of Heavy Ions in Emulsion", Phys. Rev. vol 117, pp .544-556

Ito.H, *et al*, (2015) "Mass production of the large-sized nuclear plate for J-PARC E07", JPS Conf. Proc. 2nd Int.

Symp on Sci. at J. PARC, vol 8**,** pp 021007-1-6.

Khin ThanTint, (2015), "Study on Thorium and Uranium Decay Series in Nuclear Emulsion", MDC Research Journal, *vol 6*. pp 62-70.

Takahashi H., (2003), "Study of Double-Hypernuclei with Hybrid-Emulsion Method", D. Sc Thesis, Department of Physics, Kyoto University

PHOTOLUMINESCENCE PROPERITES OF Pr^{3+} DOPED SrO-Li_2O-ZnO-B_2O_3 GLASSES FOR SOLID STATE LIGHTING

Phyoe Ei Ei Nyein[1], Mu Thida Aung[2], Win Pa Pa Hlaing[3], San Yu Swe[4]

Abstract

Pr^{3+} doped borate glasses with chemical composition of (60-x) B_2O_3 - 15ZnO -10Li_2O - 15SrO - xPr_2O_3 (x = 0, 0.25, 0.50, 0.75 mol%) had been prepared by the melt quenching technique and characterized by X-Ray Diffractometer (XRD), UV-Vis Spectrometer and Photoluminescence (PL) Spectrofluorometer. The XRD pattern confirmed the amorphous state for all the glass samples. Optical absorption spectra comprise of four transitions as the prominent absorption spectra from the ground state $^3H_4$ to the excited states within UV-Vis region. The excitation spectra of the Pr^{3+} doped glass samples were monitored at 605 nm. In the photoluminescence spectra the four peaks of down-converted emission bands are observed under excitation wavelength of blue light. The emission bands are centered at 485 nm (blue), 545 nm (green), 605 nm (orange) and 645 nm (red) at the visible region. Out of four bands, orange emission (605 nm) was the most intense. The intensity of the peaks in the emission spectra increase with increasing concentration of Pr^{3+} ions up to 0.50 mol% and then decrease. The results indicated that the glass sample with 0.50 mol% Pr^{3+} emits reddish orange color with highest intensity among the prepared glass samples.

Keywords: Pr^{3+} doped borate glasses, Photoluminescence, CIE chromaticity color co-ordinates.

Introduction

Glass signifies any amorphous solid that completely lacking in period atomic structure exhibiting a glass transition when heated towards the liquid state (J. E. Shelby *et al*, 2005). Nowadays, glass is used in numerous applications such as laser devices, optical fibers, optical waveguides, optoelectronic devices and radiation shielding materials. Rare Earth ions (RE^{3+}) doped glasses get much interesting due to their potential application in the development of various optical and optoelectronic devices, such as, solid state laser, optical amplifier, light converters, sensors, electro-chromic display devices, solid state lightning (LED's) etc. (P.P Pawar *et al*, 2016). RE^{3+} doped glasses are excellent luminescent materials due to their intense emission efficiencies corresponding to the 4f-4f and 4f-5d electronic transitions (P.P Pawar *et al*, 2016, M. Ilhan & M. K. Ekmekic, 2015). The optical properties and luminescence properties of rare earth ions in glasses depend on the chemical compositions of the glass matrix which determine the structure and nature of the bonds (A. Aiyeshah *et. al*, 2021, S. Mitru & S. Kaur, 2015). Good glass host is very important for efficient luminescence of RE^{3+} ions.

Among oxide glasses, borates glasses (B_2O_3) show remarkable properties because of the high thermal stability, lower degree of expansion in volume due to change in temperature, high transparency, low melting point and good rare-earth ion solubility owing to its network (N. Chopra *et al*, 2021, N. Chopra *et al*, 2018, Y. Zhang *et al*, 2009). Borate glasses constitute random network of either BO_3 triangles with non-bridging oxygen or BO_4 tetrahedrons with all bridging oxygen. It is used as one of glass host matrix for luminescence of rare earth ions. However, borate glass has high phonon energy, resulting in enhanced non-radioactive process that reduces luminescence

[1]Department of Physics, University for the Development of the National Races of the Union
[2] Department of Physics, Mandalar University.
[3] Department of Physics, University of Mandalay.
[4] Department of Physics, University of Mandalay.

efficiency. By doping alkali oxides or alkaline earth oxides, the luminescence properties of borate glass may vary strongly (H. Lin *et al*, 2015, L. Yuliantini *et al*, 2017). ZnO has an advantage due their network forming as well as modifying capability when enters glass network. Moreover, glasses containing metals minimize phonon energy and lead to an increase in the luminescence from excited rare-earth ion states (O. B. Aljewaw *et a*l, 2020, S. Damodaraiah *et al*, 2017). Among rare earths, most of them show visible emission while fewer such as Nd, Pr, Dy show NIR emission (M. Naftaly *et al*, 1998). Praseodymium can show both visible and NIR emission and it can also exhibit multi-photon emission under a high energy excitation, as an instance of down conversion (M. Erdem & A. Doğan, 2020, X. Zhou *et al*, 2019). The intension of the present research is to highlight the detailed photoluminescence characterization of praseodymium doped lithium strontium zinc borate glasses with the composition (60-x) B_2O_3 - 15ZnO -10Li_2O - 15SrO - xPr_2O_3 (for x = 0, 0.25, 0.50, and 0.75 mol%).

Materials and Method

Preparation of Pr^{3+} Doped Borate Glasses

Pr^{3+} doped borate glasses with different molar concentration were prepared by using melt quenching technique with the chemical compositions (60-x) B_2O_3 - 15ZnO -10Li_2O - 15SrO - xPr_2O_3 for x = 0, 0.25, 0.50, and 0.75 mol%. The details of composition of the samples used for the present work are categorized in the following list:

x = 0 : 60.00 B_2O_3 -15ZnO - 10Li_2O - 10SrO

x = 0.25 : 59.75 B_2O_3 -15ZnO - 10Li_2O - 10SrO - 0.25Pr_2O_3

x = 0.50 : 59.50 B_2O_3 -15ZnO - 10Li_2O - 10SrO - 0.50 Pr_2O_3

x = 0.75 : 59.75 B_2O_3 -15ZnO - 10Li_2O - 10SrO - 0.75Pr_2O_3

Analytical grade H_3BO_3, ZnO, $LiCO_3$, SrO and Pr_2O_3 with high purity up to 99.99% were used as starting batch materials. After batch calculations, these raw materials were weighed by using digital balance with an accuracy of ± 0.001 g, these chemicals were mixed thoroughly in an agate mortar. The total mix for each batch is 30 g. Then each batch was thoroughly grinded in an agate mortar to obtain fine and homogeneous powder. The resulting homogeneous mixture for each batch was put in an alumina crucible and melted at a temperature of 1100˚C for 1.5 hours in a temperature- controlled lifting furnace (Xiamen Tmax: SJF1600-1). The resulting molten sample was poured into a preheated steel mold. To remove sudden breaks due to thermal strains and to avoid the mechanical strains developed during the quenching process, it was annealed at 300˚C for 2 hours. The obtained undoped glass was almost transparent and colorless and all Pr^{3+} doped glasses were greenish yellow without bubble. The prepared glass samples were followed by a cooling down to room temperature. Part of prepared glass samples were ground into powder form for XRD measurement. Figure 1 and Figure 2 show the photograph for the steps in preparation of Pr^{3+} doped (60-x) B_2O_3 - 15ZnO -10Li_2O - 15SrO - xPr_2O_3 glasses and the photograph of the obtained glass samples respectively.

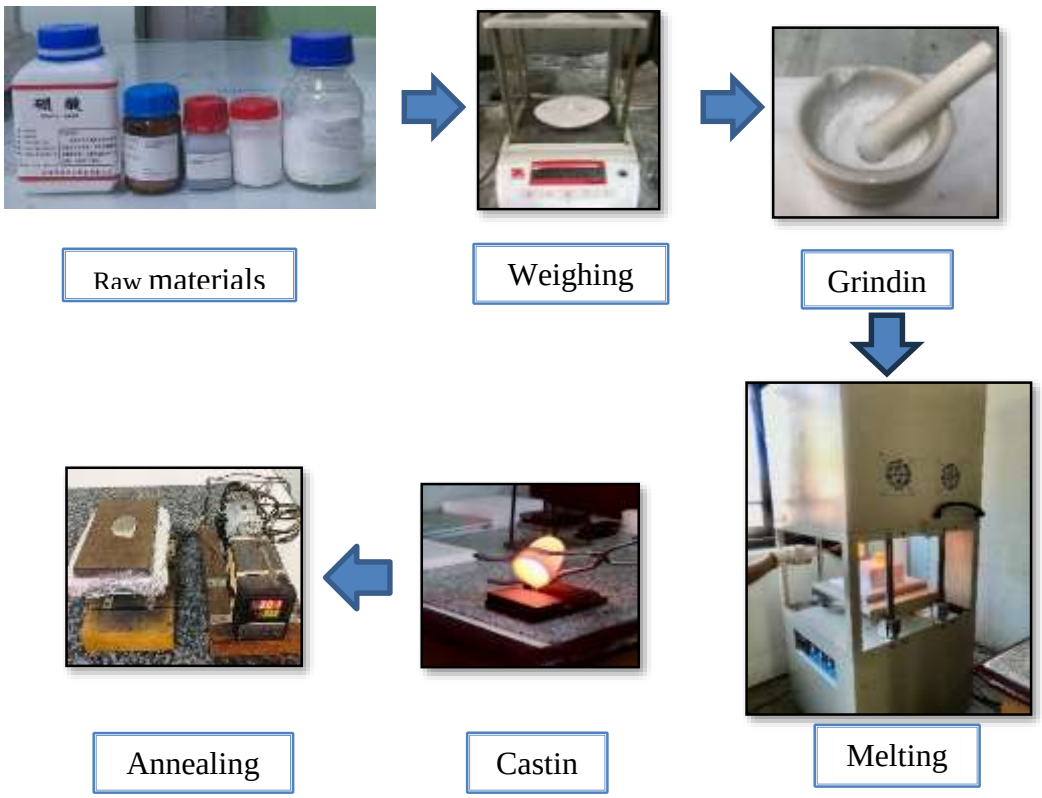

Figure 1. Photograph for the steps in preparation of Pr^{3+} doped (60-x) B_2O_3 - 15ZnO -10Li_2O - 15SrO - xPr_2O_3 glasses

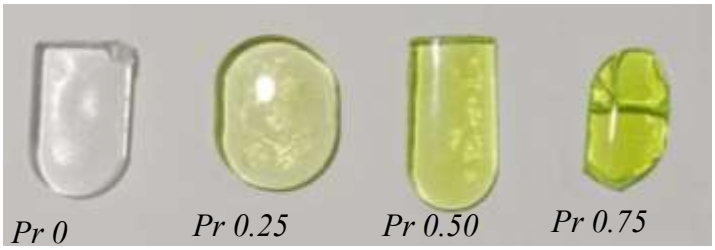

Figure 2. Photograph for the obtained glass samples

Characterization

To study the amorphous nature of the glasses, the X-ray diffraction (XRD) spectrum was recorded with X-ray diffractometer (XRD 6100 Shimadzu @ University of Magway) with copper target, operated at 40 kV and 30 mA. All data were collected at room temperature in the continuous-scan mode with a typical scanning speed of 5 degree per minute and a 2θ range of 20º to 70º. The optical absorption (UV–visible) spectrum was recorded with a Genesys 10S UV-Vis spectrophotometer (from Department of Physics, University of Mandalay) from 300 to 1000 nm, with spectral resolution of 0.1 nm. Finally, the emission and excitation were done with a FS-5 Fluorescence spectrometer (from Department of Physics, University of Mandalay) at room temperature, using a xenon flash lamp as excitation source.

Color of emission is studied via CIE (Commission International de l'Eclairage 1931) chromaticity diagram.

Results and Discussion

XRD Analysis

The XRD spectra of Pr^{3+} doped (60-x) B_2O_3 - 15ZnO -10Li_2O - 15SrO - xPr_2O_3 for x = 0, 0.25, 0.50, and 0.75 mol% are illustrated in Figure 3. It is observed that there is no definite sharp peak for all the samples. The XRD results exhibited the typical nature of the amorphous state for all the glass samples and the broad humps at lower angle indicated that there is the short -range order in glass samples.

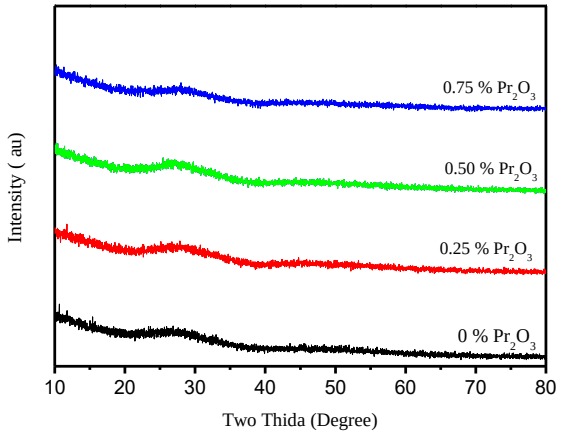

Figure 3. XRD spectra of Pr^{3+} doped (60-x) B_2O_3 - 15ZnO -10Li_2O - 15SrO - xPr_2O_3 glasses.

UV-Vis Analysis

Optical absorption spectra of (60-x) B_2O_3 - 15ZnO -10Li_2O - 15SrO - xPr_2O_3 (x = 0, 0.25, 0.50 and 0.75 mol%) glasses in the range of 300-1000 nm were measured and recorded at normal room temperature as presented in Figure 4. The spectra comprise of four prominent absorption spectra from $^3H_4$ the ground state within UV-Vis region. The absorption band are assigned the transition from the $^3H_4$ ground state to the $^3P_2$, $^3P_1$, $^3P_0$ and $^1D_2$ excited states belonging to the $4f^9$ electronic configuration of Pr^{3+} ions (M. Erdem & A. Doğan, 2020, R. Rajanavaneethakrishna *et al*, 2018, R.N.A. Prasadad *et al*, 2021). These transitions are centered at 445 nm, 470 nm, 484 nm and 660 nm respectively. All these observed transitions are in agreement with the other studied absorption data for Pr_2O_3 doped glasses. The absorption band positions of the present samples occur at almost the same wavelength. It was found that the observed absorption band intensities increase with increasing Pr_2O_3 content in the glass compositions and it signifies the good rare earth solubility of the prepared glasses. It further showed that the borate glass sample doped with 0 mol% Pr_2O_3 exhibits no detectable absorption peak in Figure 4. Different absorption transition of Pr^{3+} ions in the present glass samples were assigned with their respective wavelength and are presented in Table 1.

Table 1 The absorption peaks position and transitions of Pr^{3+} doped (60-x) B_2O_3 - 15ZnO - 10Li_2O - 15SrO - xPr_2O_3 (x = 0, 0.25, 0.50 and 0.75 mol%) glasses

Wavelength(nm)	Transition $^3H_4\rightarrow$	Refrences
444	$^3P_2$	R. Rajanavaneethakrishna *et al*, 2018
470	$^3P_1$	M. Erdem & A. Doğan ,2020
484	$^3P_0$	R.N.A Prasadad *et al*, 2021
660	$^1D_2$	Beena Bhatia1, et al, (2013)

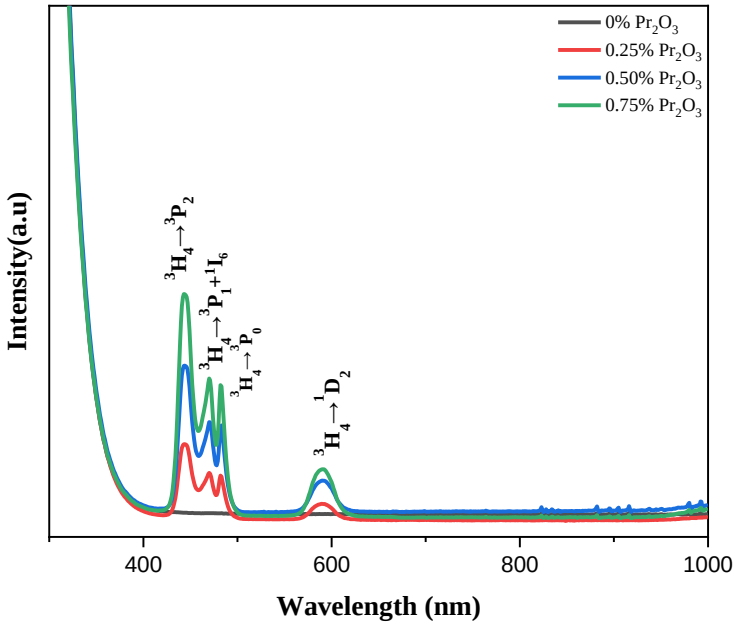

Figure 4. Optical absorption spectra of (60-x) B_2O_3 - 15ZnO -10Li_2O - 15SrO - xPr_2O_3 (x = 0, 0.25, 0.50, and 0.75 mol%)glasses for UV-Vis region.

Photoluminescence Properties

The excitation and emission spectra of (60-x) B_2O_3 - 15ZnO -10Li_2O - 15SrO - xPr_2O_3 (x = 0, 0.25, 0.50 and 0.75 mol%) glasses were carried out to study the photoluminescence properties of the present glasses. The excitation spectra, monitored at an emission wavelength of 605 nm, exhibit three excitation peaks in the blue region; namely, at 445, 470, and 483 nm, with corresponding transitions $^3H_4 \rightarrow {}^3P_2$, $^3H_4 \rightarrow {}^3P_1 + {}^3I_6$, and $^3H_4 \rightarrow {}^3P_0$, respectively (R. Rajanavaneethakrishna *et al*, 2018, R.N.A. Prasadad *et al*, 2021, K.Neeraja *et al*,2013). It was obvious that the position of peaks is not affected but the intensity of peaks is affected by the changing of concentration of Pr^{3+} as shown in Figure 5. Among those three excitation transitions, the transition $^3H_4\rightarrow {}^3P_2$ (at 445 nm) exhibits the maximum intensity as compared to the other two transitions. Hence, the transition $^3H_4\rightarrow {}^3P_2$ was selected as excitation wavelength for emission. The emission spectra of the glass samples monitored at 445 nm excitation wavelength are presented in Figure 6. It was observed four the peaks of down-converted emissions of Pr^{3+} ions located at 485 nm (blue), 545 nm (green), 605 nm (orange) and 645 nm (red) at the visible region (M. Erdem &

A. Doğan, 2020, R. Rajanavaneethakrishna *et al*, 2018, R.N.A. Prasadad *et al*, 2021). These peaks correspond to the $^3P_0 \rightarrow {}^3H_4$, $^3P_0 \rightarrow {}^3H_5$, $^3P_0 \rightarrow {}^3H_6$, $^3P_0 \rightarrow {}^3F_2$ transitions at the visible region (M. Erdem & A. Doğan, 2020, R. Rajanavaneethakrishna *et al*, 2018, R.N.A. Prasadad *et al*, 2021). In the present glass system, orange luminescence dominates. It is also found that there is no change or any significant shift in the position of emission bands with the increase in concentration of Pr_2O_3 except the intensity in the emission spectra. The luminescence intensities of the emission transitions were found to increase with increasing in Pr^{3+} ion content up to 0.5 mol% due to increasing absorption intensity from the pump source at initial concentration. However, the emission intensity was obviously decreased at 0.75 mol% of Pr_2O_3 concentration. The result indicates that the absorption saturation was achieved at this stage and emission intensity began to decrease. This is known as a quenching effect between Pr^{3+} ions and that concentration quenching may occur at higher concentration due to the non-radiative energy transfer process which takes place between nearby Pr^{3+}- Pr^{3+} ions (P. Yasaka and J. Kaewkhao, 2016, M. Shwetha and B. Eraiah, 2021, M. A. Marzouk *et al*., 2012, H. A. Abd El-Ghany,2018). In the emission spectra, the highest emission peak obtained from $^3P_0$ to $^3H_6$ transition centered at 605 nm (reddish orange region). From emission spectra, it was observed that materials show the excellent luminescence properties in visible range under blue excitation wavelength due to f-f and d-f transition of Pr^{3+} ions (V. B. Pawade *et al*, 2017). It was clearly seen that the glass sample with 0.50 mol% Pr_2O_3 emits highest intensity.

The Commission International deI'Eclairage (CIE) chromaticity coordinates are measured for all prepared glass samples by using emission spectra under the excitation of 445 nm. The CIE coordinates are used to find color of light emitted by the material. The emission spectrum shows four bands as mentioned above. From CIE chromaticity-1931, the chromaticity diagram can be plotted. Figure 7 represents the CIE plot with color coordinates for Pr^{3+} doped glass samples. The color coordinates for all glass samples are listed in Table 2. CIE color coordinates for all Pr^{3+} doped glasses were well located in reddish orange region with slight variation of co-ordinates.

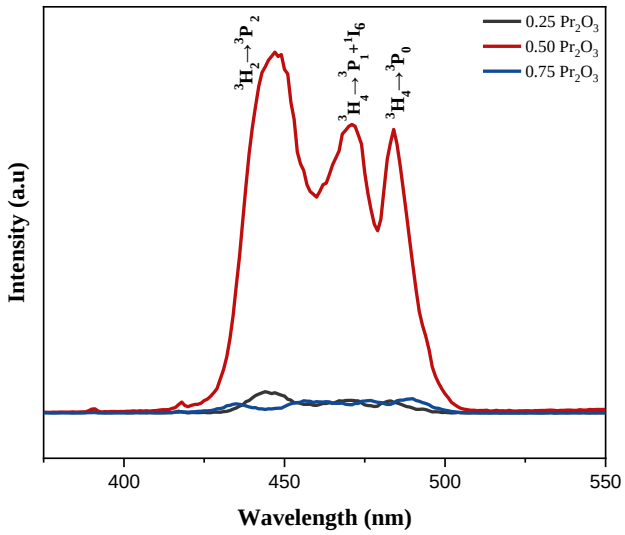

Figure 5. The excitation spectra of (60-x) B_2O_3 - 15ZnO -10Li_2O - 15SrO - xPr_2O_3 (x = 0, 0.25, 0.50, and 0.75 mol%)glasses with 603nm emission wavelength.

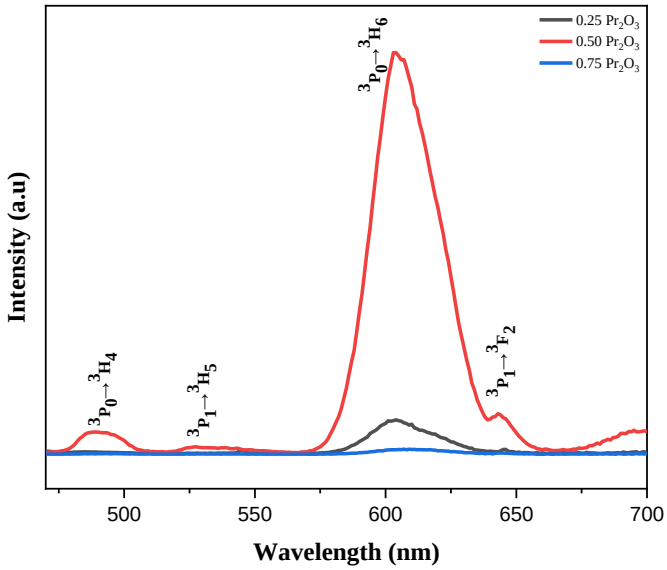

Figure 6. The emission spectra of (60-x) B_2O_3 - 15ZnO -10Li_2O - 15SrO - xPr_2O_3 (x = 0, 0.25, 0.50, and 0.75 mol%) glasses with 445 nm excitation wavelength.

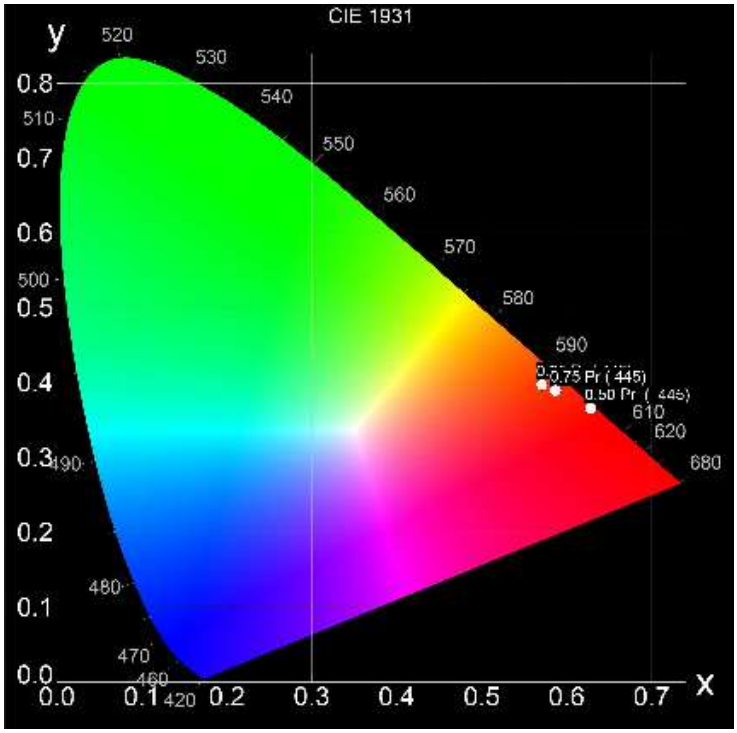

Figure 7. CIE graph of (60-x) B_2O_3 - 15ZnO -10Li_2O - 15SrO - xPr_2O_3 (x = 0, 0.25, 0.50, and 0.75 mol%) glasses

Table 2 CIE 1931 Chromaticity Color Coordinates (x, y) for Pr^{3+} doped (60-x) B_2O_3 - 15ZnO -10Li_2O - 15SrO - xPr_2O_3 glasses

Glasses	CIE coordinates	
	X coordinate	Y coordinate
0.25 Pr_2O_3	0.5710	0.3969
0.50 Pr_2O_3	0.6281	0.3652
0.75 Pr_2O_3	0.5869	0.3893

Summary and Conclusion

Pr^{3+} doped borate glasses with different molar concentration were prepared by using melt quenching technique with the chemical compositions (60-x) B_2O_3 - 15ZnO -10Li_2O - 15SrO - xPr_2O_3 (x = 0, 0.25, 0.50 and 0.75 mol%). The obtained glasses are transparent and colorless. The glasses samples were investigated by using XRD, UV- Vis and PL analysis. The measured XRD spectra confirmed the amorphous nature of the Pr^{3+} doped borate glasses. The optical absorption spectra for all glasses showed the four intense peaks due to transitions as from the $^3H_4$ ground state to the $^3P_2$, $^3P_1$, $^3P_0$, and $^1D_2$ excited states within UV-Vis region. According to PL analysis, the photoluminescence excitation spectra for the glass samples showed the strongest peak at 445 nm which has the maximum intensity and clearly indicated that the glass samples were efficiently excited by blue region. From emission spectra, it was seen that glasses show the good luminescence properties in visible range under blue light (445 nm). The results show the mechanism of down conversion by emitting the low energy photon after exciting it with high energy photon. The band at 605 nm is the highest one which is obtained from $^3P_0$ to $^3H_6$ transition (orange region). The photoluminescence intensity increases with increasing concentration of the Pr^{3+} ions up to 0.5 mol% then decrease. This decrease is due to the concentration quenching effect which is non-radiative energy transfer among excited Pr^{3+} ions. According to CIE chromaticity coordinates, the color coordinates of the present Pr^{3+} doped glasses all fall in the reddish orange region under excitation of the blue wavelength. Among three samples the sample with Pr^{3+} (0.5 mol%) showed highest emission intensity. Based on the obtained results, the studied Pr^{3+} doped glass samples may have possible application in emitting light source as the reddish orange component.

Acknowledgments

The author thanks to MYA 01 research project supported by International Science Programme (ISP) at Uppsala University.

References

Aiyeshah A, Ibrahim O, Abd El All S and Ezzeldin.F, (2021), "Effect of Rare-Earth Ions on the Optical and PL Properties of Novel Borosilicate Glass Developed from Agricultural Waste" *Materials*, vol.14, pp. 5607-5622.

Aljewaw O. B, Khalis Abdul Karim M., Mohamed Kamari H., Hafiz Mohd Zaid M., (2020) "Impact of Dy_2O_3 Substitution on the Physical, Structural and Optical Properties of Lithium–Aluminium–Borate Glass System." *Applied Science*, vol.10, pp.8183.

Abd El-Ghany H. A, (2018) "Cadmium Doped Copper Containing Phosphate Glass as a Bandpass Filter for Solar Cell Protection.", *Journal of Advanced Physics.*, vol.14, pp. 5488-5503

Beena Bhatia1, Vishal parihar, Sanjay Singh, Verma A. S., (2013) "Spectroscopic Properties of Pr3+ in Lithium Bismuth Borate Glasses" *American Journal of Condensed Matter Physics*, vol.3, Issue 3, pp. 80-88

Chopra N., Kaur S., Pandey O. P., Sharma G. and Sharma1 S., (2021) "Physical, optical and structural characterizations of Dy^{3+} -doped lead borate glasse", *ICETEST 202 IOP Conf. Series: Materials Science and Engineering* vol.1114, pp.012098.

Chopra N., Kaur S., Kaur M., Singla S., Marwaha R., Sharma G., and Heer M. S , (2018) "Optical, Physical and Structural Properties of Er^{3+} Doped Low-Phonon Energy Vitreous Matrix: $ZnO\text{-}B_2O_3\text{-}TeO_2$." *Physica Status Solidi (A)*, vol. 215, Issue 13.

Damodaraiah S., Reddy Prasad V., Babu S., Ratnakaram Y.C., (2017) "Structural and luminescence properties of Dy^{3+} doped bismuth phosphate glasses for greenish yellow light applications." *Opt. Mater.* vol.67, pp.14-24.

Erdem M. & Doğan A., (2020) "Spectral Outputs of Yb^{3+}/Pr^{3+} Doped Tellurite Glasses for Solid-State Lighting." *JOTCSA 2020*, vol.9, Issue1, pp. 21-28.

Ilhan M. & Ekmekic M.K., (2015) "Synthesis and Photoluminescence Properties of Dy^{3+} doped White light emitting $CdTa_2O_6$ Phosphar", *Journal of Solid State Chemistry***,** vol. 226, pp.243-249.

H. Lin, E.Yue-Bin Pun, X.Wang, X.Lui, (2015) "Intense visible fluorescence and energy transfer in Dy^{3+} , Tb^{3+}, Sm^{3+} and Eu^{3+} doped rare-earth borate glasses." *Journal of Alloys and Compounds*, vol.390, pp.197-201.

Marzouk M. A., Ouis M. A., Hamdy Y. M, (2012) "Spectroscopic Studies and Luminescence Spectra of Dy_2O_3 Doped Lead Phosphate Glasses." *Silicon***,** vol.4, pp. 221-227.

Mitru S. & Kaur S., (2015) "Intense Orange Emission in Pr^{3+} doped Phosphate Glasses." *Journal of Physics and Chemistry of Solids*. vol.85, pp. 245-248

Naftaly M., Jha A., & Jordan W. G., (1998) "1.3 μm fluorescence quenching in Pr-doped glasses." *Journal of Applied Physics,* vol.84, pp.1800-1804.

Neeraja K., Rao T.G.V.M., Rupesh Kumar A., Uma Lakshmi V., Veeraiah N., Rami Reddy M., (2013) "Spectroscopic properties of Sm^{3+} and V^{4+} ions in $Na_2O\text{–}SiO_2\text{–}ZrO_2$ glasses", *Journal of Molecular Structure*, vol.1054–1055, pp. 339–348.

Pawar. P.P, Munishwar. S.R & Gedam. R.S (2016) "Physical and optical properties of Dy^{3+}/Pr^{3+} Co-doped lithium borate glasses for W-LED", *Journal of Alloy and Compounds*, vol.660, pp.347-355.

Pawade V. B., Zanwar A., Birmod R. P., · Dhoble S. J., · Koao L. F., (2017) "Optical and Bandgap Study of Rare Earth Doped Phosphate Phosphor", *Journal of Materials Science: Materials in Electronics*, vol .21, pp 16306-16313

Prasadad R.N.A. et al, "Effect of modifier oxides on spectroscopic and optical properties of Pr^{3+} doped $PbO\text{-}Ro_2O_3\text{-}WO_3\text{-}B_2O_3$ glasses (with $Ro_2O = Sb_2O_3$, Al_2O_3, and Bi_2O_3)", Journal of Luminescence **230**(2021).

Rajanavaneethakrishna R., Wongdeeying C., Yasaka P., Limkitjaroenorn P., Sangwaranateen N. and Kawewkhao J., (2018) "Pr^{3+} doped BaO- $ZnO\text{-}B_2O_3\text{-}TeO_2$ glasses for laser host matrix", *Journal of Metals, Materials and Miner*als, vol.28, Issue2. pp. 47-54.

Shelby. J.E., (2005). "Introduction to Glass Science and Technology, The Royal Society of Chemistry", New York.

Shwetha M. and Eraiah B., (2021). "Influence of Dy^{3+} Ions on The Physical, Structural and Optical Properties of Lithium Zinc Phosphate Glasses", *Journal of Non-Crystalline Solids.* vol.555, pp 120622.

Yasaka P. and Kaewkhao J., (2016) "White Emission Materials from Glass Doped with Rare Earth Ions: A Review", AIP Conf. Proc. 1719, 020002, pp 1-12.

Yuliantini L., Hidayal R.H, Djamal M., Boonin K., Yasaka P., Kaewnuam E., Kaewkho J., (2017) "Development of Sm^{3+} doped ZnO-Al_2O_3-BaO-B_2O_3 glasses for optical gain medium", *Journal of Non-Crystalline Solid*, vol.482, pp 86-92

Zhou X., Deng Y., Jiang S., Xiang G., Li L, Tang X., Luo X., Pang Y., Huang X., Zhou Y., (2019) "Investigation of energy transfer in Pr^{3+}, Yb^{3+} co-doped phosphate phosphor: The role of $^3P_0$ and $^1D_2$." *Journal of Luminescence*, vol.209, pp 45–51.

Zhang Y., Zhang Y., Lu C, Sun L., Xu Z. and Ni Y., (2009) "Influence of Sm_2O_3 on the crystallization and luminescence properties of boroaluminosilicate glasses." *Materials Research Bulletin*. vol.44, pp. 179 – 183

SOLVING THE HARMONIC AND ANHARMONIC OSCILLATORS WITH MATRIX METHOD

Thei` Theint Theint Aung[1], Wai Wai Khaing[2], Nyein Thida[3]

Abstract

Attempts have been made to investigate a simple technique for solving the Schrödinger equation. This involved Matrix formulation of time independent Schrödinger equation, matrix representation of position and momentum operators, harmonic oscillators and anharmonic oscillators. Then, the numerically exact Eigen values (i.e. the possible results of a measurement of energy) and Eigen vectors for models have been investigated through matrix method and relevant numerical simulations have been implemented using Mathematica coding.

Keywords: Matrix method, Schrödinger equation, Mathematica coding

Introduction

One of the most fundamental theories of physics is quantum mechanics. The behavior of matter and energy on the scale of atomic and subatomic particles or wave can be explained by quantum mechanics. In quantum mechanics the wave function, also talk about the state function, is taken to be the most complete description that can be assigned to a physical system (Sakurai, J.J., 1994). The Schrödinger equations solutions are very useful to describe the behavior of microscopic system, macroscopic system and in all probability the entire universe. The Eigen functions are carefully chosen from a special class of functions. So, the general solutions of harmonic and shift harmonic oscillator have a very interesting property that each Eigen function is linked with a particular Eigen energy value of each potential (Kahn, K., 2008).

This research attention on the extension of the matrix mechanics but instead of just deriving a matrix method that can be used to solve an-harmonic oscillator with a general matrix expression. So, the Schrödinger equation is applied and the wavefunction is written in terms of another set of orthonormal basis wave functions. Then, the eigenvalue equation is derived. From here the matrix equation is found for the Hamiltonian operator. The target of this research now becomes to solve for this matrix equation, so as to get energy (eigenstates) and Eigen functions. So, the Hamiltonian is modified in the form of ladder operators and answered for the matrix elements for manufacture the whole process easy. The Hamiltonian matrix elements are solved with the help of Mathematica and Eigen function regardless of whether the matrix is diagonal or not.

Matrix formulation of time independent Schrödinger equation

Schrödinger equation is very useful equation in quantum mechanics that can solve the most fundamental problems. The time independent Schrödinger equation is

$$\left(-\frac{\hbar^2}{2m}\frac{d^2}{dx^2}+V(x)\right)\phi_n(x)=E\phi_n(x) \tag{1}$$

If the Hamiltonian is

$$H\phi_n(x)=E\phi_n(x) \tag{2}$$

[1] Department of Physics, Bago University
[2] Department of Physics, Sagaing University
[3] Pro-Rector, Dagon University

In the above condition, H , $\phi_n(x)$ indicated the Hamiltonian operator and the wave functions representing the state. Besides, the mass and the position are signified by *m* and *x* and the Eigen values or energy for the Hermitian operator is denoted by E_n (Franzke, M.C, et al, 2021). Then, the wavefunction $\phi_n(x)$ are rewritten by

$$\phi_n(x) = \sum_{i=0}^{\infty} c_i^{(n)} \psi_i(x) \tag{3}$$

Substituting in Equation (2) $\sum_{i=0}^{\infty} c_i^{(n)} H\psi_i(x) = E_n \phi_n(x)$

Multiplying both sides by $\psi_j^*(x)$ we have $\sum_{i=0}^{\infty} c_i^{(n)} \psi_j^*(x) H\psi_i(x) = E_n \psi_j^*(x) \phi_n(x)$. If $\int_R \psi_j^*(x) \phi_n(x)\, dx = c_j^{(n)}$, integrating above equation with respect to x over the R line

$$\sum_{i=0}^{\infty} c_i^{(n)} \int_R \psi_j^*(x) H\psi_i(x) dx = \int_R E_n \psi_j^*(x) \phi_n(x)\, dx = E_n \int_R \psi_j^*(x) \phi_n(x)\, dx$$

$$\sum_{i=0}^{\infty} c_i^{(n)} \int_R \psi_j^*(x) H\psi_i(x) dx = E_n c_j^{(n)} \tag{4}$$

Then H_{ji} is defined as $H_{ji} = \int_R \psi_j^*(x) H\psi_i(x)\, dx$

So, Equation (4) becomes, $\sum_{i=0}^{(n)} c_i^{(n)} H_{ji} = E_n c_j^{(n)}$ (5)

If *H* is chosen to be an $N \times N$ matrix, then *N* Eigenvalues and Eigen vectors will have. Specifically, *n* will go from 1 to *N* (Gupta, R., 2019,Okock, P. and Burns, T., 2015).

Ladder operators or creation and annihilation operators

To simplify the eigenvalue equation for time-independent Schrödinger equation, the two operators are introduced by

$$a_+ = \frac{1}{\sqrt{2}}(x - ip), \qquad a_- = \frac{1}{\sqrt{2}}(x + ip) \tag{6}$$

This pair are well known ladder operators with a_+ defined as the creation operator and a_- defined as the annihilation operator (Sakurai, J.J., 1994). Then, the number operator is defined as $N = a_+ a_-$, with eigenvalues *n* and Eigen functions $|n\rangle$. By the time ladder operators are rewritten in the form of position and momentum operator,

$$x = \frac{1}{\sqrt{2}}(a_+ + a_-) \qquad p = \frac{i}{\sqrt{2}}(a_+ - a_-) \tag{7}$$

So, the commutation relationships of raising and lowering operators developed

$$[a_-, a_+] = \frac{1}{2}[x+ip, x-ip] = \frac{1}{2}([x,-ip]+[ip,x]) = -i[x,p] = 1 \tag{8}$$

$$[N, a_-] = [a_+a_-, a_-] = [a_+, a_-]a_- = -a_- \tag{9}$$

$$[N, a_+] = [a_+a_-, a_+] = a_+[a_-, a_+] = a_+ \tag{10}$$

From the commutation relationships, $a_-|n\rangle = [a_-, N]|n\rangle = a_-n|n\rangle - Na_-|n\rangle$

$$Na_-|n\rangle = (n-1)(a_-|n\rangle) \tag{11}$$

where, N, $a_-|n\rangle$ and $(n-1)$ are operator, eigenvector (eigenstate) and eigenvalue. The annihilation operator $a_-|n\rangle$ is recognized by $a_-|n\rangle = c_n|n-1\rangle$. In the same way, $a_+|n\rangle$ is an eigenvector of N operator by Eigen value $(n+1)$: $a_+|n\rangle = [a_+, N]|n\rangle = a_+n|n\rangle - Na_+|n\rangle$

$$Na_+|n\rangle = (n+1)(a_+|n\rangle) \tag{12}$$

Therefore, the creation operator is recognized by $a_+|n\rangle = d_n|n+1\rangle$. Since $\langle n|N|n\rangle = \langle n|a_+a_-|n\rangle = n$ and $\langle n|a_+a_-|n\rangle = (\langle a_-n|)(a_-|n\rangle) = \langle n-1|n-1\rangle c_n^2$, $c_n = \sqrt{n}$.

Since $a_-a_+ = N+1$, from the commutation relationship:

$$d_n^2\langle n+1|n+1\rangle = \langle a_+n|a_+n\rangle = \langle n|a_-a_+|n\rangle\langle n|(N+1)|n\rangle = n+1 \tag{13}$$

So, $a_-|n\rangle = \sqrt{n}|n-1\rangle$, $a_+|n\rangle = \sqrt{n+1}|n+1\rangle$ and $N|n\rangle = n|n\rangle$. This three properties confirm with creation operator a_+, annihilation operator a_- and the number operator N yielded the quantum number n, for particles of the corresponding energy level (Sakurai, J.J., 1994).

Matrix representation of position and momentum operator

By applying the bra-ket notation, the position and momentum operator can be described

$$\hat{x}_{nm} = \langle n|x|m\rangle, \qquad \hat{p}_{nm} = \langle n|p|m\rangle \ . \tag{14}$$

Here the raising operator a_+ and lowering operator a_- will be useful. From Equation (7)

$$x = \frac{1}{\sqrt{2}}(a_+ + a_-) \ , \qquad \hat{x}_{nm} = \frac{1}{\sqrt{2}}(\langle n|a_-|m\rangle + \langle n|a_+|m\rangle) = \frac{1}{\sqrt{2}}(\langle a_+n|m\rangle + \langle n|a_+m\rangle)$$

$$\hat{x}_{nm} = \frac{1}{\sqrt{2}}\left(\langle\sqrt{n+1}\ n+1|m\rangle + \langle n|\sqrt{m+1}\ m+1\rangle\right)$$

$$\hat{x}_{nm} = \frac{1}{\sqrt{2}}\left(\sqrt{n+1}\delta_{n+1,m} + \sqrt{m+1}\delta_{n,m+1}\right) \tag{15}$$

By matrix representation, the position operator becomes

$$\hat{x} = \frac{1}{\sqrt{2}} \begin{pmatrix} 0 & \sqrt{1} & 0 & \cdots \\ \sqrt{1} & 0 & \sqrt{2} & \cdots \\ 0 & \sqrt{2} & 0 & \cdots \\ \vdots & \vdots & \vdots & \ddots \end{pmatrix} \tag{16}$$

Similarly $p = \frac{i}{\sqrt{2}}\left(a_+ - a_-\right)$, $\hat{p}_{nm} = \frac{i}{\sqrt{2}}\left(\langle n|a_+|m\rangle - \langle n|a_-|m\rangle\right) = \frac{i}{\sqrt{2}}\left(\langle n|a_+ m\rangle - \langle a_+ n|m\rangle\right)$

$$\hat{p}_{nm} = \frac{i}{\sqrt{2}}\left(\left\langle n\middle|\sqrt{m+1}\ m+1\right\rangle - \left\langle\sqrt{n+1}\ n+1\middle|m\right\rangle\right)$$

$$\hat{p}_{nm} = \frac{i}{\sqrt{2}}\left(\sqrt{m+1}\delta_{n,m+1} - \sqrt{n+1}\delta_{n+1,m}\right) \tag{17}$$

By matrix representation, the momentum operator become

$$\hat{p} = \frac{i}{\sqrt{2}} \begin{pmatrix} 0 & -\sqrt{1} & 0 & \cdots \\ \sqrt{1} & 0 & -\sqrt{2} & \cdots \\ 0 & \sqrt{2} & 0 & \cdots \\ \vdots & \vdots & \vdots & \ddots \end{pmatrix} \tag{18}$$

The Hamiltonian for the Harmonic, anharmonic oscillator problems can discover by utilizing the position and momentum operators.

Harmonic Oscillator

The harmonic oscillator is very useful in particle physics and is given by a ladder of evenly spaced energy levels. ΔE is the energy difference between two successive levels of the harmonic oscillator and the number of energy levels are endless. Nevertheless, there must be existent a minimum energy, since the energy must always be positive. Then, the simple harmonic oscillator Hamiltonian is

$$H = \frac{p^2}{2m} + \frac{1}{2}m\omega^2 x^2 \tag{19}$$

where x , p , m and ω are the position, momentum, mass and angular frequency (David, C. W., 2006). The position x and momentum p can satisfy commutation relation $[x, p] = i\hbar$. In this research, natural units for mass m, angular frequency ω and $\hbar$ are used i.e. $m = \omega = \hbar = 1$. So, the reduced Hamiltonian is $H = \frac{p^2}{2} + \frac{x^2}{2}$. By $N = a_+ a_-$, the energy levels of the harmonic oscillator come to be

$$E_n = n + \frac{1}{2} \qquad\qquad n = 0, 1, 2, ... \tag{20}$$

and the wavefunctions are come $$\psi_n(x) = \left(2^n n! \sqrt{\pi}\right)^{-1/2} e^{-x^2/2} H_n(x) \tag{21}$$

where $H_n(x)$ is a Hermite polynomial. By utilizing the operators related both position and momentum, the Hamiltonian of the quantum harmonic oscillator is composed as:

$$\hat{H} = \frac{\hat{p}^2}{2} + \frac{\hat{x}^2}{2} \tag{22}$$

It is trivial to produce the Hamiltonian matrix of the simple harmonic oscillator, since it is diagonal, i.e.

$$\hat{E} = \frac{1}{2}\begin{pmatrix} 1 & 0 & 0 & \cdots \\ 0 & 3 & 0 & \cdots \\ 0 & 0 & 5 & \cdots \\ \cdots & \cdots & \cdots & \ddots \end{pmatrix} \tag{23}$$

which is the correct list containing the eigenvalues. For this case, the Eigen functions are easy to determine, since it is a diagonal matrix. By using Equation (21) and (23), Simple Harmonic Oscillator Potential V(x), it's the first thirteen energy levels and their wave function are demonstrated in Figure 1. From this figure, Eigen Functions have a notable property that each Eigen function is related with a certain Eigen energy value of the particle.

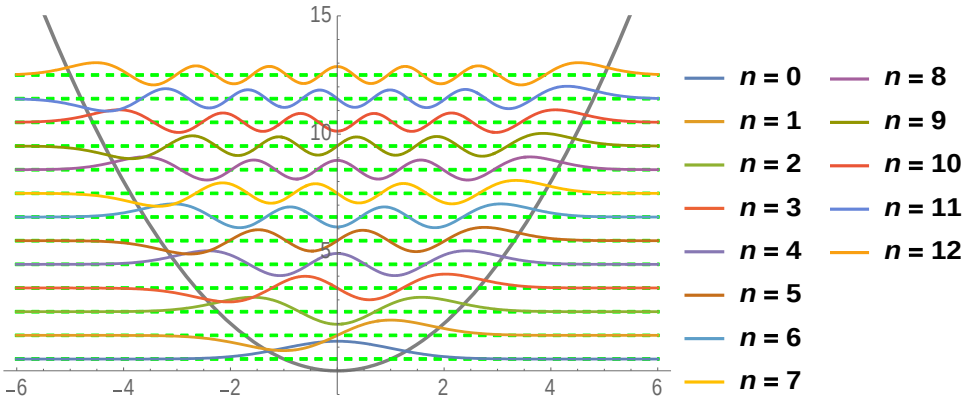

Figure 1 Simple Harmonic Oscillator Potential V(x) (Black line), the first thirteen energy levels (green dash line) and their wave function (colorful lines for each excited state)

Anharmonic Oscillator

Anharmonic oscillator, an oscillator that is not oscillating in a harmonic motion, one which diverges from the exact form of the harmonic oscillator (Pingak, R. K., Johannes, A. Z., et. al, 2021). By Equation (3), the wave function can be written in another orthonormal set form. The numerical derivation of the quartic anharmoinc oscillator is followed with the potential energy of the form

$$V(x) = ax^2 + bx^4 \tag{24}$$

In this research, the value of a is used by "0.5" for anharmonic oscillator. So, the anharmonic oscillator potential becomes

$$V(x)=\frac{x^2}{2}+bx \ ,$$

and Hamiltonian develops $$H=H_0+bH' \tag{25}$$

Applying the matrix method, the Hamiltonian Matrix's elements can be obtained by the standard method, i.e., $$H_{mn}=\langle m|H_0|n\rangle+b\langle m|x|n\rangle \tag{26}$$

The first term is the famous matrix element of unperturbed harmonic oscillation and the second term can be easily calculated using Equation (15). Once the Hamiltonian matrix elements of the an-harmonic oscillators shown above Equation (26) are calculated for a particular matrix size *N* with particular values of coupling constants to obtain *N* energy eigenvalues of the oscillators, which was completed using a athematica code in this research (Lucha, W., 1999):

$$H=\begin{pmatrix} \frac{1}{2}+\frac{3b}{4} & 0 & \frac{3b}{\sqrt{2}} & \cdots \\ 0 & \frac{3}{2}+\frac{15b}{4} & 0 & \cdots \\ \frac{3b}{\sqrt{2}} & 0 & \frac{5}{2}+\frac{27b}{4} & \cdots \\ \vdots & \vdots & \vdots & \ddots \end{pmatrix} \tag{27}$$

This diagonalizing Equation (27) resulted in *N* energy eigenvalues of the systems. When matrix of *H* is infinite, Eigen values will be given by an infinite number of. Practically, the functional basis used to construct matrices. So that, only *N* lowest basis Eigen functions of $\hat{H}_0$ are used and the rank of matrices is *N*+1. If one is especially using numerical methods, but in this case, solving energy levels using a computer program becomes easier. Now the first ten energies of the anharmonic oscillator (*b* = 0.2) for different basis states are shown in Table 1. From Table1 it obviously shows that increasing the number of basis states does have a major effect on the accuracy of the energies obtained. This result outcome comes to be more substantial as one goes to higher order anharmonicities. So, it was found that for much larger basis size, this has a more significant effect. The wave function with different basis size for energy level 8 and 9 are demonstrated by Figure 2 and 3. This figures clearly show that the wave functions are become more and more accurate by increasing the basis size *N*. Then, the potential, Eigen values and Eigen functions for the anharmonic oscillator are shown in Figure 4 as a single plot.

Table 1 The Eigen values of anharmonic oscillator at different levels *n* for different matrix dimension size *N*

n	N=20	N=50	N=100	N=200
0	0.6024051508367525	0.6024051636862472	0.6024051636862515	0.6024051636862132
1	1.9505434140535436	1.950543525634791	1.9505435256347778	1.950543525634835
2	3.5363012292982625	3.5362993632354374	3.5362993632354596	3.536299363235454
3	5.291301898243534	5.29126854258967	5.291268542589542	5.291268542589492
4	7.184415333986799	7.184456293014251	7.184456293009916	7.184456293009918
5	9.194411698495397	9.196339507067782	9.196339507035822	9.19339507035853
6	11.31115495393114	11.313238526270586	11.313238526463659	11.313238526463644

n	N=20	N=50	N=100	N=200
7	13.57964103048524	13.524907023498818	13.524907026874905	13.524907026874862
8	15.708586913924984	15.823319026413065	15.823319030455622	15.823319030455627
9	17.767683505805834	18.201980751867296	18.201980586487824	18.20198058648763
.	.	.	.	.
.	.	.	.	.
.	.	.	.	.

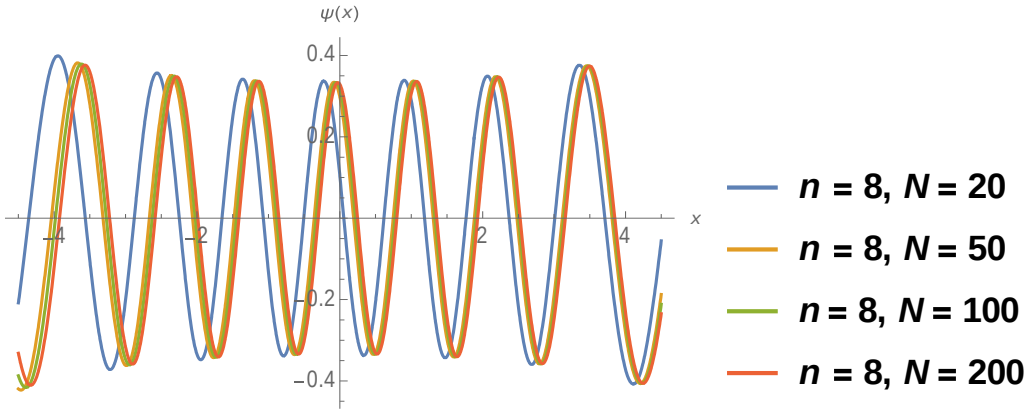

Figure 2 The wave functions of the anharmonic oscillator for energy level 8 with difference matrix dimension size *N*

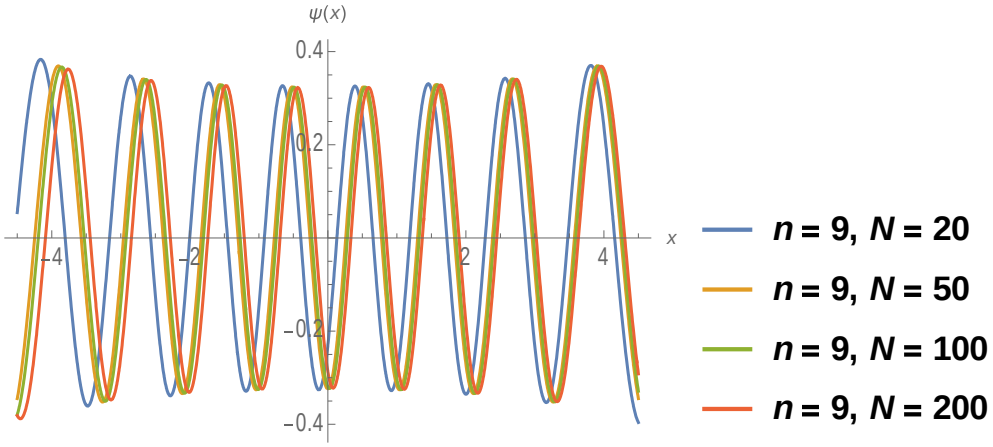

Figure 3 The wave functions of the anharmonic oscillator for energy level 9 with difference matrix dimension size *N*

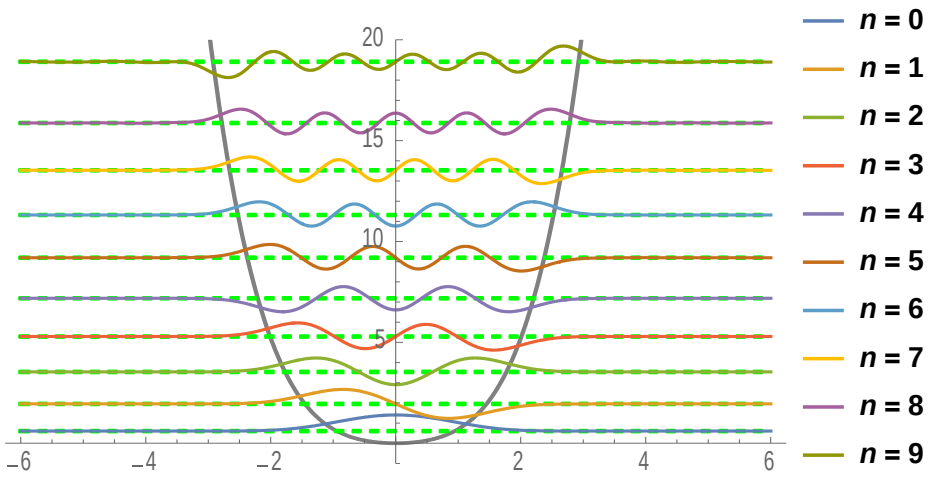

Figure 3 Anharmonic Oscillator Potential V(*x*) (Black line), the first ten energy levels (green dash line) and their wave function (colorful lines)

Conclusion

The aim of this research was to formulate a matrix method for solving the Schrödinger equation. So, the Hamiltonian matrix directly as done for the harmonic Hamiltonian equation was derived. In this step, a remarkable property has been found that each Eigen function is linked with particular Eigen energy value of the particle. According to the results of anharmonic oscillator, one can conclude that increasing the number of basis states have a major effect on the accuracy of the energies and wavefunctions. Besides, the energy values are bit by bit approching to the exact values by increasing in the number of decimal places. In this research paper, all Eigen values and Eigen functions are obtained by a result of a single computation. This is the advantage of matrix formalism. Since the matrix method can reproduce the Eigen values and its corresponding wave functions, this method is successfully modelled for the harmonic and anharmonic oscillator. Finally, this research had an adequate amount of results to make a concrete conclusion that the matrix method actually solves the Schrödinger equation, and it has a wide range of applications where it can be applied such as quantum tunneling to study a particle moving in a region of more than one constant potential or helping quantum mechanics students study solutions for anharmonic oscillators and so forth.

Acknowledgements

I would like to express my sincere thanks to Professor Dr Than Htay, Head of Department of Physics, Bago University, for his kind permission to carry out this research.

Special thanks are due to Professor Dr Thant Zin Naing, Retired Pro-Rector (Admin), International Theravāda Buddhist Missionary University, for his valuable guidance and helpful advice to carry out this work.

References

David, C. W., (2006) "The Harmonic Oscillator, The Ladder Operator Solutions," 2006. *Chemistry Education Materials*. 19. https://opencommons.uconn.edu/chem_educ/19

Franzke, M. C., Tichai, A., et al, (2021) "Excited states from eigenvector continuation: the anharmonic oscillator," August, arXiv:2108.02824v1.

Gupta, R., (2019) "Matrix Method For Solving The Schrodinger ' s Time - Independent Equation To Obtain The Eigen Functions And Eigen Energy Values of A Particle Inside The Infinite Square Well Potential," no. July, doi: 10.9790/4861-1005010105.

Kahn, K., (2008) "Quantum Harmonic Oscillator Eigenvalues and Wavefunctions :," pp. 2007–2008.

Lucha, W., (1999) "Solving The Schroedinger Equation for Bound States with Mathematica 3.0," January, arXiv:hep-ph/9811453v2.

Okock, P. and Burns, T., (2015) "A Matrix Method of Solving the Schrodinger Equation," no. January, doi: 10.13140/RG.2.2.10729.83042.

Pingak, R. K., Johannes, A. Z., et al, (2021) "Quantum Anharmonic Oscillators: A Truncated Matrix Approach," *Positron*, vol. 11, no. 1, p. 9, 2021, doi: 10.26418/positron.v11i1.44369.

Sakurai, J.J., (1994) "*Modern Quantum Mechanics Revised Edition*", ISBN 0-201-53929-2.

CORE SHELL STRUCTURE OF NICKEL FERRITE MICROSPHERE FOR THE APPLICATION OF ENERGY STORAGE DEVICES

Hsu Myat Lwin[1], Swe Zin Aye[2], Zin Min Tun[3] and Cho Cho Thet[4]

Abstract

Carbon (C) coated on the surface of nickel ferrite ($NiFe_2O_4$) is a structure which could act as a protective layer to form a unique core-shell structure. The $NiFe_2O_4$ coated with C anode material shows improved lithium-storage performances since the carbon structure is considered to serve as a conductor of electrons and provide pathways for Li-ion diffusion to improve the electronic and ionic conductivities. Carbon electrodes achieve high capacitance, fast charge-discharge rate, and long cycle life for supercapacitors. In this study, pure and $NiFe_2O_4$ coated with C was synthesized by solvothermal method and followed by precipitation method. The optimum solvothermal temperatures were investigated by varying the temperatures including 110, 150 and 180 ºC respectively. The core-shell structure was prepared based on the optimum temperature. The structural properties of the final product were characterized by Fourier-transform infrared spectroscopy (FTIR), X-ray diffraction (XRD) and the surface morphology was studied by Scanning electron microscopy (SEM).

Keywords: core-shell, carbon coated, FTIR, nickel ferrite, solvothermal, SEM

Introduction

Graphite, graphene, lithium, cobalt, manganese and nickel have been focused for the energy storage applications. Nickel (Ni) is a similar chemical property of iron, cobalt, and copper. However, it is generally only stable in aqueous solution in the + 2 oxidation state. Nickel is a ferromagnetic material and it has an excellent conductor of both electricity and heat (Lebrouhi *et al.*, 2022). Mixed transition metal oxides with spinel structures such as $NiFe_2O_4$, $ZnFe_2O_4$, $CoFe_2O_4$ have high specific capacity and lower cost as compared to other classes of anode materials for battery. Generally, a spinel ferrite is described as (AB_2O_4), where A is a divalent metal ion such as Co, Ni, Zn, Mg, Cu Mn etc. Spinel ferrite possesses two interstitial sites namely tetrahedral (A) and octahedral (B) site. The spinel ferrites are classified as normal ferrite, inverse ferrite and random ferrites. Nickel ferrite possesses inverse spinel structure. It is a soft magnetic material with moderate coercivity and with low conductivity, good electrochemical stability, and abundance in nature and saturation magnetization (Bharati *et al.*, 2020; Benrabaa *et al.*, 2010).

The performance of anode materials for lithium-ion battery requires high conductivity, biocompatibility, chemical stability, corrosion resistance, and improved mechanical strength (Geofrey Sahini and Daud Lupyana, 2023). High mechanical rigidity, photostability, and thermal and electrical conductivities are characteristics of carbon-based nanomaterials. When carbon is composited with other nanoparticles, it exhibits new and improved properties such as increased electrical conductivity and structural stability (Gorgizadeh *et al*., 2018).

Core-shell particles are made up of a shell material, such as carbon, silica, polymers, or another metal or metal oxide, around a core substance, usually a metal or metal oxide. The

[1] Nationalities Youth Resource Development Degree College (Yangon)
[2] Department of Physics, University Yangon University
[3] Department of Physics, West Yangon University
[4] Department of Physics, University of Yangon

improved properties like magnetic, optical, and surface are provided by this unique core-shell structure. Therefore, the characteristics of core-shell particles are interested for solar cells, batteries, and fuel cells. When nickel ferrite with low conductivity is coated with carbon, the electrical conductivity is increased (Azizi *et al.*, 2024). In this study, $NiFe_2O_4$ is synthesized at different temperatures of solvothermal process. Depending on the optimum structural properties, it was coated with carbon for the application of energy storage device. This research is focused on the preparation and characterization of nickel ferrite coated with carbon as an anode material for the application in lithium-ion battery.

Experimental Details

Synthesis of Nickel Ferrite

Nickel ferrite was synthesized by solvothermal method (Liu *et al.*, 2020). The starting materials are nickel nitrate hexahydrate, $Ni(NO_3)_2.6H_2O$, iron nitrate nonahydrate, $Fe(NO_3)_2.9H_2O$, glycerol, C_3H_8O and isopropyl alcohol (IPA). Firstly, 0.1089 g of $Ni(NO_3)_2.6H_2O$ and 0.303 g of $Fe(NO_3)_2.9H_2O$ were added into the mixed solvent containing 24 mL of glycerol and 120 mL of isopropanol. The mixture was stirred at room temperature until to obtain the homogeneous solution. Then, solvothermal process was conducted at the reaction temperatures including 110, 150 and 180 ºC for 6 h. At the end of reaction, the yellow particles were precipitated. After that, the precipitates were centrifuged by ethanol for several times until to get the pH of the solution became neutral. The purified precipitates were dried at 60 ºC for 3 h in air and grinded by agate motor and pestle. Finally, the as-synthesized particles were calcined at 400˚C for 2 h. The reddish-brown color of nickel ferrite nanosphere was obtained. Figure 1 shows the synthesis photo of nickel ferrite microsphere.

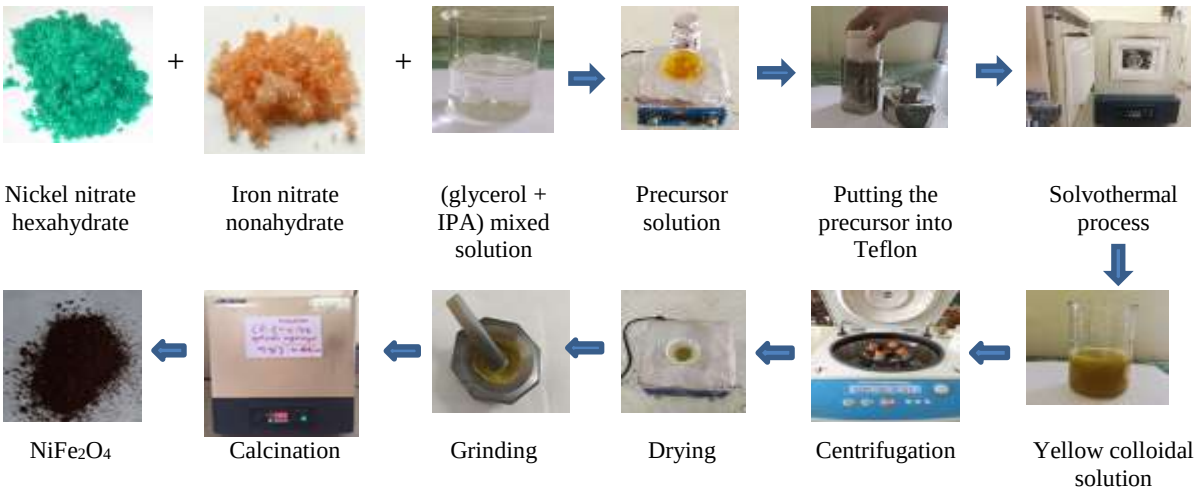

Figure 1 Synthesis photograph of nickel ferrite

Synthesis of Nickel Ferrite Coated with Carbon Microsphere

Firstly, 0.363 g of $NiFe_2O_4$ was add into the solvents containing 145.2 mL ethanol and 72.6 mL deionized water. Then, the mixed solution was sonicated for 30 min. Then, 3.63 mL of ammonium hydroxide (NH_4OH) solution was added into the previous solution and they were stirred for 15 min. After that, 0.726 g of resorcinol, $C_6H_4(OH)_2$ and 871.2 µL of formaldehyde (CH_2O) were added and continued stirring for 2 h. Next, the as-synthesized product was washed by ethanol until to obtain the pH 7. Finally, the purified product dried and annealed at 600 ºC for

2 h. The brownish black color of $NiFe_2O_4$ coated with carbon sphere was successfully obtained. The synthesis of $NiFe_2O_4$@C is presented in Figure 2.

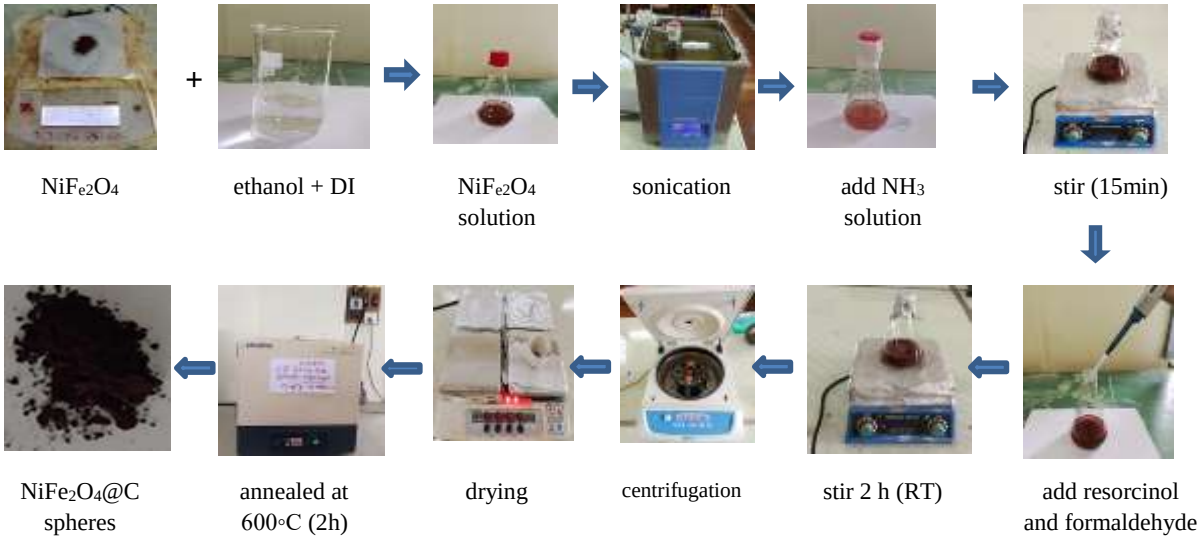

Figure 2 Synthesis photograph of nickel ferrite coated with carbon microspheres

Results and Discussion

The FTIR spectra pure $NiFe_2O_4$ and $NiFe_2O_4$@C composite are illustrated in Figure 3. The peak at 554 cm^{-1} for both pure and composite samples is assigned to the bending vibrations of the metal–oxygen (MO) bond. Only one distinct peak at 554 cm^{-1} was observed in pure $NiFe_2O_4$. For composite, one more additional peak around at 470.79 cm^{-1} was occurred. These two characteristic peaks at 554 cm^{-1} and 470 cm^{-1} were corresponded to the metal-oxygen (M-O) bond stretching vibration at the tetrahedral sites and octahedral sites (Srinivasan *et al.*, 2019). The difference between these absorption bands is due to the change in bond length (M-O) at the tetrahedral and octahedral site (Mounkachi *et al.*, 2017). Therefore, the analysis results indicate that pure $NiFe_2O_4$ has a hematite property and the $NiFe_2O_4$@C composite has a magnetite property. These results are evidence of the color of final products of pure $NiFe_2O_4$ (reddish brown)and $NiFe_2O_4$@C (brownish black) as already mentioned the different colors in their synthesis process.

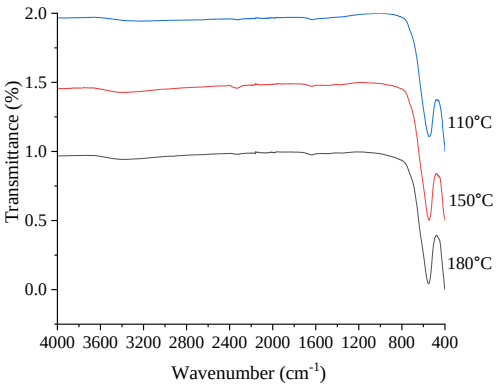

(a)

Figure 3(a) FTIR spectra of $NiFe_2O_4$ at different solvothermal reaction temperatures

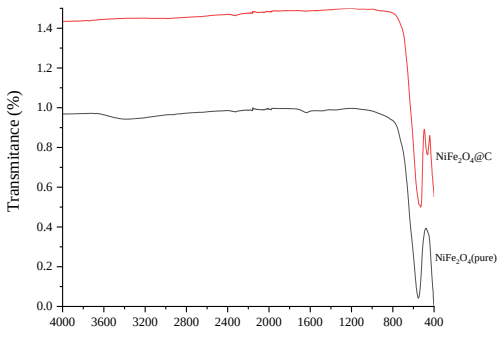

(b)

Figure 3(b) FTIR transmission spectra of $NiFe_2O_4$ and $NiFe_2O_4$@C

XRD is used to examine the crystal structure, phase formation and additionally confirmation of FTIR observation. Figure 4 shows XRD spectra of $NiFe_2O_4$ and $NiFe_2O_4$@C composite. The X-ray diffraction angles of 30.30, 35.69, 43.38, 57.38 and 63.02 degrees were related to (220), (311), (400), (511) and (440) planes. These Miller indices were informed that the formation of cubic structure of pure and composite of nickel ferrite (Mohan *et al*., 2019). The most dominant peaks were occurred at (311) plane. Among the different reaction temperatures, the better crystallinity of spinel ferrite structure was observed at 180 °C. Therefore, reaction temperature 180 ºC was the optimum temperature. The peaks and relative intensities obtained for $NiFe_2O_4$ and $NiFe_2O_4$@C composite were well-matched with the standard library file of ICDD PDF databases number-5910064. The XRD spectrum of $NiFe_2O_4$@C composite was almost as the same as pure nickel ferrite except the diffraction peak in (222) plane at 37.33 degree. This plane was the evidence of carbon peak which is well agreed with FTIR results. The compared XRD spectra of pure and coated with carbon is presented in Figure 5. The crystallite size of the materials is estimated by using the Debye Scherrer Equation (Bokuniaeva and Vorokh, 2019).

$$D = \frac{K\lambda}{\beta \cos\theta} \tag{1}$$

Where,

λ = the wavelength of the incident X-ray beam (1.5405 Å) for $CuK_{\alpha 1}$

K = shape factor

β = FWHM (full width at half maximum) (radian)

θ = diffraction angle (radian)

D = crystallite size (nm)

Average crystallite sizes of nickel ferrite at different reaction temperature is listed in Table 1. The smallest crystallite size was obtained at 180 ºC. Therefore, pure nickel ferrite synthesized at 180 ºC was chosen to composite with carbon. For the composite, the crystallite size was obtained about 26.4 nm.

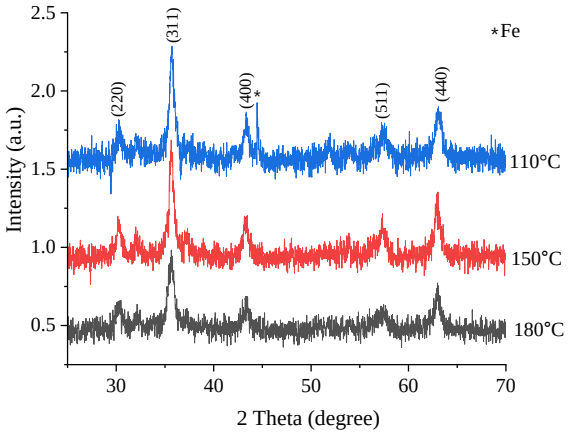

Figure 4 XRD spectra of $NiFe_2O_4$ at different solvothermal reaction temperatures

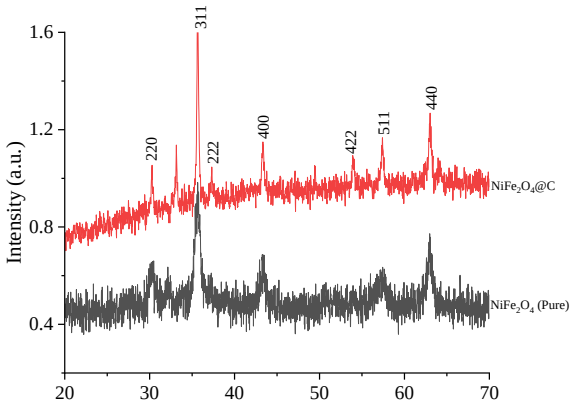

Figure 5 XRD spectra of $NiFe_2O_4$ and $NiFe_2O_4$@C

Table 1. Average crystallite size of nickel ferrite at different reaction temperatures

Solvothermal temperature (ºC)	Average crystallite size (nm)
110	12.2
150	10.1
180	8.59

Scanning electron microscopy–energy dispersive X-ray spectroscopy (*SEM-EDX*) analysis is performed in order to investigate the surface morphologies and qualitative elemental analysis of the materials. According to the SEM image, both pure and composite are found out to be spherical shape. SEM image of $NiFe_2O_4$ calcined at 400 ºC for 2 h and $NiFe_2O_4$@C composite at 600 ºC for 2 h are display in Figure 6. The average diameter of grain size of pure $NiFe_2O_4$ was 1768 nm and $NiFe_2O_4$@C composite was 1899 nm, respectively. In the surface of composites, the spheres are relatively rough because NiFe-glycerate nanospheres encountered a hydrolysis reaction in order form the form hydroxide sheets in the solvent (Liu *et al*., 2020). Thus, the diameters of nickel ferrite coated with carbon spheres were substantially large. Besides, the surfaces were also relatively rough, indicating that the carbon layer was uniformly covered to the surface of nickel ferrite. As the result, the core-shell structure of $NiFe_2O_4$@C was successfully obtained.

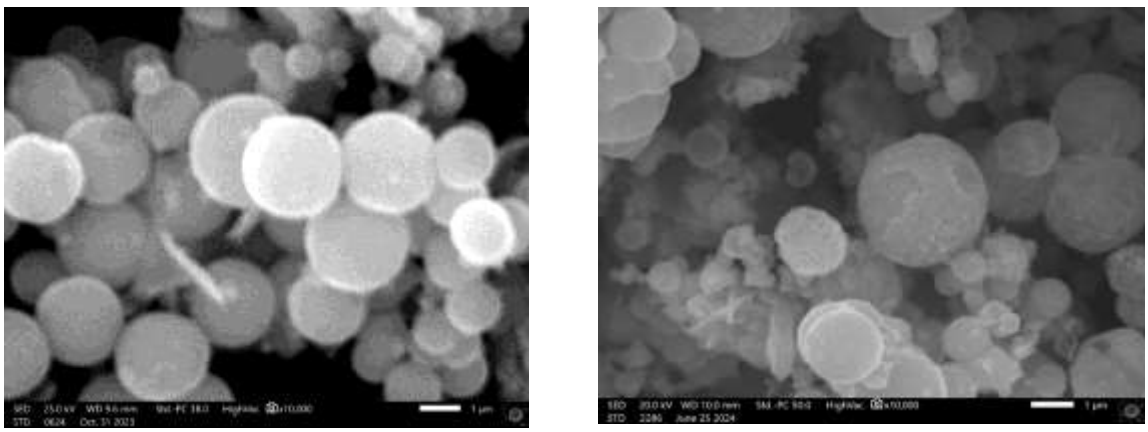

(a) (b)

Figure 6. SEM image of (a) NiFe2O4 and (b) NiFe2O4@C

Figure 7 presents the EDX spectrum of pure and composite materials. Only the particular elements were composed in their materials. These results were additionally supported to the previous observation of XRD and FTIR results. Therefore, the final product of each synthesis could be confirmed that they were high purity materials.

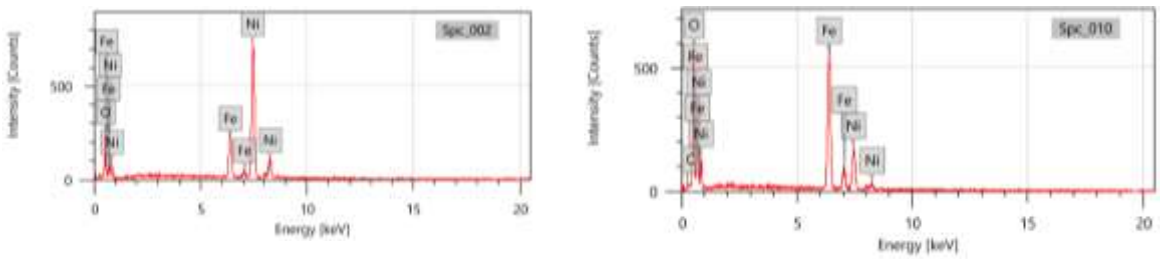

(a) (b)

Figure 7 EDX spectrum of (a) $NiFe_2O_4$ and (b) $NiFe_2O_4$@C

Conclusions

Nickel ferrite ($NiFe_2O_4$) spheres was synthesized by solvothermal method at different reaction temperatures including 110, 150 and 180 ºC. Depending on the optimum temperature, carbon coating process is performed onto the $NiFe_2O_4$. The structural properties of $NiFe_2O_4$ and $NiFe_2O_4$@C composites are characterized by FTIR, XRD and SEM. According to XRD result, the cubic and inverse spinel structure of composite materials was successfully obtained. Debye Scherrer formula suggested that the crystallite of $NiFe_2O_4$ was the smallest at the reaction temperature 180 ºC. FTIR result additionally evidenced that the functional group of targeted compounds and properties of pure $NiFe_2O_4$ is the hematite with paramagnetic core and $NiFe_2O_4$@C is the magnetite with ferromagnetic core-shell materials respectively. SEM image clearly confirmed that the core-shell structure $NiFe_2O_4$@C. EDX spectrum showed the elements composed in pure and composite materials. Therefore, all characterization results are directed to the formation of core shell materials which can be utilized the anode materials in the lithium ion battery.

Acknowledgement

We would like to acknowledge to U Htain Linn, Rector, Nationalities Youth Resource Development Degree College (Yangon), for his encouragement and allowing us to participate in this event. Our special thanks go to Dr Yin Maung Maung, Professor and Head of Department of Physics, for his kind permission to contribute this work and excellent discussion.

References

Azizi, S. et al. (2024) 'Nickel ferrite coated on carbon felt for asymmetric supercapacitor', Chemical Physics Impact, 8(November 2023), p. 100543. Available at: https://doi.org/10.1016/j.chphi.2024.100543.

Benrabaa, R. et al. (2010) Nanosized nickel ferrite catalysts for CO2 reforming of methane at low temperature: Effect of preparation method and acid-base properties, Studies in Surface Science and Catalysis. Elsevier B.V. Available at: https://doi.org/10.1016/S0167-2991(10)75047-3.

Bharati, V.A. et al. (2020) 'Structural and magnetic properties of nickel ferrite nanoparticles prepared by solution combustion method', Journal of Physics: Conference Series, 1644(1). Available at: https://doi.org/10.1088/1742-6596/1644/1/012005.

Bokuniaeva, A.O. and Vorokh, A.S. (2019) 'Estimation of particle size using the Debye equation and the Scherrer formula for polyphasic TiO2 powder', Journal of Physics: Conference Series, 1410(1). Available at: https://doi.org/10.1088/1742-6596/1410/1/012057.

Geofrey Sahini, M. and Daud Lupyana, S. (2023) 'Perspective and control of cation interdiffusion and interface reactions in solid oxide fuel cells (SOFCs)', Materials Science and Engineering: B, 292, p. 116415. Available at: https://doi.org/10.1016/j.mseb.2023.116415.

Gorgizadeh, M., Azarpira, N. and Sattarahmady, N. (2018) 'In vitro and in vivo tumor annihilation by near-infrared photothermal effect of a NiFe2O4/C nanocomposite', Colloids and Surfaces B: Biointerfaces, 170(April), pp. 393–400. Available at: https://doi.org/10.1016/j.colsurfb.2018.06.034.

Lebrouhi, B.E. et al. (2022) 'Critical materials for electrical energy storage: Li-ion batteries', Journal of Energy Storage, 55(1), pp. 1–53. Available at: https://doi.org/10.1016/j.est.2022.105471.

Liu, T. et al. (2020) 'Preparations of NiFe2O4 yolk-shell@C nanospheres and their performances as anode materials for lithium-ion batteries', Nanomaterials, 10(10), pp. 1–15. Available at: https://doi.org/10.3390/nano10101994.

Mohan, R. et al. (2019) 'Existence of exchange bias and large coercivity in NiFe2O4/CoO core–shell structured nanoparticles', Journal of Materials Science: Materials in Electronics, 30(12), pp. 11748–11753. Available at: https://doi.org/10.1007/s10854-019-01536-1.

Mounkachi, O., Hamedoun, M. and Benyoussef, A. (2017) 'Electronic and Magnetic Properties of SnFe2O4 Spinel Ferrites', Journal of Superconductivity and Novel Magnetism, 30(11), pp. 3035–3038. Available at: https://doi.org/10.1007/s10948-017-4138-x.

Srinivasan et al. (2019) 'Applications of cobalt ferrite nanoparticles.pdf', p. 18.

TEMPERATURE DEPENDENCE OF HETEROGENEOUS CdO-NiO NANOCOMPOSITE THIN FILMS

Aye Aye Aung[1], Zin Min Myat[2], Thida lwin[3], Wah Wah Thin[4]

Abstract

This research aims to synthesize the CdO-NiO nanocomposite thin films deposited on fluorine tin oxide (FTO) glass substrates were prepared by spin coating method. Cadmium sulphate, nickel sulphate, ammonia and polyethylene glycol were used as the starting materials to obtain CdO-NiO nanocomposite powders by sol-gel method at 400 ºC, 500 ºC, 600 ºC and 700 ºC for 2 hrs. Then the precursor solution of CdO-NiO nanocomposite were coated on FTO glass substrates. The phase formation, structural properties and surface morphology of nanocomposite were characterized by X-ray Diffraction (XRD) and Scanning Electron Microscopy (SEM). The absorption wavelengths and energy band gap of CdO-NiO nanocomposite thin films were measured with the help of UV-Vis Spectroscopy. CdO-NiO nanocomposite thin films can be promoted further experimental studies such as thin films solar cells, memory devices and optoelectronic materials.

Keywords: CdO, NiO, XRD, SEM and UV-Vis Spectroscopy

Introduction

Thin film technology is the development of very thin layers of material to deposit on the surface of objects, ranging from semiconductors to plate glass. Thin film offers a number of benefits to manufacturers including reduced production costs, smaller and more lightweight finished products and increased flexibility [Ashfari. B, et al, 2001]. From variety of materials including silicon and ceramic can make thin film. Thin film technologies are process for depositing and processing thin layers from a micron thick down individual atomic layer. One use of thin film technology is in semiconductor production, including development of new photovoltaic cells [Al-Juaid.F et al, 2012]. A nanocomposite is a multiphase material in which, in contrast to micro composites, one of the phases has one, two or three dimensions of less than 100 nm or the composite phases have nanoscale distances between them [Abou-Helal M.O, 2002]. Based on the matrix material, nanocomposites are classified into polymer matrix composites, metal matrix composites, and ceramic matrix composites. Nanocomposites are materials that have a solid structure in which the distance between the phases is least wise formed of dimension with nanoscale size and general form of an organic phase, or vice versa, form an organic matrix set in the organic phase [Feinle, M. S. et al, 2016]. Nanocomposite materials can exhibit individual properties such as mechanical, chemical, electrical, optical and catalytic properties [Liao.Y, Xu.Y, et al., 2013]. Nanocomposites are the heterogeneous/ hybrid materials that are produced by the mixtures of polymers with inorganic scale. Their structures are more complicated than that of micro composites [Niederberger.M, et al., 2009]. A nanocomposite combines two or more materials of which at least one is a nanomaterial with different physical and chemical properties. Nanocomposites are prepared by chemically oriented synthetic methods: soft lithography, lamination, spin coating or solution casting [Owens. G.J, et al., 2016]. The primary challenge in the processing of nanocomposite is achieving a homogeneous dispersion of the nanoparticles.The

[1] Department of Physics, Mandalay University of Distance Education
[2] Department of Physics, West Yagon University
[3] Department of Physics, Dagon University
[4] Department of Physics, Mandalay University of Distance Education

application areas for nanocomposites involves medical areas and spans many industries from electronics to automotive to sport equipment [Sule.E.E, 2013].

Materials and Methods

Sample Preparation of CdO-NiO Nanocomposite Powder

Materials

For the preparation of experimental details, the main starting chemicals cadmium sulphate ($CdSO_4$) and nickel sulphate ($NiSO_4$) are reagents used for the preparation of CdO-NiO nanocomposite. Starting materials were purchased from Academy chemical store in the downtown of Yangon. This chemical was analytically pure and directly used as received without further purification.

Methods

The synthesis method consisted of one step (1) the preparation of CdO-NiO nanocomposite powder.

Sample Preparation of CdO-NiO Nanocomposite Powder

In this work, starting chemicals such as cadmium sulphate ($CdSO_4$), nickel sulphate ($NiSO_4$), polyethylene glycol ($C_{2n}H_{4n+2}O_{n+1}$) and ammonia (NH_3) were of analytical grade and used without further purification. The CdO-NiO nanocomposites were synthesized by using sol-gel method and distilled water was used as the dissolving solvents throughout in the study. The molar ratio of 1:1 for cadmium sulphate dehydrate and nickel sulphate dehydrate were firstly dissolved in distilled water to form 0.1 M molar solution for preparing the nanocomposite. Secondly, the resulting mixed solutions were stirred vigorously onto the magnetic stirrer (1000 rpm) at room temperature for 4 hrs. While the stirring process, the reducing agents of ammonia and poly ethylene glycol were added drop by drop into the mixed solution for adjusting the pH level until 7 to obtain the CdO-NiO nanocomposite. Thirdly, the homogeneous solution was cooled to settle down for 24 hrs at room temperature. The next day upper parts of the solutions were decanted to the beaker and the obtained sludge was filtered through filter papers. Finally, the paste of CdO-NiO composite was dried at 100 ºC for 24 hrs and then calcined at 400 ºC, 500 ºC, 600 ºC and 700 ºC for 2 hrs. The structure and crystallization of CdO-NiO nanocomposites were examined by XRD machine, the surface morphological characteristics were determined by SEM and the optical properties and energy band gaps were also detected by UV-Vis Spectroscopy.

Thin Films Preparation of CdO-NiO Nanocomposite

Firstly, the 1 cm × 1 cm FTO /glass substrates were firstly cleaned. The precursor solution of CdO-NiO nanocomposites were coated onto the fluorine doped tin oxide (FTO)/glass substrates by spin coating method. The cleaning glass substrates were tested the conducting layers with digital meter. The prepared CdO-NiO nanocomposite powders were dissolved with 2-methoxyethanol ($C_3H_8O_2$) as solvent to form viscous paste at 80 °C for 3 h. This viscous paste was then coated onto fluorine doped tin oxide (FTO) / glass substrates at 2500 rpm for 30 s by spin coating technique. CdO-NiO solution was deposited onto chemically cleaned FTO conductive glass substrates. The nanocomposite layer coated films were annealed at 100 °C for 1h for diffusion films. Then, the films were cooled slowly at room temperature. The distribution and morphological characterizations of films were examined by Scanning Electron Microscopy (SEM). Optical absorption spectra of the nanocomposite films were examined using a UV- Vis spectroscopy. Figure 1(a~d) showed the photos of preparation of CdO-NiO nanocomposite thin films. The block diagram of preparation of CdO-NiO nanocomposite thin films was shown in Figure 2.

Figure 1 (a) Testing Conducting Layer

Figure 1 (b) Spinning Process

Figure 1 (c) Annealing Process

Figure 1 (d) CdO-NiO Thin Film

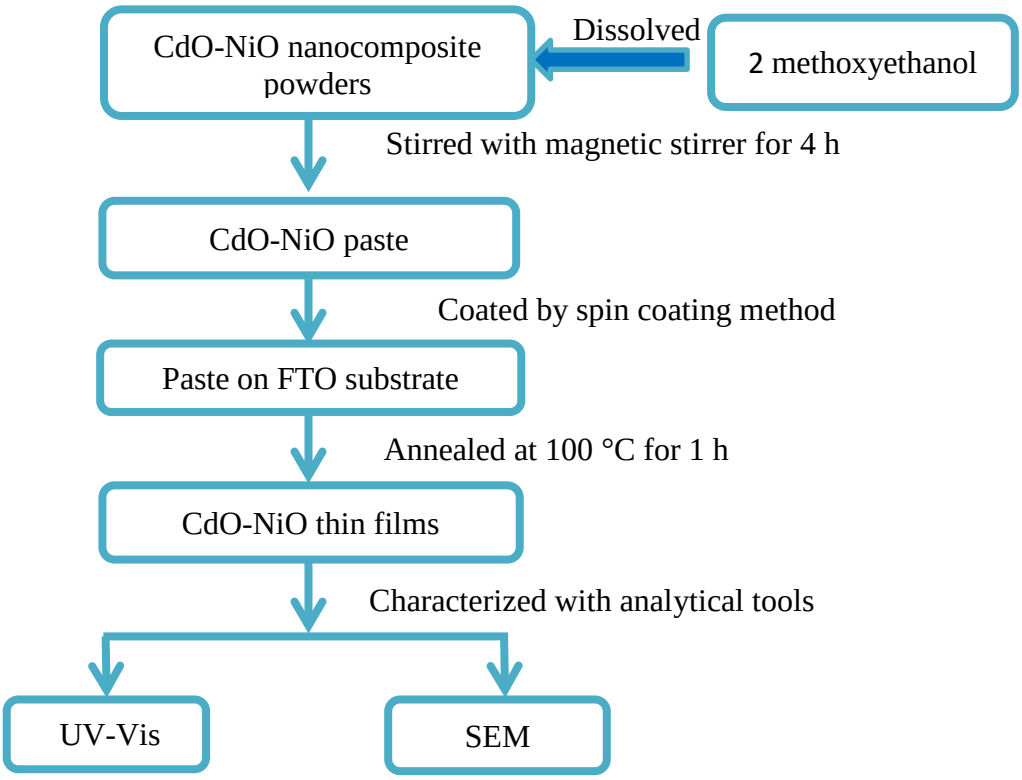

Figure 2 The Block Diagram of Preparation of CdO-NiO Nanocomposite Thin Films

Results and Discussions

Characterization Techniques

The nanocomposite synthesis of CdO-NiO was characterized by XRD, SEM, and UV-Vis spectroscopy for structural, morphological, and optical properties.

XRD Analysis of CdO-NiO Nanocomposite Powder

The structural analysis of CdO-NiO nanocomposite powders was examined by the XRD technique. To examine the crystal structure and phase formation of CdO-NiO nanocomposite powders at 400 °C, 500 °C, 600 °C and 700 °C, it was performed using monochromatic CuK_{α} radiation (λ=1.54056Å) operated at 40 kV (tube voltage) and 40 mA (tube current). The results showed that all the diffraction peaks of CdO-NiO powder can be perfectly matched with JCPDS library file for cubic structure. The distinct peaks were found to be (1 1 1), (2 0 0), (2 2 0), (3 1 1) and (2 2 2) crystal planes for CdO and (1 1 1), (2 0 0), (2 2 0) planes for NiO respectively. The average crystalline sizes of CdO-NiO nanocomposites powders at 400 °C, 500 ºC, 600 ºC, and 700 ºC were 34.2118 nm, 36.3477 nm, 41.6114 nm and 48.5123 nm respectively. The crystalline size was calculated by using Debye Scherrer's formula, ($G=\frac{0.899 \times \lambda}{B \times \cos\theta}$). The XRD pattern of CdO-NiO nanocomposite powders at different temperatures was shown in Figure 3.

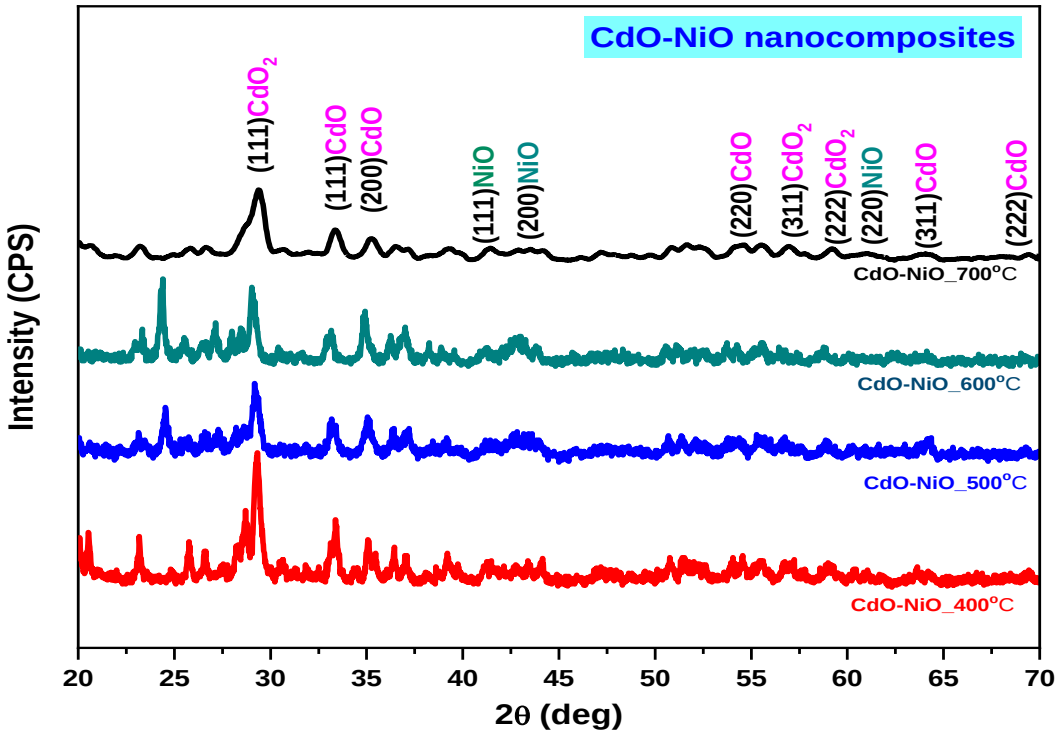

Figure 3 The XRD Pattern of CdO-NiO Nanocomposite Powders at Different Temperatures

SEM Analysis of CdO-NiO Nanocomposite Films

Surface morphology of CdO-NiO nanocomposite thin films on FTO/glass substrates were carried out by SEM analysis. SEM images of CdO-NiO nanocomposite thin films for the different temperatures at 400 ºC, 500 ºC, 600 ºC and 700 ºC were shown in Figure 4(a~d). As the detail analysis of SEM image, it was found that flat and a little crack and more uniform particle size than powder images. These images showed smaller particles features in microstructure. The grain sizes of CdO-NiO nanocomposite thin films were found to be 1.27 µm, 1.18 µm, 1.11 µm and 1.03 µm,

respectively. From SEM analysis, the surface of the films became rough, but the sizes are smaller after annealing different temperatures. On the other side, the achieving relatively films cracking was decreased with the increasing temperature.

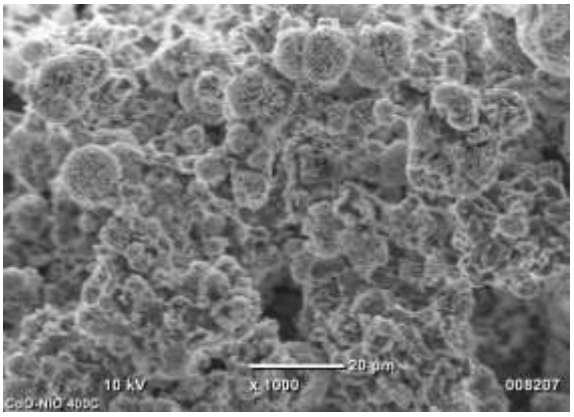

Figure 4 (a) SEM Micrograph of CdO-NiO Nanocomposite Film at 400 ºC

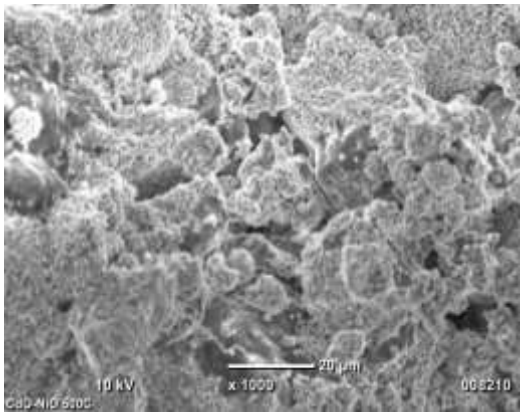

Figure 4 (b) SEM Micrograph of CdO-NiO Nanocomposite Film at 500 ºC

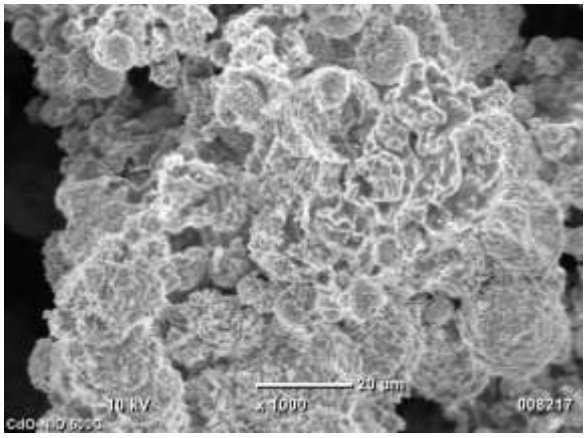

Figure 4 (c) SEM Micrograph of CdO-NiO Nanocomposite Film at 600 ºC

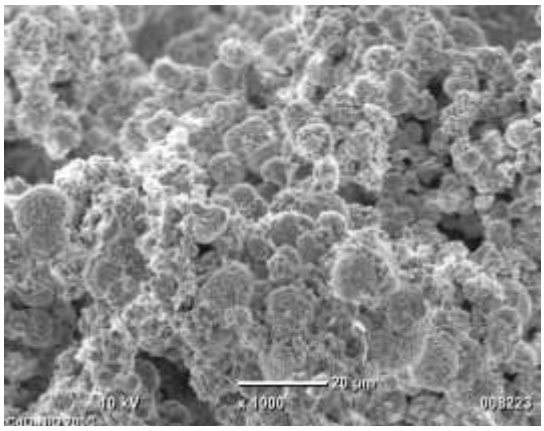

Figure 4 (d) SEM Micrograph of CdO-NiO Nanocomposite Film at 700 ºC

UV-Vis Analysis of CdO-NiO Nanocomposite Thin Films

The absorption spectrum and the energy band gap of CdO-NiO nanocomposite thin films were performed using UV-Vis spectrometer. The wavelength ranges of spectrum laid between 200 nm to 700 nm as shown in Figure 5 (a~d). UV-Vis analysis determined the variation of the absorption coefficient (α) as a function of the photon energy at room temperature. The optical band gap (E_g) was evaluated from the absorption spectrum and the optical absorption coefficient (α) near the absorption edge. The optical band gap energy in absorption edge of CdO-NiO nanocomposite thin films were given in Table 1. The alternative method to observe the band gap is calculated by Tau's relation. The $(\alpha h\upsilon)^2$ and $h\upsilon$ characteristic curve of CdO-NiO nanocomposite thin films at 400 ˚C, 500 ˚C, 600 ˚C and 700 ˚C were shown in Figure 6 (a~d). On the characteristic curve, the extrapolating the straight line onto horizontal axis ($(\alpha h\upsilon)^2 = 0$), give the values of band gap energy obtained CdO-NiO nanocomposite thin films had a direct band gap 2.69 eV at 400 ˚C, 3.83 eV at 500 ˚C, 4.05 eV at 600 ˚C and 4.29 eV at 700 ˚C respectively.

Table 1 The observed energy band gap of CdO-NiO nanocomposite thin films at different temperatures

Sr No.	Temperature (°C)	Observed energy band gap (eV)
1	400	2.69
2	500	3.83
3	600	4.05
4	700	4.29

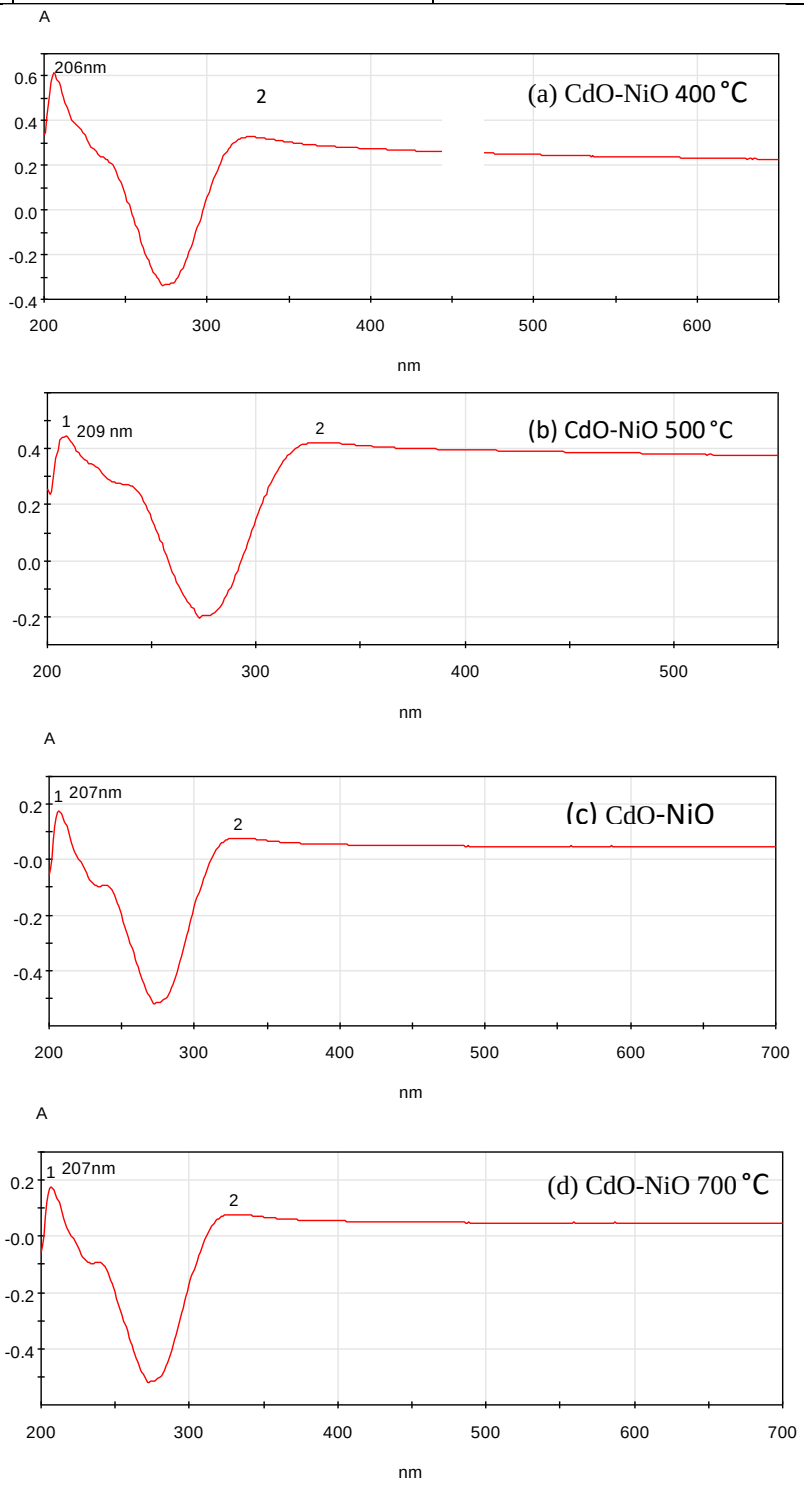

Figure 5(a~d) Absorption Spectrum of CdO-NiO Nanocomposite Film at Different Temperatures

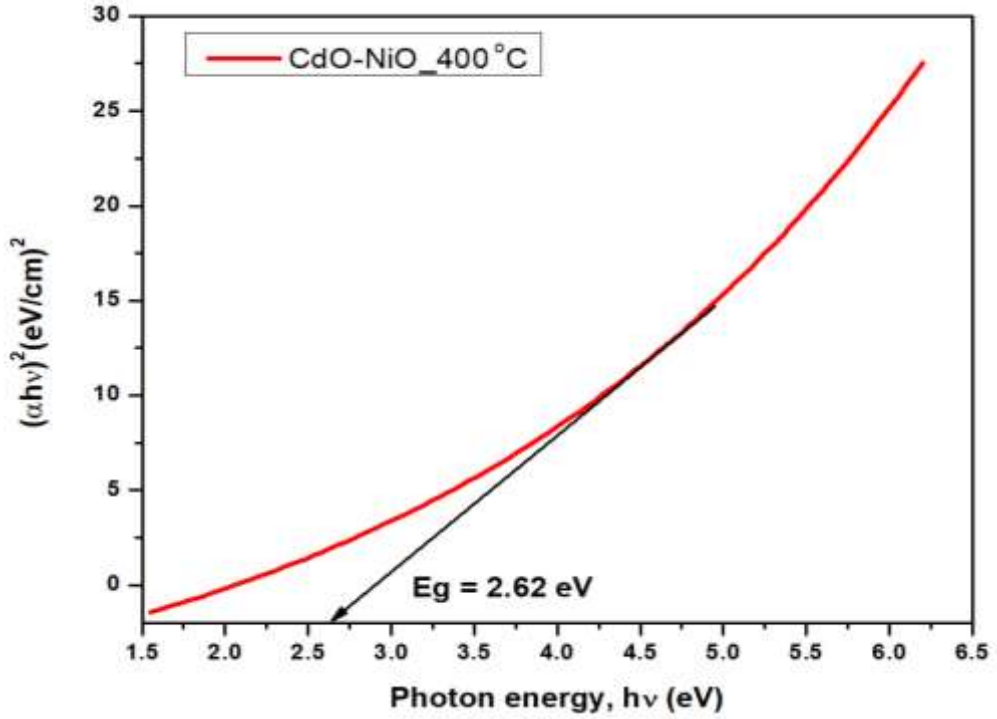

Figure 6 (a) Energy Band Gap Values of CdO-NiO Nanocomposite Thin Film at 400 °C

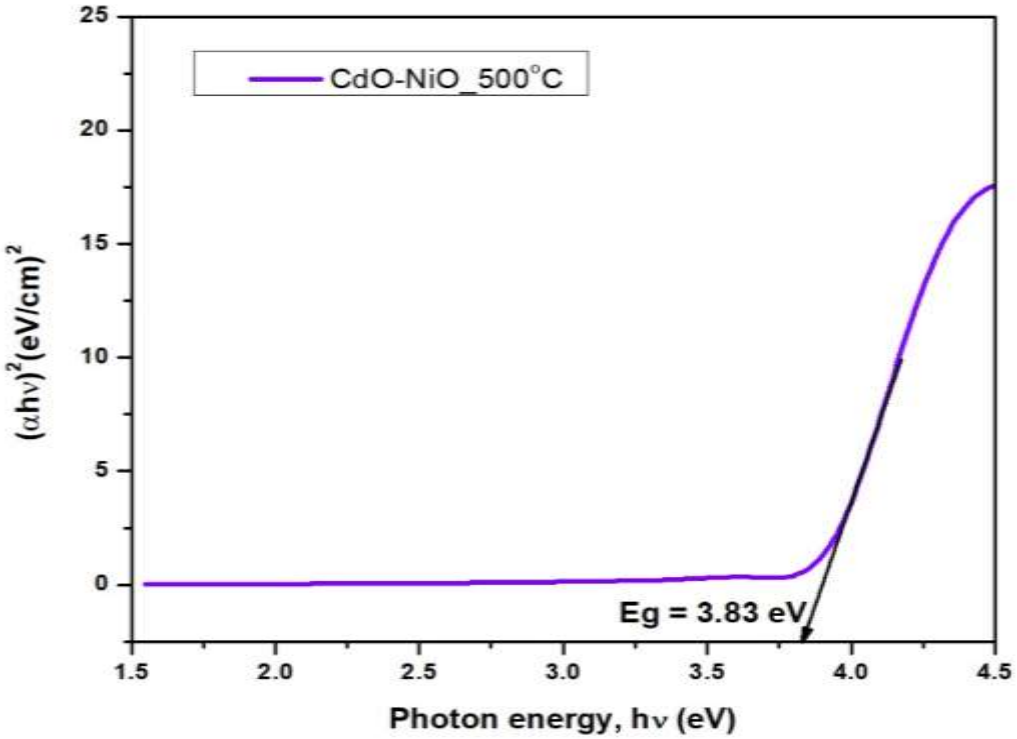

Figure 6 (b) Energy Band Gap Values of CdO-NiO Nanocomposite Thin Film at 500 °C

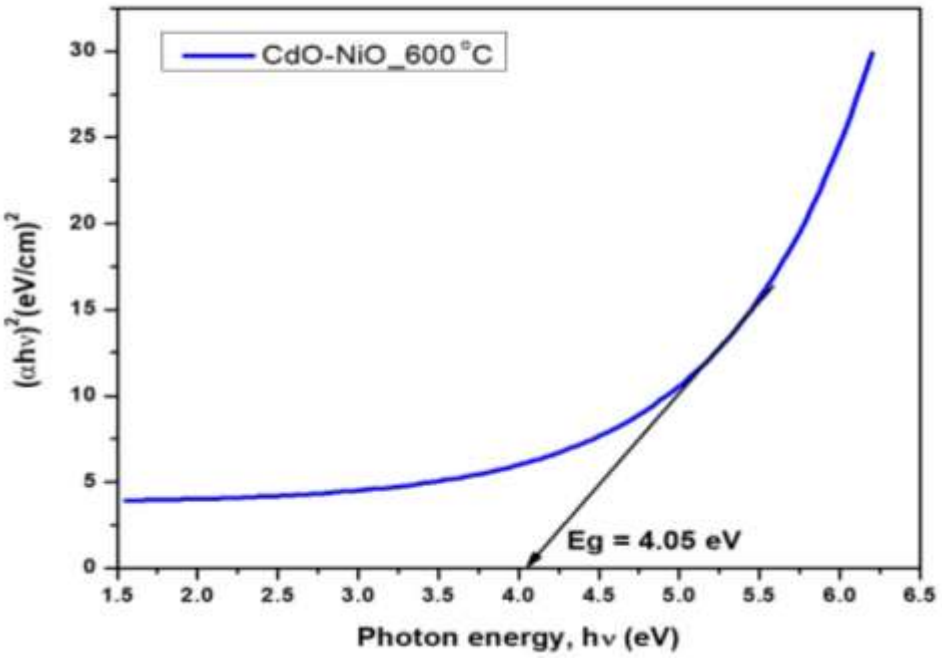

Figure 6 (c) Energy Band Gap Values of CdO-NiO Nanocomposite Thin Film at 600 °C

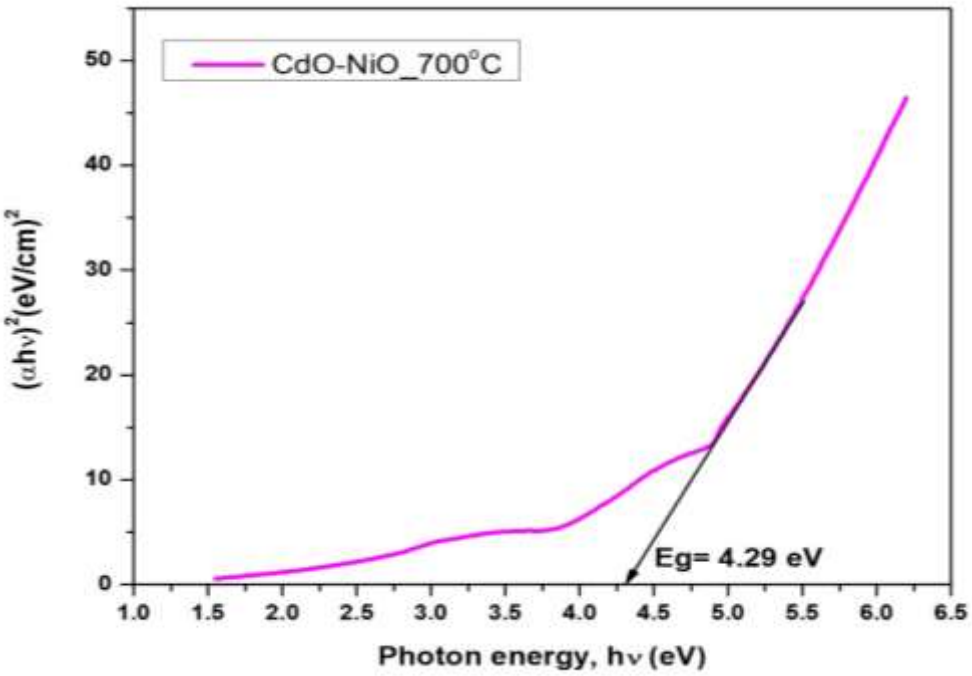

Figure 6 (d) Energy Band Gap Values of CdO-NiO Nanocomposite Thin Film at 700 °C

Conclusion

In conclusion, the temperature dependences of synthesis and characterization of CdO-NiO nanocomposites powders were firstly prepared by sol-gel reaction method at 400 ˚C, 500 ˚C, 600 ˚C and 700 ˚C respectively. Then, CdO-NiO nanocomposites thin films were be deposited onto FTO glass substrates by spin coating technique. According to XRD images, the XRD patterns of nanocomposites powders were well matched with corresponding standard library files. From the XRD results of CdO-NiO nanocomposites powder, the average crystalline sizes of CdO-NiO nanocomposites powders at 400 °C, 500 ºC, 600 ºC, and 700 ºC were 34.2118 nm, 36.3477 nm, 41.6114 nm and 48.5123 nm respectively. The crystal structures of nanocomposites powders were found to be cubic structure. When the annealing temperatures were increased, the average crystallite sizes of the CdO-NiO nanocomposites powders were also increased. From SEM analysis of CdO-NiO nanocomposite powders, some grains were large with agglomerated structures. The average grain size of the samples was 0.76 µm at 400 ºC, 0.69 µm at 500 ºC, 0.67 µm at 600 ºC and 0.55µm at 700 ºC respectively. As the results, it was concluded that the average grain sizes of the powder were decrease with increased annealing temperatures. For thin films, according to SEM results, the surface of the films became rough, but the sizes are smaller after annealing different temperatures. On the other side, the achieving relatively films cracking was increased with the decreasing temperature. According to the UV-Vis analysis results, the widest energy bandgap of CdO-NiO nanocomposites powders were 4.29 eV at 700 °C and the smallest energy bandgap was 2.69 eV at 400 °C. The intensity of absorption peak and energy band gaps increases with increasing temperatures. The experimental finding of CdO-NiO nanocomposites resulted from this research work indicated that the crystal structure, phase formation and energy band gaps were influenced by different annealing temperatures.

Acknowledgements

We would like to convey any gratitude to Dr. Khin Thant Sin, Rector, Mandalay University of Distance Education for her kind permission to perform this research. We would like to express my gratitude to Dr. Win Mar, Pro-Rector Mandalay University of Distance Education for her kind permission to perform this research. We would like to express my sincere thanks to Professor Dr. Wah Wah Thin, Head of the Department of Physics, Mandalay University of Distance Education for her kind encouragement and permission to perform this research work. We would like to thank Professor Dr Soe Soe Oo, Department of Physics, Mandalay University of Distance Education for her kind advice, encouragements and suggestions for this research.

References

Ashfari. B, et al, (2001), “single crystalline rocksalt CdO layers grown on organic molecular beam epitaxy”, Appl. Lett, vol.79, pp.470-472.

Abou-Helal MO & W.T. Seeber, (2002), Preparation of TiO_2 thin films by spray pyrolysis to be used as photocatalyst, Applied Surface Science 195,53.

Feinle, M. S. et al, (2016), ¨using, “Sol-gel synthesis of monolithic materials with hierarchical porosity,” Chemical Society Reviews, vol. 45, no. 12, pp. 3377–3399.

Liao.Y, Xu.Y, and Chan.Y., (2013),“Semiconductor nanocrystals in sol-gel derived matrices,” Physical Chemistry Chemical Physics, vol. 15, no. 33, Article ID 13704.

Merazga. A, Al-Juaid. F, Abdel-Wahab. F and Al-Amoudi. M.N, (2012), "ZnO Spin-Coating of TiO_2 photo-electrodes to enhance the efficiency of associated dye-sensitized solar cells", World J. Condensed Matter Physics. vol. 2, pp.192-196.

Niederberger.M and Pinna.N., (2009), Metal Oxide Nanoparticles in Organic Solvents: Synthesis, Formation, Assembly and Application (Engineering Materials and Processes), Springer, Berlin, Germany.

Owens. G.J, Singh. R.K, Foroutan. F et al., (2016), "Sol-gel based materials for biomedical applications," Progress in Materials Science, vol. 77, pp. 1–9.

Sule.E.E, (2013), "Photovoltaic Performance of ZnO Nanorod and ZnO: CdO Nanocomposite Layers in Dye-Sensitized Solar Cells (DSSCs)" International Journal of Photoenergy, Article ID 436831.

EFFECTS OF BUFFER LAYER ON THE SURFACE MORPHOLOGY OF ZINC TIN OXIDE (ZTO) NANOSTRUCTURE

Cho Cho Zan[1], Zin Min Tun[2] and Cho Cho Thet[3]

Abstract

The surface morphology of photoanode materials is a crucial role for the utilizing as an active layer in dye sensitized solar cell (DSSC). The formation of surface morphology of zinc-tin oxide (ZTO) nanocomposite depending on the various buffer layer were investigated in this study. ZTO on three different buffer layer such as zinc oxide (ZnO), titanium dioxide (TiO_2) and ZTO was grown by chemical bath deposition (CBD) method. The effects of growth time on the structural properties of nanocomposite were also examined by varying the growth time including 5, 10 and 15 h in the CBD process. The structural and morphological properties of the nanocomposite were confirmed by X-ray diffraction (XRD) and scanning electron microscope (SEM) results. It was found out that the different surface morphology of ZTO was obtained depending on materials of buffer layers. The increasing the growth time, the intensity of ZnO and TiO_2 peaks were also increased in ZTO film. The formation of ZTO composite seemed to be larger 15 h than 5 h and 10 h. The influence of different seed buffer layer on the growth of ZnO-TiO_2 composite structure was observed by the variation of morphologies. Nonoparticles, nanoflake and mixed nanostructure were formed for the films ZTO/ZnO, ZTO/TiO_2 and ZTO/ZTO grown by CBD method.

Keywords: chemical bath deposition (CBD), growth time, nanoflake, nanoparticles, surface morphology, ZTO film

Introduction

The buffer layer significantly influences the surface morphology of nanostructures grown by the chemical bath deposition (CBD) method. The buffer layer can act as a nucleation site for promoting uniform nucleation and growth of nanostructures. An aluminum (Al) buffer layer facilitated the formation of uniformly distributed zinc oxide (ZnO) nanoflakes by reducing the nucleation barrier (Lahewil *et al*., 2021). The type and thickness of the buffer layer can control the orientation and structure of the nanoparticles. ZnO nanowires grown on different thicknesses of ZnO seed layers show variations in their alignment and density (Azmi, Z.H *et al*., 2022). The buffer layer can improve the homogeneity of the nanoparticle surface. Proper surface preparation and choice of buffer layer material are crucial for achieving a uniform morphology (Bolshakov A D *et al*., 2019). The buffer layer can also affect the crystallinity of the nanoparticles. Studies have shown that different buffer layer materials and thicknesses can lead to variations in crystal quality and surface morphology (Bolshakov A. D *et al*., 2019). These effects are essential for tailoring the properties of nanoparticles for specific applications in electronics, optoelectronics, and energy devices.

One dimensional nanostructure such as rods, wires, and flakes are among the most promising nanostructures for the wide range of applications in electronic, optoelectronic, nanophotonic, electrochemical, and electromechanical devices due to their unique features. ZnO and TiO_2 are the most applicable materials due to their outstanding properties such as wide direct bandgap, large exciton binding energy at room temperature, and high electron mobility. Both

[1] Department of Physics, Nationalities Youth Resource Development Degree College (Yangon)
[2] Department of Physics, West Yangon University
[3] Department of Physics, University of Yangon

metal oxides possess common properties such as wide energy band gaps, nontoxic compounds, chemical stability, and inexpensive.

Recently, chemical bath deposition (CBD) method is largely used for the synthesis of nanostructures since it can provide different morphologies and different properties of the product. The types of precursor, solvent, substrate and solution process parameters such as growth time, and temperature, are important parameters in this method. Among them, type of buffer layer in CBD method is one of the most important parameters since growth of thin film on the bare substrate is inevitable. Without buffer layer, lattice mismatch between the glass or glass-coated substrate and epilayer can be increased. In this paper, ZnO, TiO_2, and ZnO-TiO_2 buffer layers on glass substrate are deposited by spin coating method. The structural and morphological properties of ZnO-TiO_2 composite nanostructure grown on different buffer layers investigated by X-ray diffraction (XRD) and scanning electron microscope (SEM) are discussed.

Experimental Details

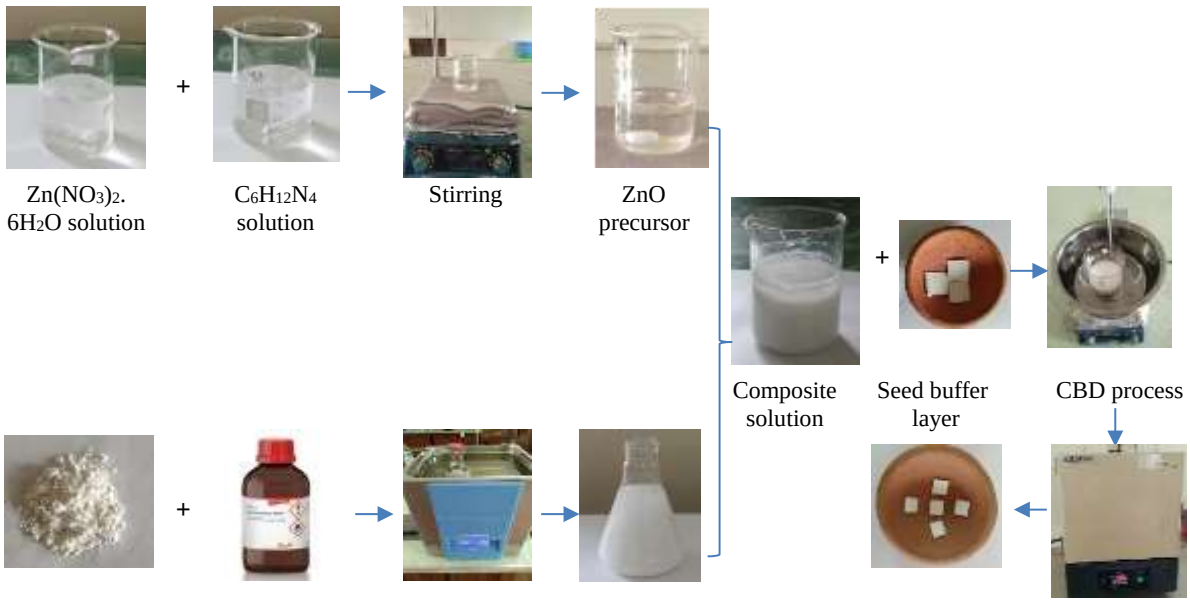

Figure 1. Synthesis photograph of ZTO composite films by CBD method

Preparation of Buffer Layer

To prepare different seed (buffer) layers, firstly glass substrates (1-inch square) were cleaned in a solution of ethanol, acetone, isopropanol, and distilled water (DW) by sonication. For ZnO and TiO_2 buffer layer, 1 g of ZnO or TiO_2 particles and 4 μL of ethanol were mixed and stirred for several days in order to form the well dissolved paste. For the preparation ZTO paste, the powders of 1 g ZnO and 1 g TiO_2 are dissolved in 8 µL of ethanol and stirred for several days. 200 µL of each paste was coated onto the glass substrates by two step-spin coating method at 3000 rpm for 30 min each. The coated ZnO, TiO_2 and ZnO-TiO_2 films were annealed at 500 ºC for 1 h. Finally, different buffer layers were successfully obtained.

Preparation of Composite Films on Buffer Layers

For the ZnO precursor solution, zinc nitrate hexahydrate, $Zn(NO_3)_2{\cdot}6H_2O$ (0.05 M) and hexamethylenetetramine (HMTA, $C_6H_{12}N_4$) (0.05 M) precursors were separately prepared at the

same concentration. These two precursors were mixed at a ratio of 1:1 volume ratio and stirred for 1 h in order to form homogeneous ZnO precursor. For the preparation of TiO_2 nanofluid, 1 g of TiO_2 powder was dissolved in 70 mL of ethanol and sonicated for 4 h in order to mix the homogeneous solution. For the composite solution, 1:1 volume ratio ZnO precursor and TiO_2 nanofluid were mixed together and they were stirrer for 1 h.

Preparation of ZTO Films by Chemical Bath Deposition (CBD) Method

For CBD growth, each buffer layers prepared by previous step was put vertically inside the composite solution and placed into the oil bath at a fixed temperature 90 ºC and grown for 5, 10 and 15 h, respectively. After the growing, the composite films were rinsed in DI water in order to remove any contamination. After that, the films were dried at room temperature. Finally, the ZTO composite films were annealed at 500 ºC for 1 h. Finally, three types of films such as ZTO/ZnO, TiO_2/ZnO and ZTO/ZTO were successfully received. Synthesis photograph for the preparation ZnO-TiO_2 composite films is displayed in Figure 1.

Results and Discussion

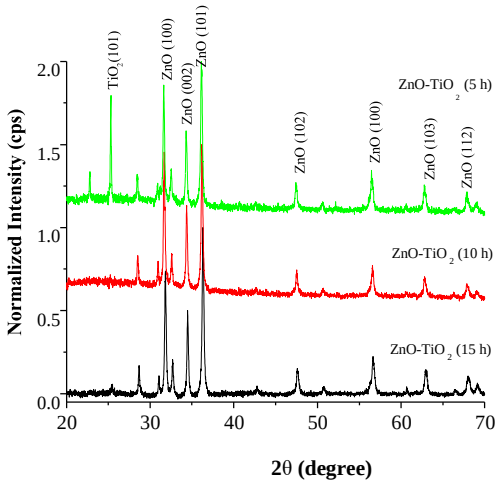

Figure 1 XRD spectrum of ZTO/ZnO film at different CBD growth time

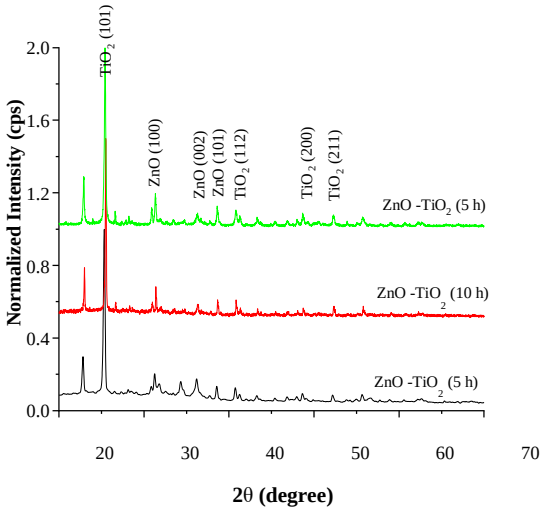

Figure 2 XRD spectrum of ZTO/TiO_2 film at different CBD growth time

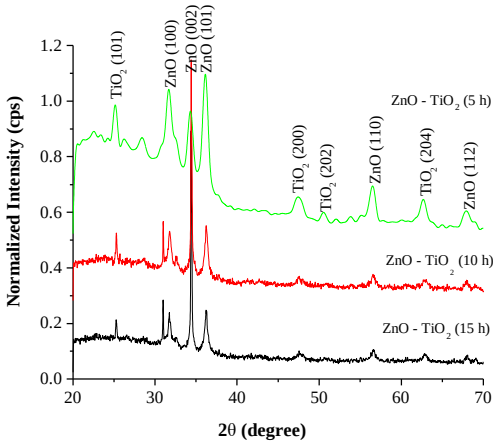

Figure 3 XRD spectrum of ZTO/ZTO film at different CBD growth time

XRD measurement was performed in order to identify the target materials. The diffraction angle 2θ degree at 31.6˚, 34.3˚, 36.2˚, 47.4˚, 56.4˚, 62.7˚, 66.1˚, 67.7˚& 68.8˚ are attributed to (100), (002), (101), (102), (110), (103), (200), (112) & (201) planes of the hexagonal crystalline structure (DB card number 9004180). The diffraction angle 2θ degree at 25.2˚, 36.9˚, 37.9˚, 38.6˚, 47.6˚, 53.9˚, 55.1˚62.1˚, 62.7˚& 68.7˚of the reflection (101), (103), (004), (112), (200), (105), (211), (213), (204) & (116) planes (DB card number 9008216) are anatase TiO_2. The amalgamation of anatase TiO_2 and hexagonal wurtzite ZnO in the mixed oxide system were also observed in all XRD spectra.

XRD spectra of ZTO films grown on ZnO, TiO_2 and ZnO-TiO_2 buffer layers at different growth times are shown in Figure 2, 3 and 4. In Figure 2, three most intensity peaks from (100), (002) and (101) were the characteristic peaks of ZnO. In addition, only TiO_2 peak from (100) is observed for 5 h growth time. When the growth time was increased to 10 h and 15 h, the peak from all ZnO peaks were also drastically increased and TiO_2 peaks was relatively decreased. Two ZTO peaks were observed.

In Figure 4, all ZnO peaks from (100), (002) and (101) were drastically decreased. In addition, only TiO_2 peak from (100) is observed for 5 h growth time. When the growth time was increased to 10 h and 15 h, the peak from all ZnO peaks were also drastically increased and TiO_2 peaks was relatively increased. Again, for the ZTO composite film on ZTO buffer layer, the intensity of ZnO peaks were higher than that of TiO_2. However, the intensity of all single peak of ZnO and TiO_2 peaks were smaller than those in ZTO/ZnO and ZTO/TiO_2 films. Six ZTO peaks were occurred for the growth time 10 and 15 h.

The SEM analysis is carried out in order to observe the surface morphology of each film depending on the various growth time. The SEM images of ZTO/ZnO films are exhibited in Figure 5. Only particles were observed. The particle size was bigger when the growth hour was increased. In Figure 6, only the flake structure was formed for the ZTO/TiO_2 films. Similarly, the flakes were bigger while increasing the growth time. When the composite films were deposited on ZTO buffer film, mixed morphology comprising of both ZnO particles and TiO_2 flake was observed. The more increasing the growth time, the more particles were formed since the ZnO peak became more prominent and TiO_2 flake were the less.

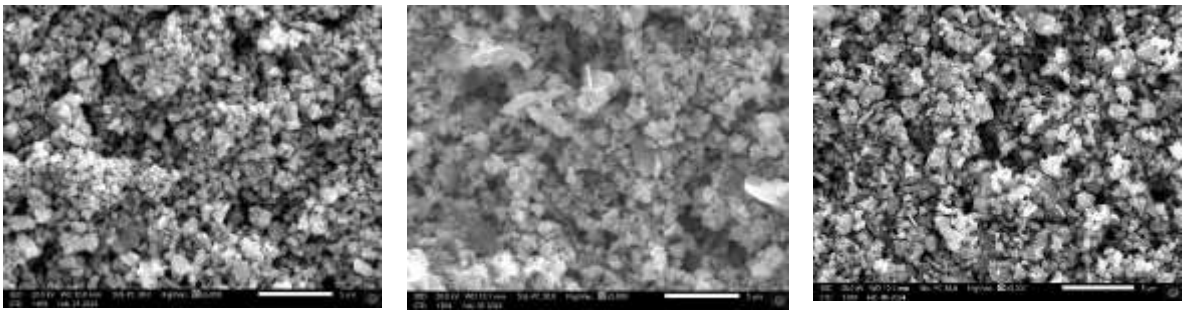

(a) (b) (c)

Figure 5 SEM images of ZTO film onto the ZnO buffer layer at the CBD growth time (a) 5 (b) 10 and 15 h

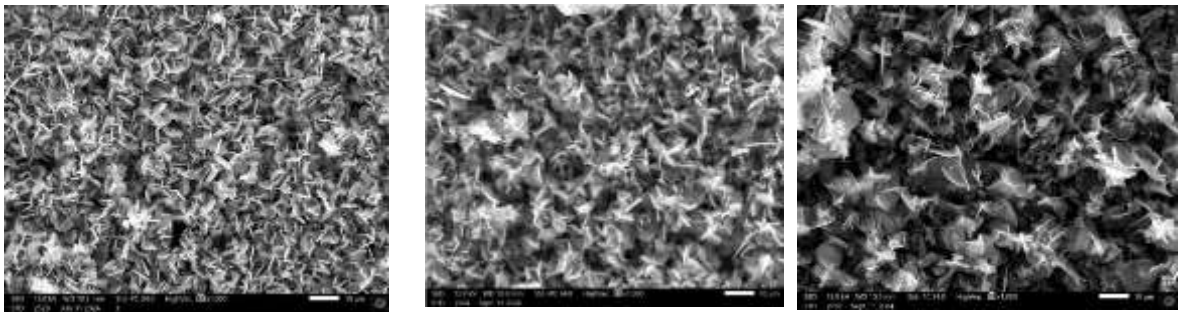

(a) (b) (c)

Figure 7 SEM images of ZTO film onto the TiO_2 buffer layer at the CBD growth time (a) 5 (b) 10 and 15 h

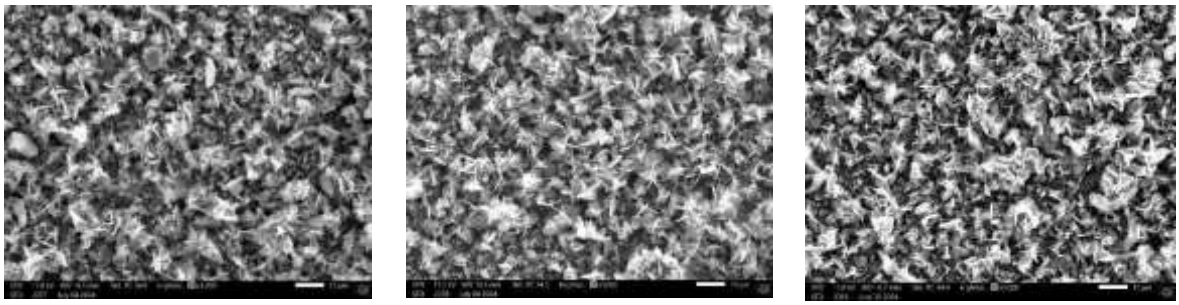

(a) (b) (c)

Figure 6 SEM images of ZTO film onto the ZTO buffer layer at the CBD growth time (a) 5 (b) 10 and 15 h

Among the structures, nanoflakes have two-dimensional (2D) and nanoparticles have one-dimensional (1D) nanostructures. Both structures have larger surface area which facilitates more efficient electron pathways and reduces recombination losses. Although both nanostructures can enhance efficiency of dye sensitized solar cell (DSSC), nanoflakes may offer better electron transport and light absorption properties. This may potentially lead to higher efficiencies of DSSC. However, the choice between nanoparticles and nanoflakes should be based on the specific requirements and design of the DSSC.

Conclusions

The surface morphologies of ZnO-TiO_2 (ZTO) composite films depending on different buffer layers grown by chemical bath deposition (CBD) method were discussed. The films grown on ZnO buffer resulted the particles. On the other hand, the flakes structure was attained when the films grown on TiO_2 buffer layer. Mixed morphology of both particles and flakes were acquired for the ZTO buffer layer. These different morphologies of the films were reflected from particular buffer layer used in CBD growth. Therefore, it can be concluded that types of materials for buffer layer are essential parameters for the formation of epilayers like particles, flakes and mixing of both particles and flakes in CBD method. Since nanoflakes can scatter light more effectively within the solar cell, higher photocurrent and better overall efficiency can be available for the ZnO-TiO_2/TiO_2 film. Therefore, this work can be applied as a photoanode materials in DCCS.

Acknowledgements

We would like to acknowledge to U Htain Linn, Rector, Nationalities Youth Resource Development Degree College (Yangon), for his encouragement and allowing us to participate in this event. Our special thanks go to Dr Yin Maung Maung, Professor and Head of Department of Physics, for his kind permission to contribute this work and excellent discussion.

References

Azmi, Z.H, et al. (2022), 'Layer on the Growth of Zinc Oxide Nanowires by Chemical Bath Deposition Method. Effect of Seed' Coatings 2022, 12, 474. https://doi.org/10.3390/ coatings12040474.

Alamdari et al. (2020) "Applsci-10-03620.Pdf," Appl. Sci., vol. 10, no. 3620, pp. 1–19, [Online]. Available: doi:10.3390/app10103620

Bolshakov A. D, et al. (2021) 'Effects of the surface preparation and buffer layer on the morphology, electronic and optical properties of the GaN nanowires on Si', *Nanotechnology* 30 395602, DOI 10.1088/ 13616528/ab2c0c.

Hamedani, N.F. and Farzaneh, F. (2006) "Synthesis of ZnONano crystals with Hexagonal (Wurtzite) Structure in Water Using Microwave Irradiation, Iran, J. Sci. Islam. Repub. vol. 17, no. 3, p. 231234.

Kalpana, V. N.et al (2018) "Biosynthesis of zinc oxide nanoparticles using culture filtrates of Aspergillus niger: Antimicrobial textiles and dye degradation studies," Open Nano, vol. 3, pp. 48–55, doi: 10.1016/j.onano.2018.06.001.

Kurapati, S. and Srivastava, P. K. (2018) "Application of Debye-Scherrer Formula in The Determination of Silver Nona Particles Shape," Int. J. Manag. Technol. Eng., vol. 8, no. XII, pp. 81–84.

Kalpana, V. N. et al. (2018) "Biosynthesis of zinc oxide nanoparticles using culture filtrates of Aspergillus niger: Antimicrobial textiles and dye degradation studies," OpenNano, vol. 3, pp. 48–55, doi: 10.1016/j.onano.2018.06.001.

Lahewil, A.S.Z., Ahmed, N.M. & Azman, N.Z.N. Structural and optical properties of ZnO nanoflakes/Al/glass via laser-assisted chemical bath deposition (LACBD) technique. *Appl. Phys. A* 127, 836 (2021). https://doi.org/10.1007/s00339-021-04996-7.

Lawrence Munguti, et al. (2021), "Effects of Zn:Ti molar ratios on the morphological, optical and photocatalytic properties of ZnO-TiO_2 nanocomposites for application in dye removal, Materials Science in Semiconductor Processing 128 (2021) 105786.

Raja, K. et al. (2014) "Synthesis, structural and optical properties of ZnO and Ni-doped ZnO hexagonal nanorods by Co-precipitation method," Spectrochim. Acta - Part A Mol. Biomol. Spectrosc., vol. 120, pp. 19–24, doi: 10.1016/j.saa.2013.09.103.

Sajiv, K.S. et al. (2021) 'Integrated photo-absorption and improved charge transport kinetics in atomically thin $MoSe_2$-incorporated nanostructured ZnO photo-anodes for dye-sensitized solar cells'. *Appl. Phys. A* 127, 966 (2021). https://doi.org/10.1007/s00339-021-05127-y.

Shuwei Hao, et al. (2024), 'Enhancing dye-sensitized solar cell efficiency through broadband near-infrared upconverting nanoparticles', *Nanoscale*, Advance Article. https://doi.org/10.1039/D4NR03962A.

Talam, S. et al. (2012) "Synthesis, Characterization, and Spectroscopic Properties ZnO Nanoparticles," ISRN Nanotechnol., vol. 2012, pp. 1–6, doi: 10.5402/2012/372505.

Vidya, Y. S. et al. (2023). "2-Deoxy-D-glucose functionalized zinc oxide nanodrug for kidney cancer treatment," Devices, J. Sci. Adv. Mater. vol. 8, no. 3, p. 100587, doi: 10.1016/j.jsamd.2023.100587.

MODELLING AND CONSTRUCTION OF SMART SOLAR EV CAR

May Myat Noe Ko Ko[1], Kyaw Kyaw[2]

Abstract

Android mobile phone plays a vital role in everyday life. This research work is planned to model and construct smart solar EV car that runs with solar energy, which helps reduce pollution and reliance on fossil fuels, making transportation cleaner and more sustainable. The constructed car has the following features, such as solar panel on its roof that convert sunlight into electricity, and storing it in a lithium battery. It includes navigation tools for monitoring energy usages in real-time. The main components used in this research work are Arduino Uno, Bluetooth (HC-06), ultrasonic sensor (HC-SRO4), Infrared obstacle avoidance sensor (KY023), solar PV, lithium batteries, L298 motors Driver, 2 DC and servo motor. The performance of the smart solar car could be control with mobile phone and it makes an eco-friendly vehicle that relies on renewable energy. This system accepts to response its movement control through the Bluetooth protocol which is used latest technologies version likes as IOT (internet of things), WiFi and others.

Keywords: Solar PV, Lithium Battery, DC motor, Ultrasonic sensor, KY-023 sensor, Android.

Introduction

The Arduino Uno development board is used to interface Bluetooth module for controlling the car. The car has two main functions. They are obstacle avoidance function and wireless control function. To detect obstacles, it used Ultrasonic and KY-023 IR sensors. A mobile phone is used to wirelessly control the car, sending commands for it to go forward, backward, left, right, and stop. The ultrasonic sensors help the car to avoid obstacles and make decisions. To enable wireless communication, Bluetooth and Wi-Fi technology are typically used. In this solar car, a Bluetooth module is used. The hardware includes a controller with a Bluetooth module connected to the solar car motors and other components. When the Android application is activated and connected to the system via Bluetooth, the car can be controlled by sending wireless commands from the mobile phone using pre-programmed functions. The vehicle can move in all four directions: left, right, forward, backward, and stop. The vehicle can also switch between automatic and manual modes. When moving forward, both motors travel in the same direction, while for reverse movement, the motors move in opposite directions. For left and right movements, either of the two motors rotate in each direction.

The Solar Renewable Energy

Humans have been using solar energy since the beginning of the century. Renewable energy comes from sustainable sources like solar energy, wind energy, bioenergy, and geo-energy. Solar energy is particularly popular because it's environmentally friendly. Solar panels made up of interconnected solar cells, capture and convert solar energy into usable electrical energy through the photovoltaic (PV) effect. These panels can be connected in series to increase the output voltage, and the energy can be stored in a lithium battery. Different types of photovoltaic panels, including monocrystalline silicon, polycrystalline silicon, and thin-film panels, are used in various applications such as solar lighting, residential units, telecommunication stations, calculators, clocks, radios, and photovoltaic power plants.

[1] Department of Physics, University of Mandalay.

[2] Department of Physics, University of Mandalay.

Components of the Obstacle Avoidance of Smart Solar EV Car

IR Sensor (KY-023) Module

The IR sensor (KY-023) module consists of an infrared LED (transmitter) and a photodiode (receiver). The LED emits an infrared pulse, and if there is an obstacle in the path of radiation, the pulse is reflected and hits the photodiode. This sensor detects obstacles by changing the sensitivity (detection range) by adjusting the brightness of the LED and the threshold of the photodiode. The left (contact side) trimmer adjusts the obstacle sensing distance. The right trimming resistor adjusts the frequency of the emitted IR pulse. Figure 1 shows the infrared obstacle avoidance sensor (KY -023) module. The technical parameters of IR sensor (KY-023) module is listed in Table 1.

Table 1. Technical parameters

Operating voltage	3.3V-5V
Operating current	≥ 20mA
Operating temperature	-10℃ -50℃
Detection distance	2 cm ~ 40cm
IR Pulse Rate	38 kHz
Effective angle	35°

Figure 1. Infrared obstacle avoidance sensor (KY-023) module.

Ultrasonic HC-SRO4 Sensor Module

The HC-SRO4 module determines the distance to the object by sending an ultrasonic pulse and receiving a delayed reflection. Based on this delay, the device determines the presence of objects and the distance to them. The ultrasonic emitter sends 8 signals at the frequency of 40 kHz, which will be reflected by objects and recorded with a microphone in this sensor module. It can measure from 3 cm to 350 cm with an accuracy of 2 mm. It is an ideal ultrasonic module for distance measurement, proximity sensors and ultrasonic detector. The technical parameters of HC-SRO4 module is given in Table 2.

Table 2. Technical parameters

Supply voltage	5V
Current operating parameter	15mA
Passive current	<2mA
Viewing angle	15°
Touch Resolution	3mm
Angle of measurement	30°

Servo Motor

These are electronic motors that turn a shaft a certain number of degrees in response to control impulse. The step of the angle of rotation depends on the type of servomotor. A simple servo motor like the SG-90 can be powered from the Arduino's 5V power output pin. The servo control pin can be connected to any digital pin on the Arduino board. Usually a servomotor turns 90° in either direction. i.e maximum movement can be 180°. It cannot rotate any further due to a built-in mechanical stop. The servo has three wires.

- Red – connected to the 5V pin or directly to the power supply;
- Brown or black –ground;
- Yellow or white –the signal is connected to any Arduino digital output.

A servo motor is controlled by sending a pulse width modulated (PWM) signal through the control wire. A pulse is sent every 20 milliseconds. Width of the pulses determine the position of the shaft. For example, a pulse of 1 ms move the shaft anticlockwise at -90°, a pulse of 1.5 ms will move the shaft at the neutral positon that 0° and a pulse of 2 ms will move the shaft clockwise at +90°.

Construction and Operation of Smart Solar EV car

The Arduino control system consists of both hardware and software components. The hardware includes the Motor driver IC (L298N), Servo motor (Tower Pro SG90), two Geared Motors, a Robot Car Chassis, and a Lithium battery. The software consists of the Bluetooth module and Android mobile phone. The main body of the car is made up of a chassis, wheels, and two DC motors. Additionally, two DC motors are used for the four wheels that drive the car. Sensors play a crucial role in electronics, particularly in robotics and automation. There are various types of sensors such as fire sensors, humidity sensors, motion sensors, temperature sensors, and Ultrasonic sensors. Ultrasonic sensors in solar cars are used to detect surroundings, avoid obstacles, and navigate towards a target area. A wheeled cart with an Ultrasonic sensor is used to detect large obstacles and measure the distance between the solar vehicle and the obstacle. Mobile control vehicles can move through the environment. Arduino can be connected to various devices used by users. Bluetooth enables short-range wireless data communication between two microcontroller systems. In this setup, it is paired with a master Bluetooth device such as a PC or Mobile Phone, making its operation transparent to the user. All data received through the serial input is immediately transmitted wirelessly. A car equipped with Bluetooth can move and rotate freely without using the Servo Motor and Ultrasonic sensor. The Ultrasonic sensor emits ultrasonic pulses and receives reflections to detect objects in its path. However, Ultrasonic sensors may not work well with small targets against large backgrounds. An ultrasonic sensor measures the distance to an object using sound waves, while a servo motor is designed for precise control of angular or linear position, velocity, and acceleration. The Motor

driver IC (L298N) is a dual full-bridge motor driver module used for DC motors in the solar car. It is used to control the direction of two DC motors and contains a dual-channel H-Bridge motor driver IC. There are two methods to control the speed and direction of the DC motor: PWM for speed control and H-Bridge for rotation control, with the direction rule method being used in this work. This module also includes a 78M05 5V regulator. The L298N Module can control up to 4 DC motors, 2 with directional and speed control. Solar vehicles require the solar energy for operation. Therefore, a 12V lithium battery is used to power and connect with Arduino. When the lithium battery is not charged, external (non-USB) power can come from an AC to DC adapter or a lithium battery. The flowchart and block diagram of smart solar EV cars are shown in Figures 2 and 3.

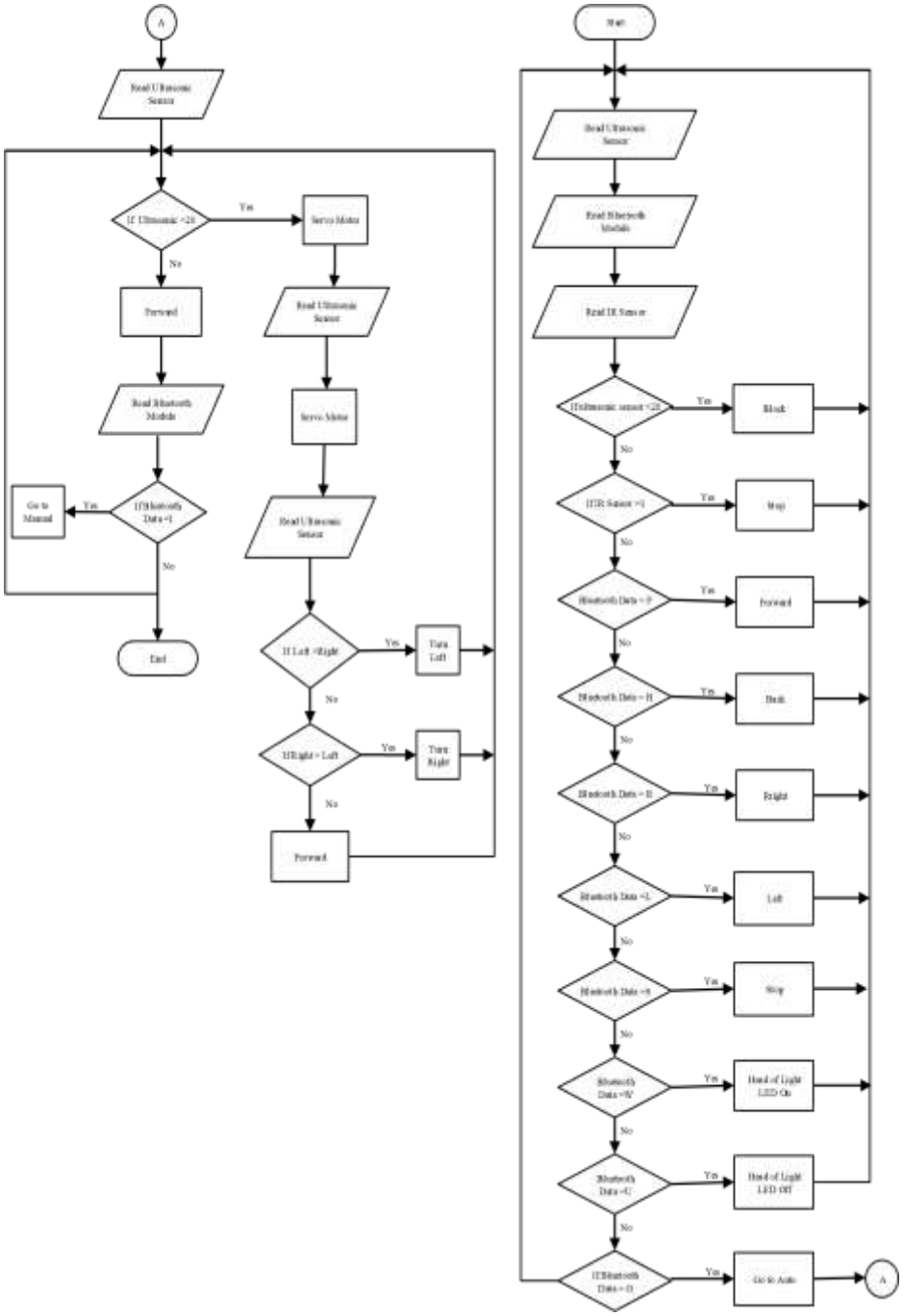

Figure 2. Flowchart of construction of smart solar EV car.

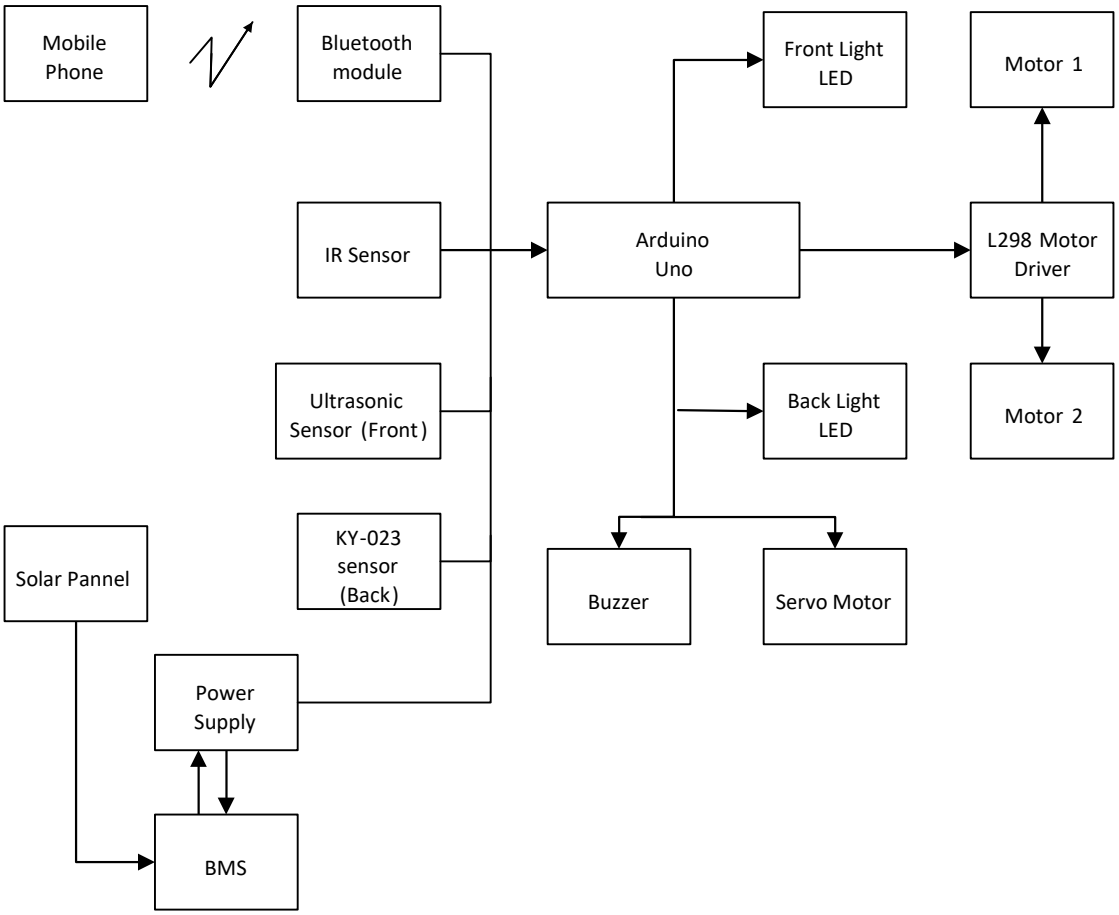

Figure 3. The complete diagram of Block Diagram for smart solar EV car.

The main control system utilizes Arduino and Bluetooth for easy data connection. The Arduino Uno board features 14 available digital I/O pins and 6 analog input pins. In this construction, 12 of these pins are used for building an obstacle-avoidance solar vehicle.

An important aspect of this study is the ability to detect obstacles using an ultrasonic sensor, which has four pins: VCC, Trig, Echo, and GND. Additionally, the KY-023 sensor module, which also has four pins (VCC, GND, EN, and OUT), is connected. The VCC and GND pins of the KY-023 are linked to the VCC of the lithium battery and the GND pin of the Uno, respectively. The button pin connects to pin 11 of the Uno, the Trigger pin connects to pin 7, and the Echo pin connects to pin 6. The Dual Full-Bridge Driver IC operates with two enable input pins and four output pins connected to the DC motor. Pins 2, 3, 4, and 5 are linked to the motor driver.

An Android application can also be utilized in this work. The RX and TX pins in the Bluetooth module connect to pins 9 and 10 on the Uno. Furthermore, pins 12 and 13 on the Uno are connected to the Forward LED and Backward LED, respectively, with the cathode of the LEDs connected to GND. The cathode of the buzzer is also connected to GND, while the anode is connected to VCC. The circuit model was designed using Proteus EDA schematic designer software, as shown in Figure 4.

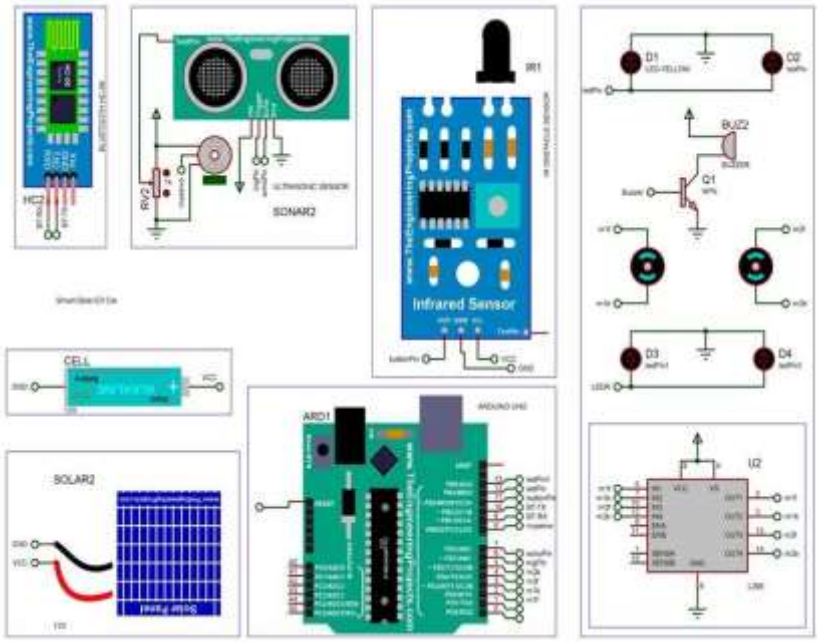

Figure 4. The complete circuit for smart solar EV car.

Results and Discussion

In this study, the Bluetooth Controller program was utilized to control a smart solar EV car using an Android phone. The program must first be installed on the phone. After the Android application is installed, the smart solar EV car can be controlled in four directions. Clicking the "UP ARROW" icon transmits the data "F" to the car to move forward. Pressing the "DOWN ARROW" icon sends the Bluetooth data "B" to the linked Bluetooth Module, causing the car to move backward. Pressing the "LEFT ARROW" icon transmits the data "L" to the linked Bluetooth Module, making the car turn left. Similarly, pressing the "RIGHT ARROW" icon sends the data "R" to the linked Bluetooth Module, causing the car to turn right. Pressing the "HEAD OF LIGHT LED" icon sends the data "W" to the linked Bluetooth Module, turning the car's LED lights on. Pressing the "HEAD OF LIGHT LED" icon again transmits the data "U" to the linked Bluetooth Module, turning the car's LED lights off. Pressing the "FORWARD LEFT" icon sends the data "G" to the linked Bluetooth Module, putting the car into "Auto Mode." Pressing the "FORWARD RIGHT" icon transmits the data "I" to the linked Bluetooth Module, switching the car to "Manual Mode". An Arduino-based Bluetooth module was constructed for the smart solar EV car. It can help overcome obstacles such as animals and other obstructions using an Ultrasonic sensor.

Figure 5. Android mobile application

An android application was developed for controlling the movement of the solar EV car. It has seven icons which perform a different set of operations. The seven keys, placed as shown in the figure of the application, are for the movement in the four directions namely forward, backward, left, and right and the fifth icon is for forward led and the sixth icon is for back led, and the seventh icon is for horn for smart solar EV car. The photograph of Android Mobile Application is described in Figure 5.

Step 1. Turn on the power supply of the circuit.

Step 2. Turn on the Bluetooth module from the phone screen.

Step 3. Open Android Application in the mobile Phone. Select the Bluetooth RC controller.

The Android Application showed in Figure 6 (a) controlled the solar vehicle, and the operation modes of solar vehicle in Figure 6 (b) in day time, or in Figure 6 (c) at night time.

Figure 6. Operation mode of obstacle avoiding of solar car

Conclusion

The smart solar EV car was designed to be controlled and modified using an Android phone. The solar panel can be utilized anywhere in the world as long as there is solar energy available. This solar energy is used to power the car, with stored electricity from the lithium battery being used at night or on cloudy days. By using renewable energy, the car does not rely on fuel, reducing carbon dioxide emissions and promoting technical development. However, in a cloudy or shaded environment, the solar car may not work at full capacity, as it requires sunlight to operate properly.

Acknowledgments

This research work was totally implemented in Electronics lab, Department of Physics, University of Mandalay.

References

Ananya A., Ashritha S. C., (2021) "Bluetooth Based Obstacle Avoiding Robot'' *International Advanced Research Journal in Science, Engineering and Technology*, Vol.8, Issue7 July.

Abhinya .C, Kirti K, Parul K, Navani J.P, (2015) "Solar Powered Vehicle" *International Journal of Electronics Research,* Vol.3, Issue 2, pp: (270-273).

Anas. E, (2019) "Arduino Bluetooth module HC-05 and HC-06", November 9.

Bijay. P, Bhoop. S, (2021) "A Review on Solar Powered Electric Vehicle", *International Journal of Recent Technology and Engineering, (IJIRT),* Vol 8, Issue 4.

Deepashir. K. M, Sachidanand P B, Latha. H.S, (2018) "Industrial Appliances Control Using Android Mobile and Bluetooth Technology" *International Journal of Engineering and Manufacturing Science*, Vol8, number 1, pp.32-42.

Deepalaxmi R, Arthi R, Malini E, Raghul M (2021) "Arduino based automatic Vehicle Control" International Journal of Scientific Research and Management (IJSRM), Vol.9, Issue-03.

Subashka R, Tarun K, Sakshi S, Aastha S, (2018) "Solar Powered Obstacle Avoiding Robot" *International Journal of Emerging Technologies in Engineering Research (IJETER)*, Vol 6, Issue 4, April.

Thamizh T, Geetha A, Usha S, Ayush. S, Varoon K, Kotikalapudi K.V, (2019) "Modelling and Emulation of Solar Powered Vehicle, (IJRTE)" *International Journal of Recent Technology and Engineering)*, Vol.7, Issue-5S2, January.

Taksade. A, Madape S, Chadakhed A, Fullare M, Bais.Y, (2024) "Robot Solar Car Based On Arduino with Bluetooth" International Journal of Research Publication and Reviews, Vol 5, no 3, pp: 52205225.

Ganeshbabu M, Gayathri P, (2022) "Automatic Solar Tracking System Using Arduino with Buck-Boost

Converter" International Research Journal of Modernization in Engineering Technology and Sciece, Vol-04, Issue-08, August.

Yan. Z, Qing. Y, and Yan Zhong. Z, (2016) "Research on Modeling and Power Algorithm of Photovoltaic Cells for Solar Cars" *Journal of Physics,* 2068 ,012024.

SYNTHESIS AND CHARACTERIZATION OF HYDROXYAPATITE EXTRACTED FROM THREE TYPES OF EGGSHELLS BY PRECIPITATION METHOD

Thi Thi Aye[1], Nyo Nyo Myint[2], Thein Aye[3], San San Thwin[4]

Abstract

In this research, hydroxyapatite (HAp) was synthesized from three types' eggshells (hen eggshells, quail eggshells, and duck eggshells) by using method of precipitation. Eggshells are a rich source of calcium carbonate, which corresponds to about 94% of the shell. Calcium carbonate ($CaCO_3$) from eggshells and orthophosphoric acid (H_3PO_4) were used as precursor to produce hydroxyapatite (HAp). The major constituent calcium carbonate ($CaCO_3$) three types' eggshells powder were heated temperature at 1000°C for 3h to obtain calcium oxide (CaO). The crystal structures, elemental concentrations of HAp powder were analyzed by X-ray diffraction (XRD), and energy dispersive X-ray fluorescence (EDXRF) techniques. And then, crystal structures, crystallite sizes of HAp powder were calculated from XRD data results. The ratio values of the calcium (Ca) to phosphorous (P) were calculated from the EDXRF results. Finally, the analysis of HAp was discussed from the calculation of all above result data. The hydroxyapatite product from waste eggshells (hen eggshells, quail eggshells, and duck eggshells) can reduce environmental pollutions. Therefore, the HAp powder was prepared in this study. The obtained hydroxyapatite powder has great potential in biomedical applications.

Keywords – hydroxyapatite, hen eggshells, quail eggshells, duck eggshells, precipitation method, XRD, EDXRF

Introduction

Over the past 30-40 years, one of the most significant developments in orthopaedics has been the use of bioceramic material for bone replacement, reconstruction and repair. Bioceramics are biocompatible ceramic materials, and commonly include bioglass, calcium phosphates (such as hydroxyapatite (HAp), β-tricalcium phosphate (β-TCP)), and biphasic calcium phosphate. Calcium phosphate ceramics has great importance in the field of tissue engineering for the biological applications [1]. One of the most common apatite used as bioceramic in medicine and dentistry is hydroxyapatite (HAp) due to its bioactivity and osteoconductive properties [2]. HAp implants have been used clinically in the form of powders, granules, cements, dense and porous blocks, biphasics, coatings, and as various composites [3]. The advantage of using HAp as a bioceramic or biomaterial compared to other bioceramics, such as Bioglass or A-W glass-ceramic, is its chemical similarity to the inorganic component of bone and tooth. Presently hydroxyapatite has received much more interest as an implant material with applications in dentistry and orthopedics [4]. Hydroxyapatite (HAp) is a main component of bone mineral but in some cases carbonate-apatite is a main hard tissue component, as in dental enamel [5]. Other applications of HAP include femoral plugs in total hip replacement and HAP coating on metal components for cementless fixation [6]. Hydroxyapatite, a naturally occurring form of calcium phosphate, is the main mineral component of bones and teeth. Chemically hydroxyapatite is $Ca_5(PO_4)_3OH$ but often written as $Ca_{10}(PO_4)_6(OH)_2$ [7]. Natural hydroxyapatite is usually extracted from biological sources or wastes such as mammalian bone (e.g. bovine, camel, and

[1] Department of Physics, Yenanchaung University
[2] Department of Physics, Yenanchaung University
[3] Department of Physics, Yenanchaung University
[4] Department of Physics, Yenanchaung University

horse), marine or aquatic sources (e.g. fish bone and fish scale), shell sources (e.g. cockle, clam, eggshell, and seashell), plants and algae and also from mineral sources (e.g. limestone) [8]. There are numerous methods have been reported for the preparation of hydroxyapatite from eggshell such as solid state reaction, hydrothermal reaction, co-precipitation reaction, sol-gel synthesis, mechano-chemical synthesis etc [9]. One of them is the sol-gel precipitation method. A simple sol-gel precipitation method can be used to prepare Nano hydroxyapatite from eggshells [10]. The main objectives of this study are to synthesis the natural HAp from shell sources (hen eggshell, duck eggshells, and quail eggshells) using precipitation method.

Materials and Methods

Materials

In this research, calcium oxide (CaO) extracted from hen eggshells, quail eggshells and duck eggshells. Hen eggshells, quail eggshells and duck eggshells were collected from Yenanchaung area in Magway Division. The needed phosphate was extracted from orthosphoric acid (H_3PO_4). Phosphoric acid, distilled water as a solvent, ammonium hydroxide (NH_4OH) as pH controller and filter paper were purchased from Academy Chemical Shop, Babetan Township in Yangon.

Preparation of three types' eggshells (hen eggshells, quail eggshells, and duck eggshells) powder

In this research, hen eggshells, quail eggshells and duck eggshells were used as a starting material for calcium oxide (CaO). Hen eggshells, quail eggshells and duck eggs were collected form Yenanchaung area in the Magway Division. In physics department laboratory at Yenanchaung University, hen eggshells, quail eggshells and duck eggs were washed with distilled water to clean. Firstly, the cleaned hen eggshells were cooked with distilled water until temperature at 100℃ has been reached for 30 minutes. When temperature at 100℃ has been reached, hen eggshells pot was put a few minute to cool. A few minute later, the shell membranes were removed from hen eggshells. Hen eggshells are cleaned with distilled water. The cleaned hen eggshells were obtained. The obtained hen eggshells were crushed with the use of laboratory motor and pestle. The hen eggshell powder was obtained. The major constituent calcium carbonate ($CaCO_3$) hen eggshell powder was heated in Protherm furnace (physics department laboratory in Yenanchaung University) at 1000 °C temperature for 3 hour to obtain calcium oxide (CaO). Finally, white calcium oxide (CaO) hen eggshell powder was obtained.

Precipitation Synthesis

Hydroxyapatite powder is extracted from hen eggshells, quail eggshells, and duck eggshell were synthesized by precipitation method. The precipitation method is simplicity of the process and cost effectiveness. The principle of this method is the reaction between calcium hydroxide and phosphoric acid with a molar ratio of Ca/P= 1.67. The calcined (CaO) powder of heneggshells, quail eggshells, and duck eggshells were mixed with distilled water to form a 1.67M $Ca(OH)_2$ solution. H_3PO_4 solution with concentration 1 M were added to these 1.67M $Ca(OH)_2$ solution by drop wise through a burette and stirred. The pH of the mixtures were measured by using pH papers; if the pH was less than 9 then the NH_4OH should be added by drop wise. The mixtures were stirred for 2hr and heated at 60°C and then filtered with filter papers. After that the mixtures were allowed to precipitation at room temperature for 24 hours. The aging solution is filtered and the precipitate is washed with distilled water. The filtration

result was dried in a furnace at 100℃. After the drying process was completed, the obtained results were heated at 900 °C for 3 hours. Finally, white powder was obtained. The procedure of hydroxyapatite powder from hen eggshells, quail eggshells, and duck eggshells by precipitation method are shown in Figures 1, 2, and 3. The flow chart of sample preparation is shown in figure 4.

Sample Powder Characterization

The obtained powder after the precipitation method were analyzed by X-ray Diffraction (XRD), and Energy Dispersive X-ray fluorescence (EDXRF) techniques. X-ray Diffraction (XRD) to identify crystal structure, crystalline size and lattice constants. Energy Dispersive X-ray fluorescence (EDXRF) technique was used to analyze the elemental concentrations of the hydroxyapatite (HAp) powder and the ratio of the value of calcium (Ca) to phosphorous (P).

Figure 1. The sample preparation of hydroxyapatite powder from hen eggshells by precipitation method

Figure 2. The sample preparation of hydroxyapatite powder from quail eggshells by precipitation method

Figure 3. The sample preparation of hydroxyapatite powder from duck eggshells by precipitation method

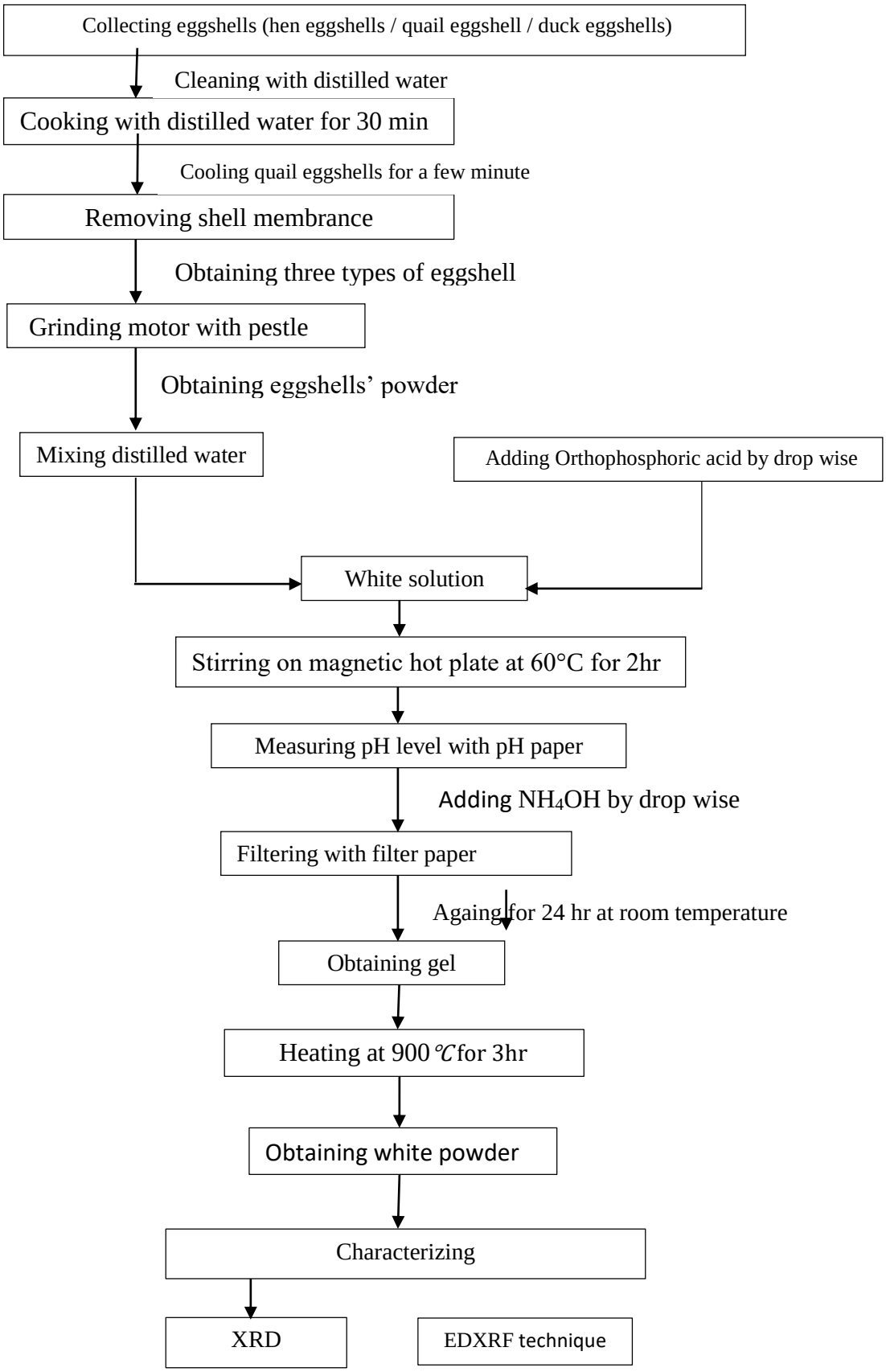

Figure 4. The flow chart of the HAp sample preparation from hen eggshells, quail shells, and duck eggshells

Results and Discussions

Characterization of HAp powder from hen eggshells, quail eggshells, and duck eggshells by (X-ray Diffraction XRD analysis)

XRD analysis is used to confirm crystal structures, crystalline sizes and lattice constants of the HAp powder from three type eggshells after the precipitation method. The powder of XRD data results similar to the HAp pattern (IJDD 00-001-1008) with a chemical reaction equal to Ca_{10} $(PO_4)_6(OH)_2$ were found. The XRD patterns of the HAp powder of hen eggshells, quail eggshells, and duck eggshells at 900℃ for 3hr are depicted in Figure 5.

The lattice constant values of hen eggshells, quail eggshells and duck eggshells are a = 10.37030 (Å), b = 10.37030 (Å), c = 37.08500 (Å), alpha (α) = 90°, beta (β) = 90°, gamma (γ) = 120°, a = 9.41800(Å), b = 9.41800(Å), c = 6.88400(Å), alpha (α) = 90, beta (β) = 90°, gamma (γ) = 120°, a = 10.43800, b= 10.43800, c = 37.15000, alpha (α) = 90°, beta (β) = 90°, gamma (γ) = 120°. So, the crystal structure of hydroxyapatite powder from hen eggshells, quail eggshells and duck eggshells were hexagonal structure (a=b≠c, α= β≠γ). The crystallite sizes for three strongest peaks of HAp powder from hen eggshells, quail eggshells, and duck eggshells were estimated by the Scherrer's equation (1). The average crystalline size of hen eggshells, quail eggshells, and duck eggshells were shown in Table (1).

$$D = \frac{k\lambda}{\beta\cos\theta} \qquad (1)$$

Where, D = The crystalline size of the particle

β = The full width of the peak at half maximum intensity located at 2θ

λ = The wavelength of X-ray radiation

k = Scherrer’s constant (k=0.94)

Energy Dispersive X-ray Fluorescence (EDXRF) analysis

Hydroxyapatite (HAp) powder from hen eggshells, quail eggshells, and duck eggshells were synthesized by EDXRF technique to confirm the elemental concentrations and the ratio of Ca/P. Figures 6 is shown the EDXRF graph of the HAp samples at 900℃ for 3hr. Table 4 was shown the elemental concentrations of HAp powder from hen eggshells, quail eggshells, and duck eggshells. The ratio of the values of calcium (Ca) to phosphorous (P) of hen eggshells, quail eggshells, and duck eggshells are 2.46, 2.87, and 2.72 from EDXRF data results. They also contain three minor elements namely these are Sr, Fe, and Zn found in the HAp powder from hen eggshells, quail eggshells, and duck eggshells.

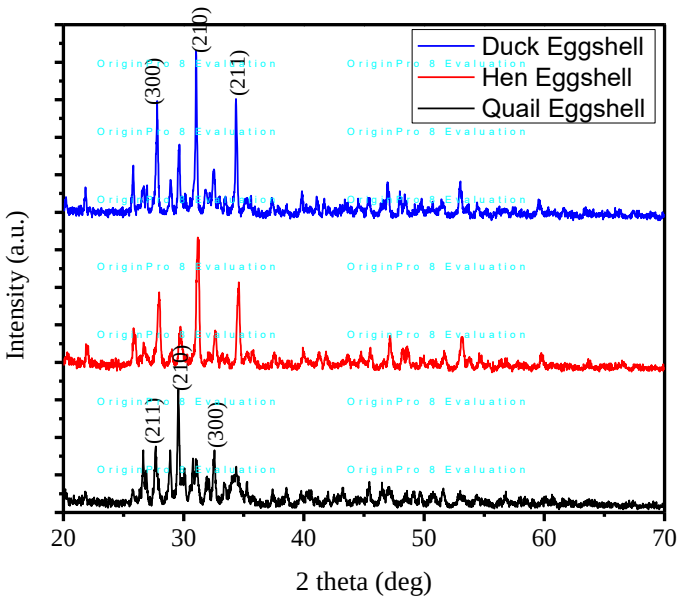

Figure 5. The XRD pattern of HAp powder from hen eggshells, quail eggshells, and duck eggshells at 900℃ for 3h

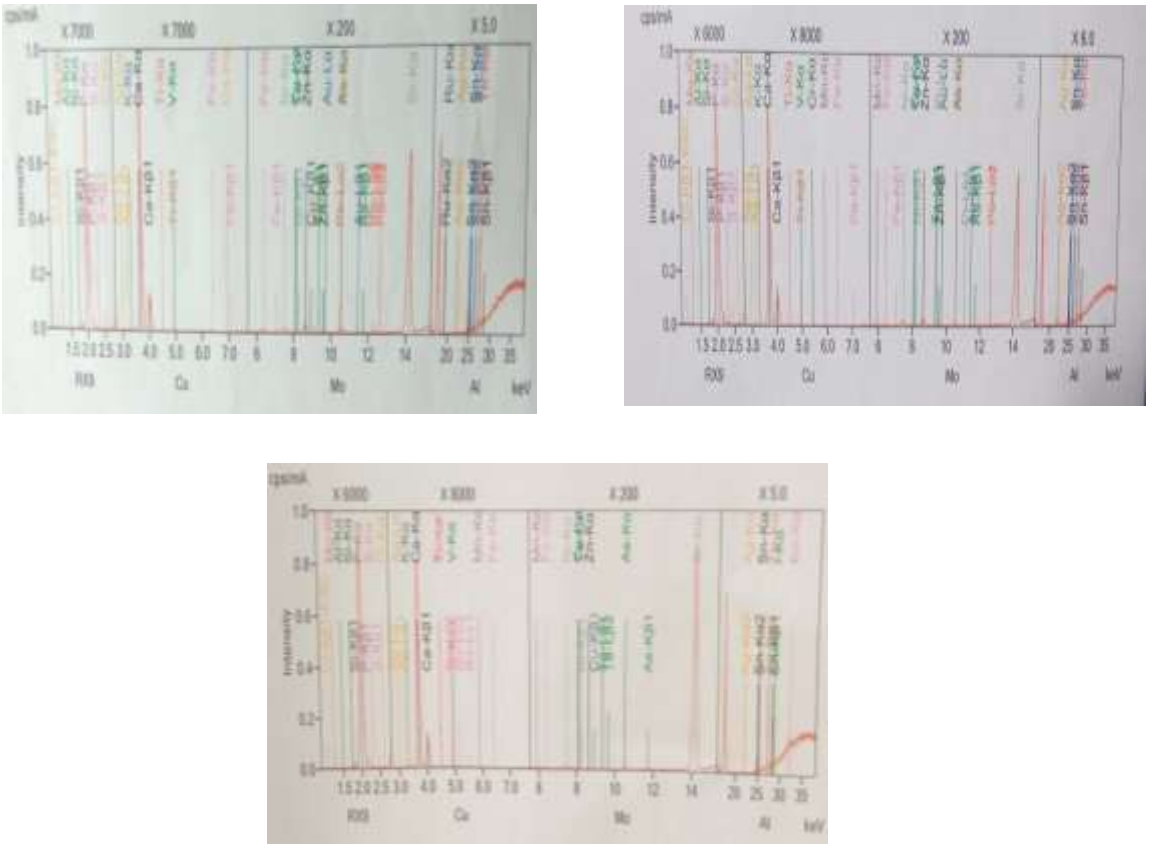

Figure 6. EDX line spectrum of HAp Sample from hen eggshells, quail eggshells and duck eggshells

Table 1. The average crystalline size for three strongest peaks of HAp sample from hen eggshells, quail eggshells, and duck eggshells at 900℃ for 3hr

Sample	Peak no	(hkl) plane	2θ (degree)	θ (radian)	FWHM (radian)	Crystalline size D(nm)	Average crystalline size
HAp 1	1	210	31.1933	15.59665	0.261	33.006022	32.380577
	2	211	34.5668	17.2834	0.2629	33.053392	
	3	300	27.9658	13.9829	0.2751	31.082316	
HAp 2	1	210	29.5856	14.7928	0.1565	54.835836	47.717258
	2	211	27.6984	13.8492	0.1989	42.965323	
	3	300	32.5538	16.2769	0.1906	45.350614	
HAp 3	1	210	31.0681	15.53405	0.1287	66.914921	57.942318
	2	211	34.3924	17.1962	0.1339	64.866571	
	3	300	27.8091	13.90455	0.2033	42.045462	

Table 4. Quantitative EDXRF results of HAp Sample from hen eggshells, quail eggshells, duck eggshells at 900℃ for 3hr

	Hen eggshells	quail eggshells	duck eggshells
Element	**Weight %**	**Weight %**	**Weight %**
Ca	**8.70**	**9.11**	**9.37**
P	**3.54**	**3.17**	**3.45**
Sr	**0.0136**	**0.0120**	**0.0190**
Fe	**0.0032**	**0.0012**	**0.0009**
Zn	**0.0021**	**0.0019**	**0.0002**

Conclusion

This research has been reported hydroxyapatite with calcium precursor from hen eggshells, quail eggshells, and duck eggshells and phosphate from H_3PO_4 were successfully synthesized by precipitation method. The average crystalline sizes were determined by using XRD results data. The mean crystalline sizes of HAp from three types of eggshells were 32.380577 nm, 47.7172582 nm, and 57.9423187 nm at 900℃ for 3hr. The lattice constant values of hen eggshells, quail eggshells and duck eggshells are a = 10.37030 (Å), b = 10.37030 (Å), and c = 37.08500 (Å), alpha (α) = 90°, beta (β) = 90°, gamma (γ) = 60°, and a = 9.41800(Å), b = 9.41800(Å), c = 6.88400(Å), alpha (α) = 90, beta (β) = 90°, gamma (γ) = 60°, and a = 10.43800, b= 10.43800, c = 37.15000, alpha (α) = 90°, beta (β) = 90°, gamma (γ) = 60°. So, the crystal structures of hydroxyapatite powder from hen eggshells, quail eggshells and duck eggshells were hexagonal structure (a=b≠c). The ratio of the values of calcium (Ca) to phosphorous (P) of hen

eggshells, quail eggshells, and duck eggshells are 2.46, 2.87, and 2.72 from EDXRF data results. Some of the impurities that may arise in the process of synthesis of hydroxyapatite based on natural sources are related to carbonate groups. The obtained HAp can be used for many biomedical applications (hard tissue replacement in medical and dental therapy). Thus, the aim of this research is to extract hydroxyapatite from shell sources (hen eggshell, duck eggshells, and quail eggshells) using a combination of chemical precipitation and calcination methods, which will also reduce the environmental impacts caused by the improper disposal of the wastes.

Acknowledgements

I also would like to thank Professor Dr San San Thwin, Head of Department of Physics and Professor Dr Khin May Oo, Department of Physics Yenanchaung University, Professor Dr Nyo Nyo Myint Department of Physics Yenanchaung University for their guidance and help through this paper. I am greatly indebted to my supervisor Dr Thein Aye, Associate Professor Department of Physics Yenanchaung University for his valuable guidance and supervision for this paper.

References

Avashnee Chetty, Ilse Wepeneer, Mona K. Marei, Yasser El Kamary, Rania M. Moussa, "HYDROXYAPATITE: SYNTHESIS, PROPERTIES, AND APPLICATIONS", page.1-57.

Bone Implants.Biomaterials", 15, 926-930. https://doi.org/10.1016/0142- 9612(94)90119-8.de Lange, G.L. and Donath, K. (1989), "Interface between Bone Tissue and Implants of Solid Hydroxyapatite or Hydroxyapatite-Coated Titanium Implants. Biomaterials", 10, 121-125. https://doi.org/10.1016/0142-9612(89)90044-6

Champion, E, (2013) "Sintering of Calcium Phosphate Bioceramics. Acta Biomaterialia", vol.9, pp.5855-5875. https://doi.org/10.1016/j.actbio.2012.11.029.

D. S. Gomes , A.M.C. Santo , G.A.Neves , R.R. Menezes, (2019)"A brief review on hydroxyapatite production and use in biomedicine",Vols65,pages282-302, http://dx.doi.org/10.1590/0366-69132019653742706,2019.

Eric M Rivera a, Miguel Araiza b, Witold Brostow c, Victor Castano a c, J. R Diaz-Estrada a, R Hernandez a, J.Rogelio Rodriguez a, (2016) "Synthesis of Hydroxyapatite from eggshells",Vols41,pages128-134,https://doi.org/10.1016/S0 167-577X(99)0011 8-4.

Moroni, A., Caja, V.L., Egger, E.L., Trinchese L. and Chao, E.Y.S. (1994) "Histomorphometry of Hydroxyapatite Coated and Uncoated Porous Titanium

N.A.S. Mohd Pu'ad, P. Koshy, H.Z. Abdullah, M.I. Idris, T.C. Lee, (2019) "Synthese of Hydroxyapatite from natural sources", Vols.5,page.1-14, https://doi.org/10.1016/ j.heliyon.

N.A.S. Mohd Pu ad, Alipal, H.Z. Abdullah, M.I.Idris, T.C. Lee, (2020) "Synthesis of eggshell derived hydroxyapatite via chemical precipitation and calcination method,"Vols42,pages 172177, https://doi.org/ 10.1016/j.matpr.

Rameshbabu, N., Rao, K.P. and Kumar, T.S.S. (2005) "Accelerated MicrowaveProcessing of Nanocrystalline Hydroxyapatite". Journal of Materials Science,40, 6319-6323. https://doi.org/10.1007/s10853-005-2957-9.

Venugopal, J. Prabhakaran, M.P., Zhang, Y., Low, S., Choon, A.T. and Ramakrishna, S, (2010)"Biomimetic Hydroxyapatite-Containing Composite Nanofibrous Substrates for Bone Tissue Engineering. Philosophical Transactions of the Royal Society A", 368, 2065-2081. https://doi.org/10.1098/rsta.2010.0012

EFFECTS OF CHEMICAL ACTIVATION PROCESS ON THE SURFACE MORPHOLOGY OF BROOM STICK -BASED ACTIVATED CARBON

Khaing Cho Thet[1], Hnin Sandar Tun[2], Zin Min Myat[3] and Cho Cho Thet[4]

Abstract

The surface morphology of anode materials plays a crucial role in determining the electrochemical performance of supercapacitors. The porous structure and pore size of anode in supercapacitor facilitates the efficient ion transport and electrolyte diffusion. In this study, the surface morphology of broom stick based materials as an anode material of supercapacitor is investigated. Activated carbon (AC) from the broom stick was prepared by two different chemical activation processes. The structure of the broom stick AC was observed by scanning electron microscope (SEM). The pore structure and size depending on the activation temperatures in each method were investigated. It was found out that the structure and pore size of AC were different depending on the activation process and activated temperature.

Keywords: activated carbon, chemical activation, porous structure, pore size and scanning electron microscope (SEM)

Introduction

Surface morphology plays a crucial role in determining the electrochemical performance of supercapacitors. A larger surface area allows for more active sites for charge storage, and thus it can enhance the capacitance. Due to their nanometer size, nanostructured materials such as nanoparticles, nanowires, and nanosheets provide a high surface area. Hierarchical pore structures can improve both energy and power density (Libber *et al*., 2024) in supercapacitor. The presence of different sizes of pores including micropore (<2 nm), mesopore (2–50 nm), and macropore (>50 nm) supports the efficient ion transportation and electrolyte diffusion in supercapacitor. Surface morphology can also influence the electrical conductivity of the electrode material in energy storage devices. Morphologies that provide structural integrity can withstand the stress of repeated charge-discharge cycles, enhancing the durability and lifespan of the supercapacitor[4]. The interaction between the electrode surface and the electrolyte is critical. A morphology that promotes better wettability and contact with the electrolyte can improve the overall electrochemical performance (Ling Miao *et al*., 2010).

The pore size in supercapacitor electrodes significantly influences their electrochemical performance. Micropores provide a large surface area for charge storage, which is beneficial for increasing capacitance. However, very small micropores may restrict the movement of larger electrolyte ions, potentially limiting the rate of charge and discharge[1]. For instance, well-aligned nanostructures can provide better pathways for electron transport, reducing resistance (Kian Keat Lee *et al*., 2014). Morphologies that provide structural integrity can withstand the stress of repeated charge-discharge cycles, enhancing the durability and lifespan of the supercapacitorhttps://pubs.rsc.org/en/content/articlehtml/2020/ma/d0ma00384k (Akhil Pradiprao Khedulkar *et al*., 2024). The interaction between the electrode surface and the electrolyte is

[1] Department of Physics, Pakokku University
[2] Department of Physics, Dawei University
[3] Department of Physics, West Yangon University
[4] Department of Physics, University of Yangon

critical. A morphology that promotes better wettability and contact with the electrolyte can improve the overall electrochemical performance (Kumar *et al*., 2021).

In this study, activated carbon is synthesized from broom stick biomass for the purpose of using as electrode materials in supercapacitor. The surface morphology of activated carbon depending on different processes of chemical activation is presented.

Experimental Details

Synthesis of Activated Biochar Powder by One-Step Chemical Activation Method

Activated carbon (AC) is prepared from the raw materials of broom stick. Firstly, the raw broom sticks were washed with fresh water in order to remove any impurities and then they were cut into small pieces. After that, they were dried in the muffle furnace at 105 °C for 1 h to remove the moisture content in the raw of broom stick. For the activation process, 10 g of dry broom stick pieces were treated with 50 g of 6 M KOH solution in Muffle furnace at 600 °C and 700 °C for 1 h. After finishing the reaction, grayish pink colour of activated carbon was obtained. Then, as-prepared AC was washed with 0.2 M of HCL solution and distilled water (DW) by centrifugation until to neutralize the base residue. Afterwards, the pure AC was dried at 80 °C for a few hours until the moisture was completely removed. Finally, the grayish pink colour of AC powder was successfully obtained. The synthesis procedure of activated AC is shown in Figure 1.

Figure 1 Synthesis process of activated biochar powders by one-step chemical activation process

Synthesis of Activated Carbon Fiber by Two-Step Chemical Activation Method

In two-step method, the ash of broom stick was firstly prepared and then it was followed by activation process. 15 g of dry broom stick pieces were burned at 600 °C and 700 °C for 1 h inside the Muffle furnace and the ash was obtained. Subsequently, activation process was followed by adding 3.11 g of the ash into 50 g KOH (6 M) solution. The mixed solution was stirred for 3 h in order to increase porosity and surface area of ash. After that, the product was centrifuged with 0.4 M of HCL solution and DW for several times until to neutralize the KOH base residue. Then, the product was heated at 80 ºC until to become the dried activated carbon. Finally, the black colour of activated carbon fiber was obtained. The experimental diagram of synthesis process of AC is presented in Figure 2.

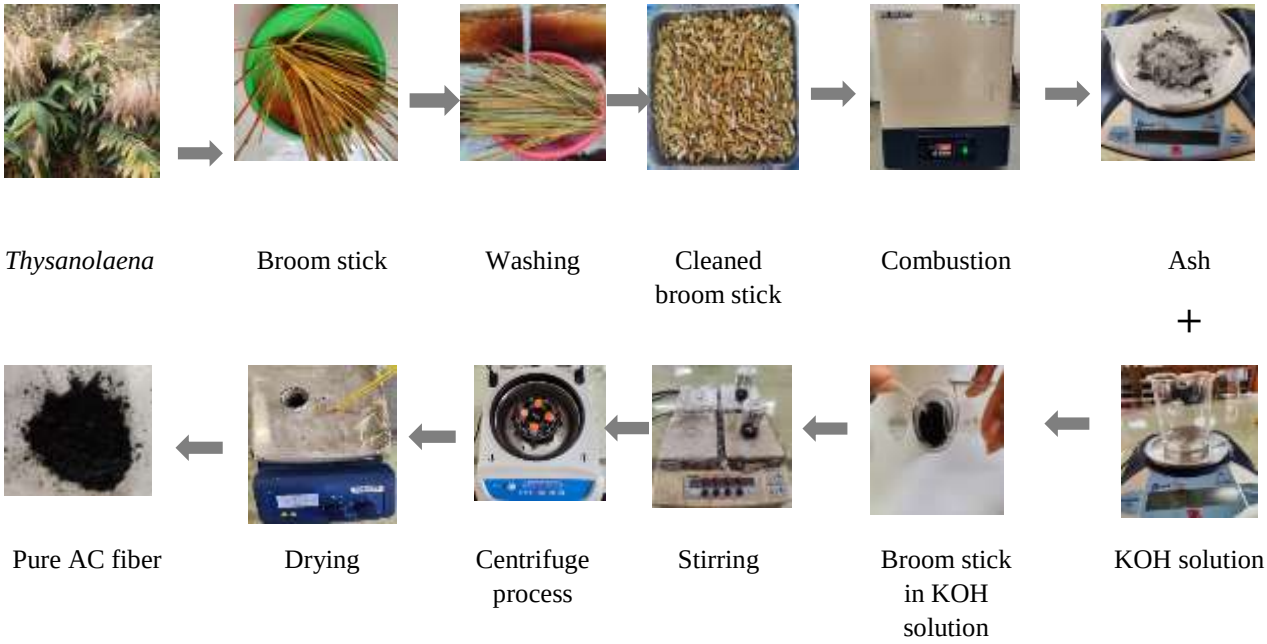

Figure 1 Synthesis process of activated carbon fibers by two-steps chemical activation process

Results and Discussion

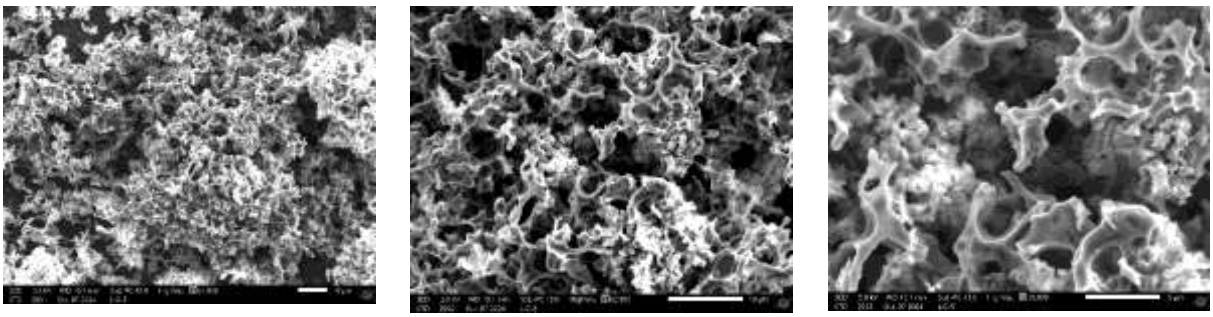

Figure 3 SEM image of broomstick synthesized by one-step chemical activation method at 600 ºC at different magnifications

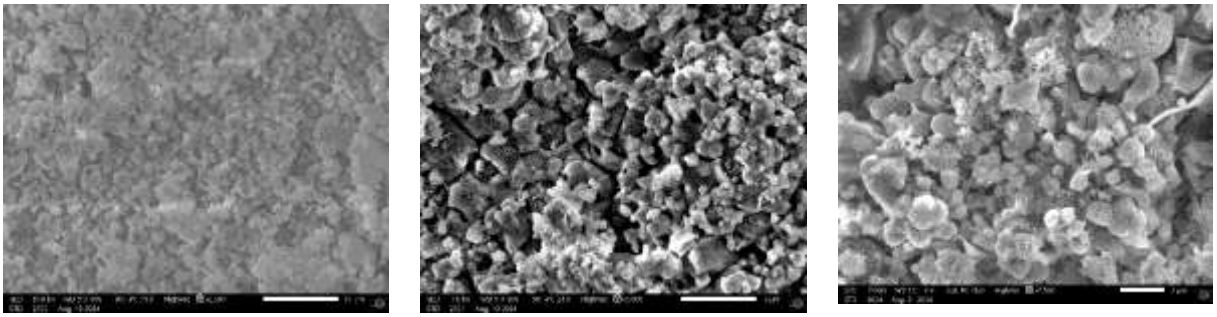

Figure 4 SEM image of broomstick synthesized by one-step chemical activation method at 700 ºC at different magnifications

SEM analysis is carried out in order to observe the surface morphology of final products depending on two different activation processes. The colour of carbon-based materials is generally black. However, the colour of final product activated by one-step method is not black. This is due to the introduction of more functional groups which can change the light absorption and reflection properties of the biochar (Rajat Kumar Sharma et al., 2022). Figure 3 and 4 exhibits the SEM images of AC activated at 600 and 700 ºC. The pore structure can be clearly seen in SEM image in broom stick activated at 600 ºC. The surface morphology AC showed a rough texture with numerous cavities and channels. In contrast, there was no porous structure in SEM image of biomass activated at 700 ºC. The surface of the AC was also more heterogeneous and less uniform.

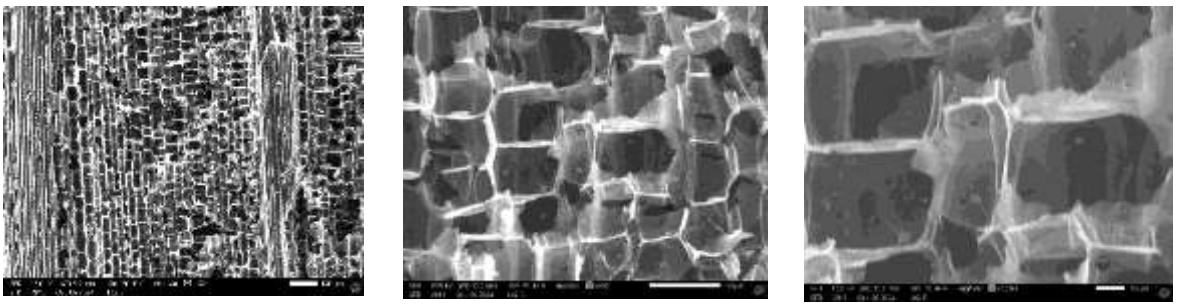

Figure 5 SEM image of broom stick synthesized by two-step chemical activationat 600 ºC at different magnifications

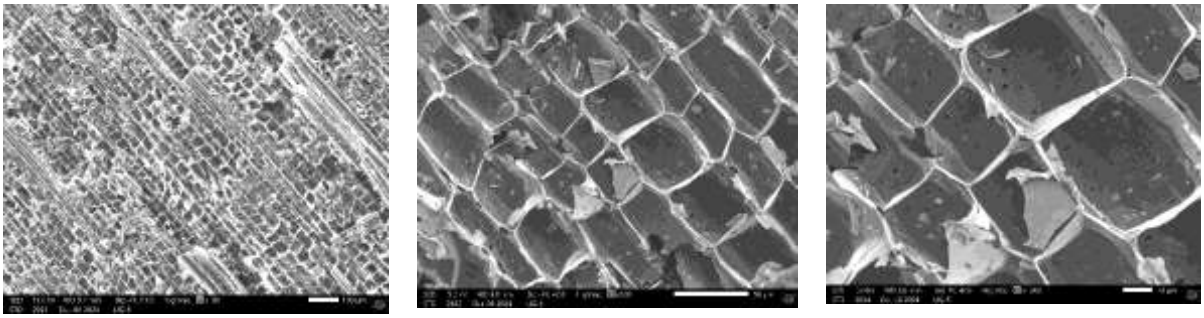

Figure 6 SEM image of broom stick synthesized by two-step chemical activationat 700 ºC at different magnifications

The SEM image of AC prepared by two-step activation process is illustrated in Figure 6 and 7. The porous fiber structures of AC were clearly revealed in this image since KOH activation created a highly porous structure by etching the ash surface. Besides, the deep black color of AC was resulted due to the high-temperature in the combustion process of broom stick. In other words, the extensive carbonization and the removal of non-carbon elements during the combustion of biomass. Besides, the fibers were well-aligned and oriented in one direction. Thus, this structure has a possibility to support the better pathways for electron transport. Moreover, the well-connected pores ensure that ions can move freely throughout the electrode material which in turn improve the both of energy and power density. The average pore size is estimated by image J software. The average pore sizes were found out that and 30.54 and 48.74 μm for 600 and 700 ºC respectively. The pore size was become smaller when the ash temperature is increased from 600 to 700 ºC. As the pore of fiber is microporous type, ion transport of the anode in supercapacitor within the porous structure is likely to be enhanced (Zhao *et al*., 2020). As a result, it is possibility to reduce the resistance and thus, it can enhance the charge/discharge rates as well as can contribute to higher power density in super capacitor (Mostafa S. Sayed *et al*., 2024). Although, microporous fiber can improve the ion transport, overall capacitance will be contributed when they are compared to micropores and mesopores due to their lower surface areas in fiber.

Conclusion

The surface morphology and structure of broom stick-based activated carbon are investigated for the application of anode materials in supercapacitor. AC was prepared by chemical activation method. In one-step method at 600 ºC, the AC with porous structure was obtained. On the other hands, no porous structure was observed at activation temperature 700 ºC. In addition, the final product in one-step method could be formed only rough and inhomogeneous particles. In contrast, the AC with porous and aligned fiber structure were observed in two-step method at both 600 and 700 ºC. The pore size estimated by image J software was also regarded that in the microporous range. Thus, a larger pore area will allow for more active sites for charge storage, enhancing the capacitance. This fiber morphology may promote better wettability and contact with the electrolyte and can improve the overall electrochemical performance in supercapacitor. In conclusion, among the different surface morphology of AC depending on activation methods, AC with hierarchical pore structures has a possibility to improve both energy and power density in supercapacitor application.

Acknowledgements

We would like to acknowledge to Prof Dr Tin Tun Aung, Rector, Pakokku University, for his allowing us to participate in this event. Our special thanks go to Prof Dr Win Mar, Head of Department of Physics, Pakokku University for her encouragement to this work. We would like to express our sincere thanks to Dr Yin Maung Maung, Professor and Head of Department of Physics, University of Yangon, for his kind permission to contribute this work and his excellent discussion.

References

Akhil Pradiprao Khedulkar, Van Dien Dang, Annadurai Thamilselvan, Ruey-an Doong, Bidhan Pandit Sustainable high-energy supercapacitors: Metal oxide-agricultural waste biochar composites paving the way for a greener future, Journal of Energy Storage 77 (2024) 109723.

Chen, S., W. Xing, J. Duan, X. Hu and S. Z. Qiao, Nanostructured morphology control for efficient supercapacitor electrodes, J. Mater. Chem. A, 2013, 1, 2941-2954. DOI: 10.1039/C2TA00627H.

Kumar A., A. Thomas, M. Garg, G. Perumal, H. S. Grewal and H. S. Arora, High performance CuO@brass supercapacitor electrodes through surface activation J. Mater. Chem. A, 2021, 9, 9327 DOI: 10.1039/D1TA00286D.

Kian Keat Lee, Wee Shong Chin and Chorng Haur Sow, Cobalt-based compounds and composites as electrode materials for high-performance electrochemical capacitors, **J. Mater. Chem. A**, 2014, **2**, 17212 **DOI:** 10.1039/C4TA02074J.

Libber, M., Gariya, N. & Kumar, M. A comprehensive analysis of supercapacitors with current limitations and emerging trends in research. J Solid State Electrochem (2024). https://doi.org/10.1007/s10008-024-06107-x.

Ling Miao, Ziyang Song, Dazhang Zhu Liangchun Li, Lihua Gan and Mingxian Liu, Recent advances in carbon-based supercapacitors , ***Mater. Adv.***, 2020,**1**, 945-966.

STUDY ON EFFECT OF MORPHOLOGY AND CRYSTALLIZATION OF TIO_2 NANOTUBES AND SPECTRAL DEPENDENT IPCE (%) OF TIO_2 NANOTUBES IN AQUEOUS SOLUTION

Moe Moe[1], Min Min Thein[2]

Abstract

The formation of TiO_2 nanotubes arrays were investigated in different electrolyte solutions. Three nanomaterials of TiO_2 were prepared by electrochemical anodization using three different electrolyte solutions:0.5 wt.% NH_4F with 4 wt.%, 6 wt.%, and 8wt.% of distilled water in ethylene glycol. SEM showed different morphologies caused by the variation in the water content of the solutions. By a change of the crystalline phase of the TiO_2 nanotubes, the oxygen vacancies increased and affected to the optical and electrical properties of TiO_2 nanotubes. To understand the interplay between the photoactivity and light absorption of TiO_2 nanotubes annealed at 300℃, incident-photon-to-current-efficiency of TiO_2 nanotubes was investigated as the function of the wavelength of incident light. IPCE% is a better parameter reflecting the spectral dependent photon response of TiO_2 nanotubes.

Keywords: Anodization, TiO_2 nanotube arrays, IPCE% of TiO_2 nanotubes

Introduction

Global warming is an aspect of climate change, referring to the long-term rise of the planet's temperatures. It is caused by increased concentrations of greenhouse gases in the atmosphere, mainly from human activities such as burning fossil fuels and farming. There are three positions on global warming: (1) that global warming is not occurring and so neither is climate change; (2) that global warming and climate change are occurring, but these are natural, cyclic events unrelated to human activity; and (3) that global warming is occurring as a result primarily of human activity and so climate change is also the result of human activity.

The current global economy is largely dependent on fossil fuels. Because of the depleting reserves and the gross environmental impact of burning fossil fuels, the identification of suitable alternative and renewable energy sources, such as hydrogen, is becoming increasingly important.

Hydrogen gas is foreseen as the future energy carrier since it is renewable and does not generate the greenhouse gas carbon dioxide in combustion.

Due to global warming, artificial changes in seasons and droughts occur. As a result, extreme temperatures, extreme cold, drought, floods, irregular rainfall, and lighting are occurring. Among these things, the greenhouse effect is caused by high temperatures and carbon dioxide. Carbon dioxide gases were detected using sensitive devices. In doing so, gas sensors are very useful for gas detection. Therefore, the properties of TiO_2 nanotubes, which are commonly used in gas sensing.

Titanium dioxide (TiO_2) is a semiconductor material that can form nanostructures and produce valuable optical and electrical properties. TiO_2 has been used in a range of industrial and consumer products. TiO_2 can be tailed into various shapes, such as nanoparticles, nanorods, nanowires, and nanotubes. Due to each tube’s growth array on the surface, nanotubes have attracted the most attention among these nanostructures. The titanium dioxide nanotube arrays

[1] Department of Physics, Meiktila University
[2] Department of Physics, University of Mandalay

have a unique nanoarchitecture, a large surface area, and higher mechanical stability than TiO_2 nanoparticles [3].

TiO_2 nanotubes can be synthesized using different types of methods, such as electrochemical anodization, the template-assisted method, and hydrothermal. Electrochemical anodization is an electrolytic technique capable of increasing the oxide layer thickness. Anodization is a facile practical approach due to its highly ordered and vertically oriented nature. All favorable properties render TiO_2 nanotubes suitable for various applications such as photocatalysis, sensors, and dye-sensitized solar cells.

Generally, the TiO_2 nanotubes require heat treatment at high temperatures to sustain crystallization. Therefore, the fabrication of TiO_2-based sensor properties could certainly promote multifunctional sensitivity behavior and high-efficiency applications that may lead to newer opportunities in disciplines as diverse as physics, chemistry, biology, medicine, and engineering. Due to the metal oxide-based semiconductor produced at a lower cost with higher productivity and performance, TiO_2 film can be used in domestic, industrial, electronics, semiconductors, refineries, metal, or other furnaces [15].

The recorded anodization current against time curves suggests that the high current density shows high chemical dissolution occurs when radicals are present in the electrolyte during anodization, which speeds up the formation of long TiO_2 nanotube arrays. Therefore, the morphology of TiO_2 nanotubes could be optimized by the proper varying water contents.

In this period, surface morphology, the crystalline phase, and photocurrent density of different TiO_2 nanotubes (4 wt.% H_2O, 6 wt.% H_2O, and 8 wt.% H_2O) were investigated. In this research work, TiO_2 nanotube arrays were fabricated by the anodization method. The changes in structure and dimension of TiO_2 nanotubes were investigated by varying the water content in the electrolyte.

Materials and Method

In the present investigation, TiO_2 nanotubes were created on pure titanium surfaces through the anodizing method using an electrolyte solution with varying water contents in the electrolyte solution. Titanium foil (thickness: 0.2 mm; purity: 99.7%) was cut into 2cm x 2cm pieces, which were ultrasonically cleaned for 5 minutes each in acetone and ethanol, then rinsed in distilled water. The samples were dried by using a hair dryer. The samples require a very efficient cleaning procedure in order to obtain an almost perfect, fine surface. Then samples were immersed into the electrochemical cell with the electrolyte solution, which is mainly based on hydrofluoric solutions or an organic solution. In order to study the variation of water contents, the experiments were performed by varying the water contents in the electrolyte by 4wt.%, 6 wt.%, and 8 wt.% of distilled water, whereas ethylene glycol is 96wt.%, 94 wt.%, and 92 wt.%. This composition of electrolyte solution was stirred for 30 minutes with a magnetic stirrer before anodizing.

Anodization was performed in a standard two-electrode electrochemical cell with Ti foil as the working electrode and a platinum rod (diameter: 1mm, purity: 99.9%) as the counter electrode connected to a DC power supply. When the DC power supply was applied between two electrodes, gas bubbles were observed at the platinum rod during anodization. The anodization was performed at room temperature under magnetic stirring. The applied voltage between the titanium sample and the platinum rod was 30 V, and the anodization time was 1 hour. The voltage was gradually increased to 30 V. The distance between titanium foil and cathode was

kept constant at 2 cm for every experiment. The as-prepared samples were ultrasonically cleaned with acetone for 1 minutes, rinsed in distilled water, and then dried in air for characterization.

Characterization

The morphologies and sizes of the TiO_2 nanotubes were investigated by Scanning Electron Microscope SEM (Phenom World, MVE 0356841799, ε00-07334). In the standard high vacuum (HV) operating mode, the MVE 0356841799 is capable of operating in extended pressure mode (EP). The MVE 0356841799 SEM operates with acceleration voltage. The elemental composition as atomic percentage (At %) of oxygen, titanium, and fluorine were measured by energy dispersive X-ray spectroscopy at 10 keV (EDS). Nanotubes were studied by X-ray diffraction using a Bruker D8 powder diffractometer operating in the reflection mode with Cu Kα radiation (40 kV, 30 mA) diffracted beam monochromator. (Cu-Kα radiation, $\lambda = 1.5406$ nm) starting from 0.2 to 15 kV and can attain magnification up to 135, 000 X. X-ray diffraction (XRD) is a versatile, non-destructive technique that reveals detailed information about the chemical composition and crystallographic structure of the sample.

Potentiostatic Voltammetry

Photoelectrochemical (PEC) properties of TiO_2 nanotubes were investigated using the CS350 electrochemical workstation. The linear sweep photoelectrochemical measurements were done in a standard three-electrode system containing TiO_2 nanotubes as the working electrode, a Pt rod as the counter electrode, and Ag/AgCl as the reference electrode. The photocurrent density measurements were done using a 1M KOH solution with the addition of 1 wt.% of ethylene glycol in both the dark and light irradiation conditions. Linear sweep photovoltammetry was obtained with a scan rate of 0.05 V/s in a potential window of -1 V to +1 V. 100 W LED light sources with different wavelengths (Red 665 nm, Yellow 590 nm, Green 515 nm, and UV 370 nm) were used as the light sources.

Results and Discussion

TiO_2 nanotubes were grown in electrolyte solution with varying water content concentrations. In order to look for an optimal concentration of water content in electrolyte, we have studied the dependence of morphology and size of TiO_2 nanotube arrays on the water contents in electrolyte solution. Figure(1)(a), (b), and (c) show SEM images of TiO_2 nanotubes prepared from the electrolyte solution with water contents of 4 wt.%, 6 wt.%, and 8 wt.%.

In the SEM image of water content of 4 wt.% figure(1(a)), nanotubes were formed at the most parts of the sample. The amount of water (4 wt.%) and the amount of ammonium fluoride (0.5 wt.%) in electrolyte are in equilibrium state for nanotubes formation. It was found that the sizes of the nanotubes are homogeneous in larger areas. The circular diameter well defined. It was found small ripples and sponges in the nanotubes. The size distribution histogram figure (2(a)) indicates that the diameter of nanotubes ranges from 20 nm to 75 nm with maximum frequency of size 45 nm-50 nm. The amount of water (4 wt.%) and the amount of ammonium fluoride (0.5 wt.%) are at optimum condition.

In the SEM image of water content of 6 wt.% figure(1(b)), the circular diameter well defined. It was found a lot of ripples and sponges in the nanotubes. The size distribution histogram figure(2(b)) indicates that the diameter of nanotubes ranges from 40 nm to 85 nm with maximum frequency of size 55 nm-60 nm.

In the SEM image of water content of 8 wt.% figure (1(c)), the circular diameter well defined. It was found a lot of ripples and sponges in the nanotubes. The size distribution histogram figure (2(c)) indicates that the diameter of nanotubes ranges from 35 nm to 85 nm with maximum frequency of size 50 nm-55 nm.

As we can see, different morphologies were obtained, the wall thickness increases, and both the inner diameter and the control in the concentration of water in the electrolyte solutions increase. Therefore, the nanotubes trend to form random packets without a particular shape on the top of nanotube arrays. On the contrary, a low concentration of water (4 wt.%, 6 wt.% and 8 wt.%) promotes self-organization and self-ordering of the TiO_2 nanostructures, causing the wall thickness to be thinner and the circular diameter well defined. Thereby, the nanotubes synthesized with 4 wt. % and 6 wt.% (H_2O distilled) obtained a better ordering and organization than the nanotubes synthesized with 8 wt.% content of water in electrolyte solution.

Additionally, Table 1 shows the elemental composition of the TiO_2 films on the titanium substrate after electrochemical anodization. For all samples, the ratio between Ti and O is similar, however, the TiO_2 films closest to their stoichiometry are the samples 4 wt % and 6 wt % films with the lowest contents of water because they have approximated ratio of 1:2, 1:1.97 ($Ti \leq O_x$), these ratios are attributed to titanium substrate and complete oxidation. Therefore, these can be seen that the films contain elements of the electrolyte solution such as F, O etc.

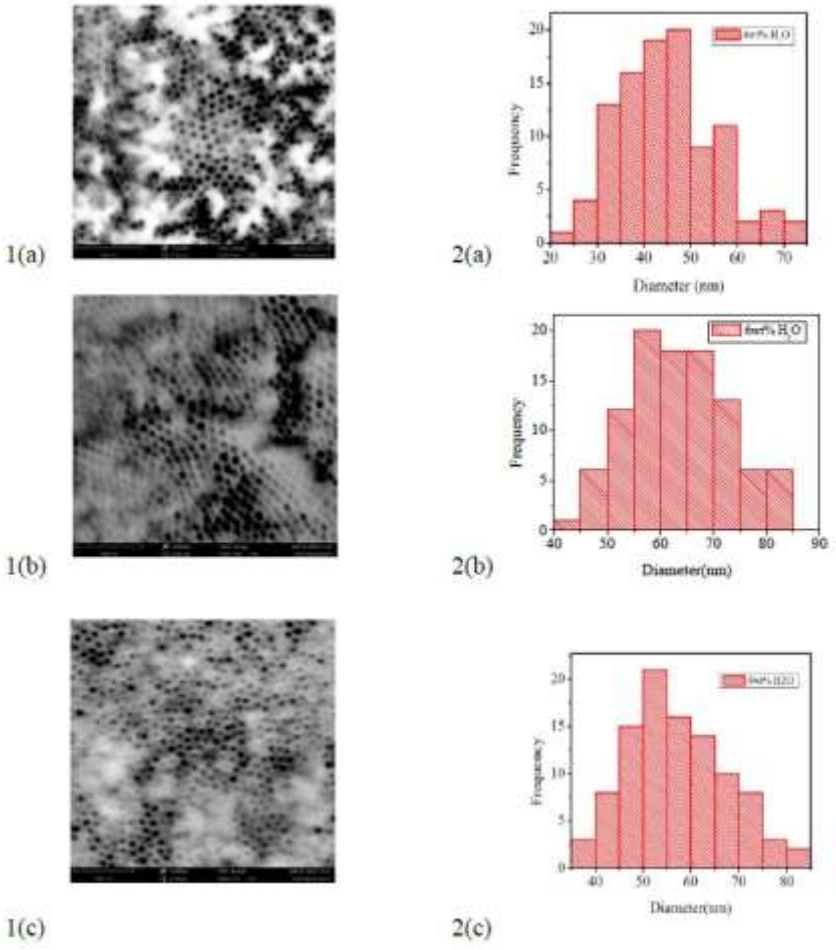

Figure1(a-c) SEM images of titanium nanotube sample obtained at 30V for anodization time of 1hr.

Figure2(a-c) Size distribution histogram for TiO_2 nanotubes prepared from electrolyte solution with varying water content.

Table 1. elemental composition of the TiO_2 nanotubes prepared by eletrochemical anodization

Sample Name	Water content in lectrolyte solution	O At %	Ti At %	F At %
Sample 1 (4 wt % H_2O)	4 wt %	58.96 ± 1.55	27.62 ± 0.31	13.43 ±0.77
Sample 2 (6 wt % H_2O)	6 wt %	59.69 ±1.45	30.31 ± 0.30	10.01 ± 0.61
Sample 3 (8 wt % H_2O)	8 wt %	59.04 ±1.42	31.91 ± 0.30	9.06 ± 0.58

For the crystalline phase of TiO_2 nanotubes, an XRD study was carried out. Figure 3 shows the XRD patterns of TiO_2 nanotubes annealed at 300 °C. After thermal treatment 300 °C, the amorphous structure is converted to the anatase crystalline phase. The typical peaks were observed at 25.5, 38.5, 40.5, 48.8, 53.2, and 63.2, corresponding to the planes (101), (103), (112), (200), (105) and (213), respectively. Anatase phase is a crystalline structure used in gas sensing since it presents better chemical and structural stability and higher catalytic activity than other structures of TiO_2 (rutile and brookite). It was seen that the crystallized sizes of TiO_2 nanotubes decrease as the temperature increases with varying water content in the electrolyte solution. Among the anatase annealed at 300 ℃ , the largest peak intensity is found in the 6 wt.% and 4 wt % H_2O samples.

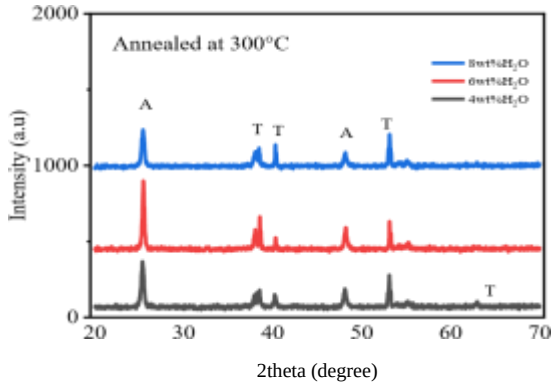

Figure (3) XRD patterns of TiO_2 nanotube samples annealed at 300 ℃ ("A" and "T" stand for- Anatase phase and pure Titanium respectively).

The photocurrent generated from TiO_2 nanotubes in a KOH aqueous solution was measured in the dark. Figure 4 shows a linear sweep voltammogram for TiO_2 nanotubes (4 wt.% H_2O, 6 wt.% H_2O, and 8 wt.% H_2O) annealed at 300 °C in the dark. The peak current densities for electrochemical reduction were obtained from linear sweep voltammograms. The peak current densities are 0.35 mA/cm^2, 0.59 mA/cm^2, and 0.56 mA/cm^2 for TiO_2 nanotubes (4 wt.% H_2O, 6wt.% H_2O, and 8 wt.% H_2O) annealed at 300 ℃ in the dark.

The spectral-dependent current densities of TiO_2 nanotubes (4 wt.% H_2O, 6 wt.% H_2O, and 8 wt.% H_2O) annealed at 300 ℃ were also extracted from linear sweep voltammograms (-1.0 V to 1.0 V) under light illumination with different wavelengths. Figure 4(a-d) shows the linear sweep voltammograms of TiO_2 nanotubes under light with different wavelengths. The current density extracted from linear sweep measurements is tabulated in Table (2).

The higher current for electrochemical reduction under UV light illumination (wavelength 370 nm) is attributed to the larger band gap of TiO_2, which can only be activated under UV. In addition, we found that the photocatalytic activity of TiO_2 nanotubes was significantly influenced by varying the water content in the electrolyte solution. Based on the results (Table 2), under light illumination with a particular wavelength, the TiO_2 nanotubes of the 6 wt.% H_2O sample annealed at 300 °C produced a higher current density, which is attributed to the higher anatase crystalline phase of the TiO_2 nanotubes

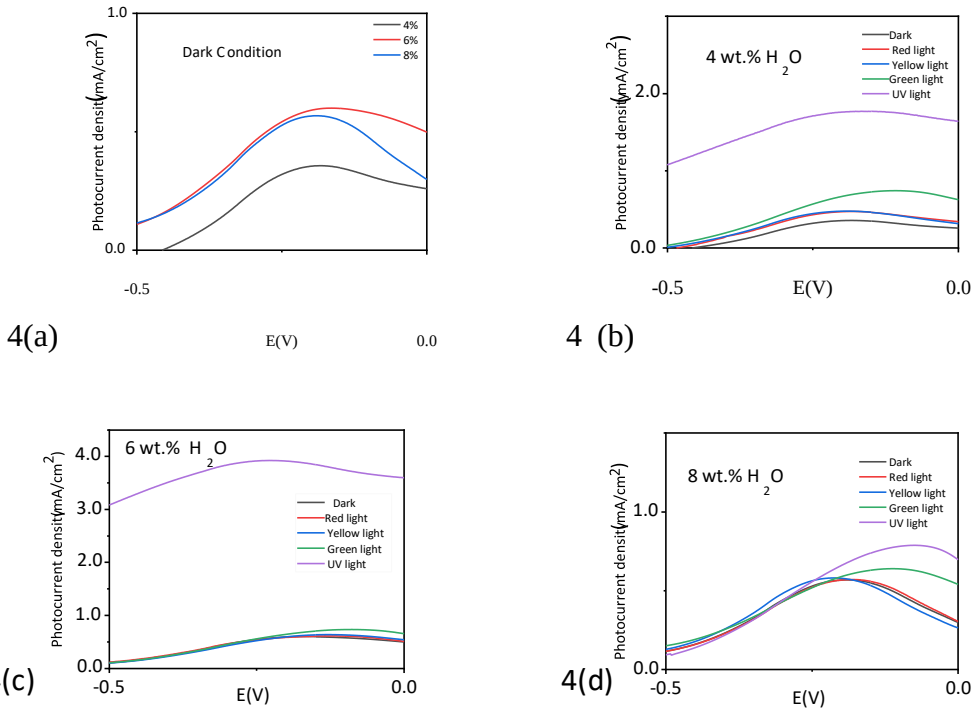

Figure 4(a) Linear sweep voltammograms in dark of TiO_2 (4 wt.% H_2O, 6 wt.% H_2O and 8 wt.% H_2O) nanotubes annealed at 300 ℃. Figure 4(b-d) linear sweet voltammograms of TiO_2 nanotubes (4 wt.% H_2O, 6 wt.% H_2O, and 8 wt.% H_2O) annealed at 300 ℃ under light with different wavelengths (Red, Yellow, Green, UV).

Table 4.2 Spectral dependent photocurrent density of TiO_2 nanotubes

Samples (varying the water content)	**Light sources with wavelength**	**Photocurrent density (mA/cm^2)**	**IPCE%**
Sample(4wt.%H_2O)	Red (665nm)	0.48	0.54
	Yellow (590nm)	0.48	0.61
	Green (515nm)	0.67	0.99
	UV (370nm)	1.76	3.63
Sample(6wt.%H_2O)	Red (665nm)	0.59	0.68
	Yellow (590nm)	0.59	0.77
	Green (515nm)	0.64	0.95
	UV (370nm)	3.92	8.06

Samples (varying the water content)	**Light sources with wavelength**	**Photocurrent density (mA/cm^2)**	**IPCE%**
Sample(8wt.%H_2O)	Red (665nm)	0.57	0.65
	Yellow (590nm)	0.57	0.74
	Green (515nm)	0.59	0.87
	UV (370nm)	0.66	1.36

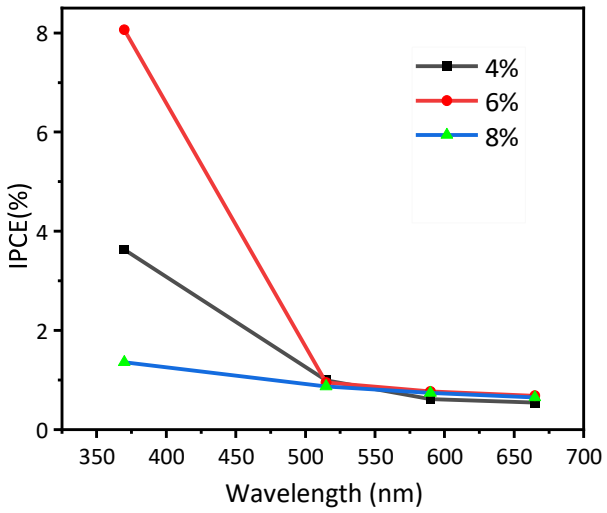

Figure (5) Incident-photon-to-current-efficiency (IPCE %) of TiO_2 nanotubes (4 wt.% H_2O, 6 wt.% H_2O, 8 wt.% H_2O) under light with different wavelengths.

Conclusion

Anodic TiO_2 nanotubes were synthesized by the anodization method by varying the water contents in the electrolyte solution. The influence of the water contents on the TiO_2 nanotubes, physical properties was investigated. Varying the water contents in the electrolyte solution significantly affected the morphology of the nanotubes. One-dimensional TiO_2 nanotubes of diameters 45–50 nm, 55–60 nm, and 50-55 nm has been developed from the respective electrolyte solutions of water content of 4 wt.%, 6 wt.%, and 8 wt.% using the anodization technique. It has been found that the size of nanotubes is not varied according to the water content of the electrolyte solution. Morphology differences could change the value of the band gap energy of the nanotubes. Two processes of oxide layer formation on Ti foil and oxide layer dissolution by fluoride need to be harmonic for the development of well-ordered TiO_2 nanotubes. Among them, well-defined morphologies were achieved in electrolytes with 4 wt.% and 6 wt.% water contents.

The effect of annealing temperature on the formation of crystalline phases of TiO_2 nanotubes was also studied by X-ray diffraction. It was seen that the crystallized sizes of TiO_2 nanotubes decrease as the temperature increases with varying water content in the electrolyte solution. Annealed at 300 ℃ samples, anatase peaks were found. When comparing the anatase peaks annealed at 300 ℃, it was found that the anatase peaks annealed at 300 ℃ have greater

peak intensity. Among the anatase peaks annealed at 300 ℃, the largest peak intensity was found in the 6 wt.% H_2O sample.

The photoelectrochemical response of TiO_2 nanotubes annealed at 300 °C in a KOH aqueous solution was also investigated under illumination with different wavelengths (red, yellow, green, and UV) using linear sweep voltammetry. Under different wavelengths of light, the current densities of the 4 wt.% H_2O and 6 wt.% H_2O samples were the best. But in light with different wavelengths, UV color is better. For all samples, UV light absorption is better because the anatase phase shows better light absorption under UV light.

Acknowledgement

I would like to express my profound gratitude to Dr Ba Han, Rector, Meiktila University, Dr Kyaw Linn, Pro-rector, Meiktila University, and Dr Min Thar, Pro-rector, Meiktila University, for the allowance to present this research paper. I am greatly indebted to Professor Dr Khin Khin San, Head of Department, Professor Dr Lae Lae Kyaing, Department of Physics, Meiktila University, for their permission for submitting the research paper.

References

A. Arenas-Hernandez et al., "A study of the effect of morphology on the optical and electrical properties of TiO_2 nanotubes for gas sensing applications" Eur. Phys. J. Appl. Phys. **90**(2020)30102.

Filip Dvorak et al, "One-dimensional anodic TiO_2 nanotubes coated by atomic layer deposition: Towards advanced Applications", J. apmt.**14**(2019)1-20.

Linsebigler A.L et al., "Fabrication of TiO_2 Nanotube Thin Films and Their Gas Sensing Properties" J.Sens.**95**(1995)735-758.

Lizhen Wu et al, "What happens if anodic TiO_2 nanotubes are soaked in H_3PO_4 at room temperature for a long time", Electrochem. Communications.**105**(2019) 1388-2481.

O.K. Varghese et al., "Influence of Anatase Titanium Dioxide Nanotube Arrays on Humidity Sensor Synthesized by Electrochemical Anodization" J.Mater.Res.**84**:6-2(2022)43-52.

Sevda Jafari et al., "Templated synthesis of TiO_2 nanotube macrostructures and their photocatalytic properties" Int. J.Nano.Med.**15**(2020)3447-3470.

S. Park et al., "Effects of Functionalization of TiO_2 Nanotube Array Sensors with Pd Nanoparticles on their Selectivity" Sensors.**14**(2014)15849-15860.

TANG Yu-xin et al., "Preparation of TiO_2 nanotube on glass by anodization of Ti films at room temperature" J. Am. Chem. Soc.**130**(2008)13364.

Xu Tian et al., "Gas sensors based on TiO_2 nanostructured materials for the detection of hazardous gases" J. Nano. Mater.**12**(2022)1131.

V.Aroutiounian *et al.*, "Study of Gas-Sensing Properties of Titanium Nanotubes for Health and Safety Applications" Chem.Proc. **9**(2021)25133.

Xin Zhou et al, "Photoelectrochemical performance of TiO_2 photoanodes: Nanotubes versus nanoflake electrode", Electrochem. Communications.**124** (2021)106937.

Z. Jedi-soltanabadi et al., "Enhanced physical properties of the anodic TiO_2 nanotubes via proper anodization time" J. Appl. Phys. **12**(2018)135-139.

EFFECTS OF DRYING TEMPERATURES ON THE CRYSTALLITE SIZES OF METHYL AMMONIUM LEAD IODIDE PEROVSKITE ABSORBER LAYER

Hnin Yu Wai[1], Zin Min Tun[2] and Cho Cho Thet[3]

Abstract

In recent years, perovskite solar cells have attracted as a potentially inexpensive and high-performing materials for photovoltaic systems. The effects of drying temperature on the structural properties of methyl ammonium lead iodide ($CH_3NH_3PbI_3$) perovskite film, absorber layer in perovskite solar cell, was investigated in order to use on an electron transport layer (ETL) in perovskite solar cell. Perovskite film at different drying temperatures was prepared by two-steps spin coating method. Zinc stannate (Zn_2SnO_4) materials for electron collection layer was synthesized by chemical precipitation method. The optimum drying temperatures of $CH_3NH_3PbI_3$ perovskite absorber layer were varied by changing the drying temperatures at room temperature, 60, 100, and 150 ºC respectively. The crystal structures of final products of each layer were characterized by X-ray diffraction (XRD) technique. The surface morphology of $CH_3NH_3PbI_3/Zn_2SnO_4$/FTO films was observed by scanning electron microscope (SEM). The optimum drying temperature for perovskite absorber layer was found out to be 100 ºC for 30 min in air.

Keywords: perovskite, $CH_3NH_3PbI_3$, Zn_2SnO_4, spin coating, drying temperature, crystallite size

Introduction

Todays, environmental pollution is seriously causing due to the consumption of fossil energy globally. Thus, a great demand of renewable and sustainable energy sources is faced all over the world. The transformation of sunlight into electricity is considered one of the most hopeful researches to solve this situation without affecting the environment. Among the various kinds of solar cells, organic-inorganic hybrid perovskite solar cells (PSCs) have emerged as a potential candidate because of their high photovoltaic efficiency beyond 25% (Kheralla, A. and Chetty, N., 2021). Lead halide perovskites have great attention due to the development of simple thin-film deposition technology and low cost. They possess the outstanding photovoltaic performance including wide light harvesting in visible region, high absorption coefficients, low exciton binding energies, and long diffusion lengths high charge carrier mobility, and tunable direct bandgap (Dou, J., Zhang, Y., *et al*., 2019) and (Guo, R. *et al*., 2021). These properties lead to the candidates for the next generation of photovoltaic technology. The most commonly used perovskite absorber is methyl ammonium lead trihalide ($CH_3NH_3PbX_3$, where X is a halogen ion such as iodide, bromide, or chloride). It has an optical bandgap between ~1.55 and 2.3 eV, depending on halide content (Miah, M.H. *et al*., 2024).

The instability of PSCs is mainly depending on the environmental influences such as moisture, ultraviolet light, thermal, ion migration as well as the crystal structure, charge transporting layers (Wang, R. *et al*., 2019). It is remarkable that the crystal structure is influenced by the annealing temperature. The higher annealing temperatures and longer times can form the larger aggregated grains at the surface of the $MAPbI_3$ films (Rajendra Kumar, G. *et al*., 2016). To improve the photovoltaic performance, it is crucial to develop new materials for every layer of

[1] Department of Physics, East Yangon University
[2] Department of Physics, West Yangon University
[3] Department of Physics, University of Yangon

PSCs. They include the transparent conductive oxides layer, electron-transporting layers, perovskite absorber layers, hole-transporting layers and metal electrodes.

Among the key component in PSCs, the ETLs is largely affect for interfacial carrier extraction and electron transporting, which are significantly relevant to photovoltaic performance (Liu, X. *et al*., 2022).

For electron transporting layer of PSCs, stannate family has been greatly interested in the last decade because its photocatalytic properties such as high electrical conductivity and low visible absorption. The spinel type zinc stannate Zn_2SnO_4 is one of the important members of stannate family. It is a n-type semiconductor which has wide band gap of 3.6 eV and electron mobility of 10^{-15} cm^2 V^{-1} s^{-1} (Dou, J., Shen, D., *et al*., 2019). Because of its properties, it can be applied in many fields of applications such as gas sensor, synergistic flame retardants, solar cells, luminescence materials, anode electrode for Li-ion batteries, and degradation of organic pollutants (Mekprasart, W. *et al*., 2016). In this work, the effect of annealing temperature on the perovskite layer which is spin-coated on the electron transport layer of Zn_2SnO_4/FTO will be investigated.

Experimental Details

Preparation of Zn_2SnO_4/ FTO Film

Zn_2SnO_4 particles was synthesized by chemical precipitation method. Zinc sulfate heptahydrate ($ZnSO_4.7H_2O$) and tin (IV) chloride pentahydrate ($SnCl_4.5H_2O$) are used as the starting materials. Sodium hydroxide (NaOH) and distilled water (DW) are used as the precipitating agent and a solvent. Firstly, 2 M of $ZnSO_4.7H_2O$ solution and 1 M of $SnCl_4.5H_2O$ solution were separately prepared by DW. In addition, the zinc sulfate solution was sonicated for 30 min in order to get a homogeneous solution. Later, the two solutions were mixed and stirred for 30 min at room temperature. Then, pH of the solution was adjusted by using 1 M of NaOH until to become the pH 9.5. The solution was stirred for 6 h at 70 ºC and aged for 16 h. The white precipitates were rinsed with DW for several times until the pH of the solution became neutral. Finally, the precipitates were dried at 80 ˚C and they were grinded by agate mortar and pestle. The fine powder was calcined at 1000 ºC for 1 h. Finally, Zn_2SnO_4 particles were successfully obtained.

For the film formation, fluorine doped tin oxide coated *glass* (FTO) is used as a substrate. FTO substrate was cleaned by ultrasonic cleaning in ethanol, acetone and distilled water for 30 min in each solvent respectively. The Zn_2SnO_4/FTO film is prepared by spin coating method. 1 g of Zn_2SnO_4 is dissolved in 4 mL of mixed solvent containing IPA and ethanol (volume 1:1 %). The solution was stirred continuously for several days and Zn_2SnO_4 solution was obtained. 50 μL of Zn_2SnO_4 solution was spin coated onto the 1×1 cm^2 of FTO at 3000 rpm for 60 s. Then, Zn_2SnO_4/FTO film was dried at 100 ºC for 30 min inside the muffle furnace. The preparation procedure of Zn_2SnO_4/ FTO film is expressed in Figure 1.

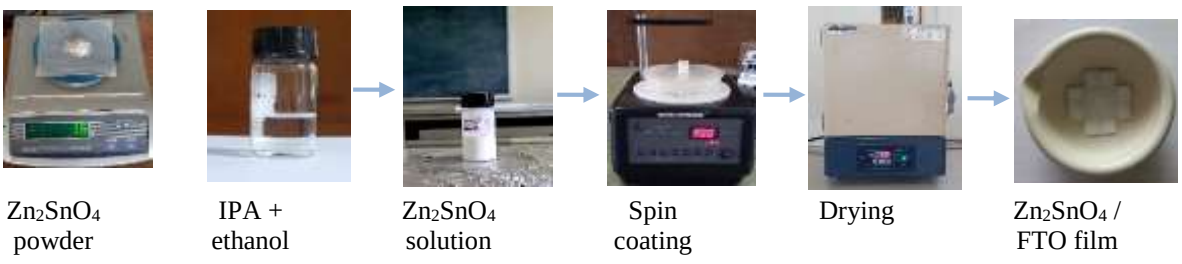

Figure 1. Photograph of the preparation of Zn_2SnO_4/ FTO film

Preparation of Perovskite Absorber Layer

Perovskite absorber layer ($CH_3NH_3PbI_3$) is prepared by two-steps spin coating method. In the first step, 2.305 g of PbI_2 powder was mixed with 5 mL of mixed solution containing dimethylformamide (DMF) and dimethyl sulfoxide (DMSO). The DMF to DMSO was volume 9:1 %. Then, PbI_2 solution was stirred at 60 ºC for 2 h and the well dissolved solution was filtered by filter paper. The clear PbI_2 filtrate was obtained. The thin PbI_2 film was spin-coated from a clear 50 μL of PbI_2 solution at 3,000 rpm for 30 s and 1500 rpm for another 30 s on **Zn_2SnO_4/FTO layer** in order to form the PbI_2/**Zn_2SnO_4/FTO layer**.

For the second step, CH_3NH_3I (MAI) solution was prepared by adding 0.0159 g of MAI into 1 mL of 2-propanol and it was stirred for 2 h. After that, 50 μL of MAI solution was spin-coated onto the previous layer to form $CH_3NH_3PbI_3$ perovskite films. Then, the films were dried at room temperature (RT), 60, 100 and 150 ºC in the muffle furnace for 30 min respectively. Finally, **$CH_3NH_3PbI_3$/Zn_2SnO_4/FTO film was successfully obtained.** The varying of drying temperature is carried out in order to investigate the crystallinity and crystallite size of perovskite layer for the further step in the fabrication of solar cell.

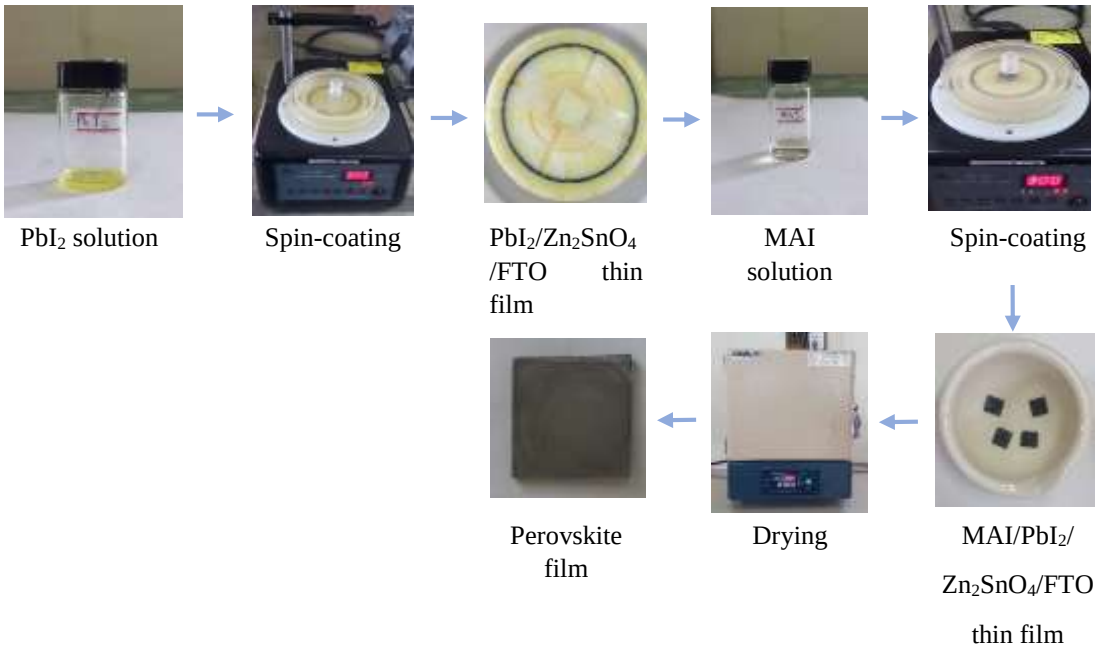

Figure 2 Photograph of the preparation of $CH_3NH_3PbI_3/Zn_2SnO_4$/FTO film

Results and Discussion

In this work, XRD measurements are carried out to confirm the electron collection layer (zinc stannate) and perovskite absorber layer ($CH_3NH_3PbI_3$). XRD spectra of Zn_2SnO_4 powder calcined at 1000 ºC for 1 h are shown in Figure 3(a). The X-ray diffraction peaks for (111), (220), (311), (222), (400), (331), (422), (511), (440), (531), (442), (620), (533), (622), (444) and (711) planes were confirmed that the formation of *inverse spinel structure* of Zn_2SnO_4 with *stable phase.* These Miller indices indicated that the zinc stannate is cubic crystal structure.

As indicated in Figure 3(b), the peak observed at the 14.01° was corresponded to the first reflection of the perovskite phase. All the remaining peaks were also related to $CH_3NH_3PbI_3$. The crystal structure of perovskite absorber layer was found out to be orthorhombic structure. The

average crystallite size of Zn_2SnO_4 and perovskite was calculated by the Debye-Scherrer Equation as below.

$$D = \frac{K\lambda}{\beta \cos\theta} \quad (1)$$

where,

λ = wavelength of the incident X-ray beam
K = shape factor
β = width at half maximum (FWHM)
θ = diffraction angle
D = crystallite size

The average crystallite size of Zn_2SnO_4 was obtained 66.50 nm. Table 1 is listed for the $CH_3NH_3PbI_3/Zn_2SnO_4$/FTO at different drying temperatures. The crystallite size was the smallest for the film dried at 100 ºC since most of the OH groups were removed at this temperature and thus the crystallite is the reduced. As a result, the biggest size is obtained at the lowest drying temperature. However, when the temperature was increased to 150 ºC, the size was tended to increase again due to thermal expansion (Zamkovskaya, A. *et al*. 2017).

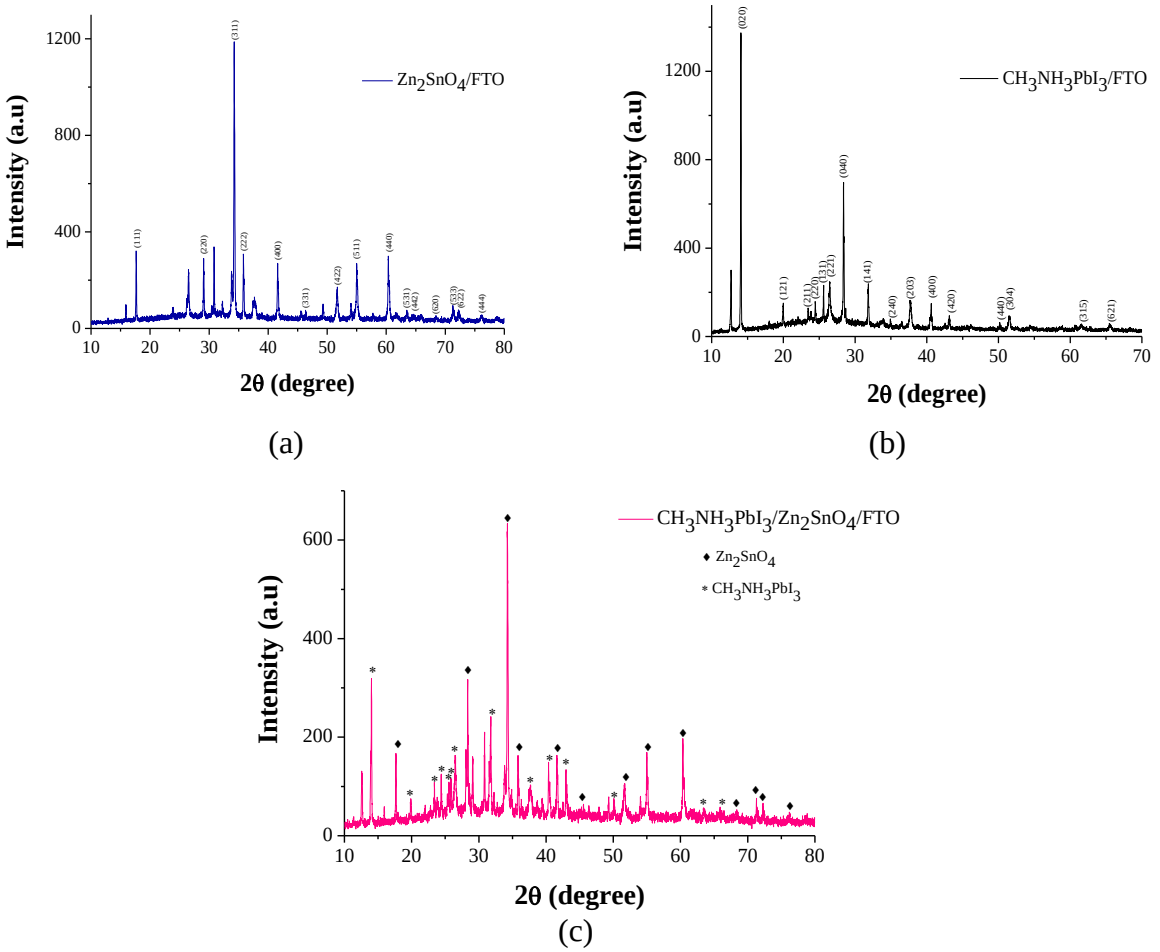

Figure 3 XRD spectrum of (a) Zn_2SnO_4/FTO film, (b) $CH_3NH_3PbI_3$/FTO film and (c) $CH_3NH_3PbI_3/Zn_2SnO_4$/FTO film

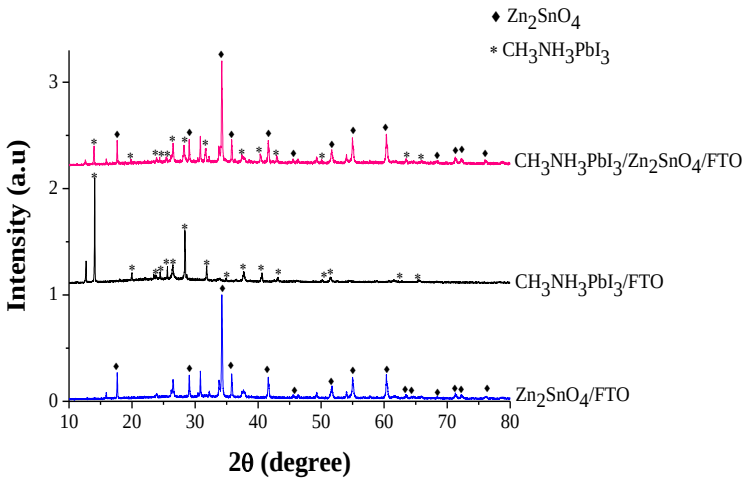

Figure 4 XRD spectra of different layers on FTO substrate

The typical XRD pattern of thin film dried at different temperatures are exhibited in Figure 5. The symbols * indicated the peaks from $CH_3NH_3PbI_3$. All the remaining peaks were corresponded to Zn_2SnO_4. In all temperatures, all perovskite peaks were found at 14.01°. However, the most intense peak of perovskite was occurred at 100 ºC among the different temperatures.

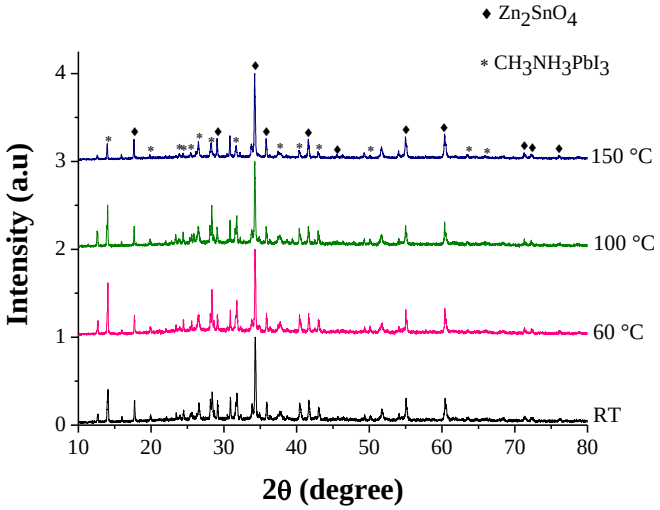

Figure 4 XRD spectra CH3NH3PbI3/ Zn2SnO4/ FTO film

Table 1. XRD parameters of $CH_3NH_3PbI_3$/ Zn_2SnO_4/ FTO film

Drying temperature (ºC)	Lattice parameters (Å)			Average crystallite size (nm)
	a	b	c	
RT	8.91	12.69	8.73	68.3
60	8.92	12.69	8.52	46.7
100	8.82	12.66	8.56	24.9
150	8.94	12.75	8.68	66.8

SEM measurement is conducted in order to study each layer formation in the film. The SEM micrograph in Figure 6 shows the cross-section of $CH_3NH_3PbI_3/Zn_2SnO_4$/FTO film. Glass, FTO, Zn_2SnO_4 and $CH_3NH_3PbI_3$ layers were distinctly observed in the image. This image supports the formation of each spin-coated layer that were previously presented in the XRD results.

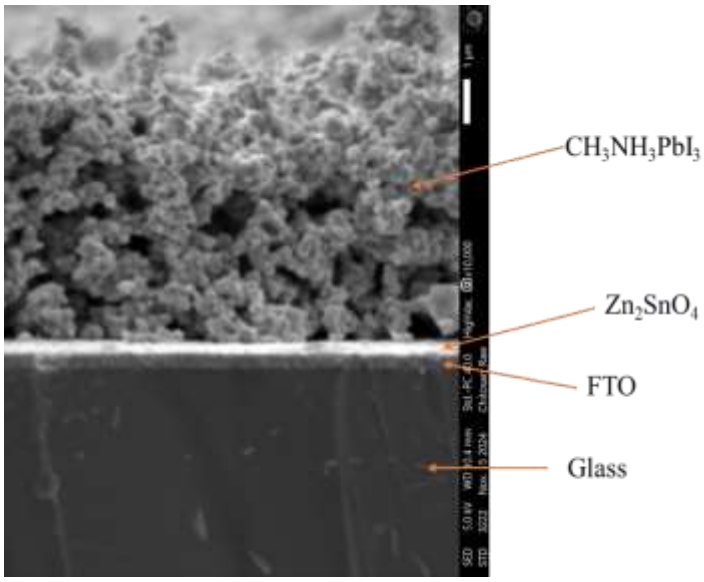

Figure 6 Cross-section SEM image of $CH_3NH_3PbI_3/Zn_2SnO_4$/FTO film

Conclusions

Methyl ammonium lead iodide ($CH_3NH_3PbI_3$), perovskite absorber layer, on zinc stannate (Zn_2SnO_4) was successfully prepared by two-steps spin coating method. Zn_2SnO_4 was synthesized by chemical precipitation method. According to XRD results, the crystal structure of Zn_2SnO_4 and $CH_3NH_3PbI_3$ were cubic and orthorhombic respectively. The crystallite sizes estimated by Debye-Scherrer formula was occurred 66.5 nm for Zn_2SnO_4 and 68.3, 46.7, 24.9 and 66.8 nm respectively for $CH_3NH_3PbI_3$ at RT, 60, 100 and 150 ºC. The sharpest peak for finger print of perovskite and the smallest crystallite sizes were observed at 100 ºC. Although the crystallite depending on drying temperatures were changed, they have the crystal structures. Thus, it can be concluded that 100 ºC is the optimum the drying temperature for the formation of perovskite layer.

Acknowledgements

We would like to acknowledge to Prof Dr Nay Win Oo, Rector, East Yangon University, for his encouragement and allowing us to participate in this event. Our special thanks go to Dr Hmwe Hmwe Kyu, Professor and Head of Department of Physics, East Yangon University, for her kind permission to contribute this work excellent discussion.

References

Dou, J., Shen, D., et al. (2019) 'Highly Efficient Perovskite Solar Cells Based on a Zn2SnO4 Compact Layer', ACS Applied Materials and Interfaces, 11(40), pp. 36553–36559. Available at: https://doi.org/10.1021/acsami.9b09209.

Dou, J., Zhang, Y., et al. (2019) 'Highly efficient Zn2SnO4 perovskite solar cells through band alignment engineering', Chemical Communications, 55(97), pp. 14673–14676. Available at: https://doi.org/10.1039/c9cc07398a.

Guo, R. et al. (2021) 'Ambient processed (110) preferred MAPbI3thin films for highly efficient perovskite solar cells', Nanoscale Advances, 3(7), pp. 2056–2064. Available at: https://doi.org/10.1039/d0na01029d.

Kheralla, A. and Chetty, N. (2021) 'A review of experimental and computational attempts to remedy stability issues of perovskite solar cells', Heliyon, 7(2), p. e06211. Available at: https://doi.org/10.1016/j.heliyon.2021.e06211.

Liu, X. et al. (2022) 'Area-Scalable Zn2SnO4Electron Transport Layer for Highly Efficient and Stable Perovskite Solar Modules', ACS Applied Materials and Interfaces, 14(20), pp. 23297–23306. Available at: https://doi.org/10.1021/acsami.1c24757.

Mekprasart, W. et al. (2016) 'Synthesis and characterization of cubic-like zinc stannate powders prepared by co-precipitation method', Chiang Mai Journal of Science, 43(2), pp. 345–350.

Miah, M.H. et al. (2024) 'Band gap tuning of perovskite solar cells for enhancing the efficiency and stability: issues and prospects', RSC Advances, 14(23), pp. 15876–15906. Available at: https://doi.org/10.1039/d4ra01640h.

Rajendra Kumar, G. et al. (2016) 'Phase transition kinetics and surface binding states of methylammonium lead iodide perovskite', Physical Chemistry Chemical Physics, 18(10), pp. 7284–7292. Available at: https://doi.org/10.1039/c5cp06232b.

Wang, R. et al. (2019) 'A Review of Perovskites Solar Cell Stability', Advanced Functional Materials, 29(47), pp. 1–25. Available at: https://doi.org/10.1002/adfm.201808843.

Zamkovskaya, A. et al. (2017) 'X-ray diffraction investigations of the thermal expansion of iron borate FeBO3 crystals', Journal of Physics: Conference Series, 929(1). Available at: https://doi.org/10.1088/1742-6596/929/1/012030.

CONSTRUCTION OF PHOTODIODE BASED ACTIVE DETECTOR FOR RADON DETECTION

Myint Myint Win[1], Hnin Yu Khaing[2], Kyaw Kyaw[3]

Abstract

The main objective of this research work is to construct and analyze the photodiode based active detector for radon detection in air. It was intended to operate in pulse counting mode for real-time measurements. The constructed system is relatively simple, low-cost and reproducible, made of inexpensive and easy to acquire electronics components. The commercial low-cost Si-PIN planar photodiode SLCD-61N5 with an area of 10×10 mm^2 was used as a sensor for detection of alpha particles. An ATmega2560 microcontroller (MCU) based Arduino MEGA development was interfaced to the electrical circuit of the device to count the logic pulses and connected to a computer to send and save the detected data. Electrical pulse signals corresponding to the strike of the alpha particles on the photodiode, distinguishable from noise, were observed in the radon detection analysis. It was observed that the sensitivity response of the constructed system increased with a higher reverse voltage applied to the photodiode. The stability of the constructed radon detector was also analyzed for long-term measurements. It could be said that the constructed system detected the presence of radon gas in order to obtain exact concentrations values in air.

Keywords: Radon, alpha particles, photodiode, Arduino MEGA, concentration

Introduction

Radon, ^{222}Rn, is a naturally occurring gas. It is colorless, odorless, tasteless, almost chemically inert, and radioactive. It is the heaviest noble gas with the highest melting point, boiling point, critical temperature, and critical pressure. Radon is also soluble in cold water and such property increases the mobility of the gas in the environment [*UNSCEAR and UNEP*]. Radon is a radioactive gas that occurs naturally from the decay of ^{238}U. These elements could present in rocks, soils and even in building materials that contain radon progenitor radionuclides. After its formation, the gas diffuses into the atmosphere and tends to get into the buildings. Houses built in sites with a high concentration of radon can lead to an accumulation of this gas and consequently turning to be an important risk factor for human health [*Cothern C., et al*]. The main concern is not due to the gas itself but it is due to the solid short half-life decay products produced as free ions. As a consequence of the strong probability for these ions to be electrostatically attached to aerosols, these clusters can remain in suspension, being easily inhaled and deposited in different regions of the respiratory tract. Some of the radon progeny emit alpha particles that react strongly with matter depositing all their energy in a small volume in the lung tissue. Consequently, these constant irradiation damages the cells and can lead to the increase of probability of getting lung cancer [*Lubin H., et al*]. Exposure to ionizing radiation from natural sources is continuous and inevitable for all living organisms. About 13% of the radiation origin can be from outer space, like cosmic rays, and 67% as terrestrial radionuclides from the Earths' crust present everywhere in the environment including in the human body. Due to their short range, just a few centimeters(cm)s in air, the detector should be placed near the source. The development of photodiode based active detector for radon monitoring will allow continuous evaluation of radon levels in short-term and long-term measurements. In this research

[1] Department of Physics, Mandalay University of Distance Education
[2] Department of Physics, Mandalay University of Distance Education
[3] Department of Physics, University of Mandalay

photodiode based active detector for radon detection was constructed by using Arduino ATmega2560 microcontroller, GLCD and Si-PIN photodiode.

Radon measurement system consists of a chamber within a silicon photodiode was placed inside. Radon from surrounding air entered by diffusion or actively pumped into the chamber and the positively charged progeny are collected on the surface of the photodiode [*Takeuchi Y., et al*]. Then when the charged alpha particles, from the progeny decay, stroked the surface of the photodiode its energy was absorbed along its track whose length was dependent on the energy of the incident particle. Electron/hole pairs were created in its path by coulomb interactions between the ionizing particle and the detection material. The electron/hole pairs were then separated by the electric field present in the photodiode junction in opposite directions. The photodiode operated in reversed bias mode, so electrons and holes migrated to the n-layer (cathode) and p-layer (anode), respectively, generating a flow of current in an external circuit. The produced charge was proportional to the energy of the particle incident [*Knoll F., et al*]. Fig 1 shows the schematic diagram of a Si-PIN photodiode cross section for charged particle detection.

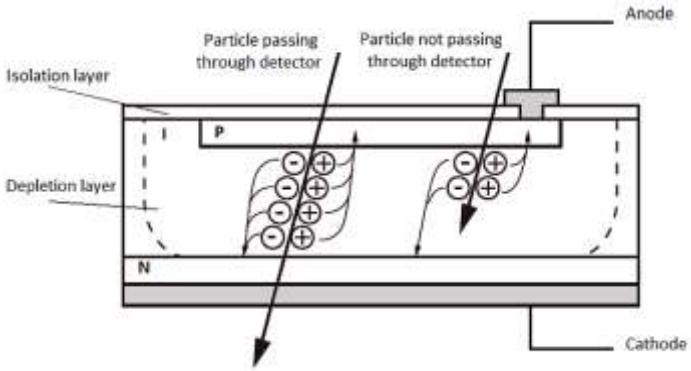

Figure 1. Schematic diagram of a Si-PIN photodiode cross section for charged particle detection [*HAMAMATSU*].

Photodiodes have a number of advantages such as good quantum efficiency, small ionization energy, good energy resolution, high stability, response timing characteristics, compact in size, low cost and simplicity of operation. However, electronic noise is a major problem due to the small signal amplitude. In this study, Si-PIN photodiode SLCD-61N5 was used as alpha particles detector for radon detection in air. Despite the desirable feature of superior energy resolution, a simple approach of pulse counting related with radon detection was taken in this work. The construction of photodiode based active detector for radon detection was divided into three main parts: the detector, preamplifier and signal processing, and the data acquisition system for pulse counting. A block diagram of hardware system for radon detection system is illustrated in Fig 2.

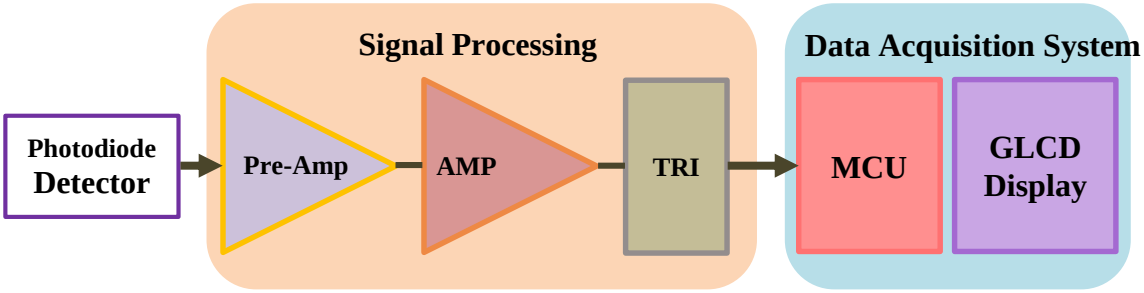

Figure 2. The block diagram of hardware system for radon detection system.

System Components and Circuit Operation

A low-cost photodiode SLCD-61N5 was used to detect alpha particles from the decay of radon and its progeny, under room temperature conditions. The active area of the photodiode is 10×10 mm^2. To achieve an efficient collection of charge created by the incident particles, and reverse external voltage was applied to the photodiode. For the SLCD-61N5 photodiode, the breakdown voltage is -20 V. The designed preamplifier circuit for photodiode is shown in Fig 3. The serial connected resistor R1 limited the reverse biasing current to avoid the increasement of the leakage current. The coupling capacitor C1 blocked the DC bias signals and coupled the detected ac signals from the collected charges. When a charged particle strikes the sensitive area of the photodiode a small current is generated with the amplitude proportional to the deposited energy. This current signal could be converted to a voltage signal using a transimpedance amplifier. Since the photodiode polarity was reversed and the current signal entered on the negative input of the op-amp, the output of the preamplifier would be a positive pulse. In order to have a conversion without significant degradation of the intrinsic signal-to-noise ratio, the preamplifier must be located as close as possible to the detector diode and the op-amp used must have a FET (Field-Effect Transistor) input stage. The op-amp employed in this research work was a dual LF442 low power JFET input operational amplifier, with high gain bandwidth (1 MHz) and high slew rate (1 V/μs) according to its specifications.

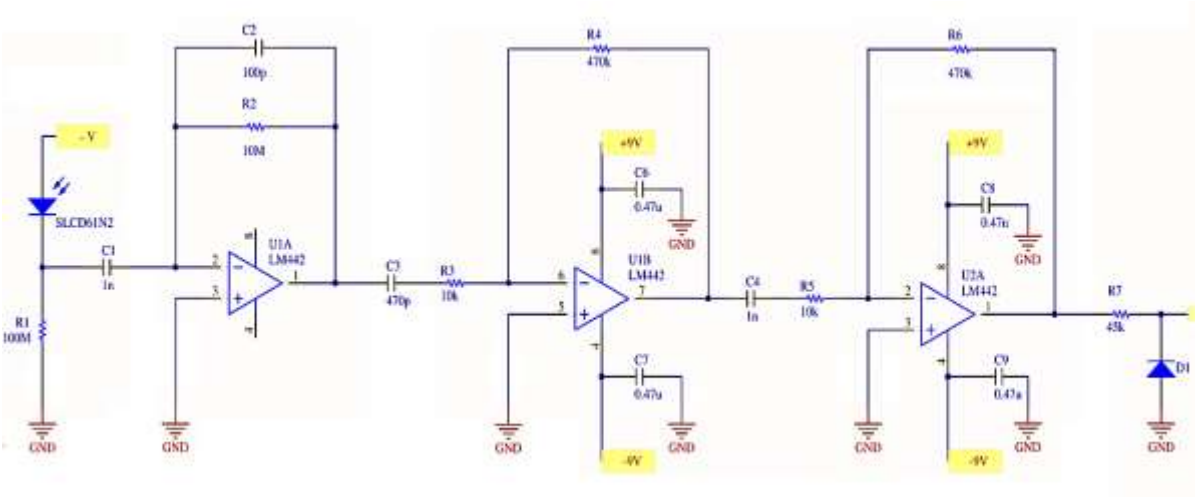

Figure 3. The constructed preamplifier circuit for photodiode detector.

When the sensor was exposed to the radon rich atmosphere, alpha particles could be detected with the maximum energy of 7.69 MeV, which corresponds to the decay of the ^{214}Po radon daughter. The maximum output voltage of the signal to be in the order of magnitude of a

few 27 mV. In order to increase the amplitude of this signal from the mV range into the 1 V ~ 5 V range, and to make the possible accurate pulse detection, two stages of amplification were implemented. The resistors R4 and R6 set the voltage gain in the order of two thousand, being sufficient for the output signal to be in the desired range. The coupling between amplifiers was conducted by coupling capacitors also working as filters. A diode limiter circuit was placed on the output of the amplifier to limit the negative phase of the amplifier output signal. For counting the pulses from radiation detector, amplifier output signal was converted into logic pulses with a discriminator that produced a logic pulse, with a fixed height, when the input pulse is above a certain threshold level. This allowed to reject noise and small pulses from background radiation. The logic pulse represented the information that was recorded only the presence or absence of a particle hitting the detector.

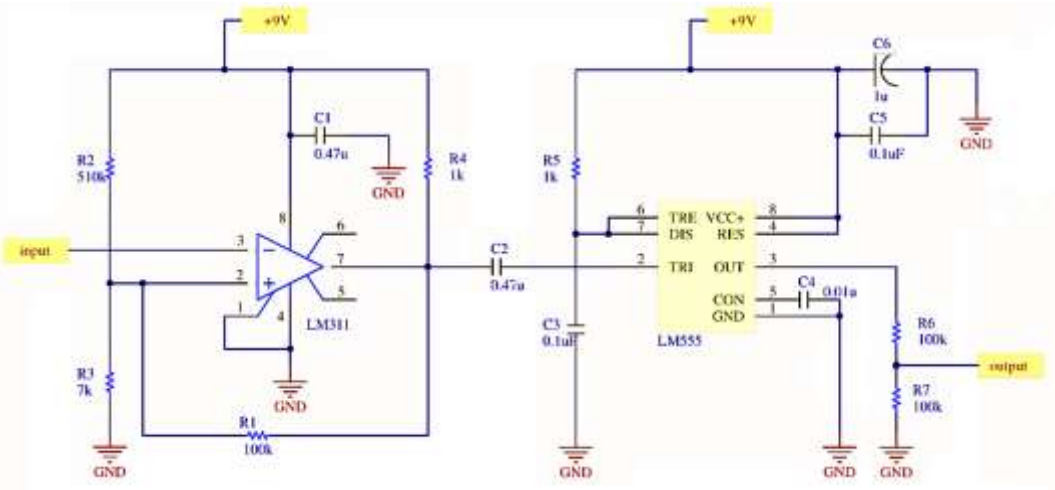

Figure 4. LM311 and NE555 based discriminator and pulse trigging circuit.

LM311 and NE555 based discriminator and pulse trigging circuit is illustrated in Fig 4. Due to the comparator input signal being noisy around the threshold value, a feedback resistor R1 was implemented. The function of this resistor was to make the circuit have two input thresholds, instead of just one, preventing multiple triggering and consequently false pulse detection. The output signal was fed to the Arduino MEGA to count, store and display the number of pulses detected, corresponding to the presence of the radon in the air. The signal entering into the Arduino was a square impulse. The transition of a state from LOW to HIGH means one interaction on the photodiode, and consequently one more count. When one of these signals arrive at Arduino's interrupt pin, an interrupt to the microcontroller was obtained and logic state changed value (from LOW to HIGH). These operations were controlled by software to take account when the signal is rising. To count the number of detected impulses, the state variable was checked and recorded the number of impulses detected at 10 minutes intervals. And the obtained results were displayed on the LCD and the count variable was reset.

Results and Discussion

Performance Analysis

To analyze the performance of the constructed circuit, ac signal output from the function generator was fed to the photodiode detector input and measured the voltage response at three different test points (TP) on the circuit. TP1 corresponded to the amplifier output, TP2 analyzed the trigger output, and TP3 checked the NE555 timer output. Due to the mixing with noise, the output signal of the preamplifier was not observable with the digital oscilloscope. Fig 5 shows the signal observed at TP1 in absence of incident charged particles. Since its amplitude, about

100 mV, was lower than trigger threshold, no signal was observed at TP2 and TP3. The measurement of this signal amplitude was important to get a reasonable future threshold value. Fig 6 and Fig 7 show the signals observed at TP1, TP2 and TP3 when the uranium salt-based photo-luminance object was placed above the photodiode detector. The amplitude of the pulses at TP1 was in a range from 400 mV to 1.8 V. It was sufficient to set the trigger and characteristic signals were observed at TP2 and TP3. It could be seen that the signal from TP1 was a positive pulse whose amplitude was much higher than the noise. According to the presence of these signals, it could identify them as the interactions of charged particles in the photodiode.

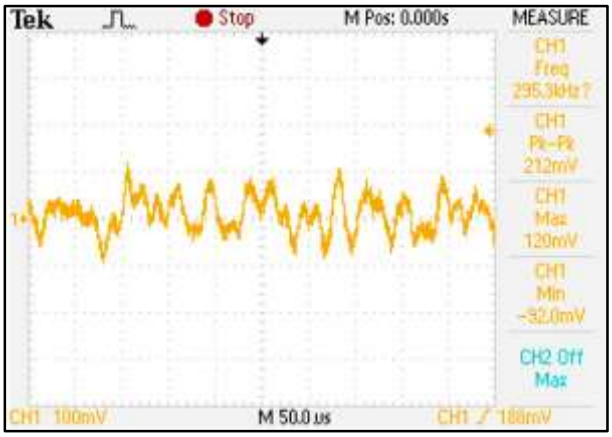

Figure 5. The signal observed at TP1 in absence of incident charged particles.

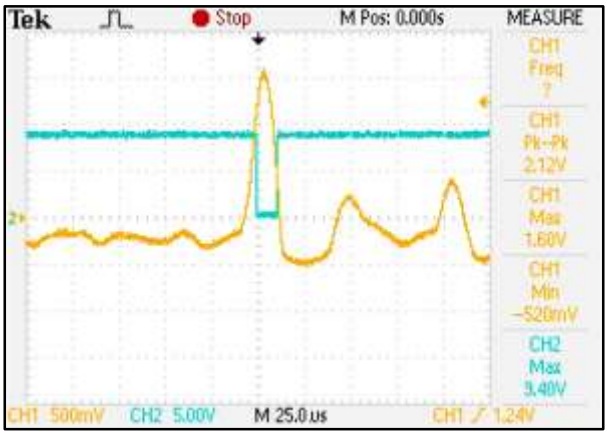

Figure 6. The signals observed at TP1(orange) and TP2(cyan) when the charged particle was detected.

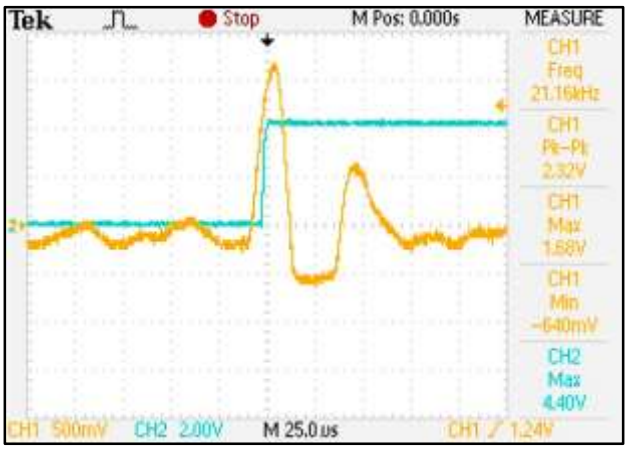

Figure 7. show the signals observed at TP1(orange) and TP3(cyan) when the charged particle was detected.

Detection Response Analysis with Biasing Voltage

Fig 8 illustrates the measurement results of the constructed radon detection system for three different values of biasing voltage. Each experimental dot corresponds to the sum of counts acquired in a ten-minute interval.

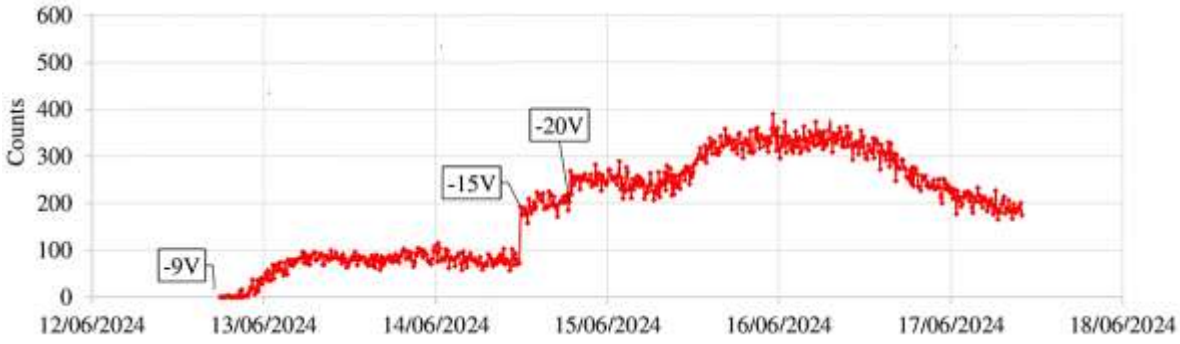

Figure 8. The measurement results of the constructed radon detection system for three different values of biasing voltage.

When the applied biased voltage of -9 V, it was possible to observe a progressive increase in the number of counts. However, it did not show sufficient sensitivity to detect radon level fluctuations. When biased at -15 V, it could be seen an increase in the number of counts but a sufficient acquisition was not acquired. It could be compared with -9V biasing voltage, there was no distinguishable peaks were observed. With the applied voltage of -20 V, the sensitivity of the constructed detector increased and it was being possible to observe the radon level fluctuations. Therefore, the detection response was shown to be affected by the biased voltage applied to the photodiode, with the increase of the biased voltage, increasing the sensitivity of the detector. It could be said that this effect may be due to the increase of the electrostatic attraction or due to the larger collection of charges in the depletion region of the junction of the photodiode. It was also estimated that the acquisition time necessary to have the required data statistics was observed about 4 days to 1 day respectively.

Conclusion

In this research work, active sensor for radon detection in air was designed and constructed with silicon PIN photodiode working in counter mode. It is remarkable that the detector has a low fabrication cost, and it has a good performance for alpha particle detection. The design of the detector circuit was mainly focus on that simply counted the pulses generated by the charged particles hitting the photodetector. The signal generated by the sensor fed an electronic circuit composed of LF442 op-amp based preamplifier and transimpedance amplifier, LM311 based discriminator, NE555 timer and data logging and display system with Arduino MEGA development board which can also connect to a computer for data acquisition. The detection response of the constructed system was carried out with different biasing potential -9 V, -15 V and -20 V. It was observed that the detection response was affected by the applied potential to the photodiode, increasing the sensitivity of the detector with the increase of the biasing voltage. Despite the low bias voltage, in all cases it was possible to detect pulses since the deposited energy was high enough to generate pulses above the electronic noise. The constructed radon detector could be implemented as portable device for working powered only with batteries, and using a memory card shield attached to the Arduino to store the data.

Acknowledgements

I would like to express my special thanks to Rector, Dr Khin Thant Sin and Pro-Rector, Dr Win Mar and Dr Lae Lae Kyaing Mandalay University of Distance Education for giving permission to submit this research paper. The author would like to thank Professor Dr Wah Wah Thin, Head of Department of Physics and Professor Dr Soe Soe Oo, Department of Physics, Mandalay University of Distance Education, for their kind permission to carry out this research. I have appreciated the support I received from everyone who gives me unconditional support and aid.

References

Cothern, C. R., and J.E. Smith, (2013) Environmental Radon. *Springer Science & Business Media*, ISBN 978-1-4899-0475-1.

HAMAMATSU. Opto-semiconductor Handbook: Si detectors for high energy particles (Chapter 10). accessed 11th july 2018. https://www.hamamatsu.com/sp/ssd/doc_en.html.

Knoll G. F., (2009) Radiation detection and measurement. Wiley India Pvt. Ltd.

Lubin, J.H., J.D. Boice, C. Edling., and R.W. Hornung, (1995) "Lung cancer in radon-exposed miners and estimation of risk from indoor exposure" *JNCI: Journal of the National Cancer Institute*, vol. 87(11), pp. 817–827.

Takeuchi, Y., K. Okumura, and H. Okazawa, (1999) "Development of high sensitivity radon detectors" *Nuclear Instruments and Methods in Physics Research Section A: Accelerators, Spectrometers, Detectors and Associated Equipment*, vol. 421(1-2), pp. 334–341.

UNEP. (2016) Radiation: Effects and Sources. *United Nations Environment Programme*, ISBN 978-92-807-3517-8

UNSCEAR. (2000) Sources and effects of ionizing radiation: sources, Vol 1. *United Nations Scientific Committee on the Effects of Atomic Radiation publications*, ISBN 92-1-142238-8.

INVESTIGATING PROTON STOPPING POWER AND RANGE IN ALUMINUM TARGETS

Zin Zin Phyoe[1], Thandar Oo[2], Htun Htun Oo[3]

Abstract

Proton beams biological effects depend on their stopping power, defined as the rate at which a material absorbs the kinetic energy of a charged particle. The Bethe-Bloch formula is used for the calculations of stopping power of proton in aluminum, the incident proton energies ranging from 0.1 MeV to 100 MeV. The mean excitation energy which is a crucial parameter is also explored for accurate stopping power calculations. Stopping power and range values were computed using a FORTRAN-90 program, showing close agreement with SRIM-2013 databases.

Keywords: proton, Bethe-Bloch formula, aluminum, mean excitation energy, stopping power

Introduction

The interaction of energetic charged particles, such as protons, with matter spans in various fields including particle physics, medicine, and materials science. Among the fundamental quantities characterizing this interaction, stopping power and range are of paramount importance. Stopping power denotes the rate of energy loss experienced by a charged particle as it traverses a material, while range represents the distance a particle can travel before coming to rest. Understanding these parameters is crucial for a wide range of applications, including proton therapy, ion implantation and particle detection.

In this research, we focus on elucidating the stopping power and range of protons in aluminum, a widely used material in various technological and industrial domains. Despite its seeming simplicity, the interaction of protons with aluminum involves complex physical phenomena, including electronic and nuclear stopping mechanisms, scattering processes, and energy transfer mechanisms. The dependence of stopping power and range on factors such as proton energy, target material properties and experimental conditions necessitates a comprehensive investigation for precise modeling and practical utilization [1][2][3].

The motivation behind this study stems from the necessity to enhance our understanding of proton-matter interactions in aluminum and to provide accurate data for applications spanning from materials engineering to radiation therapy. By employing state-of-the-art theoretical models, computational simulations, and experimental techniques, we aim to discern the intricate interplay of factors governing proton penetration into aluminum and unravel the underlying physics governing stopping power and range [4][5][6].

This research paper is organized as follows: We begin by presenting a brief overview of the theoretical framework underpinning proton stopping power and range calculations. Subsequently, we delve into the specific characteristics of aluminum as a target material, outlining its structural properties and relevance in various technological domains. Following this, we detail the methodologies employed in our investigation, encompassing computational simulations and experimental setups designed for precise measurements. We then present and analyze our results, highlighting the dependence of stopping power and range on key parameters

[1] Department of physics, Meiktila University
[2] Department of physics, Meiktila University
[3] Department of physics, Yadanabon University

such as proton energy and target thickness, with a comparison to established databases like SRIM-2013. Finally, we discuss the implications of our findings and their significance for applications ranging from proton therapy to materials science.

Through this interdisciplinary endeavor, we aspire to contribute to the burgeoning field of proton-matter interactions, offering valuable insights into the behavior of charged particles in aluminum and paving the way for advancements in diverse technological realms.

Background Theory

Bohr's formula for stopping power is derived from a classical perspective and provides a fundamental understanding of the energy loss of heavy charged particles, such as protons, as they traverse a material. The formula is expressed as [7]:

$$-\frac{dE}{dx} = \frac{Z^2 e^4 n}{4\pi\varepsilon_0^2\, m_e\, v^2}\left[\ln\left(\frac{2m_e v^2}{\langle I\rangle}\right)\right] \tag{1}$$

This equation can be simplified as

$$-\frac{dE}{dx} = \frac{4\pi(\hbar c)^2 Z^2 \alpha^2 n}{m_e c^2 \beta^2}\left[\ln\left(\frac{2m_e c^2 \beta^2}{\langle I\rangle}\right)\right] \tag{2}$$

This relation was first derived by Bohr and is known as Bohr's relation for stopping power. Complete relativistic calculations were performed by Bohr and Bethe and they modified Bohr's stopping power relation as

$$-\frac{dE}{dx} = \frac{4\pi(\hbar c)^2 Z^2 \alpha^2 n}{m_e c^2 \beta^2}\left[\ln\left(\frac{2m_e c^2 \beta^2}{\langle I\rangle(1-\beta^2)}\right) - \beta^2\right] \tag{3}$$

This relation is also known as the Bethe-Bloch formula.

where:

$\frac{dE}{dx}$ represents the energy loss per unit path length.

$\hbar$ is the reduced Planck's constant.

c is the speed of light.

α is the fine structure constant.

n is the electron density in the stopping material.

m_e is the electron rest mass.

Z is the atomic number of the incident particle.

β is the velocity of the incident particle relative to the speed of light.

$\langle I \rangle$ is the mean excitation energy of the target material.

This formula illustrates the complex interplay between various factors such as atomic properties, particle velocity, and material characteristics in determining the energy loss of charged particles in matter. An approximate equation of $\langle I \rangle$ for $Z > 12$ [8] is,

$$\langle \mathrm{I} \rangle \text{ eV} = (9.76 + 58.8\, \mathrm{Z}^{-1.19})\, \mathrm{Z} \tag{4}$$

Range of Charged Particles

Heavy charged particles lose small fraction of energy in each collision and suffer a large number of collisions before they are finally stopped by the medium. During this motion, they move in a straight line in the forward direction. The average distance travelled by a charged particle before it comes to rest is called the range of the charged particle. To derive an expression for the range of charged particle, let $\boldsymbol{E_i}$ be the kinetic energy at the time of entry in the medium and assume that it loses *dE* energy in travelling a distance *dx*. So, the range R is

$$R = \int_{E_i}^{0} dx = -\int_{0}^{E_i} dx \tag{5}$$

By changing variable,

$$\boldsymbol{R} = \int_{0}^{\mathrm{E_i}} \left(-\frac{\mathrm{dE}}{\mathrm{dx}}\right)^{-1} (-\mathrm{dE}) = \int_{0}^{\mathrm{E_i}} \left(\frac{\mathrm{dE}}{\mathrm{dx}}\right)^{-1} \mathrm{dE} \tag{6}$$

This equation cannot solve analytically and we use numerical method.

Results and Discussions

The stopping power for protons traversing in material is similar to that for heavy charged particles. The interaction of incident protons with atomic electrons in aluminum, leading to excitation and ionization, can be calculated from Bethe's theory, and it is called the "Collisional Stopping Power" such as the electronic stopping power. For these calculations, we use the Eq. (3) with the help of FORTRAN-90 program. The incident energies of protons 0.1 MeV-100 MeV are used in the stopping power calculation. In running the program for calculation, the density of aluminum 2.702 gcm^{-3} and electron charged density ($\mathbf{n = 7.841 \times 10^{23}\, \frac{atoms}{cm^3}}$) are used, these values are shown in Table 1. This study also explores the mean excitation energy for aluminum, essential for accurate stopping power calculations. Thus, firstly in running the program, we use the mean excitation energy $\langle\, \mathbf{I} \,\rangle$ in Eq. (4) for aluminum targets. But, the data results are little different when the comparison with the databases in SRIM-2013 code. Thus, when we fit the mean excitation energy at $\langle\, \mathbf{I} \,\rangle = \mathbf{166\ eV}$, the results are observed that good in agreement with the results in SRIM-2013 code which are shown in Table 2. In which, we also present the error percentage between these two results. Figure 1 shows the two results are observed that good in agreement in the energy range from 0.1 MeV - 100 MeV. According to this figure, the incident energy of proton increases, the stopping power decreases in material. For the calculations of proton range, Eq. (6) is used. Table 3 shows the difference between the values of the range of proton in aluminum with the FORTRAN-90 program and SRIM-2013 code values. According to these results, increases the range of proton in target material while increasing the incident energy of the proton. The results are good in agreement as shown in Figure 2 between 0.1 MeV - 100 MeV.

Table 1. Basic Data Used in Calculations

Target	**Density(ρ) g/cm^3**	**Atomic number Z**	**Mass number A**	**n ($\frac{atoms}{cm^3}$)**
Aluminum	2.702	13	26.98154	7.841×10^{23}

Table 2 The proton energy in MeV and comparison between the FORTRAN-90 program and SRIM-2013 code for the stopping power of proton in aluminum

Energy of proton (MeV)	**Stopping Power of proton in aluminum (MeVcm^{-1})**		
	Results by FORTRAN-90	**Results by SRIM-2013**	**Error%**
0.1	509.61	1215.62	58.07
0.2	904.72	1007.84	10.23
0.3	856.74	858.69	0.22
0.4	777.52	754.39	3.06
0.5	705.83	677.66	4.15
1	483.20	472.57	2.25
2	307.04	299.38	2.55
3	230.38	225.23	2.28
4	186.56	182.95	1.97
5	157.86	155.20	1.71
6	137.46	135.45	1.48
7	122.14	120.56	1.31
8	110.18	108.92	1.15
9	100.55	99.51	1.04
10	92.61	91.76	0.93
20	53.60	53.39	0.39
30	38.85	38.80	0.14
40	30.95	30.93	0.09
50	25.99	25.99	0.01
60	22.56	22.57	0.00
70	20.05	20.06	0.01
80	18.13	18.13	0.00
90	16.60	16.62	0.07
100	15.36	15.37	0.03

Table 3 Proton range in aluminum target and energy for proton in 0.1 MeV - 100 MeV

Energy of proton (MeV)	Ranges of proton in aluminum (cm)		
	Results by FORTRAN-90	Results by SRIM-2013	Error%
0.1	2.0×10^{-4}	8.45×10^{-5}	136.60
0.2	3.3×10^{-4}	1.73×10^{-4}	90.75
0.3	4.3×10^{-4}	2.80×10^{-4}	53.57
0.4	5.6×10^{-4}	4.03×10^{-4}	38.95
0.5	6.9×10^{-4}	5.42×10^{-4}	27.30
1	1.57×10^{-3}	1.43×10^{-3}	9.79
2	4.24×10^{-3}	4.16×10^{-3}	1.84
3	8.06×10^{-3}	8.04×10^{-3}	0.27
4	1.29×10^{-2}	1.29×10^{-2}	0.15
5	1.88×10^{-2}	1.88×10^{-2}	0.16
6	2.56×10^{-2}	2.58×10^{-2}	0.89
7	3.33×10^{-2}	3.35×10^{-2}	0.59
8	4.19×10^{-2}	4.22×10^{-2}	0.61
9	5.14×10^{-2}	5.18×10^{-2}	0.67
10	6.18×10^{-2}	6.22×10^{-2}	0.61
20	2.09×10^{-1}	2.11×10^{-1}	0.52
30	4.32×10^{-1}	4.33×10^{-1}	0.23
40	7.24×10^{-1}	7.23×10^{-1}	0.06
50	1.08×10^{0}	1.08×10^{0}	0.20
60	1.49×10^{0}	1.49×10^{0}	0.20
70	1.96×10^{0}	1.96×10^{0}	0.25
80	2.48×10^{0}	2.48×10^{0}	0.29
90	3.06×10^{0}	3.06×10^{0}	0.26
100	3.68×10^{0}	3.68×10^{0}	0.27

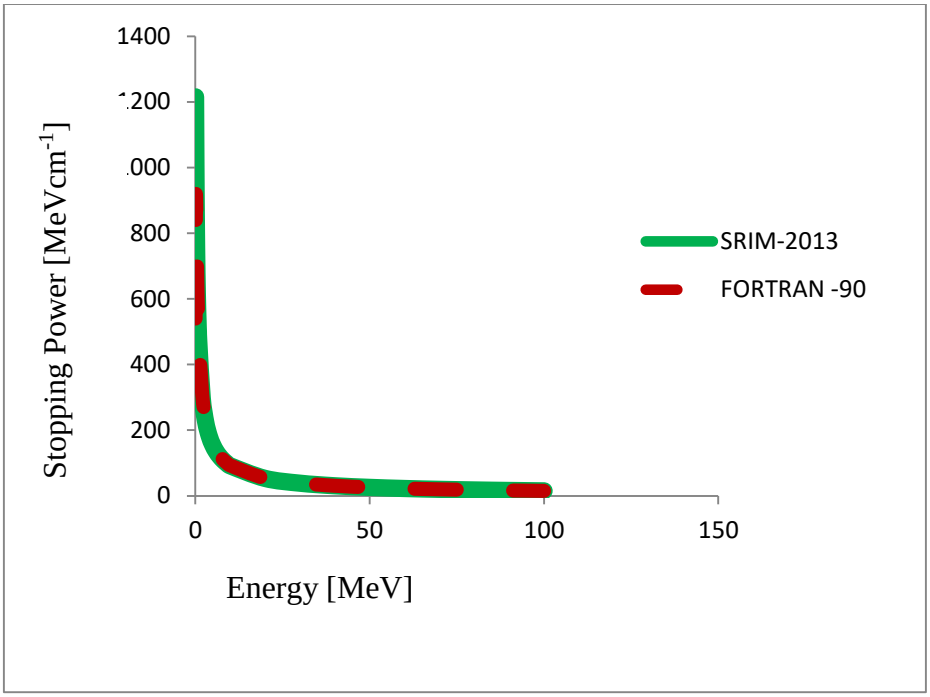

Figure 1 Plot of the stopping power of proton versus energy in aluminum for the FORTRAN-90 results with the mean excitation energy ⟨ I ⟩ = 166 eV and SRIM-2013 code

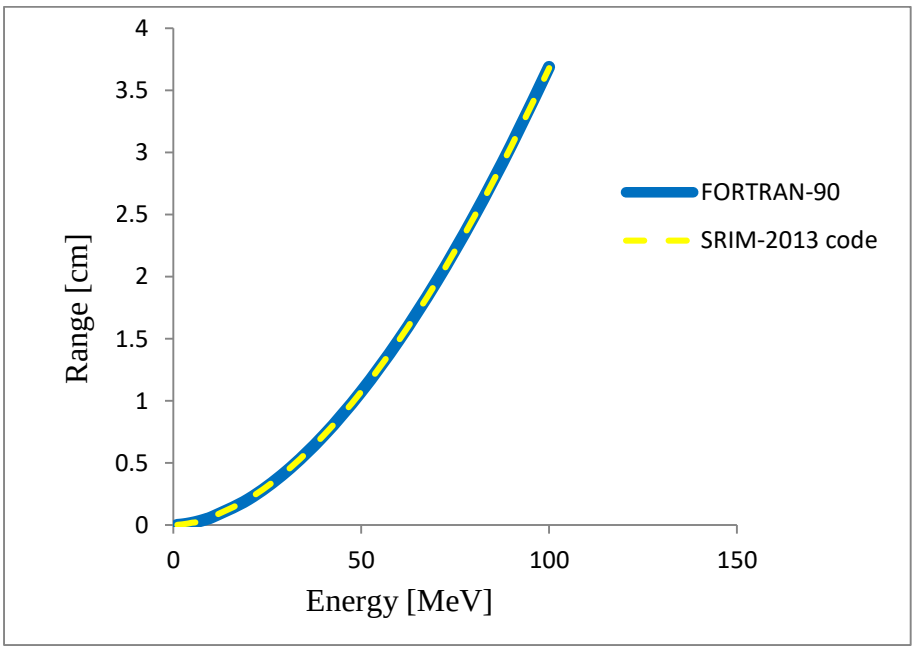

Figure 2 Plot of the proton range values versus proton energy in aluminum with the mean excitation energy ⟨ I ⟩ = 166 eV for the FORTRAN-90 results comparison with SRIM-2013 code

Conclusion

This research has effectively demonstrated the use of the Bethe-Bloch formula to determine the stopping power and range of protons in aluminum targets. The calculated values using the FORTRAN-90 program which are align closely with the standard values provided by

the SRIM-2013 code. Our results confirm that as the incident energy of protons increases, their stopping power decreases, while the protons range in the target material increases. Aluminum is strong and durable which is much lighter than other materials, providing effective protection against radiation without compromising structural integrity. Compared to other materials, aluminum is relatively inexpensive and widely available, making it a cost effective choice for radiation shielding. These properties make aluminum which is a popular choice for radiation shielding in many industries, including medical, aerospace, and nuclear applications. In radiation therapy, aluminum is used to shield certain parts of the body from unnecessary radiation exposure. This helps to protect healthy tissues and organs while focusing the radiation on the cancerous cells. The study underscores the robustness of the Bethe-Bloch formula for calculating the stopping power of heavy charged particles. Proton energy ranges and target thickness must be carefully selected for applications like radiation therapy, where protons need to stop precisely within the target area. Future research will extend these findings to other target materials and more complex interactions, advancing medical physics and materials science. The methodologies and the results presented in this study can provide a solid foundation for future work aimed at optimizing proton beam applications.

Acknowledgement

We would like to tender our sincere thanks to Professor Dr. Khin Khin San, Head of Department of Physics, Meiktila University for her kind permission and encouragement in preparing this research paper. Special thanks to Professor Dr. Daw Hla Win (Retire) from Meiktila University for her advice that made this research paper easier. Finally, we are extremely thankful to Professor Dr. Htun Htun Oo, Department of Physics, Yadanabon University, for his supervision and guidance to carry out this research paper.

References

Berger, M.J., and Seltzer, S. M., NASA SP-3012, (1964).

Kornberg, R. D. "The Stopping Power of Aluminum in Proton Beams." Nuclear Physics A, 119(2), 333–344 (1968).

Mittal, V.K., Verma, R.C., & Gupta, S.C. "Introduction to Nuclear and Particle Physics" (3rd printing). PHI Learning Private limited (2013)

Phelps, A. V., & Gemmell, D. S. "Proton Beam Characterization and Calibration." Medical Physics, 21(4), 549–563 (1994).

Sigmund, S. "Stopping of Ions in Matter." Journal of Applied Physics, 32(3), 566–578 (1961).

Trellue, H. R., & Howerton, L. M. "Stopping Power of Aluminum for Protons." Physical Review, 127(3), 768–773 (1962).

Wehner, G. K., & McLean, D. A. "Aluminum: Properties and Physical Metallurgy." ASM International (1984).

Ziegler, J. F. "The Stopping and Range of Ions in Matter." Pergamon press (1985).

ANALYSIS OF ELEMENTAL CONCENTRATIONS IN AGRICULTURAL SOIL AND VEGETABLE SAMPLES IN SIN GYAUNG LAY VILLAGE OF PYIN OO LWIN TOWNSHIP

Mar Mar Htay[1], May Zin Oo[2], Khin Than Tint[3]

Abstract

The present study investigated the elemental concentrations of agricultural soil and seasonal vegetables in Sin Gyaung Lay village of Pyin Oo Lwin township, Mandalay Region. The elemental concentrations of agricultural soil samples and vegetable samples were analyzed by using Energy Dispersive X-Ray Fluorescence Spectrometry (EDXRF) and Atomic Absorption Spectroscopy (AAS) techniques. The results obtained Mn ranged from 0.16 % to 0.52 %, Fe ranged from 18.60 % to 26.80 %, Ni ranged from 0.05 % to 0.08 %, Cu ranged from 0.03 % to 0.04 %, Zn ranged from 0.26 % to 0.34 %, As ranged from 0.01 % to 0.02 %, Pb ranged from 0.06 % to 0.13 % respectively in agricultural soil samples. The results obtained show that the concentration of Mn ranged from 0.04 % to 0.17 %, Fe ranged from 0.69 % to 0.97 %, Ni ranged from 0.05 % to 0.10 %, Cu ranged from 0.04 % to 0.07 %, Zn ranged from 0.16 % to 0.19 % were found in vegetable samples, while that Pb value 0.003 % was found in Yellow Mustard sample. According to the AAS analysis, the concentrations of Cr, Cu, Zn, Cd and Pb in soil and vegetable samples were found to be within the WHO standards. However, the concentration of Mn slightly exceeded the WHO value in soil sample S-3. The transfer factor for Pb was consistently found to be 1 in all samples, while the transfer factors for Mn, Fe and Zn were less than 1. Additionally, the transfer factor values for Cu and Cd were greater than 1. The findings highlight the importance of regular monitoring and sustainable agricultural practices to mitigate heavy metal contamination in food crops.

Keywords: EDXRF, Yellow Mustard, Carrot, Bok Choy, Elemental concentrations

Introduction

Pollution of the environment with toxic heavy metals has developed into one of the major issues of concern for human beings. Heavy metals can be highly toxic when they combine with various environmental components, including water, soil, air, humans, and other living organisms that may be exposed through the food chain. The majority of these metals are found in the biosphere, such as in water, soils, and rocks, and are also released into the environment from human activities, mainly commercial and industrial. Agriculture is the main source of the human food supply, and it aims to provide safe products with minimal environmental impacts (M. I. Atta *et al.,* 2023). Soil is a supportive layer for all living things in the world. The most important role of soil is to provide a medium for plant growth, which helps in recycling the nutrients and resources needed by plants. However, both essential and toxic elements were present in vegetables in a wide range of concentrations, as they can absorb metals from the soil (F. Abrham *et al.,* 2021). Vegetables absorb heavy metals from contaminated soils as well as from polluted environmental deposits through the roots and incorporate them into the edible parts of plant tissues or deposit them on the surface of vegetables. Vegetables are edible parts of plants that are a fundamental part of human daily meals (B. S. Sagagi *et al.,* 2022).

[1] Department of Physics, University of Mandalay.
[2] Department of Physics, University of Mandalay.
[3] Department of Physics, University of Mandalay.

The presence of heavy metals in soil is a major concern for public health. When plants are grown in polluted environments, they can accumulate high concentrations of heavy metals, posing serious risks to human health when consumed. Heavy metals are toxic because they tend to build up in plants and animals, concentrate in the food chain, and target specific organs in the body. Heavy metals, such as lead (Pb), nickel (Ni), copper (Cu), and selenium (Se), are contaminants that can be found on the surface and in the tissue of fresh vegetables and can be harmful to both plants and humans, even at low concentrations. Soil pollution can be caused by misuse of the soil, poor agricultural practices, disposal of industrial and urban wastes, and the application of chemical fertilizers and herbicides. Heavy metal accumulations in soil are a concern in agricultural production due to its adverse effects on food quality, crop growth, and environmental health.

Experimental Arrangement and Measurement

Sample Collection and Preparation

Sin Gyaung Lay village is located between North latitudes 21° 58′ 5″ and 21° 58′ 21″ between East Longitudes 96° 29′ 3″ and 96° 29′ 19″. It is located about 6.5 miles south of Pyin Oo Lwin. The figure of the study area, sample collection and sample preparation are shown in Figure (1) to Figure (3). Agricultural soil samples, Yellow Mustard, Carrot and Bok Choy samples were collected from the target area of Sin Gyaung Lay village. The soil samples were collected from the study area by using PVC pipe. All samples were collected in polythene bags to avoid direct sunlight. The edible part of the vegetable samples (Yellow Mustard, Carrot and Bok Choy) was washed with tap water and distilled water. After then vegetable samples were cut into small pieces and allowed to dry at room temperature for two weeks. The dry samples were crushed into fine powder using mortar and pestle. After crushing, the powder samples were sieved with mesh for particles size distribution. Before elemental concentrations analysis, all fine powder samples were stored in polythene bags. Finally prepared samples were analyzed for elemental concentrations by using Energy-Dispersive X-ray Fluorescence (EDXRF) at Kyaukse University without any chemical treatment. The coordinates of the sampling location for the study area are presented in Table (1).

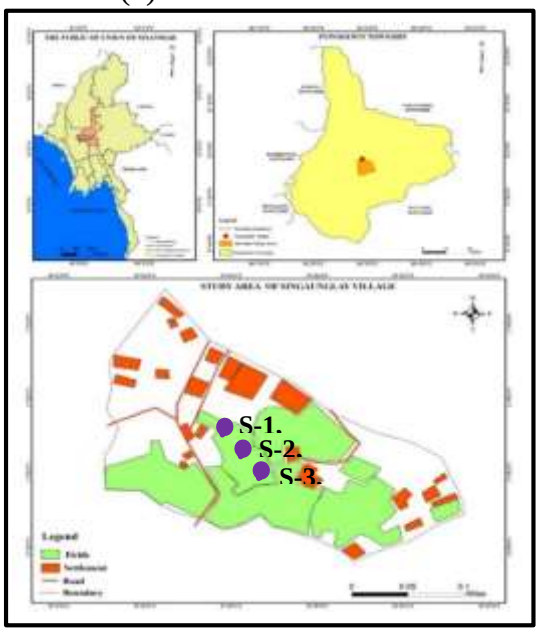

Figure 1. Geographical Map of Sin Gyaung Lay village, Pyin Oo Lwin Township

Table 1. Description of Samples List

Samples Code	Characteristics	Location
Yellow Mustard Soil sample (S-1)	clay	Latt: E 22° 37′ 38″
		Long: N 96° 48′ 30″
Carrot Soil sample (S-2)	clay	Latt: E 22° 37′ 25″
		Long: N 96° 47′ 33″
Bok Choy Soil sample (S-3)	clay	Latt: E 22° 37′ 24″
		Long: N 96° 48′ 28″
Vegetable sample(V-1)	Yellow Mustard	Latt: E 22° 37′ 38″
		Long: N 96° 48′ 30″
Vegetable sample(V-2)	Carrot	Latt: E 22° 37′ 25″
		Long: N 96° 47′ 33″
Vegetable sample(V-3)	Bok Choy	Latt: E 22° 37′ 24″
		Long: N 96° 48′ 28″

Figure 2. Collection and preparation of soil samples

Figure 3. Collection and preparation of vegetable samples

Energy Dispersive X-Ray Fluorescent Spectrometry

Energy Dispersive X-ray Fluorescence (EDXRF) is an analytical method used to qualitatively and quantitatively determine elements in a sample, regardless of their chemical form (P. Wobrauschek *et al.*, 2010). XRF spectrometry is a technique that exposes a sample to excitation X-rays and then measures the specific fluorescence X-ray energies emitted from the sample (T. Moriyama, 2013). Typical applications for EDXRF include analyzing agricultural materials, medical samples, archaeological and historical objects, paintings, fine art objects, as well as environmental samples like soil, ores, water, and aerosol particles. The method is based on the fundamental parameter approach and uses specific expressions for polychromatic excitation and intermediate thick samples. In this system, the X-ray tube was activated using a palladium (Pd) anode target. To enhance sensitivity, the exciting radiation can be optimized by using secondary targets instead of filters. A secondary target material is stimulated by the primary X-rays from the X-ray tube and then emits secondary X-rays that are characteristic of the elemental composition of the target. X-rays emitted from the secondary target were detected by a silicon drift detector (SDD). The system operated at 50 kV and 50 W, and the irradiation chamber was filled with helium gas. The automatic sample changer can hold a maximum of 15 samples. The total measurement time for each sample was 600 seconds. The measured spectra were analyzed using the Advanced RPF-SQX Fundamentals Parameters software, which includes Scattering FP. The photograph and schematic diagram of the EDXRF can be seen in Figure (4).

Figure 4. Photograph of Energy Dispersive X-ray Fluorescence Spectrometry (EDXRF)

Atomic Absorption Spectroscopy

Atomic Absorption spectroscopy is a technique used to determine the elemental composition of an analyte through its electromagnetic or mass spectrum. Atomic Absorption (AA) occurs when a ground-state atom absorbs energy in the form of light at a specific wavelength, causing the atom to transition to an excited state. The amount of light energy absorbed at this wavelength increases as the number of atoms of the selected element in the light path also increases. The relationship between the amount of light absorbed and the concentration of analytes present in known standards can be used to determine unknown sample concentrations by measuring the amount of light they absorb. The photograph of AAS is shown in Figure (5)

Figure 5. Atomic Absorption Spectroscopy (AAS) (Perkin Elmer AA900H),Universities Research Center, University of Yangon

Transfer Factor (TF)

The transfer factor is used to describe the movement of a contaminant (heavy metal) form soil to plants. The transfer factor was calculated by the following equation:

$$TF = \frac{C_{plant}}{C_{soil}}$$

C_{plant} is the metal concentration in edible parts of vegetables and C_{soil} is the metal concentration in soil (W. A. Iyama *et al*., 2022).

Results and Discussion

The individual results obtained for each elemental concentration values are shown in Table (2). The highest elemental concentration values of Ni, Cu, Zn and Pb were found in soil sample S-1. Moreover, the height concentration values of Mn, Fe and As were found in soil sample S-3. The height concentration values of Mn and Fe were found in sample V-3 and the height concentration of Ni, Cu and Zn were found in samples V-2. The concentration value of Pb was found only in vegetable sample V-1 while the concentration value of as was not found in all vegetable samples. The comparison of the data is shown in Figure (6) and Figure (7).

According to AAS results, the concentration values of Mn ranged from 2.23 mg/L to 3.07 mg/L. The concentration value of Mn slightly exceeded the WHO value of 3 mg/L in soil sample S-3. The concentration values of Fe ranged from 39.64 mg/L to 42.14 mg/L. The concentration values of Fe are the height in all soils and vegetable samples as it is abundant elements in nature. The concentration values of Cu ranged from 0.05 mg/L to 0.08 mg/L and Cd ranged from 0.01 mg/L to 0.02 mg/L. The concentration values of Cu and Cd was found below the WHO permissible limit value is 1. The concentration value of Zn ranged from 1.12 mg/L to 1.14 mg/L. The concentration value of Zn was found below the WHO limit of 3 mg/L in soil sample. In vegetable samples, the concentration values of Mn ranged from 0.04 mg/L to 0.08 mg/L and Fe ranged from 0.3 mg/L to 0.53 mg/L. The concentration values of Cu are 0.06 mg/L to 0.08 mg/L and the WHO standard of Cu is 0.73 mg/L. The concentration values of Cd were found 0.02 mg/L in all vegetable samples and the WHO values of Cd is 0.1 mg/L. The concentration values of Pb ranged from 0.02 mg/L to 0.03 mg/L and the WHO value of Pb is 0.3 mg/L. The concentration value of Zn, Cd and Pb were found below the WHO limits. The elemental concentrations of soil and vegetable samples are shown in Table (3) and the comparison of heavy metal concentrations in soil and vegetable samples are shown in Figure (8) and Figure (9). The transfer factor values of Mn, Fe and Zn were found below 1. Whereas the transfer factor value of Pb was found 1 in all samples. The transfer factor values of Cu were found below 1 except for V-2. The transfer factor value of Cd was found exceed 1 except for V-3. The comparison of Trans Factor values for vegetables samples are shown in Table (4) and Figure (10).

Table 2. Elemental concentrations of soil and vegetable samples (EDXRF results)

Elements	Elemental Concentrations (mass%)					
	S-1	**V-1**	**S-2**	**V-2**	**S-3**	**V-3**
Mn	0.16	0.08	0.23	0.04	0.52	0.17
Fe	18.6	0.69	21.6	0.87	26.8	0.97
Ni	0.08	0.05	0.05	0.1	0.06	0.08
Cu	0.04	0.04	0.03	0.07	0.04	0.04
Zn	0.34	0.17	0.26	0.19	0.26	0.16
As	0.01	ND	0.01	ND	0.02	ND
Pb	0.13	0.003	0.06	ND	0.1	ND

ND–Not Detected

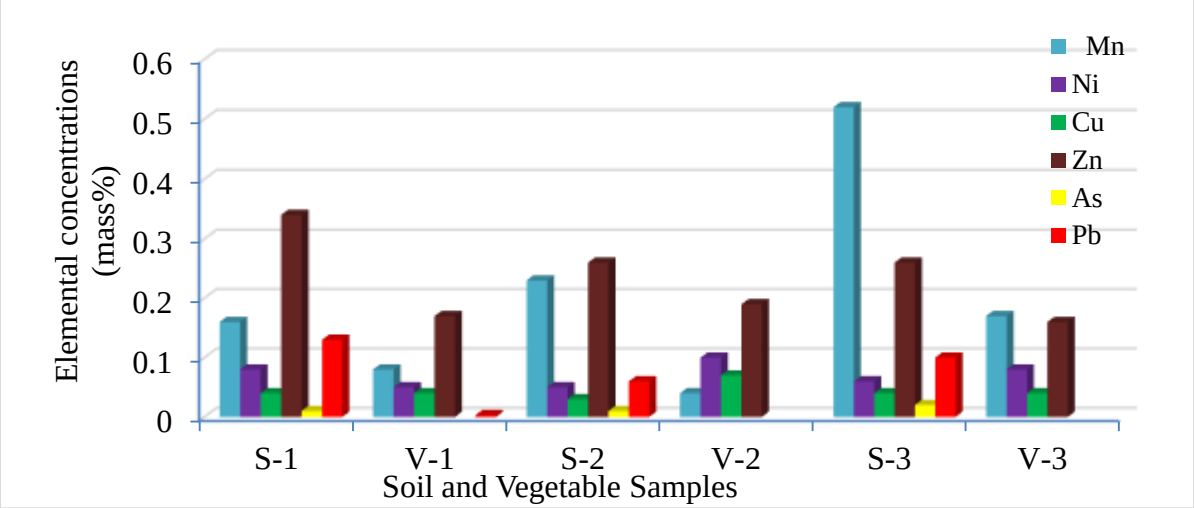

Figure 6. The comparison of elemental concentrations in soil and vegetable samples

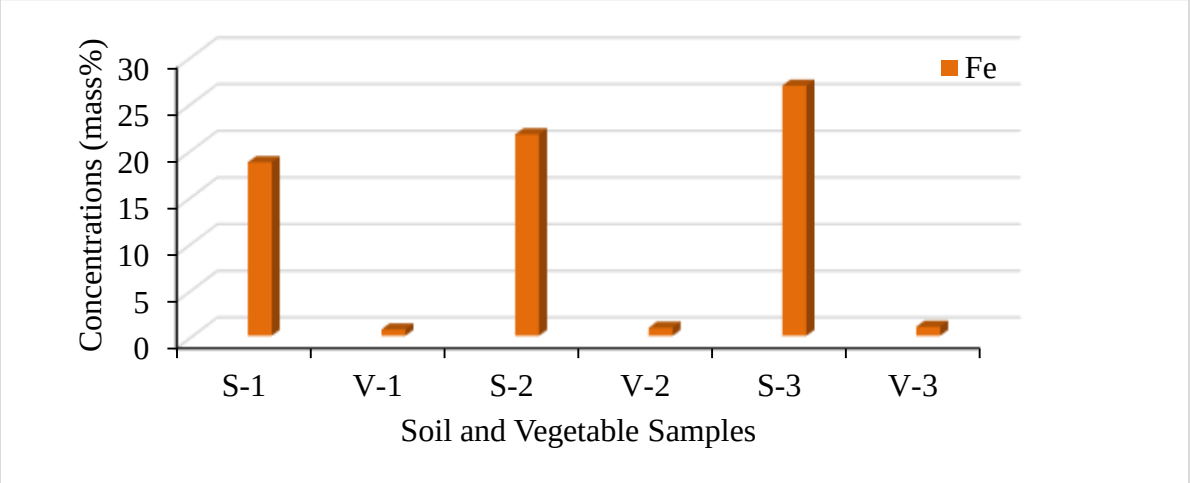

Figure 7. The comparison of iron concentrations in soil and vegetable samples

Table 3. Elemental concentrations of soil and vegetable samples (AAS results)

Elements	Elemental Concentrations (mg/L)					
	S-1	**V-1**	**S-2**	**V-2**	**S-3**	**V-3**
Mn	2.23	0.05	2.57	0.04	3.07	0.08
Fe	39.64	0.3	39.95	0.39	42.14	0.53
Cu	0.08	0.07	0.05	0.08	0.07	0.06
Zn	1.14	0.17	1.12	0.23	1.1	0.18
Cd	0.01	0.02	0.01	0.02	0.02	0.02
Pb	0.03	0.03	0.02	0.02	0.03	0.03

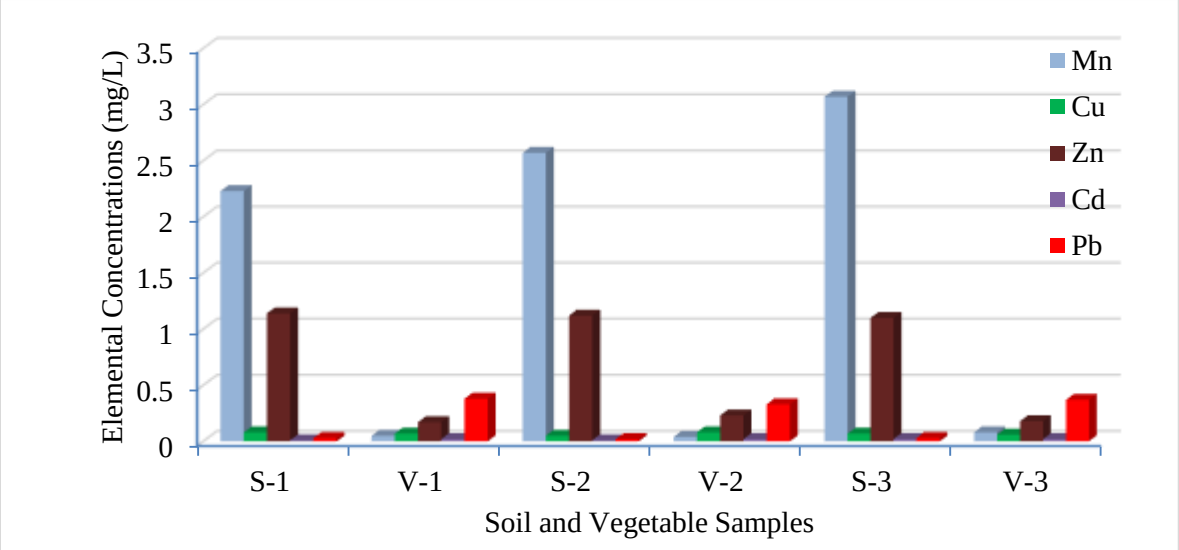

Figure 8. The comparison of heavy metal concentrations in soil and vegetable samples

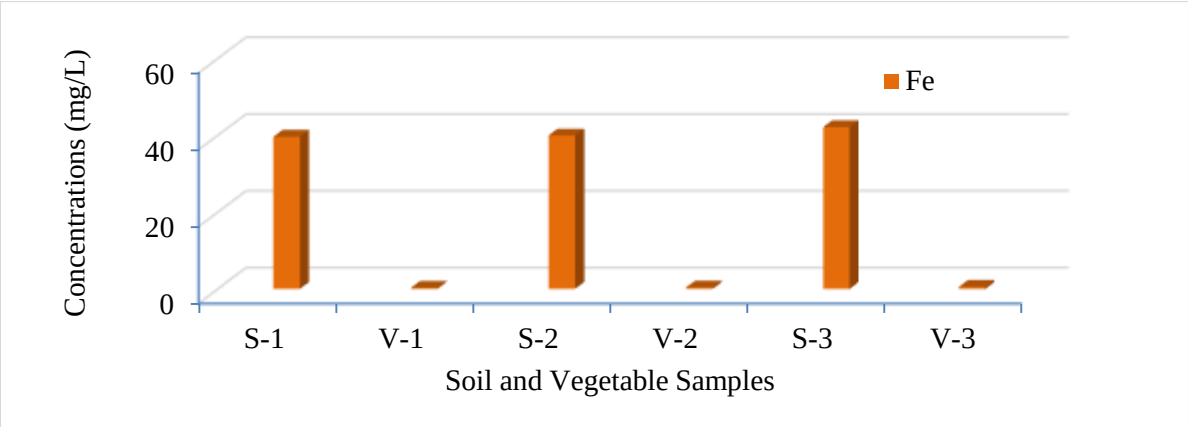

Figure 9. The comparison of iron concentrations in soil and vegetable samples

Table 4. The comparison of Trans Factor values for vegetables samples

Elements	TF (V-1)	TF (V-2)	TF (V-3)
Mn	0.02	0.01	0.03
Fe	0.01	0.01	0.01
Cu	0.9	1.2	0.9
Zn	0.12	0.2	0.2
Cd	2	2	1
Pb	1	1	1

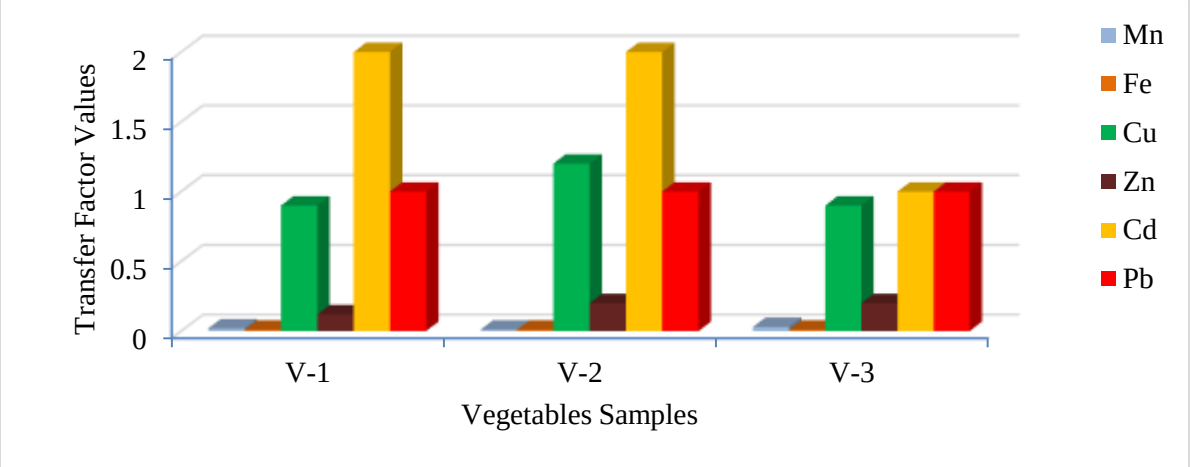

Figure 10. The comparison of Trans Factor values for vegetables samples

Conclusion

In the present study, according to EDXRF analysis, the elemental concentrations in soil samples are in order of Fe>Zn>Mn>Pb>Ni>Cu>As while the elemental concentrations in the vegetable samples are in order of Fe>Zn>Ni>Mn>Cu>Pb. Whereas the concentration of As was not found in all vegetable samples.

According to the AAS analysis, the concentration of Cr, Cu, Zn, Cd and Pb in soils and vegetable samples were found within the range of WHO standards, whereas the concentration of Mn was found slightly exceed WHO value in soil samples S-3. The transfer factor value of Pb was found 1 in all samples whereas the transfer factor value of Mn, Fe and Zn was found below 1. Moreover, the transfer factor values of Cu and Cd were found greater than 1. The findings emphasize the importance of regular monitoring and sustainable agricultural practices to migrate heavy metal contamination in food crops.

Acknowledgments

We would like to acknowledge with deepest gratitude to Dr Nyein Wint Lwin, Professor and Head, Department of Physics, University of Mandalay, for her kind permission, invaluable advice and encouragement and providing all the departmental facilities. We also thankful to Dr San Yu Swe, Professor, Department of Physics, University of Mandalay, for her kind suggestions and invaluable advice in this research.

References

B. S. Sagagi *et al*., "Assessment of accumulation of heavy metals in soil, irrigation water and vegetative parts of lettuce and cabbage grown along Wawan Rafi, Jigawa State, Nigeria", J. Environ. Monit. Assess., 194(10) (2022) 194-699.Kokate, C.K. (2000). Practical Pharmacognosy. New Gyan Offset Printers, Delhi.

E. Aweng *et al*., "Heavy Metal Concentration of Irrigation Water, Soils and Fruit Vegetables in KOTA BHARU Area, Kelantan, Malaysia", J. Appl. Sci. Environ. Sanit. 6(4) (2011) 463-470.Heywood V.H., R.K. Burmmitt, A. Culham, O. Seberg. (2007). Flowering Plants Families of the World, Canada: Firefly Books.

H.M. Naser *et al*., "Heavy Metal Levels in Vegetables with Growth Stage and Plant Species Variations", J. Agril. Res. 36(4): 563-574, (2011).

M. I. Atta *et a*l., "Amassing of heavy metals in soils, vegetables and crop plants irrigated with wastewater: Health risk assessment of heavy metals in Dera Ghazi Khan, Punjab, Pakistan", J. Front.Plant Sci.13(2023) 4-21.

P. Wobrauschek *et al.,* "Energy Dispersive, X-ray Fluorescence Analysis", (2010).

T. Moriyama, "Analysis of trace impurities in pharmaceutical products using polarized EDXRF spectrometer NEX CG", J. Rigaku, 29(2), (2013) 19-21.

V.D. Beniwal *et al*., "Physico-Chemical Parameter: An Indicator of Water Pollution", J.Environ.Res.5(5) (2021)1-7.

W. A. Iyama *et al*., "Assessment of Heavy Metals in Agricultural Soils and Plant (Vernonia amygdalina Delile) in Port Harcourt Metropolis, Nigeria", J. Agriculture, 12(27) (2022), 1-21.

World Health Organisation (WHO), (2007). Report of 33rd meeting, Joint FAO/WHO Joint Expert Committee on Food Additives, Toxicological evaluation of certain food additives and contami-nants No. 24, International Programme on Chemical Safety, WHO, Geneva.

Z. Kilic., "Water Pollution: Causes, Negative Effects and Prevention Methods", J. Institude Sci.Technol 3(1) (2021) 129-132.

DESIGN ON RADIO FREQUENCY IDENTIFICATION (RFID) BASED SMART DOOR LOCK SYSTEM

Win Moh Moh Maung[1], Hnin Yu Khaing[2], Kyaw Kyaw[3]

Abstract

A smart door lock is an electric lock that allows unlocking and locking without keys. Classical locking systems, such as lock and key, Deadbolts, Door chain and Mortise locks, have usages and security limitations. The main objective of this research work is to design and construct RFID-based smart door lock system with Arduino UNO development board. When a predefined or programmed ID card was located and swiped in front of an RFID reader module, the lock was slide and opened and short pulse of alarm sound produced through the buzzer. When there is no RFID card, the door could be opened with Bluetooth protocol from the mobile phone. The duration of the open and close condition is assigned as 5 s for proper door crossing. It could sense the human and big thing which are passed through the door for longer than 5 s, the constructed system automatically adjusted the duration of the door for opening and closing. By using this system, the security of the home can be enhanced and smart living style can also obtain with very low cost.

Keywords: Smart door lock, RFID, Arduino, Bluetooth, duration

Introduction

Today's technology age, people want their life is completely automated in electrical appliances. Along with the increasingly rapid development in microcontroller, it encourages to innovate and create a tool that is more effective and efficient [Ajami, S., *et al*]. The smart door lock is the one type of gate, known as door, which is used in a building to pass in and out [Anaza, S. O., *et al*]. This door has been used as a gate for building to enhance the security. The sliding doors are used for narrow spaces and they are looked more comfortable. The problems discussed in this research work are the absence of electrical applications to manipulate the open and close conditions of the sliding doors with RFID card, and the absence of a conventional door security system that can strengthen the home security. The investigated sliding door system is now applied conventionally and automatically. Conventional sliding doors are also door which are equipped with the sliding door for human entering or exit. The smart sliding door does not require human intervention to open or close the door, because it is equipped with a passive infrared sensor (PIR). The door would open and close immediately when the human's infrared radiation was detected. The smartcard based security system implemented a smart card, such as RFID and Magnetic cards, for opening and locking doors, which replaces the manual lock [Batool, A., *et al*]. In this study, RFID technology was used to access the door for opening while the closing would be automatic. This research also uses a Bluetooth connection to open the smart door with mobile phone automatically. The door sliding system uses L298N drove DC motors, RFID module, LCD display and ATmega328P microcontroller (MCU) based Arduino Uno R3 development board. Radio Frequency Identification (RFID) is a technology that uses radio frequencies to identify objects [Gangi, R. R., *et al*]. The main objective of this research work is to design and construct a smart door lock system (automatic sliding door) that can detect an RFID card to access the door for opening automatic. RFID system supported to

[1] Department of Physics, Mandalay University of Distance Education.

[2] Department of Physics, Mandalay University of Distance Education.

[3] Department of Physics, University of Mandalay.

strengthen the security level of a building's access. In this study the smart door security control system that has been built based on analyzing the hardware and software based system. The performance tests were carried out to investigate the feasibility of working hardware and control programs of the smart door control system. The performance efficiency of the automatic sliding door control system was analyzed and the system performance was quite efficient.

Materials and Method

A block diagram of the smart door implementation system was illustrated in Fig.1. The input block consisted of a RFID module and Bluetooth modules. Whereas in the process section, there was a microcontroller that conducted as a brain of the constructed system. On the output portion, there was a DC motor as a door opener, LCD 16x2, which was implemented to display notifications about the condition of the door and alarm sound produced from the buzzer and indicator LEDs.

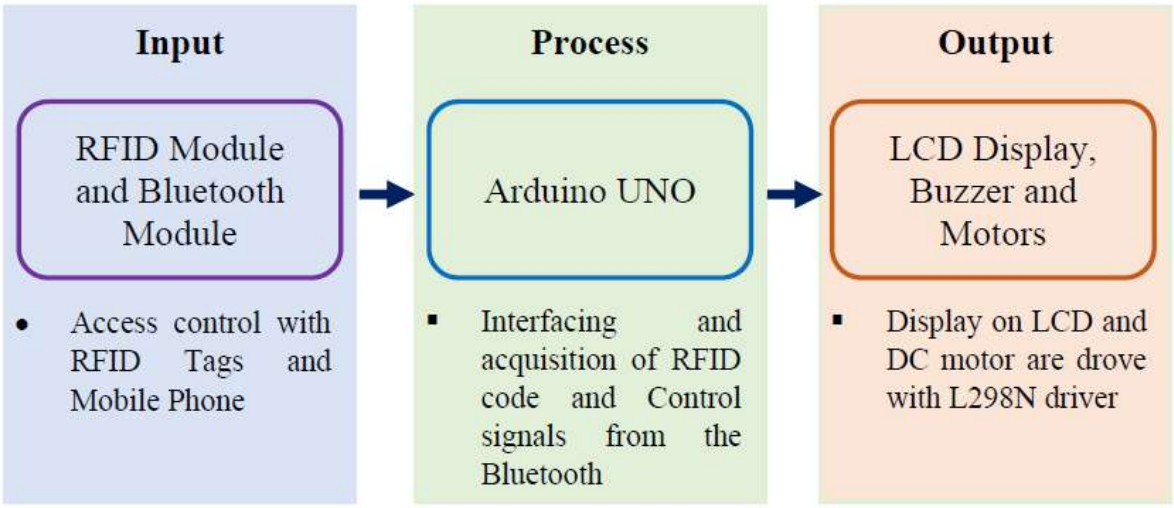

Figure 1. The block diagram of the smart sliding door lock system.

The system architecture presented in Figure.2 explained the control process of the constructed system being built. The system architecture was used to define components that were more specifically structured so that they could address current and future needs. The system architecture flow explained the process of data input, data processing, and data output.

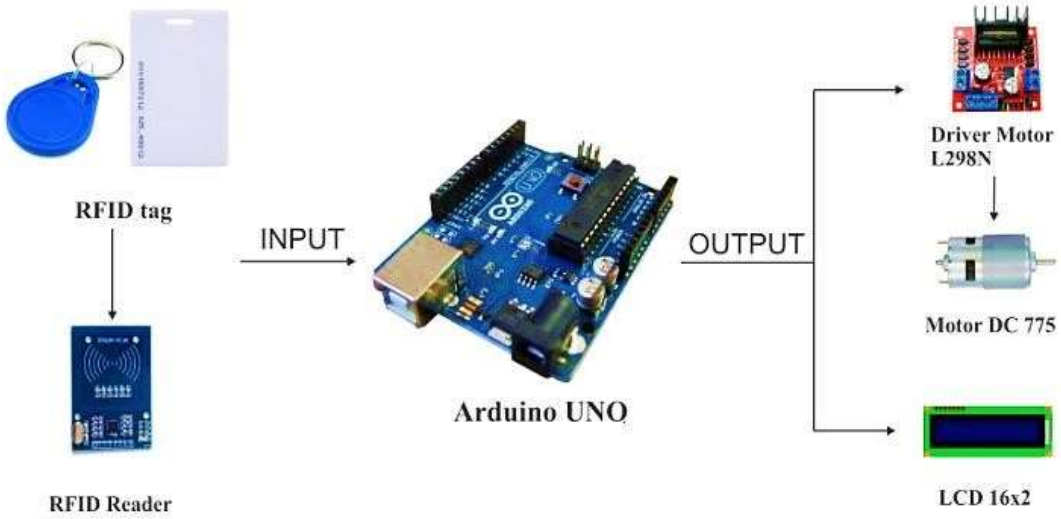

Figure 2. The system architecture of the constructed system.

The smart door control algorithm presented in Fig.3 is based on the security requirement. It was programmed in Arduino IDE and uploaded into the microcontroller to obtain the objective of the research work. This constructed program was based on a process model and formulated with artificial intelligence. The design of the mechanical sliding mechanism for smart sliding door is presented in Fig.4. This system consisted of several electronic components to make smart sliding doors. This constructed system consisted of an RFID reader module for detecting RFID data and DC motors for slide door movement. Based on Fig. 4, the function of each component was explained in Table 1. Arduino IDE was conducted to write programs, compile, and upload to Arduino boards. Arduino IDE was embedded with the AVR-dude program to convert executable code into a hexadecimal encoding file that was uploaded into the Arduino main program memory by the loader program.

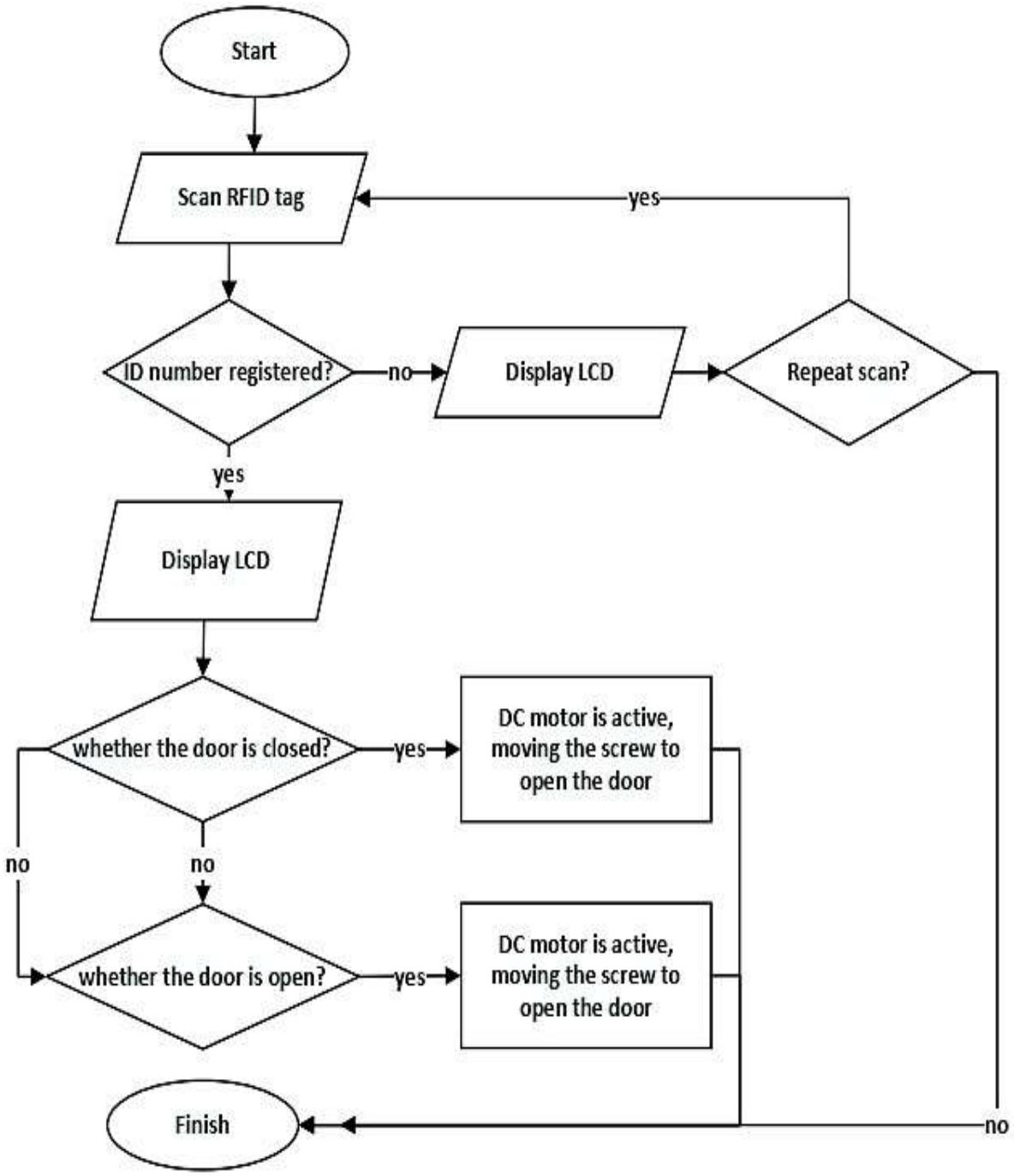

Figure 3. The flow chart of the smart door algorithm.

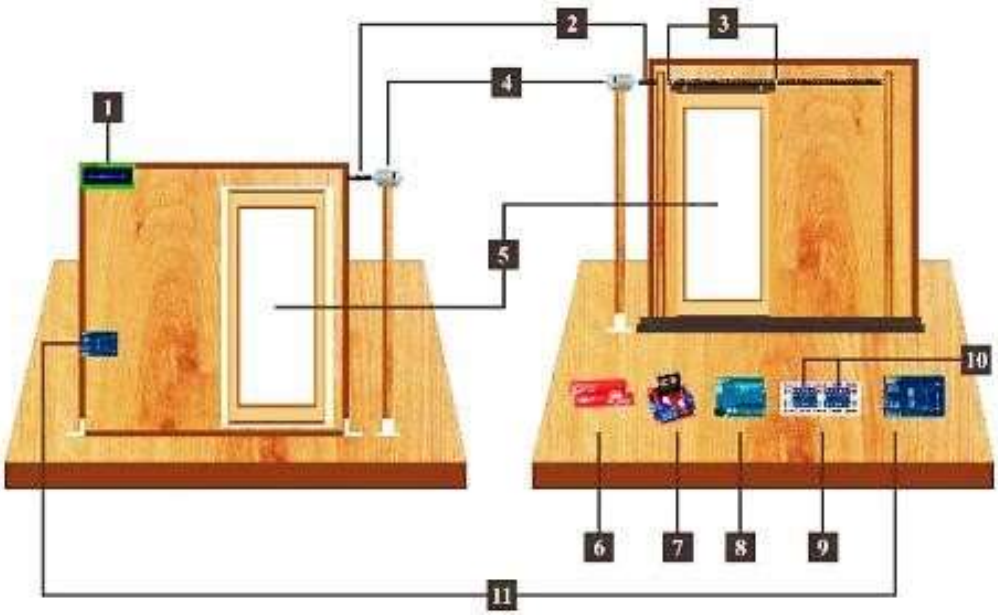

Figure 4. The mechanical hardware system for the constructed smart door.

Table 1. The functions of the individual electrical components.

No.	Name	Function
1	LCD 1602 Display	Functioning as information display
2	Outer Thread	Functioning as sliding door mover
3	Inner Thread	Functioning as sliding door mover
4	DC Motor	To drive the door open or close
5	Sliding Door	To work as the gate for the room
6	12 V Power Supply	To provide the DC supply to the system
7	L298N Motor Driver	To drive the DC motor with speed and direction control
8	Arduino UNO	Serves as the main controller
9	PCB Board	Using for interconnection of the circuit components
10	Bluetooth Module	To communicate with mobile phone
11	RFID Reader	To read the predefined RFID tags and cards

Experimental Circuit Operation

The Sliding Door was a gate where people give boundaries or areas that could provide insider understanding, entry and exit, and here and there. The sliding door was one type of door used in a building. In addition to being a security, the door also showed the character of a building. The sliding door was a door that opened the lid by sliding the door left or right. For movement, rails and wheels were setup above and below the sliding door. This type of door was the right solution to make the room look more spacious. In this research work, the smart door

was constructed as automatic sliding door with touchless and mobile phone controllable capability.

RFID technology was a wireless system that allowed tag information to be read by placing the electromagnetic field closer. RFID was a general terminology for non-contact technology that used radio waves to identify objects automatically. The combination of antenna and microchip was called an RFID card or RFID tag and worked in conjunction with an RFID reader module. They were properly interfaced with Arduino UNO development board. Arduino Uno was a microcontroller board based on ATmega328P. This board had 14 digital input and output pins, 6 of which could be used as PWM signal outputs for DC motor speed control, 6 analog input able pins, 16 MHz quartz crystals resonance, USB header, DC power outlets, ICSP headers, and reset button. The control program for the constructed system was designed with Arduino IDE. DC motor was an actuator that converted direct current electrical energy into mechanical energy and it was used to activate the sliding door. The speed and direction of the sliding door was controlled with Arduino and L298N motor driver module. The speed control was controlled with the PWM out of the Arduino and it was set to 50 % duty cycle for normal speed of door opening and closing. The information system of the constructed system was implemented with 1602 LCD display. It was interfaced with MCU in serial mode. To obtain the desired contrast level of the LCD display, the wiper V_0 pin was adjusted with the 10 kΩ potentiometer.

All of the interfaced electronics components were assembled on the PCB copper clad. The PCB artwork was designed with Pad2Pad PCB design software. The components layout and PCB Trace layer are illustrated in Fig.5. The bottom layer was copper trace layer and top layer was designed for components layer. The PCB was constructed as single layer PCB to reduce complexity for assembling and soldering.

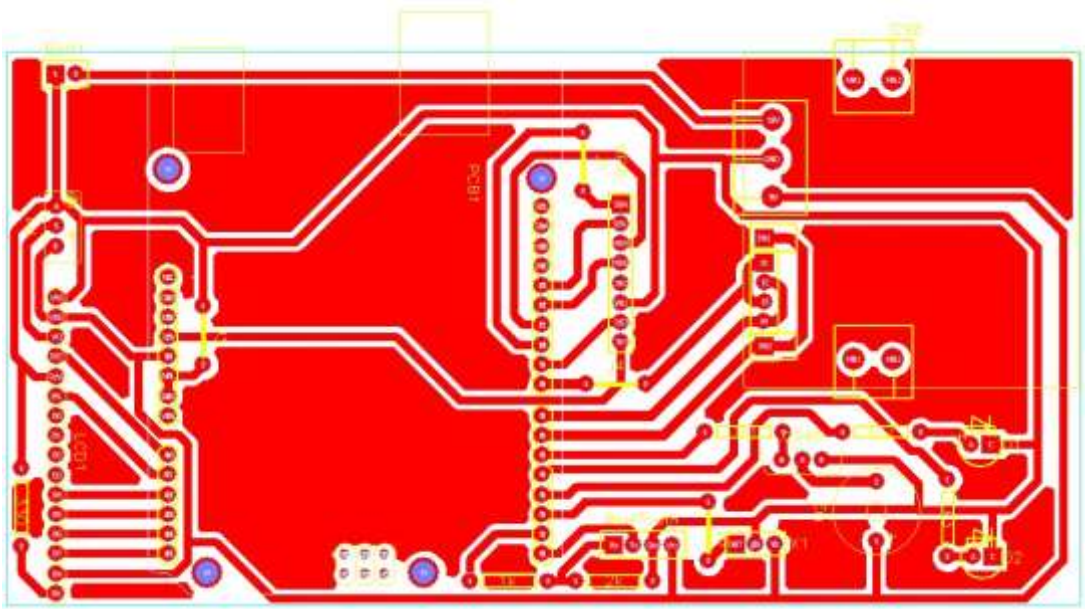

Figure 5. The components layout and PCB trace layer of the constructed system.

Results and Discussion

Performance analysis was a trial based on the correctness of input and output criteria, and the action of the smart door security control system and also included data validation and input error handling. The trial in Fig.6(a) was a standby (closed) condition of the system (wherein the experiments to be carried out that the sliding door was in a closed condition and also had not received any input or input from RFID tags or cards.

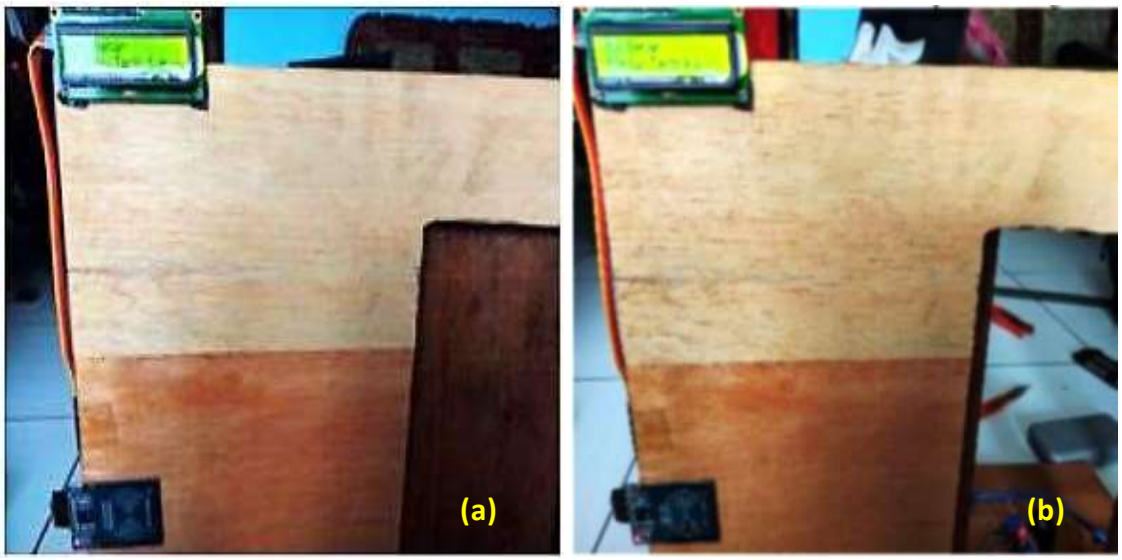

Figure 6. The standby condition of the system

Test in Fig.6(b) was to give an open door command. The scanned ID number would then be detected by the RFID reader module. When the RFID card information were sent correctly, the LCD displayed the notification in the form of "Open Door" and followed by an active DC motor moving the axial to open the door.

The system test on the door command could not be opened or closed. When the ID number that had been scanned was wrong. The system would send to the LCD display a notification "Incorrect ID" so that the DC motor would not be active and would not be able to move the axial to open and close the door.

The ID number "4BEC450B" was predefined in the RFID tags and these ID number could be used to open and close the door. The results of the RFID tag trial are presented in Table 2.

Table 2. The ID detection analysis with different tags and cards.

No.	RFID Tags	Detected ID	Detected Speed (s)	Conditions
1	Tag1	4BEC450B	0.9	Correct
2	Tag2	EBC3EC0A	1.4	Incorrect
3	Tag3	4BECEC0A	1.6	Incorrect
4	Card1	4BEC450B	0.7	Correct
5	Card2	EBC3EC0A	1.6	Incorrect

The constructed system could function with a supply voltage, as evidenced by the standby 16x2 LCD displaying "Smart Door Lock" in the first row, "Scan Your RFID" in the second row, and the digital multimeter showed the consuming DC voltage of 5 V DC. The system could not function when there was no supply voltage, as evidenced by the state of the 16x2 LCD not displaying anything.

Based on the study's results, it was concluded that the overall work process of the prototype system, especially the smart door using Radio Frequency Identification ID-12 technology based on Arduino Uno R3 ATmega328P, produced by the system could be used for intelligent door locking system. Person, who do not have to enter the door without RFID tag or card. System development added several supporting components that were used to reduce the occurrence of problems with relays that affected the drop bolt lock or solenoid door lock.

Conclusion

Implementation of smart automatic sliding door using RFID, Bluetooth and Arduino made it easy for home owner to open and close the door without using human power, without using conventional door locks, and the door can be tightly closed and cannot be shifted manually. The heavier the load was on the door; the sliding power of the door would be reduced. With the use of this system, the security of the home was more awake. Based on the results of the study, the implementation of smart automatic sliding doors would indicate visually with LED and produce an alarm, when the ID received by the RFID module did not match. The time taken for the RFID reader to read the tag was 2 s for human access while the waiting period between the opening and closing of the gate are 10 s. This innovation gives a progressive automation in different procedures running from modern divisions to home control.

Acknowledgements

I would like to express my special thanks to Rector, Dr Khin Thant Sin and Pro-Rectors, Dr Win Mar and Dr Lae Lae Kyaing of Mandalay University of Distance Education for giving permission to submit this research paper. The author would like to thank Professor Dr Wah Wah Thin, Head of Department of Physics and Professor Dr Soe Soe Oo, Department of Physics, Mandalay University of Distance Education, for their kind permission to carry out this research. I am deeply grateful to my supervisor, Dr Kyaw Kyaw, Associate Professor, Department of Physics, University of Mandalay and Dr Hnin Yu Khaing, Associate Professor, Department of Physics, Mandalay University of Distance Education. I have appreciated the support I received from everyone who gives me unconditional support and aid.

References

Ajami, S., and R. Arab-Chdegani, (2013) “What are the most important Barriers to Implementing Radio Frequency Identification Device (RFID) in Healthcare System”, *Journal of Info Technology and Software Engineering*, vol. 7: E004, pp. 34-39.

Anaza, S. O., J. D. Jiya, and Y. S. Haruna, (2017) “A Review of Intelligent Lock System” *American Journal of Engineering Research*, vol. 6(6), pp. 9-15.

Anushri, J., L. K. Vijay, and N. Barkha, (2015) “RFID and GSM Based Attendance Monitoring System using Door locking/unlocking System and Its Hardware Implementation”, *Journal of Management Engineering and Information Technology*, vol. 2(3), pp. 5-10.

Batool, A., and A. Sima, (2015) “Radio Frequency Identification and Rescue Victims in Earthquake”, *International Journal of Health System & Disaster Management*, vol. 3(5), pp. 1-5.

Expresscorp (2022) How Does RFID Work for Vehicle Gate Entry, express identification made simple, https://www.expresscorp.com (Accessed Date 10.9.2024)

Gangi, R. R., and S. S. Gollapudi, (2013) "Locker Opening and Closing System using RFID, Fingerprint, Password and GSM", *International Journal of Emerging Trends & Technology in Computer Science*, vol. 2(2), pp.142-145.

Hua, L., W. Hong-jun, S. Zhen, L. Qing-hua, and W. Xiao, (2010) "Application of RFlD in Agricultural Seed Quality", *The 8th World Congress on Intelligent Control and Automation*, vol.6, pp.9.

TWO TYPES OF PRESERVING OPERATORS AND THEIR STABILITY*

Saw Yu Mon[1]

Abstract

In this paper, we first introduce orthogonality preserving operators, approximately orthogonality preserving operators on inner product spaces and their properties. Next, we discuss some properties of orthogonality preserving operators and approximately orthogonality preserving operators that are true for right-angle preserving when the operator is linear. Finally, we show the stability between approximate right-angle preserving and right-angle. preserving.

Keywords: Orthogonality preserving operators; Right-angle preserving operators; Stability

1 Preliminaries.

In this section, we introduce some definitions and examples. Let X and Y be two inner product spaces over the same field $\mathbb{K} = \mathbb{R}$ or $\mathbb{C}$ with the inner products denoted by $\langle \cdot, \cdot \rangle$ and the associated norms denoted by $\| \cdot \|$. As usual, vectors x and y are said to be ***orthogonal*** $(x \perp y)$, if $\langle x, y \rangle = 0$. $\mathbb{K}$ denotes the field $\mathbb{R}$ of real or the field $\mathbb{C}$ of complex numbers. For some $\varepsilon \in [0,1)$, an element x of an inner product space X is said to be ***approximate orthogonal*** to an element $y \in X$ if $|\langle x, y \rangle| \leq \varepsilon \|x\| \ \|y\|$. We also say that x and y are **ε-*orthogonal*** and we write $x \perp^{\varepsilon} y$. Let H be an infinite dimensional Hilbert space and $B(H)$ be the space of all bounded linear operators acting on H. T is a ***similarity*** if there exists $\gamma \geq 0$ such that $\|T(x)\| = \gamma \|x\|$, for all $x \in X$. We choose $\gamma = 1$, we get $\|T(x)\| = \|x\|$, for all $x \in X, T$ is ***isometry***. We have known that every unitary operator on H is an isometry. If $T \in B(H)$, then $\langle T(x), y \rangle$ is linear in x, conjugate-linear in y, and bounded. There exists a unique $T^* \in B(H)$ for which $\langle T(x), y \rangle = \langle x, T^*(y) \rangle, x, y \in H$ and so that $\|T^*\| = \|T\|$.

1.1 Definition. [2] *Let X and Y be two inner product spaces over the same field $\mathbb{K} = \mathbb{R}$ or $\mathbb{C}$. A mapping $T : X \to Y$ is called **orthogonality preserving (OP)** if $x \perp y$ implies $T(x) \perp T(y)$, for all $x, y \in X$ and is called **strongly orthogonality preserving (SOP)** if $x \perp y \Leftrightarrow T(x) \perp T(y)$, for all $x, y \in X$.*

1.2 Definition. [3] *Let X and Y be real inner product spaces and $T : X \to Y$ be an operator. T is said to be the **right-angle preserving operator (RAP)** if for all $x, y, z \in X$ such that $x - z \perp y - z$ implies $T(x) - T(z) \perp T(y) - T(z)$.*

---

* First Prize (2024)

[1] Department of Mathematics, University of Yangon

1.3 Definition. $[2]$ *Let* X *and* Y *be two inner product spaces over the same field* $\mathbb{K} = \mathbb{R}$ *or* $\mathbb{C}$. *A mapping* $T : X \to Y$ *is called approximately orthogonality preserving (ε-OP) if and only if for all* $x, y \in X$ *such that* $x \perp y \Rightarrow T(x) \perp^{\varepsilon} T(y)$ *with some* $\varepsilon \in [0,1)$.

The following example shows that a linear solution of approximately orthogonality preserving need not satisfy orthogonality preserving.

1.4 Example. *Let* $\varepsilon \in (0,1)$ *and* $T : \mathbb{R}^2 \to \mathbb{R}^2$ *be given by*

$$T(x_1, x_2) = \left(x_1, \sqrt{1-\varepsilon}\, x_2\right).$$

Fix $x = (x_1, x_2)$, $y = (y_1, y_2) \in \mathbb{R}^2$ *such that* $x \perp y$. *That is,* $x_1 y_1 = -x_2 y_2$.

If $x_1 x_2 y_1 y_2 = 0$, *then* $x_1 y_1 = 0$ *and hence*

$$\begin{aligned}\langle T(x), T(y)\rangle &= \left\langle (x_1, \sqrt{1-\varepsilon}\, x_2), (y_1, \sqrt{1-\varepsilon}\, y_2)\right\rangle \\ &= x_1 y_1 + (1-\varepsilon) x_2 y_2 \\ &= x_1 y_1 + (1-\varepsilon)(-x_1 y_1) \\ &= 0.\end{aligned}$$

Therefore $T(x) \perp T(y)$.

Thus we assume $x_1 x_2 y_1 y_2 \neq 0$ *and define* $a = \dfrac{x_1}{x_2} = \dfrac{-y_2}{y_1} \neq 0.$

We have

$$\begin{aligned}\frac{|\langle T(x), T(y)\rangle|}{\|T(x)\|\ \|T(y)\|} &= \frac{|x_1 y_1 + (1-\varepsilon) x_2 y_2|}{\sqrt{x_1^2 + (1-\varepsilon) x_2^2}\sqrt{y_1^2 + (1-\varepsilon) y_2^2}} \\ &= \frac{|-x_2 y_2 + (1-\varepsilon) x_2 y_2|}{\sqrt{x_1^2 + (1-\varepsilon) x_2^2}\sqrt{y_1^2 + (1-\varepsilon) y_2^2}} \\ &= \frac{\varepsilon |x_2 y_2|}{\sqrt{x_1^2 + (1-\varepsilon) x_2^2}\sqrt{y_1^2 + (1-\varepsilon) y_2^2}} \\ &= \frac{\varepsilon}{\sqrt{\dfrac{x_1^2 + (1-\varepsilon) x_2^2}{x_2^2}}\sqrt{\dfrac{y_1^2 + (1-\varepsilon) y_2^2}{y_2^2}}} \\ &= \frac{\varepsilon}{\sqrt{a^2 + (1-\varepsilon)}\sqrt{\dfrac{1}{a^2} + (1-\varepsilon)}} \\ &= \frac{\varepsilon}{\sqrt{1 + (1-\varepsilon)^2 + (1-\varepsilon)(a^2 + \dfrac{1}{a^2})}}.\end{aligned}$$

Since $(1-\varepsilon)>0,\ (a^2+\frac{1}{a^2})>0$ *and* $\sqrt{1+(1-\varepsilon)^2+(1-\varepsilon)(a^2+\frac{1}{a^2})}>1,\ \frac{\left|\langle T(x),T(y)\rangle\right|}{\|T(x)\|\ \|T(y)\|}<\varepsilon.$

Therefore $T(x)\perp^{\varepsilon}T(y)$. *Clearly, T does not preserve inner product.*

1.5 Definition. [3] *Let* X *and* Y *be real inner product spaces and* $T:X\to Y$ *be an operator. For* $\varepsilon\in[0,1)$, T *is said to be the* ***approximate right-angle preserving(ε-RAP)*** *if for all* $x,y,z\in X$ *such that*

$$x-z\perp y-z \ \text{ implies } T(x)-T(z)\perp^{\varepsilon}T(y)-T(z).$$

1.6 Example. *Let* $\varepsilon\in[0,1)$, and $T:\mathbb{R}^2\to\mathbb{R}^2$ *be defined by*

$$T(x_1,x_2)=(4-\sqrt{\varepsilon}x_1,4-2\sqrt{\varepsilon}x_2).$$

Let $x=(x_1,x_2),y=(y_1,y_2),z=(z_1,z_2)\in\mathbb{R}^2$ *such that* $x-z\perp y-z$. *That is*

$$(x_1-z_1)(y_1-z_1)=-(x_2-z_2)(y_2-z_2).$$

Now, we assume that $(x_1-z_1)(y_1-z_1)(x_2-z_2)(y_2-z_2)\neq 0$ *and define*

$$a=\frac{x_1-z_1}{x_2-z_2}=-\frac{(y_2-z_2)}{y_1-z_1}\neq 0.$$

Then we have

$$\frac{\left|\langle T(x)-T(z),T(y)-T(z)\rangle\right|}{\|T(x)-T(z)\|\ \|T(y)-T(z)\|}$$

$$=\frac{\left|\left\langle\left(-\sqrt{\varepsilon}(x_1-z_1),-2\sqrt{\varepsilon}(x_2-z_2)\right),\left(-\sqrt{\varepsilon}(y_1-z_1),-2\sqrt{\varepsilon}(y_2-z_2)\right)\right\rangle\right|}{\sqrt{\varepsilon(x_1-z_1)^2+4\varepsilon(x_2-z_2)^2}\sqrt{\varepsilon(y_1-z_1)^2+4\varepsilon(y_2-z_2)^2}}$$

$$=\frac{\left|\varepsilon(x_1-z_1)(y_1-z_1)+4\varepsilon(x_2-z_2)(y_2-z_2)\right|}{\left[\varepsilon^2(x_1-z_1)^2(y_1-z_1)^2+16\varepsilon^2(x_2-z_2)^2(y_2-z_2)^2+4\varepsilon^2(x_2-z_2)^2(y_1-z_1)^2+4\varepsilon^2(x_1-z_1)^2(y_2-z_2)^2\right]^{\frac{1}{2}}}$$

$$=\frac{\left|3\varepsilon(x_2-z_2)(y_2-z_2)\right|}{\left[17\varepsilon^2(x_2-z_2)^2(y_2-z_2)^2+4\varepsilon^2\left(\left(\frac{x_2-z_2}{x_1-z_1}\right)^2+\left(\frac{y_2-z_2}{y_1-z_1}\right)^2\right)(x_2-z_2)^2(y_2-z_2)^2\right]^{\frac{1}{2}}}$$

$$=\frac{\left|3\varepsilon(x_2-z_2)(y_2-z_2)\right|}{\left[17+4\left(\frac{1}{a^2}+a^2\right)\right]^{\frac{1}{2}}\varepsilon(x_2-z_2)(y_2-z_2)}=\frac{3}{\left[17+4\left(\frac{1}{a^2}+a^2\right)\right]^{\frac{1}{2}}}<\varepsilon.$$

Thus $T(x)-T(z)\perp^{\varepsilon}T(y)-T(z)$. *Hence T is approximate right-angle preserving.*

2 Orthogonality Preserving Operators and Right-Angle Preserving Operators

In this section, we discuss the properties of orthogonality and right-angle preserving operators. We investigate right-angle preserving normal operators in $B(H)$ as orthogonality preserving normal operators in $B(H)$.

2.1 Properties of Orthogonality Preserving Operators

We start with equivalent conditions for an orthogonality preserving operator. We present the relation between an orthogonality preserving operator and its adjoint, and the relation between a bounded linear orthogonality preserving normal operator and its adjoint.

2.1 Theorem. [2] *Let X and Y be two inner product spaces over the same field $\mathbb{K}$.*

For a nonvanishing operator $T : X \to Y$ the following conditions are equivalent:

(1) *T is linear and orthogonality preserving.*

(2) *T is linear and there exists $\gamma > 0$ such that $\|T(x)\| = \gamma \|x\|$, for all $x \in X$.*

(3) *There exists $\gamma > 0$ such that $\langle T(x), T(y) \rangle = \gamma^2 \langle x, y \rangle$, for all $x, y \in X$.*

Proof. See [2]. ■

2.2 Theorem. [1] *Let H be a Hilbert space and $T \in B(H)$. If T is an orthogonality preserving operator, then so are T^*T and $|T|$, where T^* is adjoint of T* and $|T| = \sqrt{T^*T}$.

Proof. Let x, y be two orthogonal elements of H. Since T is orthogonality preserving,

we have

$$\langle T(x), T(y) \rangle = 0 \text{ which implies } \langle x, T^*T(y) \rangle = 0.$$

By using orthogonality preserving of T,

$$\langle T(x), TT^*T(y) \rangle = 0 \text{ which implies } \langle T^*T(x), T^*T(y) \rangle = 0.$$

Hence T^*T is orthogonality preserving.

Again, for $|T| = \sqrt{T^*T}, \langle x, T^*T(y) \rangle = 0$ gives

$$\langle x, |T|^2 (y) \rangle = 0.$$

Therefore

$$\langle |T|(x), |T|(y) \rangle = 0.$$

Thus $|T|$ is orthogonality preserving. ■

2.3 Theorem. [1] *Let H be a Hilbert space and T be a bounded linear orthogonality preserving operator on H. Then T^* is a bounded linear orthogonality preserving operator on H if and only if T* is normal.

Proof. Let T be orthogonality preserving. Suppose that T is normal.

That is

$$T^*T = TT^*.$$

We show that T^* is orthogonality preserving. Let x, y be two orthogonal elements of H. Since T is orthogonality preserving,

$$\langle T(x), T(y)\rangle = 0 \text{ which implies } \langle x, T^*T(y)\rangle = 0.$$

Since T is normal,

$$\langle x, TT^*(y)\rangle = 0 \text{ which implies } \langle T^*(x), T^*(y)\rangle = 0.$$

Hence T^* is orthogonality preserving.

Conversely, suppose that T and T^* are orthogonality preserving. By the condition (2) of Theorem 2.1, there exist $\gamma, \gamma' > 0$ such that

$$\|T(x)\| = \gamma \|x\|$$

and

$$\|T^*(x)\| = \gamma' \|x\|$$

for all $x \in H$. Thus

$$\|T\| = \gamma \text{ and } \|T^*\| = \gamma'.$$

But $\|T\| = \|T^*\|$, so that $\gamma' = \gamma$. By Theorem 2.2, $TT^*, T^*T, |T|$ and $|T^*|$ are orthogonality preserving. Since $T^*(x) \in H$,

$$\|TT^*(x)\| = \gamma \|T^*(x)\| = \gamma \cdot \gamma \|x\| = \gamma^2 \|x\|.$$

Also, for $|T| = (T^*T)^{\frac{1}{2}}$ and $|T^*| = (TT^*)^{\frac{1}{2}}$, the scalar is equal to γ.

Now, we have

$$\begin{aligned}\langle (T^*T - TT^*)(x), (T^*T - TT^*)(x)\rangle &= \|T^*T(x)\|^2 + \|TT^*(x)\|^2 - \langle T^*T(x), TT^*(x)\rangle - \langle TT^*(x), T^*T(x)\rangle \\ &= 2\gamma^4 \|x\|^2 - \langle T^*T(x), TT^*(x)\rangle - \langle TT^*(x), T^*T(x)\rangle.\end{aligned}$$

Also, by using polarization identity

$$\begin{aligned}\left\langle T^*T(x), TT^*(x)\right\rangle &= \left\langle |T|^2(x), TT^*(x)\right\rangle \\ &= \left\langle |T|(x), |T|TT^*(x)\right\rangle \\ &= \frac{1}{4}\sum_{k=0}^{3} i^k \left\langle |T|(x)+i^k|T|TT^*(x), |T|(x)+i^k|T|TT^*(x)\right\rangle \\ &= \frac{1}{4}\sum_{k=0}^{3} i^k \left\| |T|\left(x+i^kTT^*(x)\right)\right\|^2 \\ &= \frac{1}{4}\gamma^2\sum_{k=0}^{3} i^k \left\langle x+i^kTT^*(x), x+i^kTT^*(x)\right\rangle \\ &= \gamma^2\left\langle x, TT^*(x)\right\rangle \\ &= \gamma^4\|x\|^2.\end{aligned}$$

Hence $\left\langle T^*T(x), TT^*(x)\right\rangle = \gamma^4\|x\|^2$. Also, $\left\langle TT^*(x), T^*T(x)\right\rangle = \gamma^4\|x\|^2$ by changing the role of T by T^*. Therefore, we have

$$\left\langle T^*T(x)-TT^*(x), T^*T(x)-TT^*(x)\right\rangle = 2\gamma^4\|x\|^2-\gamma^4\|x\|^2-\gamma^4\|x\|^2 = 0$$

for every $x\in H$. Thus $\left\|T^*T-TT^*\right\| = 0$ and so $TT^* = T^*T$. Hence T is normal. ■

2.2 Properties of Right-Angle Preserving Operators

In this subsection, we show every right-angle preserving operator is orthogonality preserving. We express equivalent conditions for a right-angle preserving operator. We examine the relation between a bounded linear right-angle preserving normal operator and its adjoint and the relation between a right-angle preserving operator and its adjoint. We prove that every unitary operator on H is an orthogonality preserving operator and this result is true for a right-angle preserving operator.

2.4 Lemma. *Let H be a Hilbert space and $T\in B(H)$. If T is right-angle preserving, then T is orthogonality preserving.*

Proof. Suppose that T is right-angle preserving and T is linear. Let $u = x-z$ and $v = y-z$ with $u\perp v$. By right-angle preserving,

$$T(x)-T(z)\perp T(y)-T(z).$$

But T is linear, so that

$$T(x-z)\perp T(y-z).$$

That is, $T(u)\perp T(v)$. Thus T is orthogonality preserving. ■

2.5 Theorem. [3] *Let X and Y be real inner product spaces and $T: X\to Y$ be an operator. The following conditions are equivalent*:

(1) *T satisfies right-angle preserving and $T(0)=0$;*

(2) *T satisfies orthogonality preserving and T is continuous and linear*;

(3) *T satisfies orthogonality preserving and T is linear*;

(4) *T is linear and satisfies $\|T(x)\| = \gamma\|x\|, x \in X$ for some constant $\gamma \geq 0$*;

(5) *T satisfies $\langle T(x), T(y)\rangle = \gamma^2 \langle x, y\rangle, x, y \in X$ for some constant $\gamma \geq 0$*;

(6) *T satisfies orthogonality preserving and T is additive.*

Proof. See [3]. ■

2.6 Theorem. *Let H be a Hilbert space and T be a bounded linear right-angle preserving operator on H. Then T^* is a bounded linear right-angle preserving operator on H if and only if T is normal.*

Proof. Let T be right-angle preserving. Suppose that T is normal. Then $T^*T = TT^*$. We show that T^* is right-angle preserving. Let $x - z$ and $y - z$ be two orthogonal elements of H. Since T is right-angle preserving, we have

$$\langle T(x) - T(z), T(y) - T(z)\rangle = 0.$$

Since T is linear, $\langle T(x-z), T(y-z)\rangle = 0$. It follows that $\langle x - z, T^*T(y-z)\rangle = 0$.

Since T is normal, $\langle x - z, TT^*(y-z)\rangle = 0$. Thus we have $\langle T^*(x-z), T^*(y-z)\rangle = 0$.

Since T^* is linear, we have

$$\langle T^*(x) - T^*(z), T^*(y) - T^*(z)\rangle = 0.$$

Hence T^* is right-angle preserving. By Lemma 2.4, T and T^* are orthogonality preserving. By the second part of Theorem 2.3, we can prove that T is normal. ■

It is obvious that T^*T and $|T|$ are linear if $T \in B(H)$. So we obtain the following theorem.

2.7 Theorem. *Let H be a Hilbert space and $T \in B(H)$. If T is a right-angle preserving operator, then so are T^*T and $|T|$, where T^* is adjoint of T and $|T| = \sqrt{T^*T}$.*

2.8 Theorem. *Let T be a unitary operator in $B(H)$. Then T is orthogonality preserving and right-angle preserving.*

Proof. Suppose $x \perp y$, for all $x, y \in H$. Since every unitary operator on a Hilbert space H is isometry, we have

$$\langle T(x), T(y)\rangle = \langle x, y\rangle = 0.$$

Hence T is orthogonality preserving.

Again, suppose $x - z \perp y - z$, for all $x, y, z \in H$. Since every unitary operator on a Hilbert space H is isometry, we have

$$\langle T(x-z), T(y-z)\rangle = \langle x-z, y-z\rangle = 0.$$

Moreover T is linear, so $\langle T(x)-T(z), T(y)-T(z)\rangle = 0$. That is,

$$T(x)-T(z) \perp T(y)-T(z).$$

Hence T is right-angle preserving. ■

3 Stability Problems

In this section, we omit some properties of approximately orthogonality and approximate right-angle preserving operators. These operators can be extensively studied in [2,3]. We show the relation between approximate right-angle preserving and approximately orthogonality preserving. We present quasi-linear and some stability problems. We prove that Chmielinski's stability question for right-angle preserving and approximate right-angle preserving; see [3].

3.1 Theorem. [2] *Let X and Y be (real or complex) inner product spaces.*

Let $T: X \to Y$ be a nonzero linear operator satisfying approximately orthogonality preserving with some $\varepsilon \in [0,1)$. Then T is injective, continuous and there exists $\gamma > 0$ such that

(1) $$\left|\langle T(x), T(y)\rangle - \gamma^2 \langle x, y\rangle\right| \le \delta \min\left\{\gamma^2 \|x\| \, \|y\|, \|T(x)\| \, \|T(y)\|\right\}, \; x, y \in X,$$

with $\delta = 4\varepsilon\left(\dfrac{1}{1-\varepsilon} + \sqrt{\dfrac{1+\varepsilon}{1-\varepsilon}}\right)$.

Conversely, if $T: X \to Y$ satisfies **(1)** *with some $\delta \ge 0$ and $\gamma > 0$, then T is a quasi-linear, approximately orthogonality preserving operator. More precisely, T satisfies*

$$\|T(x+y)-T(x)-T(y)\| \le 2\sqrt{\delta}\gamma(\|x\|+\|y\|), \; x, y \in X,$$

$$\|T(\lambda x)-\lambda T(x)\| \le 2\sqrt{\delta}\gamma|\lambda|\|x\|, \; x \in X, \; \lambda \in \mathbb{K}$$

and $x \perp y \Rightarrow T(x) \perp^{\delta} T(y); T(x) \perp T(y) \Rightarrow x \perp^{\delta} y$, *for* $x, y \in X$.

Proof. See [2]. ■

3.2 Theorem. [3] *Let X and Y be real inner product spaces and $T: X \to Y$ be an operator. If T satisfies approximately orthogonality preserving and T is additive, then T satisfies approximate right-angle preserving and $T(0) = 0$.*

Proof. See [3]. ■

3.3 Theorem. *Let X and Y be real inner product spaces and $T: X \to Y$ be an operator. For $\varepsilon \in [0,1)$, if T is approximate right-angle preserving and linear, then T is approximately orthogonality preserving.*

Proof. If T is approximate right-angle preserving, then

$$x-z \perp y-z \text{ implies } T(x)-T(z) \perp^{\varepsilon} T(y)-T(z),$$

where $x,\ y,\ x-z,\ y-z \in X$.

Let $u=x-z,\ v=y-z$. If $u \perp v$ then $\langle u,v\rangle = 0$.

$$\begin{aligned}
\left|\langle T(u),T(v)\rangle\right| &= \left|\langle T(x-z),T(y-z)\rangle\right| \\
&= \left|\langle T(x)-T(z),T(y)-T(z)\rangle\right| \\
&\le \varepsilon \left\|T(x)-T(z)\right\| \ \left\|T(y)-T(z)\right\| \\
&= \varepsilon \left\|T(x-z)\right\| \ \left\|T(y-z)\right\| \\
&= \varepsilon \left\|T(u)\right\| \ \left\|T(v)\right\|.
\end{aligned}$$

This means that $T(u) \perp^{\varepsilon} T(v)$. Hence every linear approximate right-angle preserving operator is approximately orthogonality preserving. ■

The stability of the orthogonality preserving property has been studied in [4]. The following theorem is used in Corollary 3.8.

3.4 Theorem. [3] *Let X, Y be inner product spaces and let X be finite-dimensional. Then there exists a continuous function $\delta:[0,1)\to[0,+\infty)$ with the property $\lim_{\varepsilon\to 0^+}\delta(\varepsilon)=0$ such that for each linear operator $f: X \to Y$ satisfying approximately orthogonality preserving one finds a linear, orthogonality preserving one $T: X \to Y$ such that*

$$\|f-T\| \le \delta(\varepsilon)\min\{\|f\|,\ \|T\|\}.$$

The mapping δ depends, actually, only on the dimension of X.

3.5 Lemma. [2] *Let X and Y be two inner product spaces over the same field $\mathbb{K} =$ □ or □. Suppose that $T: X \to Y$ satisfies, with some $\delta \ge 0$ and $\gamma > 0$, the functional inequality*

(1) $$\left|\langle T(x),T(y)\rangle - \gamma^2 \langle x,y\rangle\right| \le \delta\gamma^2 \|x\| \ \|y\|,\ x,\ y \in X.$$

Then T is quasi-linear. That is, T is quasi-additive and quasi-homogeneous.

We need the following proposition for establishing our next corollary.

3.6 Proposition. [3] *Let $f: X \to Y$ satisfy right-angle preserving and $f(0)=0$. Suppose that $g: X \to Y$ satisfies*

$$\left\|f(x)-g(x)\right\| \le M\left\|f(x)\right\|,\ x \in X$$

with some constant $M < \frac{1}{4}$. Then g satisfies approximately orthogonality preserving

with $\varepsilon = \dfrac{M(M+2)}{(1-M)^2}$ *and*

$$\|g(x+y)-g(x)-g(y)\| \le 2\sqrt{\varepsilon}\left(\|g(x)\|+\|g(y)\|\right),\ x,\ y \in X;$$

$$\|g(\lambda x)-\lambda g(x)\| \le 2\sqrt{\varepsilon}\,|\lambda|\,\|g(x)\|,\ x \in X,\ \lambda \in \mathbb{R}.$$

Proof. Suppose that $f : X \to Y$ *satisfy right-angle preserving and* $f(0)=0$. *By Theorem 2.5, f satisfies* $\|f(x)\| = \gamma\|x\|$ *and* $\langle f(x), f(y)\rangle = \gamma^2\langle x, y\rangle,\ x,\ y \in X$ for some constant $\gamma \ge 0$. And then f is linear. Thus we have for arbitrary $x,\ y \in X$:

$$\begin{aligned}
\left|\langle g(x), g(y)\rangle - \gamma^2\langle x, y\rangle\right| &= \left|\langle g(x), g(y)\rangle - \langle f(x), f(y)\rangle\right| \\
&= \left|\langle g(x), g(y)\rangle - \langle f(x), g(y)\rangle + \langle f(x), g(y)\rangle - \langle f(x), f(y)\rangle\right| \\
&= \left|\langle g(x)-f(x), g(y)-f(y)+f(y)\rangle + \langle f(x), g(y)-f(y)\rangle\right| \\
&= \left|\langle g(x)-f(x), g(y)-f(y)\rangle + \langle g(x)-f(x), f(y)\rangle + \langle f(x), g(y)-f(y)\rangle\right|
\end{aligned}$$

By Cauchy-Schwarz Inequality,

$$\begin{aligned}
\left|\langle g(x), g(y)\rangle - \gamma^2\langle x, y\rangle\right| &\le \|g(x)-f(x)\|\ \|g(y)-f(y)\| + \|g(x)-f(x)\|\ \|f(y)\| + \|f(x)\|\ \|g(y)-f(y)\| \\
&\le M^2\|f(x)\|\ \|f(y)\| + M\|f(x)\|\ \|f(y)\| + M\|f(x)\|\ \|f(y)\| \\
&= M^2\gamma^2\|x\|\ \|y\| + 2M\gamma^2\|x\|\ \|y\| \\
&= M(M+2)\gamma^2\|x\|\ \|y\|.
\end{aligned}$$

By Lemma 3.5, we get, for any $x,\ y \in X,\ \lambda \in \mathbb{R}$;

$$\begin{aligned}
\|g(x+y)-g(x)-g(y)\| &\le 2\sqrt{M(M+2)}\gamma\left(\|x\|+\|y\|\right) \\
&= 2\sqrt{M(M+2)}\left(\|f(x)\|+\|f(y)\|\right);
\end{aligned}$$

$$\begin{aligned}
\|g(\lambda x)-\lambda g(x)\| &\le 2\sqrt{M(M+2)}\gamma\,|\lambda|\,\|x\| \\
&= 2\sqrt{M(M+2)}\,|\lambda|\,\|f(x)\|.
\end{aligned}$$

Since $\|f(x)\| - \|g(x)\| \le M\|f(x)\|$,

$$\begin{aligned}
\|f(x)\| - M\|f(x)\| &\le \|g(x)\| \\
\|f(x)\| &\le \frac{\|g(x)\|}{1-M}.
\end{aligned}$$

Therefore

$$\left|\langle g(x), g(y)\rangle - \gamma^2 \langle x, y\rangle\right| \le M(M+2)\|f(x)\| \ \|f(y)\|$$
$$\le \frac{M(M+2)}{(1-M)^2}\|g(x)\| \ \|g(y)\|.$$

Letting $\varepsilon = \dfrac{M(M+2)}{(1-M)^2}$. According to converse of Theorem 3.1, we have $x \perp y$ implies $g(x) \perp^{\varepsilon} g(y)$ and

$$\|g(x+y) - g(x) - g(y)\| \le 2\sqrt{\varepsilon}\left(\|g(x)\| + \|g(y)\|\right),\ x,\ y \in X.$$
$$\|g(\lambda x) - \lambda g(x)\| \le 2\sqrt{\varepsilon}\,|\lambda|\|g(x)\|,\ x \in X,\ \lambda \in \square.$$

■

3.7 Corollary. [3] *If f satisfies right-angle preserving, $f(0) = 0$ (whence f is linear) and $g : X \to Y$ is a linear operator satisfying, with $M < \dfrac{1}{4}$,*

$$\|f - g\| \le M\|f\|,$$

then g is approximate right-angle preserving.

Proof. According to the above Proposition 3.6, we get g is approximately orthogonality preserving and since g is linear. It follows from Theorem 3.2 that g is approximate right-angle preserving. ■

According to the reverse statement in Corollary 3.7, we show the following corollary.

3.8 Corollary. *If a linear operator $g : X \to Y$ satisfies approximate right-angle preserving (with some $\varepsilon > 0$), then there exists a linear operator f satisfying right angle preserving such that an estimation of*

$$\|f - g\| \le M\|f\|, \text{ with } M < \frac{1}{4}.$$

Proof. By Theorem 3.3, if g is approximate right-angle preserving and linear, then g is approximately orthogonality preserving. It follows from Theorem 3.4 that there exists linear f and satisfying orthogonality preserving, hence f is a right-angle preserving operator such that

$$\|g - f\| \le \delta(\varepsilon)\min\{\|g\|,\ \|f\|\}$$
$$\|f - g\| \le M\|f\|.$$

■

Conclusion

This research paper discusses orthogonality preserving and right-angle preserving operators on inner product spaces and Hilbert spaces. We see that some properties of bounded linear orthogonality preserving operators and stability of orthogonality property are also true for right-angle preserving. We finally present the stability of two types of preserving operators.

Acknowledgements

I would like to express my gratitude towards my professor, Dr. Aung Kyaw, Head of Department of Mathematics, University of Yangon, for his kind permission to do this research paper and for all the support and encouragement he gave me. I am very grateful to my professor, Dr. Yin Yin Su Win, Department of Mathematics, University of Yangon, for the valuable encouragement she gave me in preparing this research paper. I also acknowledge all my teachers throughout my student life. Finally, I would like to express my heartfelt thank you to the Myanmar Academy of Arts and Science for the invitation to participate in 24th Arts and Science Research Conference.

References

E. Ansari-Piri, R. G. Sanati and M. Kardel, (2017) "A characterization of orthogonality preserving operators" *Bulletin of The.Iranian Mathematical Society,* vol. 43, issue 7, pp. 2495-2505.

E. Kreyszig, (1978) *Introductory Functional Analysis with Applications,* John Wiley and Sons. Inc., New York.

J. Chmieliński, (2005) "Linear mappings approximately preserving orthogonality" *Journal of Mathematical Analysis and Applications,* vol. 304, pp. 158-169.

J. Chmieliński, (2006) "On some approximate functional relations stemming from orthogonality preserving property" *Journal of Inequalities in Pure and Applied Mathematics,* vol. 7, Issue 3, Article 85.

J. Chmieliński, (2006) "Stability of the orthogonality preserving property in finite-dimensional inner product spaces" *Journal of Mathematical Analysis and Applications,* vol. 318, pp. 433-443.

THE BLOOD FLOWS RATE IN THE BLOOD VESSELS*

Khin Pyone Hmwe[1]

Abstract

The blood flows in the blood vessels are considered. The velocities profile in the cylindrical blood vessels along the radial direction and axial direction are calculated. The equations of the blood flow rate and the blood pressure are determined by Navier-stokes equation and equation of continuity. This paper discusses a mathematical relation Hagen Poiseuille's equation about how much blood flow through an individual blood vessel and what would the rate of blood flow affect.

Keywords: velocity profile, the rate of blood flow, the blood pressure

Introduction

All the vessels are assumed to be the same in nature excluding their size, length and cross-sectional areas. The blood is the viscous fluid. The steady laminar flows of viscous incompressible fluid between two infinite stationary parallel plates are studied. Plane Couette flow is calculated that the lower plate is moving and the upper plate is at rest [6]. The steady laminar flow of without body forces for viscous incompressible fluid through an infinite circular pipe and two coaxial circular cylinders are discussed [8]. This flow is axi-symmetry and steady. The cardiovascular system equation is calculated by Navier-Stokes equation in the cylindrical coordinates [2]. The velocities of radial direction and axial direction in an axi-symmetry flow are considered [7].

In this paper, modeling of the blood flow rate and the flow rate of the blood flow in the blood vessel are produced by the cardiovascular system equation. Modeling of the blood pressure is calculated from the blood flow rate equation.

2. The governing equation

The velocity components in the r,θ and z directions are u,v and w respectively.

The Navier-Stokes equation in the cylindrical coordinates is given by

$$(1)\ \frac{\partial u}{\partial t}+u\frac{\partial u}{\partial r}+\frac{v}{r}\frac{\partial u}{\partial \theta}-\frac{v^2}{r}+w\frac{\partial u}{\partial z}=-\frac{1}{\rho}\frac{\partial p}{\partial r}+\upsilon\left[\frac{\partial}{\partial r}\left(\frac{1}{r}\frac{\partial}{\partial r}(ru)\right)+\frac{1}{r^2}\frac{\partial^2 u}{\partial \theta^2}-\frac{2}{r^2}\frac{\partial v}{\partial \theta}+\frac{\partial^2 u}{\partial z^2}\right],$$

$$(2)\ \frac{\partial v}{\partial t}+u\frac{\partial v}{\partial r}+\frac{v}{r}\frac{\partial v}{\partial \theta}+\frac{uv}{r}+w\frac{\partial v}{\partial z}=-\frac{1}{\rho}\frac{\partial p}{\partial \theta}+\upsilon\left[\frac{\partial}{\partial r}\left(\frac{1}{r}\frac{\partial}{\partial r}(rv)\right)+\frac{1}{r^2}\frac{\partial^2 v}{\partial \theta^2}-\frac{2}{r^2}\frac{\partial u}{\partial \theta}+\frac{\partial^2 v}{\partial z^2}\right],$$

$$(3)\ \frac{\partial w}{\partial t}+u\frac{\partial w}{\partial r}+\frac{v}{r}\frac{\partial w}{\partial \theta}+w\frac{\partial w}{\partial z}=-\frac{1}{\rho}\frac{\partial p}{\partial z}+\upsilon\left[\frac{1}{r}\frac{\partial}{\partial r}\left(r\frac{\partial w}{\partial r}\right)+\frac{1}{r^2}\frac{\partial^2 w}{\partial \theta^2}+\frac{\partial^2 w}{\partial z^2}\right],$$

where $\rho=$density, $\upsilon=\dfrac{\mu}{\rho}$ viscosity of fluid, and $p=$the fluid pressure.

The fluid is axi-symmetry with the assumption of no tangential velocity $(v=0)$ and the remaining quantities are independent of z. A change of variables on the Navier-Stokes equation in the cylindrical coordinates system:

---

* Second Prize (2024)

[1] Department of Mathematics, Bago University

$$(4)\ \frac{\partial w}{\partial t}+f\frac{\partial w}{\partial r}+w\frac{\partial w}{\partial z}=-\frac{1}{\rho}\frac{\partial p}{\partial z}+\upsilon\left[\frac{1}{r}\frac{\partial}{\partial r}\left(r\frac{\partial w}{\partial r}\right)+\frac{\partial^2 w}{\partial z^2}\right],$$

$$(5)\frac{\partial f}{\partial t}+f\frac{\partial f}{\partial r}+w\frac{\partial f}{\partial z}=-\frac{1}{\rho}\frac{\partial p}{\partial z}+\upsilon\left[\frac{1}{r}\frac{\partial}{\partial r}\left(r\frac{\partial f}{\partial r}\right)+\frac{\partial^2 f}{\partial z^2}-\frac{f}{r^2}\right],$$

$$(6)\frac{1}{r}\frac{\partial}{\partial r}(rf)+\frac{\partial w}{\partial z}=0.$$

The equations (4) and (5) reduce to

$$(7)\frac{\partial w}{\partial t}+f\frac{\partial w}{\partial r}+w\frac{\partial w}{\partial z}=-\frac{1}{\rho}\frac{\partial p}{\partial z}+\upsilon\left[\frac{\partial^2 w}{\partial r^2}+\frac{1}{r}\frac{\partial w}{\partial r}+\frac{\partial^2 w}{\partial z^2}\right],$$

$$(8)\frac{\partial f}{\partial t}+f\frac{\partial f}{\partial r}+w\frac{\partial f}{\partial z}=-\frac{1}{\rho}\frac{\partial p}{\partial z}+\upsilon\left[\frac{\partial^2 f}{\partial r^2}+\frac{1}{r}\frac{\partial f}{\partial r}+\frac{\partial^2 f}{\partial z^2}-\frac{f}{r^2}\right],$$

where f be the radial flow component and w be the axial flow components in z - direction. The equation of continuity can be written as:

$$(9)\frac{\partial \rho}{\partial t}+\frac{\partial(\rho w)}{\partial z}=0\,.$$

Define a new variable which is the radial coordinate transformation, given by:

$$(10)\quad \gamma=\frac{r}{R(z,t)},$$

where $R(z,t)$ be the inner radius of the vessel, r is the radial direction.

By using equation (10) in equation (7),

$$(11)\quad \frac{\partial w}{\partial t}+(\frac{\partial w}{\partial \gamma}\cdot\frac{\partial \gamma}{\partial R}\cdot\frac{\partial R}{\partial t})+f(\frac{\partial w}{\partial \gamma}\cdot\frac{\partial \gamma}{\partial r})+w(\frac{\partial w}{\partial z}+\frac{\partial w}{\partial \gamma}\cdot\frac{\partial \gamma}{\partial R}\cdot\frac{\partial R}{\partial z})$$
$$=-\frac{1}{\rho}\frac{\partial p}{\partial z}+\frac{\mu}{\rho}\left[(\frac{\partial w}{\partial \gamma}\cdot\frac{\partial \gamma}{\partial r})(\frac{\partial w}{\partial \gamma}\cdot\frac{\partial \gamma}{\partial r})+\frac{1}{r}(\frac{\partial w}{\partial \gamma}\cdot\frac{\partial \gamma}{\partial r})+(\frac{\partial w}{\partial \gamma}\cdot\frac{\partial \gamma}{\partial z})(\frac{\partial w}{\partial \gamma}\cdot\frac{\partial \gamma}{\partial z})\right].$$

Then Substituting $\frac{\partial \gamma}{\partial R}=\frac{\partial}{\partial R}(\frac{r}{R}),\frac{\partial \gamma}{\partial r}=\frac{\partial}{\partial r}(\frac{r}{R})$ and $\frac{\partial \gamma}{\partial z}=\frac{\partial}{\partial z}(\frac{r}{R})$ in equation (11),

$$\frac{\partial w}{\partial t}+\left(\frac{\partial w}{\partial \gamma}\cdot\frac{\partial}{\partial R}(\frac{r}{R}).\frac{\partial R}{\partial t}\right)+f\left(\frac{\partial w}{\partial \gamma}\cdot\frac{\partial}{\partial r}(\frac{r}{R})\right)+w\left(\frac{\partial w}{\partial z}\cdot\frac{\partial w}{\partial \gamma}\cdot\frac{\partial \gamma}{\partial R}(\frac{r}{R})\cdot\frac{\partial R}{\partial z}\right)$$
$$=-\frac{1}{\rho}\frac{\partial p}{\partial z}+\frac{\mu}{\rho}\left[\left(\frac{\partial w}{\partial \gamma}\cdot\frac{\partial}{\partial r}(\frac{r}{R})\right)\left(\frac{\partial w}{\partial \gamma}\cdot\frac{\partial}{\partial r}(\frac{r}{R})\right)+\frac{1}{r}\left(\frac{\partial w}{\partial \gamma}\cdot\frac{\partial}{\partial r}(\frac{r}{R})\right)+\left(\frac{\partial w}{\partial \gamma}\cdot\frac{\partial}{\partial z}(\frac{r}{R})\right)\left(\frac{\partial w}{\partial \gamma}\cdot\frac{\partial}{\partial z}(\frac{r}{R})\right)\right](12)$$
$$\frac{\partial w}{\partial t}+\left(\frac{\partial w}{\partial \gamma}(\frac{-r}{R^2}).\frac{\partial R}{\partial t}\right)+f\left(\frac{\partial w}{\partial \gamma}(\frac{1}{R})\right)+w\left(\frac{\partial w}{\partial z}+\frac{\partial w}{\partial \gamma}(\frac{-r}{R^2})\frac{\partial R}{\partial z}\right)$$

$$= -\frac{1}{\rho}\frac{\partial p}{\partial z} + \frac{\mu}{\rho}\left[\left(\frac{\partial w}{\partial \gamma}(\frac{1}{R})\right)\left(\frac{\partial w}{\partial \gamma}(\frac{1}{R})\right) + \frac{1}{r}\left(\frac{\partial w}{\partial r}(\frac{1}{R})\right)\right].$$

By Factorizing and simplifying the left-hand side of equation (12),

(13) $$\frac{\partial w}{\partial t} - \frac{1}{R}\left[\gamma(\frac{\partial R}{\partial t} + \frac{\partial R}{\partial z}) - f\right]\frac{\partial w}{\partial \gamma} + w\frac{\partial w}{\partial z} = -\frac{1}{\rho}\frac{\partial p}{\partial z} + \frac{\mu}{\rho R^2}\left[\frac{\partial^2 w}{\partial \gamma^2} + \frac{1}{\gamma}\frac{\partial w}{\partial \gamma}\right].$$

From equation (6),

(14) $$\frac{\partial f}{\partial r} + \frac{f}{r} + \frac{\partial w}{\partial z} = 0.$$

By using the radial coordinate transformation equation (10),

$$\frac{\partial f}{\partial \gamma}\frac{\partial \gamma}{\partial r} + \frac{f}{r} + \left(\frac{\partial w}{\partial \gamma}\cdot\frac{\partial \gamma}{\partial R}\cdot\frac{\partial R}{\partial z}\right) + \frac{\partial w}{\partial z} = 0$$

$$\frac{\partial f}{\partial \gamma}\frac{1}{R} + \frac{f}{r} - \frac{\partial w}{\partial \gamma}\frac{r}{R^2}\cdot\frac{\partial R}{\partial z} + \frac{\partial w}{\partial z} = 0.$$

By substituting $r = \gamma R$,

(15) $$\frac{\partial f}{\partial \gamma}\frac{1}{R} + \frac{f}{\gamma R} - \frac{\partial w}{\partial \gamma}\frac{r}{R^2}\cdot\frac{\partial R}{\partial z} + \frac{\partial w}{\partial z} = 0.$$

Multiplying equation (15) by γR,

$$\gamma\frac{\partial f}{\partial \gamma} + f - \gamma^2\frac{\partial w}{\partial \gamma}\cdot\frac{\partial R}{\partial z} + \gamma R\frac{\partial w}{\partial z} = 0.$$

Integrating the equation with respect to γ,

$$\int_0^\gamma \gamma\frac{\partial f}{\partial \gamma}d\gamma + \int_0^\gamma f d\gamma + \int_0^\gamma \gamma R\frac{\partial w}{\partial z}d\gamma - \int_0^\gamma \gamma^2\frac{\partial w}{\partial \gamma}\cdot\frac{\partial R}{\partial z}d\gamma = 0.$$

Since $w(0,\ z,\ t) = f(0,z,t) = 0,$

$$\gamma f(\gamma,z,t) + R\int_0^\gamma \gamma\frac{\partial w}{\partial z}d\gamma - \frac{\partial R}{\partial z}\gamma^2 w + \frac{\partial R}{\partial z}\int_0^\gamma 2w\gamma d\gamma = 0,$$

$$\gamma f(\gamma,z,t) = -R\int_0^\gamma \gamma\frac{\partial w}{\partial z}d\gamma + \frac{\partial R}{\partial z}\gamma^2 w - \frac{\partial R}{\partial z}\int_0^\gamma 2w\gamma d\gamma.$$

Dividing by γ,

(16) $$f(\gamma,z,t) = \gamma\frac{\partial R}{\partial z}w - \frac{R}{\gamma}\int_0^\gamma \gamma\frac{\partial w}{\partial z}d\gamma - \frac{2}{\gamma}\frac{\partial R}{\partial z}\int_0^\gamma w\gamma d\gamma,$$

where $f(\gamma)$ represents an arbitrary function satisfying

(*) $$\int_0^1 \gamma f(\gamma)d\gamma = 1.$$

Boundary conditions are

$$f(\gamma,z,t)\big|_{\gamma=0}=0,\quad \frac{\partial w}{\partial \gamma}(\gamma,z,t)\Big|_{\gamma=0}=0,$$

$$f(\gamma,z,t)\big|_{\gamma=1}=\frac{\partial R}{\partial t},\quad w(\gamma,z,t)\big|_{\gamma=1}=0.$$

The function γ must satisfy the condition $f(1)=0$ since $\frac{\partial w}{\partial z}=0$ on $\gamma=1$.

Let $f(\gamma)$ be a power series in γ truncated to finite order N and imposing the conditions equation $(*)$ and $f(1)=0$.

(17) Let $f(\gamma)=\frac{2}{N}\sum_{k=1}^{N}\frac{k+1}{k}(\gamma^{2k}-1)$.

From equation (16),

$$-\int_0^1 \gamma\frac{\partial w}{\partial z}d\gamma=\int_0^1 \gamma f(\gamma)\frac{1}{R}\frac{\partial R}{\partial t}d\gamma+\frac{2}{R}\frac{\partial R}{\partial z}\int_0^1 \gamma w d\gamma,$$

$$-\int_0^1 \gamma\frac{\partial w}{\partial z}d\gamma=\int_0^1\left[\gamma f(\gamma)\frac{1}{R}\frac{\partial R}{\partial t}+\frac{2}{R}\frac{\partial R}{\partial z}\gamma w\right]d\gamma,$$

(18) $$-\int_0^1 \gamma\frac{\partial w}{\partial z}d\gamma=\int_0^1 \gamma\left[\frac{f(\gamma)}{R}\frac{\partial R}{\partial t}+\frac{2w}{R}\frac{\partial R}{\partial z}\right]d\gamma.$$

Taking approximation of considering the equality between the integral to integrands for equation (18),

(19) $$-\frac{\partial w}{\partial z}=\frac{f(\gamma)}{R}\frac{\partial R}{\partial t}+\frac{2w}{R}\frac{\partial R}{\partial z}.$$

Substituting the equation (17) into equation (19),

$$-\frac{\partial w}{\partial z}=\frac{2w}{R}\frac{\partial R}{\partial z}-\frac{1}{R}\frac{\partial R}{\partial t}\left[-\frac{2}{N}\sum_{k=1}^{N}\frac{k+1}{k}(\gamma^{2k}-1)\right],$$

(20) $$\frac{\partial w}{\partial z}=-\frac{2w}{R}\frac{\partial R}{\partial z}+\frac{1}{R}\frac{\partial R}{\partial t}\left[\frac{2}{N}\sum_{k=1}^{N}\frac{k+1}{k}(\gamma^{2k}-1)\right].$$

Substituting equation (20) into equation (16),

$$f(\gamma,z,t)=\gamma\frac{\partial R}{\partial z}w-\frac{R}{\gamma}\int_0^\gamma \gamma\left[-\frac{2w}{R}\frac{\partial R}{\partial z}+\frac{2}{R}\frac{\partial R}{\partial t}\left(\frac{1}{N}\sum_{k=1}^{N}\frac{k+1}{k}(\gamma^{2k}-1)\right)\right]d\gamma-\frac{2}{\gamma}\frac{\partial R}{\partial z}\int_0^\gamma w\gamma d\gamma,$$

$$f(\gamma,z,t)=\gamma\frac{\partial R}{\partial z}w+\frac{R}{\gamma}\int_0^\gamma \gamma\frac{2w}{R}\frac{\partial R}{\partial z}d\gamma-\frac{R}{\gamma}\int_0^\gamma\frac{2\gamma}{R}\frac{\partial R}{\partial t}\frac{1}{N}\sum_{k=1}^{N}\frac{k+1}{k}(\gamma^{2k}-1)d\gamma-\frac{2}{\gamma}\frac{\partial R}{\partial z}\int_0^\gamma w\gamma d\gamma,$$

$$f(\gamma,z,t)=\gamma\frac{\partial R}{\partial z}w+\frac{2}{\gamma}\frac{\partial R}{\partial z}\int_0^\gamma w\gamma d\gamma-\frac{2}{\gamma N}\frac{\partial R}{\partial t}\sum_{k=1}^{N}\frac{k+1}{k}\int_0^\gamma(\gamma^{2k+1}-\gamma)d\gamma-\frac{2}{\gamma}\frac{\partial R}{\partial z}\int_0^\gamma w\gamma d\gamma,$$

(21) $$f(\gamma,z,t)=\gamma\frac{\partial R}{\partial z}w-\frac{2}{\gamma N}\frac{\partial R}{\partial t}\sum_{k=1}^{N}\frac{k+1}{k}\int_0^{\gamma}(\gamma^{2k+1}-\gamma)d\gamma\,.$$

Integrating and expanding equation (21), the velocity profile in the radial direction is

(22) $$f(\gamma,z,t)=\gamma\frac{\partial R}{\partial z}w+\gamma\frac{\partial R}{\partial t}-\frac{\gamma}{N}\frac{\partial R}{\partial t}\sum_{k=1}^{N}\frac{1}{k}\left(\gamma^{2k}-1\right).$$

Assume the velocity profile in the axial direction is

(23) $$w(\gamma,z,t)=\sum_{k=1}^{N}q_k(\gamma^{2k}-1)\,.$$

Choose $N=1$,

(24) $$f(\gamma,z,t)=\gamma\frac{\partial R}{\partial z}w+\gamma\frac{\partial R}{\partial t}-\frac{\partial R}{\partial t}\gamma(\gamma^{2k}-1)\,,$$

(25) $$w(\gamma,z,t)=q(z,t)(\gamma^2-1)\,.$$

Using the equation of axil and radial velocity profile, radial coordinate and the continuity equation Plugging equations (24) and (25) into equations (13) and (14), the Navier-Stokes equations get the forms as below to determine the variable $q(z,t)$ and $R(z,t)$.

(26) $$\frac{\partial q}{\partial t}-\frac{4q}{R}\frac{\partial R}{\partial t}-\frac{2q^2}{R}\frac{\partial R}{\partial z}+\frac{4\mu}{R^2}+\frac{1}{\rho}\frac{\partial p}{\partial z}=0\,,$$

(27) $$2\frac{\partial R}{\partial t}+\frac{R}{2}\frac{\partial q}{\partial z}+q\frac{\partial R}{\partial z}=0\,.$$

Multiplying equation (27) with π,

(28) $$2\pi\frac{\partial R}{\partial t}+\frac{\pi R}{2}\frac{\partial q}{\partial z}+\pi q\frac{\partial R}{\partial z}=0\,.$$

The cross-sectional area of the blood vessel is

(29) $$S=\pi R^2.$$

The blood flow rate is given by

(30) $$Q=\int\int w\partial\gamma=\frac{1}{2}q\pi R^2\,.$$

By using the chain rule, $\frac{\partial Q}{\partial z}$ and $\frac{\partial S}{\partial t}$ are obtained as:

$$\frac{\partial Q}{\partial z}=\pi qR\frac{\partial R}{\partial z}+\frac{\pi R^2}{2}\frac{\partial q}{\partial z}\,,$$

$$\frac{\partial S}{\partial t}=2\pi R\frac{\partial R}{\partial t}\,.$$

Substituting in equation (28),

$$\frac{1}{R}\left(\frac{\partial S}{\partial t}+\frac{\partial Q}{\partial z}\right)=0\,,$$

(31) $$\frac{\partial S}{\partial t}+\frac{\partial Q}{\partial z}=0\,.$$

Inserting the value of $\frac{\partial q}{\partial t},\frac{\partial q}{\partial z},\frac{\partial R}{\partial t},\frac{\partial R}{\partial z}$ in equation (12), another differential equation is obtained.

(32) $$\frac{\partial Q}{\partial t}+\frac{2Q}{S}\frac{\partial Q}{\partial z}-\frac{2Q^2}{S^2}\frac{\partial S}{\partial z}+\frac{4\pi\mu}{S}Q+\frac{S}{2\rho}\frac{\partial p}{\partial z}=0,\ \text{where}\ \frac{\partial Q}{\partial z}=-\frac{\partial S}{\partial t}\,.$$

This equation is called the cardiovascular system equation.

3. Modeling of the blood flow rate

The cross-section area of the blood vessel remains unchanged with time and constant over distance. The pressure gradient is also constant over the distance.

Thus $\frac{\partial S}{\partial t}=0$ and $\frac{\partial S}{\partial z}=0.$

The cardiovascular system equation becomes,

(33) $$\frac{\partial Q}{\partial t}+\frac{4\pi\mu}{S}Q+\frac{S}{2\rho}\frac{\partial p}{\partial z}=0.$$

This is the one - dimensional mathematical model of the blood flow rate.

4 The flow rate of the blood flow

Let 'μ' be a liquid of coefficient of viscosity flow in streamline motion through a horizontal tube of radius *R* and length *L*.

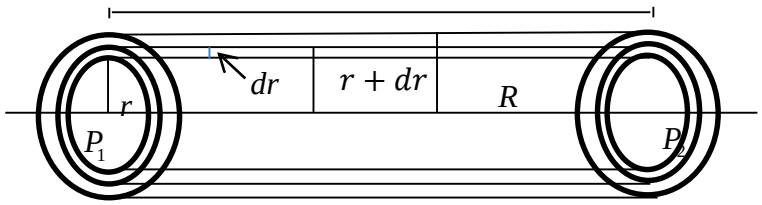

Figure 1

The resistance force is given by

$F_R=\mu A\frac{dv}{dr}$, (*A* = area of the imaginary cylinder)

(34) $$F_R=\mu 2\pi rL\frac{dv}{dr}$$

and if *P* is the pressure difference between the two ends, then force (F_a) accelerating the liquid is given by

$F_a = P\ A$, (A= area of the opening of the imaginary)

(35) $F_a = P\ \pi r^2$.

For steady flow of liquid,

$$F_R = -F_a$$

$$\mu L 2\pi r \frac{dv}{dr} = -P\pi r^2$$

$$dv = \frac{-P}{2\mu l} r dr\ .$$

By integrating,

(36) $$v = \frac{-P}{2\mu L}\frac{r^2}{2} + C_1 .$$

At $v = 0, r = R,$ so equation (36) can be written as

$$0 = \frac{-P}{2\mu L}\frac{R^2}{2} + C_1$$

$$C_1 = \frac{-PR^2}{4\mu l}.$$

Substituting the value of C_1 in equation (36),

$$v = \frac{-P}{2\mu l}\frac{r^2}{2} + \frac{PR^2}{4\mu l},$$

(37) $$v = \frac{-P}{4\mu l}(R^2 - r^2).$$

Then imagine co-axial tube of radius $r + dr$, enclosing the imaginary tube of radius r.

Thus, the area between the two tubes is $2\pi r dr$.

So, volumetric of liquid passing through the area is

$Q\ =\ A.v\quad = 2\pi r dr.v.$

So, volumetric of liquid (Q) passing forward through whole tube is

$$Q = \int_0^R 2\pi r v dr$$

$$= \int_0^R 2\pi r \frac{P}{4\mu l}(R^2 - r^2) dr$$

$$= \frac{1}{2}\frac{\pi P}{\mu l}\left[\frac{2R^4 - R^4}{4}\right],$$

(38) $$Q = \frac{\pi P R^4}{8\mu L}.$$

This equation is the flow rate of the blood flow. The volumetric flow rate is directly proportional to the pressure gradient and radius. It is inversely proportional to the viscosity of the blood. Thus, a small change in channel radius can causes a small change in flow rate and a small change in radius can cause a small in pressure gradient. An effective way of changing blood pressure is change in vessel radius.

3.1Example

The blood flow through a large artery of radius 2.5 *mm* is found to be 20 *cm* long. The pressure across the artery ends is 380 *Pa*, the rate of the blood flow can be calculated.

The blood viscosity $\mu = 0.0027 Ns/m^2$

Radius of a large artery $R = 2.5\ mm = 2.5(10^{-3})\ m$

The length of the artery $L = 20\ cm = 0.20\ mm$

The difference of pressure = 380 *Pa*

The rate of blood flow is

$$Q = \frac{\pi P R^4}{8\mu L} = 1.0789(10^{-5})\ m^3/s.$$

4. Modeling of the blood pressure

The relation between blood flow rate and the pressure is given by

$$Q = \frac{\pi R^4 P}{8\mu L},$$

where L is the length, P is pressure gradient and R is the radius of vessel.

Substituting in equation (33),

$$\frac{\pi R^4}{8\mu L}\frac{dP}{dt} + \frac{4\pi\mu}{S}\frac{\pi R^4}{8L\mu}P + \frac{S}{2S}\frac{\partial P}{\partial z} = 0.$$

$$\frac{dP}{dt} + \frac{4\mu}{R^2}P + \frac{4\mu L}{\rho R^2}\frac{\partial P}{\partial z} = 0. \quad (39)$$

This equation is the mathematical model of the blood pressure in the body.

4.1 Example

Blood is flowing through an artery of radius 2 *mm* at a rate of 40 *cm/s*. The flow rate and the volume that passes through the artery in a period of 1*s* can be determined.

The radius of an artery $r = 2\ mm = 0.2\ cm.$

The speed of the blood flow $v = 40\ cm/s.$

The volumetric flow rate $Q = Av$

$$Q = 3.14(0.2)^2 40$$
$$Q = 5.024 cm^3/s$$

The volume passes through the artery in $1s = Qt = 5.024\ cm^3$.

4.2 Example

The heart of a resting adult pumps blood at a rate of 5 liter per minute. The rate of volumetric flow per second can be evaluated.

The blood flow rate $Q = 5.00\ L/\ min$

To calculate the volumetric flow rate in centimeter cube per second,

$$5 \text{ liter} = 5000\ cm^3$$

$$Q = \frac{5000}{60} = 83.3\ cm^3/s.$$

To evaluate the volumetric flow rate in meter cube per second,

$$5 \text{ liters} = \frac{5}{1000} m$$

$$Q = \frac{5}{1000 \times 60} = 83.3 \times 10^{-6}\ m^3/s.$$

Conclusion

The goal of this paper was to represent a mathematical model of the blood flow. This model is able to show that the blood flow rate is influenced by the change of cross-sectional area and the pressure gradient. The model can also show that the blood pressure is influenced by both of the cross-sectional area and the length of the blood vessel.

Acknowledgements

I would like to give my deepest appreciation to my Rector Dr Aye Aye Khaing and Pro-Rectors Dr SanYu Maw and Dr Aye Aye Khaing Myint, Bago University, for permitting me to submit this research paper.

My major thanks go to my Professor Dr Htwe Myint Kyi, Head of the Department of Mathematics, Bago University, for her permission and support concerning this research paper. I would like to thank all the teachers who were always ready to give me the best whenever I need help.

References

Batchelor, G.K., (1967) *An Introduction to Fluid Dynamics*, Cambridge University Press, Cambridge.

Jonathan, B.F., and M. M. Orescanin, (2011) "Cellular flow in a small blood vessel", Journal of Fluid Mechanics, Cambridge University, vol. 671, pp466-490.

Kundu, P.K., I.M. Cohen, & D.R. Dowling, (2012) *Fluid Mechanics*, Sixth Edition, Elsevier Inc.

Milne-Thomson, L.M., (1968) *Theoretical hydrodynamics*, Macmillian & Co.Ltd., London.

O'Neill, M.E., & F. Chorlton, (1986) *Ideal and Incompressible Fluid Dynamics*, Ellis Horwood Ltd., England.

Raisinghania, M.D., (2010) *Fluid Dynamics*, S. Chand & Company Ltd., Ram Nagar, New Delhi.

Secomb, T.W., R. Skalak, N. Özkaya, J.F. Gross, (1986) "Flow of axisymmetric red blood cells in narrow capillaries" Journal of Fluid Mechanics, Cambridge University, vol. 163, pp 405-423.

Tasos, C.P., C.G. Georgios, A.N. Alexandrou, (2000) *Viscous Fluid Flow*, CRC Press, Boca Raton London New York Washington, D.C.

ANALYSIS OF IMAGE ENHANCEMENT ON MEDICAL ENDOSCOPIC IMAGE*

Aung Thiha[1], Myat Su Hlaing[2], Soe Mya Mya Aye[3]

Abstract

In clinical surgery, the quality of endoscopic image is degraded by noise. Bloods, illumination changes, specular reflection and other factors contributes to noise affect doctor's judgement, and cause high operation risk. In this research, degraded image is restored by using linear and non-linear methods to make better enhancement. For noise removal, arithmetic mean, harmonic mean, contraharmonic mean and median filters are used. Unsharp masking_filter is used to make sharping image. Gamma correction method is used for color enhancement and tone-mapping. The simulation programs are written using MATLAB. Both linear and non-linear filters are analyzed for specific image processing. The results of these two classes of filter are compared by Image Quality Assessment (IQA). This research assists the physicians to determine the diseases by applying linear and non-linear filter over the endoscopic image that have degraded factors.

Keywords: Endoscopic image, degraded image, image restoration, IQA

Introduction

Image processing begins with the capture of an analog image by suitable devices, which is then converted to digital image before the image is processed by computer for better visual appearance to a human viewer. Most image have noise which creates blur and degrade the quality of image. Filtering is a technique for modifying or enhancing an image. Spatial domain operation or filtering is the processed value for the current pixel depends on both itself and surrounding pixels. Hence Filtering is a neighborhood operation, in which the value of any given pixel in the output image is determined by applying some algorithm to the values of the pixels in the neighborhood of the corresponding input pixel.

In fiber-optic endoscopes, various optical viewing bundles are used to transmit images. Images transmitted to the top of the bundles by each optical fiber yield an image through a focusing lens, with the resulting image viewed through an eyepiece. Optical fibers are prone to damage and damaged optical fiber bundles affect the clarity of the image. To overcome this problem, video-endoscopy was developed in 1990s, using charge-coupled devices (CCDs). CCDs consist of an array of individual photocells, called picture elements or pixels, that receive photons reflected back from the mucosal surface and produce electrons in proportion to the light reflected on the CCDs. The variable charge thus generated is electronically transmitted to a video processor and converted into a digital image. The resolution of images depends on the number of pixels in the array, with higher the pixel density providing a higher resolution for detailed images of a lesion. (Fang et al., 2021)

Endoscopic image is a very wide class of medical images obtained by examining various organs and body cavities by via the special optoelectronic device endoscope. The types of endoscopies are: gastroscopy-examination of stomach, colposcopy-examination of cervix, laparoscopy-examination of abdominal cavity, etc. During endoscopy, physician performs a visual examination of organ surface and makes decision about diagnosis, possible biopsy; also he can perform surgical interventions (endo-surgery).

---

*Special Award (2024)

[1] Department of Computer Studies, University of Yangon
[2] Department of Computer Studies, Dagon University
[3] Department of Computer Studies, University of Yangon

Image Enhancement Techniques

Image enhancement refers to the process of highlighting certain information of an image, weakening or removing any unnecessary information according to specific needs. (Chris, 2010) Some of image enhancement are eliminating noise, revealing blurred details, and adjusting levels to highlight features of an image. (Gonzalez, 2002) Image enhancement can be made by using linear and non-linear filters. In linear filters, arithmetic mean filter, harmonic mean filter and contraharmonic mean filter can be used for noise removal. In non-linear filters, median filter can be used for noise removal. For contrast level enhancement, gamma correction filter that is under non-linear filter can be used. For sharping image, unsharp masking filter can be used that is under linear filters.

Linear Filters

Linear filtering modifies an image *"f" by* replacing the value at each pixel with some linear function of the values of nearby pixels. (Castleman, 1996) Spatial linear filtering is the filtering operations that are performed directly on the pixels of an image.

Common linear filters are:

a. Arithmetic mean filter
b. Unsharp masking filter
c. Harmonic mean filter
d. Contraharmonic mean filter

a. Arithmetic Mean Filter

Arithmetic mean filter calculates the average value in a set of pixel values. In other words, summing up all pixel values within the set and divide them by the size of that set. (Jae, 1990) The principle of this filter matches perfectly with it name, as each pixel in the targeted image is replaced with the mean value of pixels surrounding it. The mathematical formulation for the mean filter is given by:

$$f(x.y) = \frac{1}{MN}\sum_{(m,n)\in W} I(m,n)$$

where: I = the noisy image, f = the restored image and (m, n) = the row and column coordinate respectively, within a window W of size $m \times n$ where the operation takes place centered on input pixels at (x, y).

b. Unsharp Masking Filter

Unsharp mask filtering is method that boosts the high frequency edge information in images. (Jaehne, 2005) The unsharp masking process consists of the following steps:

Step 1. Blur the original image

Step 2. Subtract the blur image from the original (the difference is called the mask)

Step 3. Add the mask to the original

$\bar{f}(x,y)$ denoted the blurred image, the mask in equation form is given by:

$$g(x,y)_{mask} = f(x,y) - \bar{f}(x,y)$$

Then, add a weighted portion of the mask back to the original image:

$$g(x,y) = f(x,y) + kg(x,y)_{mask}$$

where include a weight, k (k ≥ 0), for generality. When k=1, this process has unsharp masking.

c. Harmonic Mean Filter

Let S_{xy} represent the set of coordinates in a rectangular sub-image window of size $m \times n$, centered at point (x,y). The harmonic mean filtering operation of the restored image is given by the expression:

$$\hat{f}(x,y) = \frac{mn}{\sum_{(r,c)\in S_{x,y}} \frac{1}{g(r,c)}}$$

d. Contraharmonic Mean Filter

The contraharmonic mean filtering operation yields a restored image based on the expression:

$$\hat{f}(x,y) = \frac{\sum_{(r,c)\in S_{x,y}} g(r,c)^{Q+1}}{\sum_{(r,c)\in S_{x,y}} g(r,c)^{Q}}$$

where Q is called the order of the filter. Note that the contraharmonic filter reduces to the arithmetic mean filter if Q=0, and to the harmonic mean filter if Q = -1.

Non-Linear Filters

Non-linear filters, all filters which are not linear- are more diverse and difficult to categorize. (Russ, 1995) Non-linear spatial filter also operates on neighborhoods.

Common non-linear filters are:

a. Gamma Correction Filter

b. Median filter

a. Gamma Correction Filter

Gamma correction controls the overall brightness of an image. Power law transformation has the general form

$$s = cr^{\gamma}$$

where s and r are the output and input pixel values, respectively, c and γ are the positive constants. (Astola, 1997) Gamma can be any value between 0 and infinity. If γ is 1 (the default), the mapping is linear. If gamma is less than 1, the mapping is weighted toward higher(brighter) output value. If γ is greater than 1, the mapping is weighted toward lower(daker) output value.

b. Median Filter

The median filter operates by sorting the pixel values within a neighborhood, then finding the median value from that ordered list and the replacing the original pixel by this median value in output image. The mathematical formulation for median filter is given as follows:

$$f(x, y) = median\{I(m, n)|(m, n) \in W\}$$

where I = noisy image, f = restored image and (m, n) = row and column coordinate respectively, within a window W of size $m \times n$ where the operation takes place. (Russ, 2007)

Design of the Proposed System

The proposed system is designed to enhance the medical endoscopic image. For noise removal, in the need of the system, the original endoscopic image is added two types of noise that are Gaussian and Salt & Pepper noise. Noisy image is filtered using arithmetic mean, contraharmonic mean, harmonic mean and median filter methods.

For the contrast level controlling, the original image is inputted and that image is filtered using unsharp masking and gamma correction filter. The output image and input image are accessed by using Image Quality Assessment (IQA). Image Quality Assessment will include Mean Square Error (MSE), Peak Signal to Noise Ratio (PSNR), and Structural Similarity Index Method (SSIM). Figure 1 show the architecture of the image filtering for proposed system.

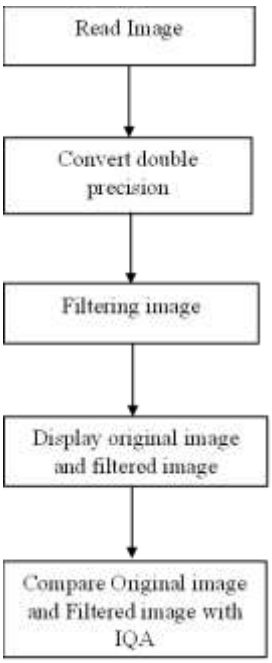

Figure 1 Architecture of the Image Filtering of the Proposed System

The general architecture of the proposed system is shown in Figure 1. The following steps are involved in architecture of the proposed system:

Step 1. Reading the input image
Step 2. Converting the input image into double precision
Step 3. Filtering process of the inputted endoscopic image
Step 4. Showing the original image and filtered image
Step 5. Comparing the original image and filtered image by Image Quality Assessment

Implementation of the Proposed System

The image processing toolbox is distributed by MathWorks that contains a collection of functions for performing different operation specifically for signal and image processing. If "Load Image" button is clicked in the form, dialog box will appear to choose the input image. Endoscopic image enhancement system is shown in Figure 2.

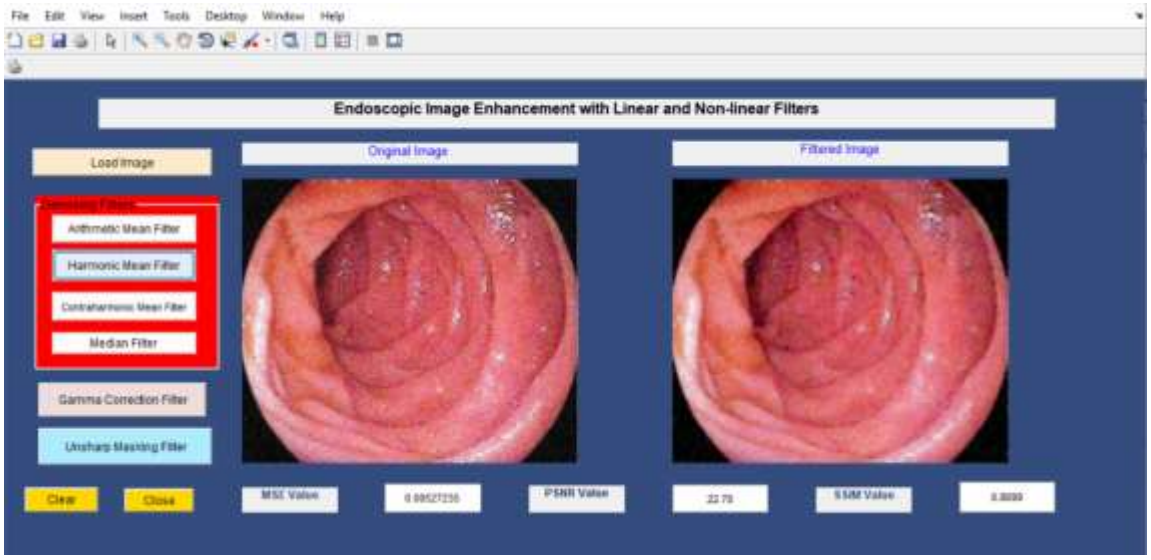

Figure 2 Endoscopic Image Enhancement for Proposed System

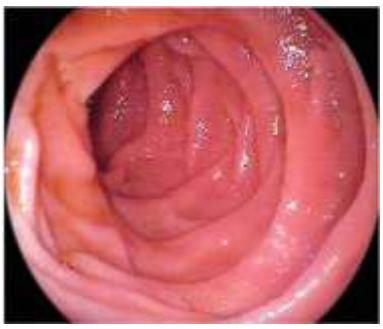

Figure 3 Endoscopic Image

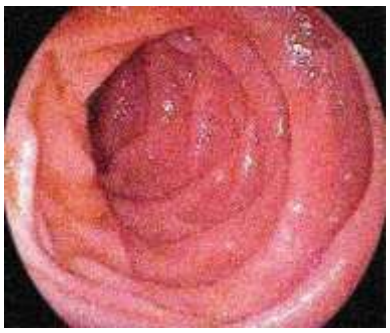

Figure 4 Endoscopic Image with Gaussian Noise Level 0.01

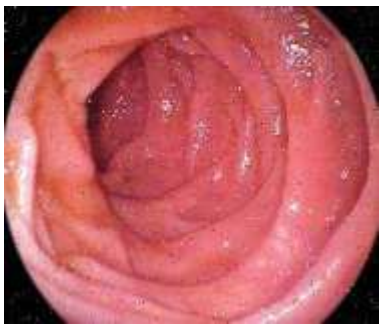

Figure 5 Endoscopic Image with Salt & Pepper Noise Level 0.01

Figure 3 shows the endoscopic image. Figure 4 shows the endoscopic image with 0.01 gaussian noise. The endoscopic image with 0.01 salt & pepper noise is shown in Figure 5. For image noise testing, the original image is added salt and pepper noise with changing noise density. In adding noise, **imnoise** function is used. In salt and pepper noise, noise levels are tested from 0.001 to 0.05. For another noise testing, the original image is added gaussian noise with changing noise density. In gaussian noise, noise level is tested from 0.01 to 0.25.

The simulation for edge enhancement is based on the unsharp masking theory. This filter does not need noisy image to input because the characteristic of this filter is sharping the edge. In this simulation program, scaling constant numbers 0.2, 0.5, 0.8, 1.1, 1.4 have been used. Initially the input image is needed to load from the location of the stored files. Constant number must be entered from input box to apply the filter.

In the harmonic mean and contraharmonic mean filter, the color value of each pixel is replaced with the harmonic mean of color values of the pixels in a surrounding region. These filters will be tested by adding gaussian noise and salt and pepper noise with changing variable and sigma.

In gamma correction filter, endoscopic image is inputted from the location of stored files. This filter does not need to add noise because gamma correction controls the overall brightness of the inputted image. The value of gamma is assigned in this simulation program. The inputted image is adjusted using gamma value.

The median filter operates by sorting the pixel values within the neighborhood, the median value within the window replaces the original value. In this simulation program median filter will be tested for noise removal. First, the noisy image due to Gaussian or Salt& Pepper noise are inputted and he inputted image is filtered by splitting three color channels.

Result and Discussion

Image quality can be assessed using two methods: subjective and objective. Subjective methods are based on the perceptual assessment of a human viewer about the attributes of an image, while objective methods are based on computational models that can predict perceptual image quality. In the endoscopic image evaluation, doctor's subjective evaluation is still the main technique that is used to verify image quality. In this system, to verify the performance of tissue vascular, brightness, and color enhancement, image quality assessment is defined as: (1) mean square error (MSE) (2) peak-signal-to-noise ratio (PSNR) (3) structural similarity index (SSIM).

The proposed system aims for enhancing the image. For noise removal, the proposed system needs to test noise level with image quality assessment. First, the original image is added with gaussian noise. When the gaussian noise level are increased from 0.01 to 0.25, the values of MSE are increased and PSNR values are decreased. The values of SSIM are decreased from 1. When the salt and pepper noise level are increased from 0.001 to 0.05, the values of MSE are increased and PSNR values are decreased. The values of SSIM are decreased from 1. Figure 6 shows the graph diagram of Gaussian noise range from 0.01 to 0.25. Figure 7 illustrates the diagram of Salt and Pepper Noise Range from 0.001 to 0.05.

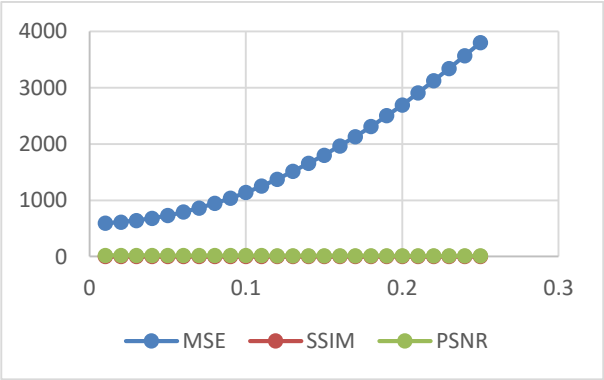

Figure 6 Graph Diagram of Gaussian Noise Range from 0.01 to 0.25

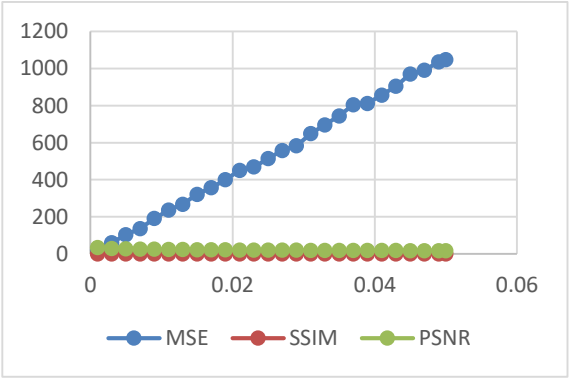

Figure 7 Graph Diagram of Salt and Pepper Noise Range from 0.001 to 0.05

After applying the arithmetic mean filter to the various gaussian noise level image, the values of MSE are significantly decreased. The values of PSNR are increased and SSIM values are closely increased to 1. Figure 8 shows Gaussian Noise Level after Arithmetic Mean Filter

with 2×2 Window Size applied. The results of the metric values for salt and pepper noise level after applying arithmetic mean filter is shown as diagram in Figure 9. Figure 10 show the size 2x2 arithmetic mean filter window applied over gaussian noise 0.01. Figure 11 also show the arithmetic mean filter with window size 2x2 applied over salt & pepper noise 0.01.

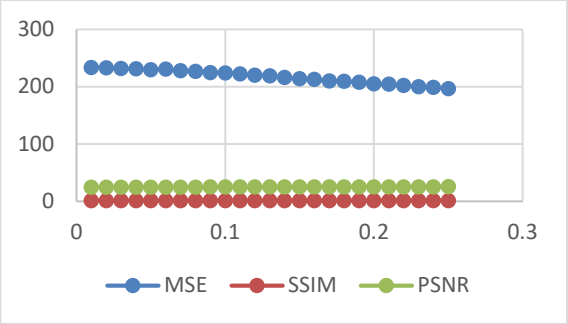

Figure 8 Gaussian Noise Level after Arithmetic Mean Filter with 2×2 Window Size applied

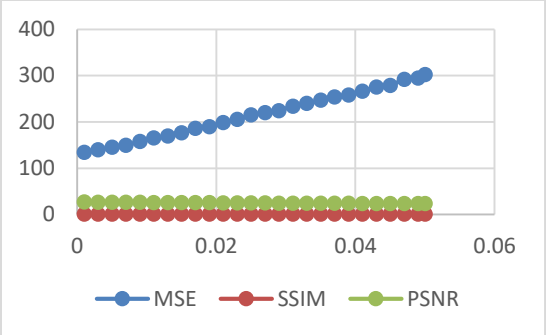

Figure 9 Salt & Pepper Noise Level after applying Arithmetic Mean Filter with 2×2 Window Size

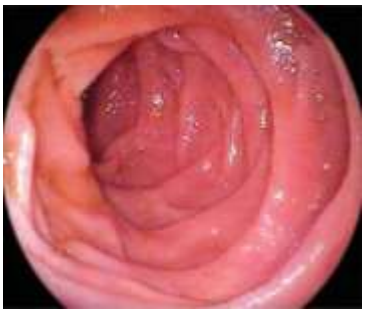

Figure 10 Applied Arithmetic Mean with Size 2 Window over Gaussian Noise 0.01

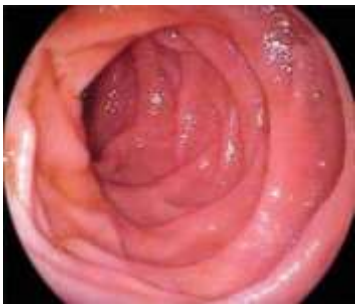

Figure 11 Applied Arithmetic Mean with Size 2 Window on Salt & Pepper Noise 0.01

After applying the unsharp masking filter to the original image by changing the constant number from 0.2 to 1.4, the values of MSE are increased and SSIM values are decreased. If scaling constant number is over 1.5, endoscopic images likely contain some noises. Figure 12 illustrates the metric values for Unsharp Masking Filter. Figure 13 shows the unsharp masking filter with constant 1.4.

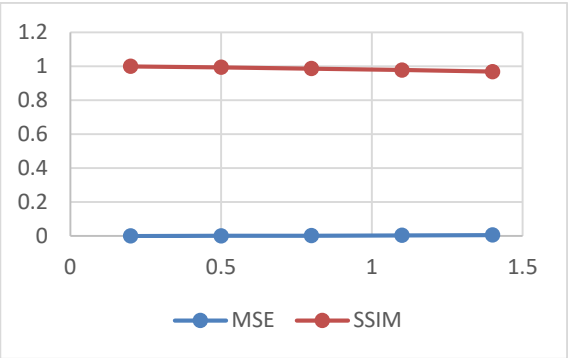

Figure 12 Graph Diagram of Metric Values for Unsharp Masking Filter

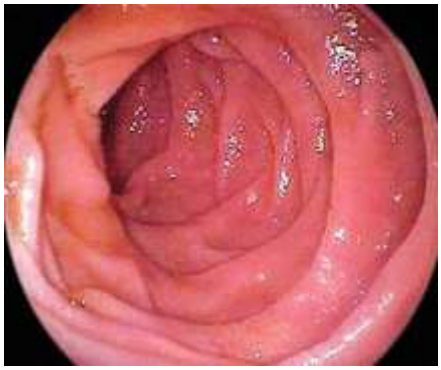

Figure 13 Applied Unsharp Masking Filter with constant 1.4

After applying harmonic mean filter to the gaussian noise, the value of MSE significantly decrease from 593.8053 to 0.0033. Therefore, error value decreases over 500. The value of SSIM increases from 0.8256 to 0.9332. The value of PSNR also increase from 20.3944 to 24.7892. After applying the harmonic mean filter to the various salt and pepper noise level images, the values of MSE are significantly decreased. The values of PSNR are decreased and SSIM values are decreased from 1. Figure 14 shows the diagram of Metric Values for Harmonic Mean Filter with Variable Sigma of Gaussian Noise. Figure 15 shows the metric values for Harmonic Mean Filter with Variable Density of Salt and Pepper Noise. Figure 16 illustrate the result of harmonic mean filter over gaussian noise 0.01. Figure 17 also demonstrates the result of harmonic mean filter over salt & pepper noise 0.01.

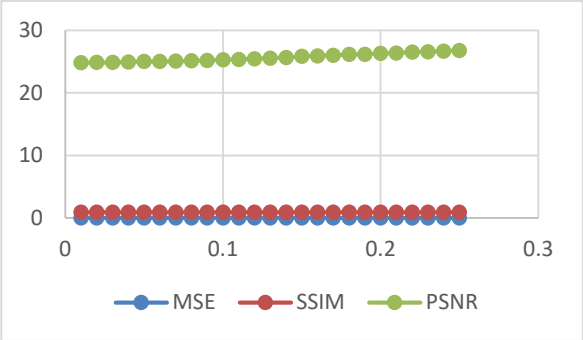

Figure 14 Diagram of Metric Values for Harmonic Mean Filter with Variable Sigma of Gaussian Noise

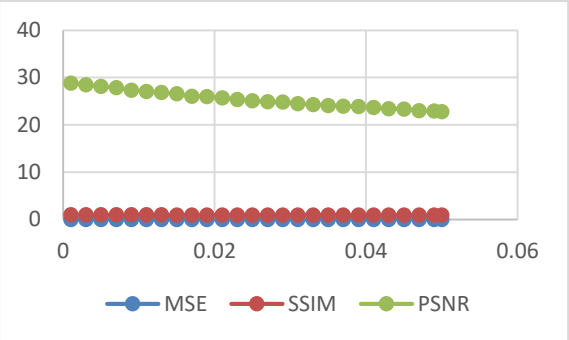

Figure 15 Metric Values for Harmonic Mean Filter with Various of Salt and Pepper Noise

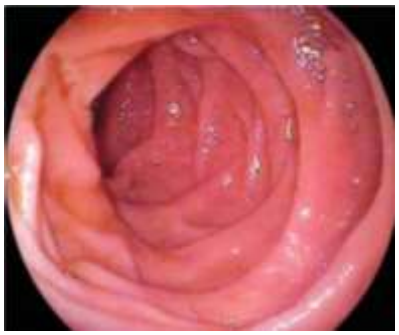

Figure 16 Harmonic Mean Filtered Image Over Gaussian Noise 0.01

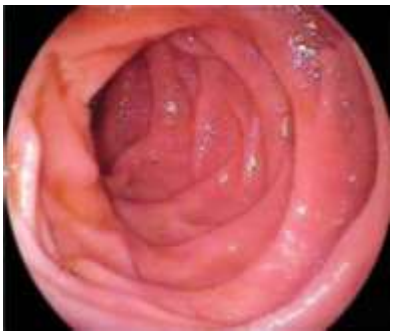

Figure 17 Harmonic Mean Filtered Image Over Salt & Pepper Noise 0.01

After applying contraharmonic mean filter to the gaussian noise, the value of MSE decrease from 593.8053 to 0.0033. The value of SSIM increase from 0.8256 to 0.9411. The value of PSNR also increase from 20.3944 to 24.8386. After applying contraharmonic mean filter to salt and pepper noise, MSE value decrease from 21.0299 to 0.0016. SSIM value decrease from 0.9918 to 0.977. PSNR value also decrease from 34.9024 to 28.0764. Figure 18 demonstrate the metric values for Gaussian noise after applying contrahoarmonic mean filter. Figure 19 shows metric values for salt and pepper noise after applying contraharmonic mean filter. Figure 20 shows the result of contraharmonic mean filtered over gaussian noise 0.01. Figure 21 shows the result of contraharmonic mean filtered over salt & pepper noise 0.01.

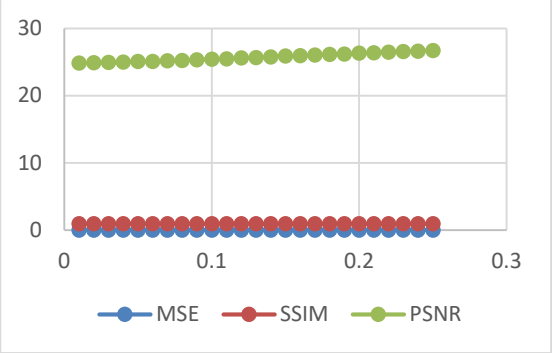

Figure 18 Metric Values for Gaussian Noise after Contraharmonic Mean Filtered

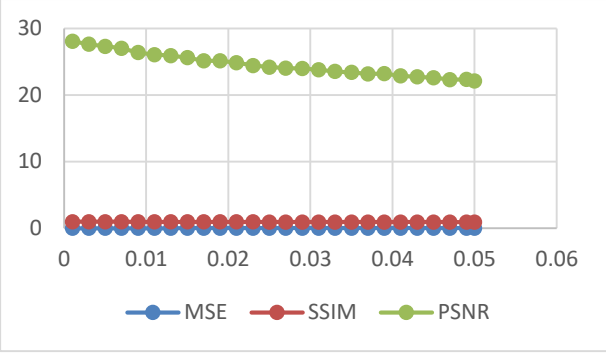

Figure 19 Metric Values for Salt and Pepper Noise after Contraharmonic Mean Filtered

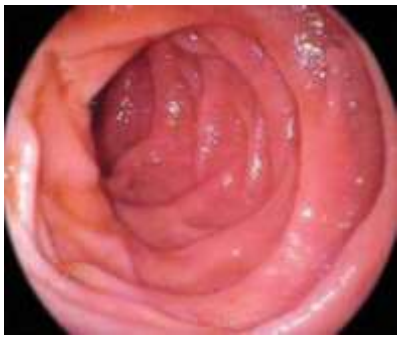

Figure 20 Contraharmonic Mean Filtered Image Over Gaussian Noise 0.01

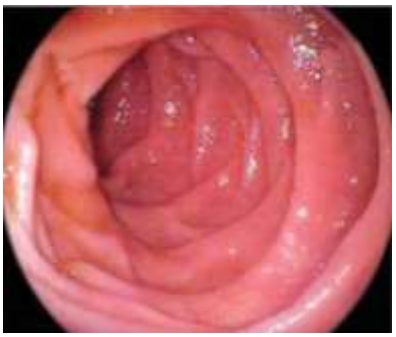

Figure 21 Contraharmonic Mean Filtered Over Salt & Pepper Noise 0.01

After applying the gamma correction filter to the original image by changing the gamma value from 0.5 to 1.5, the values of the MSE are decreased and SSIM values are increased. When the gamma value is 1, the values of MSE 0 and SSIM value is perfectly 1. When gamma value is less than 1, endoscopic images will brighter. When gamma value is greater than 1, endoscopic images will darker. Figure 22 shows the diagram of the metric values of gamma correction. Figure 23 illustrates the gamma correction filtered with gamma value 1.2.

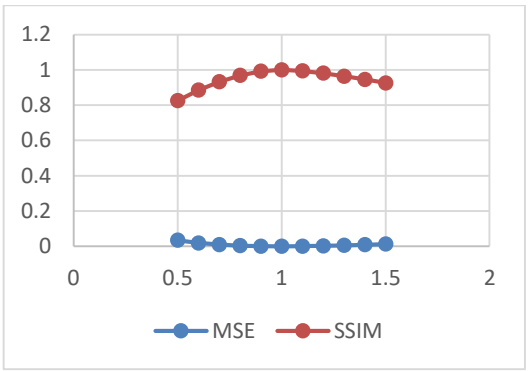

Figure 22 Diagram of the Metric Values of Gamma Correction with MSE and SSIM

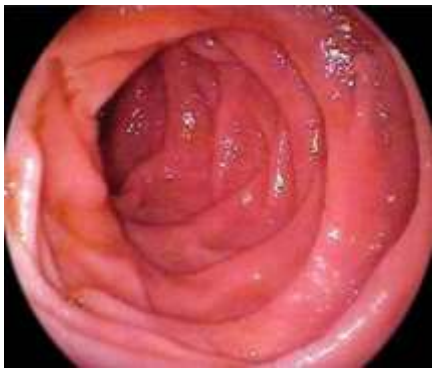

Figure 23 Gamma Correction Filtered with Gamma Value 1.2

After applying median filter to the gaussian noise, the value of MSE decrease from 593.8053 to 145.9388. The SSIM value increase from 0.8256 to 0.9533. The PSNR value also

increase from 20.3944 to 26.4891. After applying median filter to salt and pepper noise, MSE value decrease from 21.0299 to 16.5762. SSIM value slightly increase from 0.9918 to 0.9941. PSNR value also increase from 34.9024 to 35.936. Figure 24 shows the diagram of the metric values of various Gaussian noise level image after applying median filter. Figure 25 demonstrates the diagram of the metric values of various salt and pepper noise level image after applying median filter. Figure 26 shows the result of median filtered over gaussian noise 0.01. Figure 27 shows the result of median filtered over salt & pepper noise 0.01.

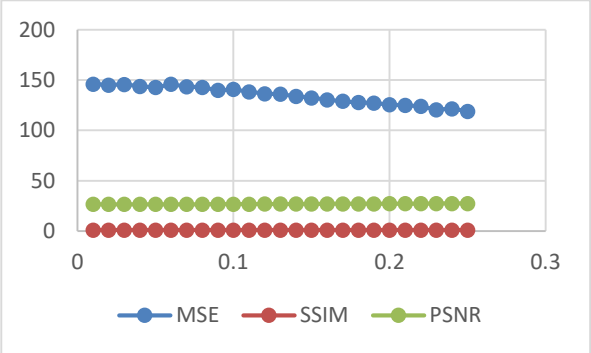

Figure 24 Metric Values of Gaussian Noise Level Image after Applying Median Filter

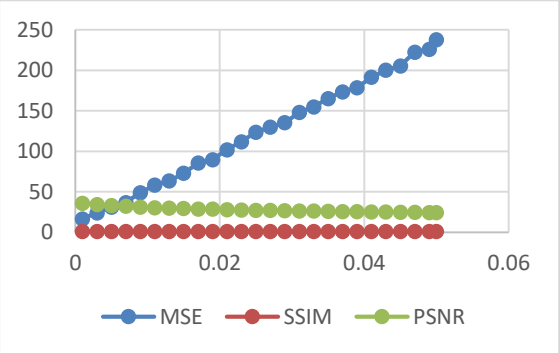

Figure 25 Metric Values of Salt & Pepper Noise Level after Applying Median Filter

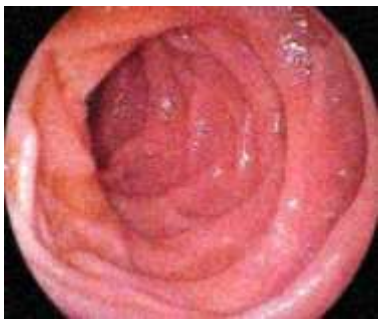

Figure 26 Median Filtered Image on Gaussian Noise 0.01

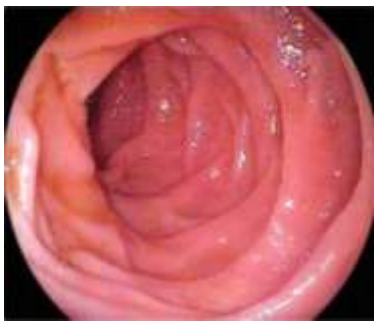

Figure 27 Median Filtered Image on Salt & Pepper Noise 0.01

When the noise level increases, the original image becomes vague. Gaussian noise level is tested from 0.01 to 0.25. Salt and pepper noise density is tested from 0.001 to 0.05. Table 1 shows the IQA values of Gaussian noise level 0.01 and salt & pepper noise level 0.001. Table 2 shows the comparison of denoising filter IQA values after removing Gaussian noise level 0.01. Table 3 also shows the comparison of denoising filter IQA values after removing salt and pepper noise level 0.001.

Table 1. IQA Values of Gaussian Noise Level 0.01 and Salt & Pepper Noise Level 0.001

Type of Noise	MSE	SSIM	PSNR
Gaussian Noise	593.8053	0.8256	20.3944
Salt & Pepper Noise	21.0299	0.9918	34.9024

Table 2. Comparison of Each Denoising Filter IQA Values after Removing Gaussian Noise 0.01

Type of Denoising Filters	MSE	SSIM	PSNR
Arithmetic Mean Filter	233.3288	0.9332	24.4511
Harmonic Mean Filter	0.0033	0.9358	24.7892
Contraharmonic Mean Filter	0.0033	0.9411	24.8386
Median Filter	145.9388	0.9533	26.4891

Table 3 Comparison of Each Denoising Filter IQA Values after Removing Salt & Pepper Noise Level 0.001

Type of Denoising Filters	MSE	SSIM	PSNR
Arithmetic Mean Filter	134.3917	0.9631	26.8471
Harmonic Mean Filter	0.0013	0.9784	28.8166
Contraharmonic Mean Filter	0.0016	0.977	28.0764
Median Filter	16.5762	0.9941	35.936

Arithmetic mean filter, harmonic mean filter and contraharmonic mean filter work better when removing Gaussian noise compared to removing the salt and pepper noise. Median filter is introduced to overcome the limitation of type of mean filter; therefore, it works better when removing salt and pepper noise comparing to removing Gaussian noise. But median filter not only remove the noise but also preserve the edges of image. For noise removal, only small size of window is considered to use for removing noise. This can see when the bigger size of window is applied the image tends to become more blurred when the filtering job is done.

Gamma correction filter, different gamma values are compared from 0.5 to 1.5 for color contrast enhancement. When gamma value is 1, the color of the original image will not be changed. When gamma value is greater than 1, the color of the image will darker. When gamma value is less than 1, the color of the image will brighter.

Unsharp masking filter, different scaling factors are compared to find scaling factor that gives the best enhancement of the edges in the image. The k value is measured from k=0.2 to 1.4. The scaling constant 0.8 is chosen because the edge is enhanced nicely without amplify the false edge(noise). The false edge can be found on when k =1.4 compared to the original image.

Conclusion

In conclusion, different filters have different strengths and weaknesses. Different types of filters are needed when solving image processing problems. Sometimes a nonlinear filter may work better than a linear filter. In image restoration, the nonlinear filters can be filtered than linear filters. While the linear filter can remove the noise, the nonlinear filter not only removes the noise but also can preserve edges. Because a single filter is no needed to remove noise, but a range of filters are needed, depending on the situation encountered.

Linear for specific endoscopic image processing tasks were analyzed: arithmetic mean filter, unsharp masking filter, harmonic mean filter, contraharmonic mean filter as a linear filter

type. Nonlinear filter for endoscopic image processing tasks were analyzed: gamma correction filter and median filter as a nonlinear filter type. The requirements of the filters to remove unwanted artefacts(noise) and to enhance edge and to control contrast level of image were identified. By using this research in medical field, physicians can improve to decide the diseases.

Acknowledgement

I would like to give my warmest thanks to Professor Dr. Myat Su Hlaing, Head of Department of Computer Studies, Dagon University for guiding me through all the stages of doing my research. I would like to express my special thanks to Professor Dr. Soe Mya Mya Aye, Head of Department of Computer Studies, University of Yangon for her kind permission and valuable suggestions to carry out this research.

References

Astola J.& Kuosmanen P. (1997), *Fundamentals of nonlinear digital filtering*. Electronic engineering systems series, CRC Press.

Castleman, K. R., (1996) Digital Image Processing. Second ed., Englewood Cliffs, New Jersey: Prentice Hall.

Chris, S.& Brecken, T. (2010). Fundamental of Digital Image Processing: A Practical Approach with Example in Matlab.

Fang, S., Xu, C., Feng, B. & Zhu, Y. (2021) Color Endoscopic Image Enhancement Technology Based on Nonlinear Unsharp Mask and CLAHE. In Proceedings of the 2021 IEEE 6th International Conference on Signal and Image Processing (ICSIP).

Gonzalez, R.& Woods R., (2002) Digital Image Processing. Upper Saddle River, New Jersey: Prentice Hall

Jaehne B., (2005). Digital Image Processing. Heidelberg, Germany: Springer-Verlag Berlin.

Jae S. Lim. (1990). Two Dimensional Signal and Image Processing. Englewoods Cliff, NJ: Prentice Hall.

Russ, J. C. (1995) The Image Processing Handbook. Second ed, Boca Raton, Florida: CRC Press.

Russ, J. C. (2007). The Image Processing Handbook 5th Edition. Raleigh, North Carolina: Taylor & Francis Group.

EXPLORING DIMENSIONALITY REDUCTION TECHNIQUES: A MULTIFACETED ANALYSIS OF PCA, t-SNE, AND UMAP ON DIVERSE DATASETS

Pwint Phyu Khine [1], Thet Thet Hlaing[2] & Soe Mya Mya Aye[3]

Abstract

As the amount of data volumes grows, the increasing dimensionality of datasets poses significant challenges for data analysis and interpretation. Dimensionality reduction techniques play a critical role by selecting or synthesizing essential dimensions to manage heterogeneous data regardless of structures (structured or unstructured) effectively. This research explores various dimensionality reduction methods, applied to multiple datasets, to enhance analytical insights and visualization during the exploratory phase.

Keywords: Dimensionality Reduction, Machine Learning, Heterogeneous Data, Big Data, PCA, tSNE, UMAP

Introduction

Dimensionality reduction is the process of projecting high-dimensional data into a lower-dimensional subspace, capturing its essential features to alleviate the "curse of dimensionality" (Lespinats et al., 2022). This technique is essential for improving machine learning model performance by simplifying the dataset and enabling efficient handling of high-dimensional spaces (Bingham & Mannila, 2001). While dimensionality reduction facilitates data analysis, careful consideration is necessary to preserve the inherent characteristics of both structured and unstructured data. Structured data, with defined attributes, presents unique challenges in feature selection, especially for large-scale datasets. Unstructured data such as images and time series, in contrast, brings complexities due to its high dimensionality and varied formats. The curse of dimensionality arises because high-dimensional data often lacks structure, making traditional clustering and organizational methods less effective. To address this, dimensionality reduction methods condense data into the most meaningful components, which allows for more robust generalization, improved model efficiency, and reduced redundancy and noise. In applications, reducing data dimensions enables faster processing, better classification in image analysis, and more insightful data interpretation in healthcare. Ultimately, dimensionality reduction offers a systematic way to address the challenges of heterogeneous data, facilitating stronger insights and decisions.

Theoretical Background

Curse of Dimensionality

As dimensionality increases, the volume of the data space expands rapidly, resulting in “data sparsity”. Data points are spread thinly across space which is similar to objects such as planets, satellites, rocks, etc. floating in literal space. A minuscule difference in direction will make a moving vehicle such as a rocket change its direction, landing on a foreign planet instead

[1] Department of Computer Studies, University of Yangon
[2] Department of Computer Studies, University of Yangon
[3] Department of Computer Studies, University of Yangon

of earth. This sparsity means that effective data analysis requires exponentially larger datasets to provide reliable results. In many scenarios, each dimension variable can assume several values leading to a large number of possible combinations. This phenomenon is called "combinatorial explosion". As dimensions increase, the sampling volume grows exponentially, creating additional complexity. Each added dimension drastically increases the size of the sampling space, meaning far more points are required to maintain the same correctness, intensifying the effects of both combinatorial explosion and data sparsity.

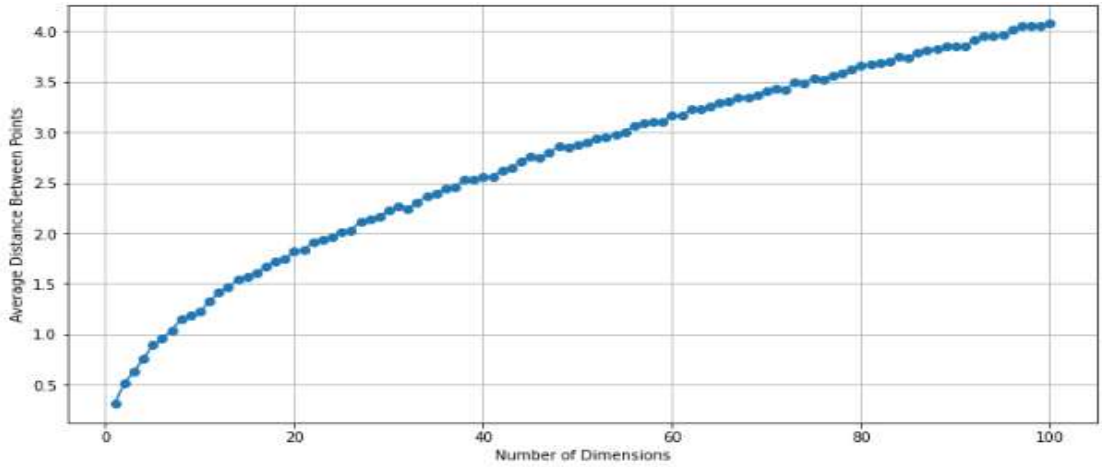

Figure 1: Curve of Dimensionality: Average Distance Between Points as Dimensions Increase leading to data sparsity and combinational explosion

Types of Dimensionality Reduction Methods

Dimensionality reduction techniques are commonly categorized as linear or non-linear and can also be grouped by computational approach, including matrix-based, manifold learning, and deep learning methods. Each approach offers specific methods tailored to different data structures and analysis needs. Matrix-based techniques, like Principal Component Analysis (PCA), capture maximum variance by projecting high-dimensional data onto a lower-dimensional linear subspace (Jolliffe & Cadima, 2016). PCA is primarily suited for structured data but can be adapted for non-linear data through Kernel PCA, which applies kernel functions to map data with complex relationships. Manifold learning techniques, such as t-distributed Stochastic Neighbor Embedding (t-SNE) and Uniform Manifold Approximation and Projection (UMAP), address non-linear relationships by assuming data lies on a lower-dimensional manifold within high-dimensional space. t-SNE emphasizes local data clusters (Hinton & Roweis, 2002; Maaten & Hinton, 2008), while UMAP captures both local and global structures (McInnes et al., 2018). Deep learning methods, particularly Autoencoders, use neural networks to create a latent representation, capturing non-linear features. Variations like Stacked Autoencoders and Deep Belief Networks (DBNs), including Restricted Boltzmann Machines (RBMs), further enhance the ability to capture complex patterns, making them effective for high-dimensional, unstructured data, such as images and audio. These methods—PCA, t-SNE, UMAP, and Autoencoders—are feature projection techniques, producing new, informative features in a lower-dimensional space, facilitating Exploratory Data analysis (EDA), visualization, and modeling. To establish a robust basis for implementing dimensionality reduction techniques, this section explores the theoretical foundations of PCA, t-SNE, and

UMAP. A thorough understanding of these methods is essential to justify their application and effectiveness in the context of this research.

Principal Component Analysis (PCA)

For data X with n number of samples and p features, PCA is by first centering the data by subtracting the mean of each feature from the corresponding feature values.

The covariance matrix ∑ of the centered data is calculated to understand the relationships between the features.

$$X_{\text{centered}} = X - \text{mean}(X)$$

$$\Sigma = \frac{1}{n} X_{\text{centered}}^{T} X_{\text{centered}}$$

Eigenvalue decomposition is performed to extract eigenvalues λi and eigenvectors v_i of the covariance matrix ∑ for maximum variance.

$$\Sigma \mathbf{v}_i = \lambda_i \mathbf{v}_i$$

Sorting and selecting the components to give the required top k eigenvectors in a new feature space is performed where V_k is the matrix with the top k eigenvectors as columns, and Z represents the transformed reduced data. The selected PC are then projected for visualization.

$$Z = X_{\text{centered}} \mathbf{V}_k$$

Incremental PCA is used for large memory footage datasets i.e. digit datasets. IPCA is good for big data as it performs the above-mentioned PCA step incrementally based on available memory space.

t-Stochastic Neighbor Embedding (t-SNE)

t-SNE emphasizes preserving the local structure by placing similar data points closer together in lower dimensions, making it highly effective for visualizing clusters. The t-SNE model transformed into a two-dimensional space **c**alculates the Pairwise Affinities in high dimension. The conditional probability of affinity $p_{j|i}$ is calculated for data points x_i and x_j where variance parameter σ controls the perplexity i.e. number of neighbors:

$$p_{j|i} = \frac{\exp(-\|x_i - x_j\|^2 / 2\sigma_i^2)}{\sum_{k \neq i} \exp(-\|x_i - x_k\|^2 / 2\sigma_i^2)}$$

tSNE got its name from the use of Student's t-distribution for the similarity of points in a low dimensional plane. The data point in the low dimensional plane is represented as q_{ij}.

$$q_{ij} = \frac{(1 + \|y_i - y_j\|^2)^{-1}}{\sum_{k \neq l} (1 + \|y_k - y_l\|^2)^{-1}}$$

tSNE finds the embeddings y_i that minimizes the divergence between high dimensional distribution P and low dimensional distribution Q by using Kullback-Leibler (KL) divergence.

$$\mathrm{KL}(P||Q) = \sum_{i \neq j} p_{ij} \log \frac{p_{ij}}{q_{ij}}$$

Various perplexity values were tested (e.g., 5 to 50) to evaluate their impact on the embedding quality. The denser dataset will require more perplexity however it comes with a longer time in computation.

Uniform Manifold Approximation and Projection (UMAP)

Manifold learning techniques assume that high-dimensional data lies on a lower-dimensional, curved manifold within a higher-dimensional space. While t-SNE emphasizes preserving local structures, UMAP balances both local and global structures, making it effective for visualizing complex data patterns, especially in clustering. UMAP constructs a weighted graph in high dimensions, capturing inherent structure through a fuzzy topological model, which is then projected to a lower-dimensional space. Built on Riemannian geometry and topological data analysis, UMAP uses fuzzy simplicial sets to model data structure, enabling computational efficiency and meaningful, interpretable embeddings. This robustness makes UMAP widely applicable in fields like bioinformatics, NLP, and image processing, where both cluster separation and structure preservation are essential.

Various neighborhood sizes (n_neighbors) and minimum distances (min_dist) were tested to optimize both the granularity of local structure and the extent of global structure preservation in the embedding. For each data point x_i, find its k-nearest neighbors and calculate the edge weights using a kernel function. This is based on the distance between points, transformed into a fuzzy set representation. The probability of connection p_{ij} is defined with p_i as the distance to the nearest neighbor of x_i and σ_i is used to fix the number of neighbors:

$$p_{ij} = \exp\left(-\frac{\|x_i - x_j\| - \rho_i}{\sigma_i}\right)$$

In the low-dimensional space, a similar fuzzy simplicial complex is built, initialized randomly or with spectral embedding. Optimizing the embedding in low-dimensional embedding is done by calculating the cross-entropy between the high-dimensional and low-dimensional fuzzy simplicial sets, where qij is the probability of connection in the low-dimensional space, dependent on the current embedding. By applying UMAP, Visualization for both distinct clusters and gradients within continuous datasets is more efficient.

$$C = \sum_{(i,j)} p_{ij} \log \frac{p_{ij}}{q_{ij}} + (1 - p_{ij}) \log \frac{1 - p_{ij}}{1 - q_{ij}}$$

These dimensionality reduction techniques, each tailored for different types of data and analysis objectives, allow for more efficient storage, processing, and visualization of high-dimensional datasets, improving computational efficiency and interpretability. These methods are particularly beneficial for **Exploratory Data Analysis** (EDA), especially in the **Visualization** stage for complex, high-dimensional data.

Implementation

Datasets

This study applies dimensionality reduction techniques to different datasets, demonstrating distinct behaviors based on the inherent nature of each dataset. Synthetics data is also generated to illustrate the overall operations using Swiss roll problem. Data points in higher dimension 3D plane is projected in 2D plane by using PCA, tSNE and UMAP. The resulted visualization shows whether they are possible for reconstruction, synthesis generation, and local structure preservation, and global data structure.

PCA is not well-suited for the Swiss Roll due to its inability to handle nonlinear data effectively. It shows moderate reconstruction error and fails to preserve local structure. t-SNE captures local structure better (high trustworthiness and continuity) but has high KL divergence, indicating difficulties with global distribution preservation as it fails to maintain global structure. UMAP also preserves local relationships well but slightly less than t-SNE. Its lower KL divergence and cross-entropy suggest a somewhat better balance between local and global structures. For this dataset, UMAP and t-SNE both provide good representations of local structure, making them preferable for visualizing continuous, nonlinear data like the Swiss Roll. In open box problem, PCA can maintain its almost entire global structure in lower dimension, and UMAP somehow can do it leading to possible potential for data compression and synthetic data generation. t-SNE is impossible in these areas although further researches should be done to investigate these cases.

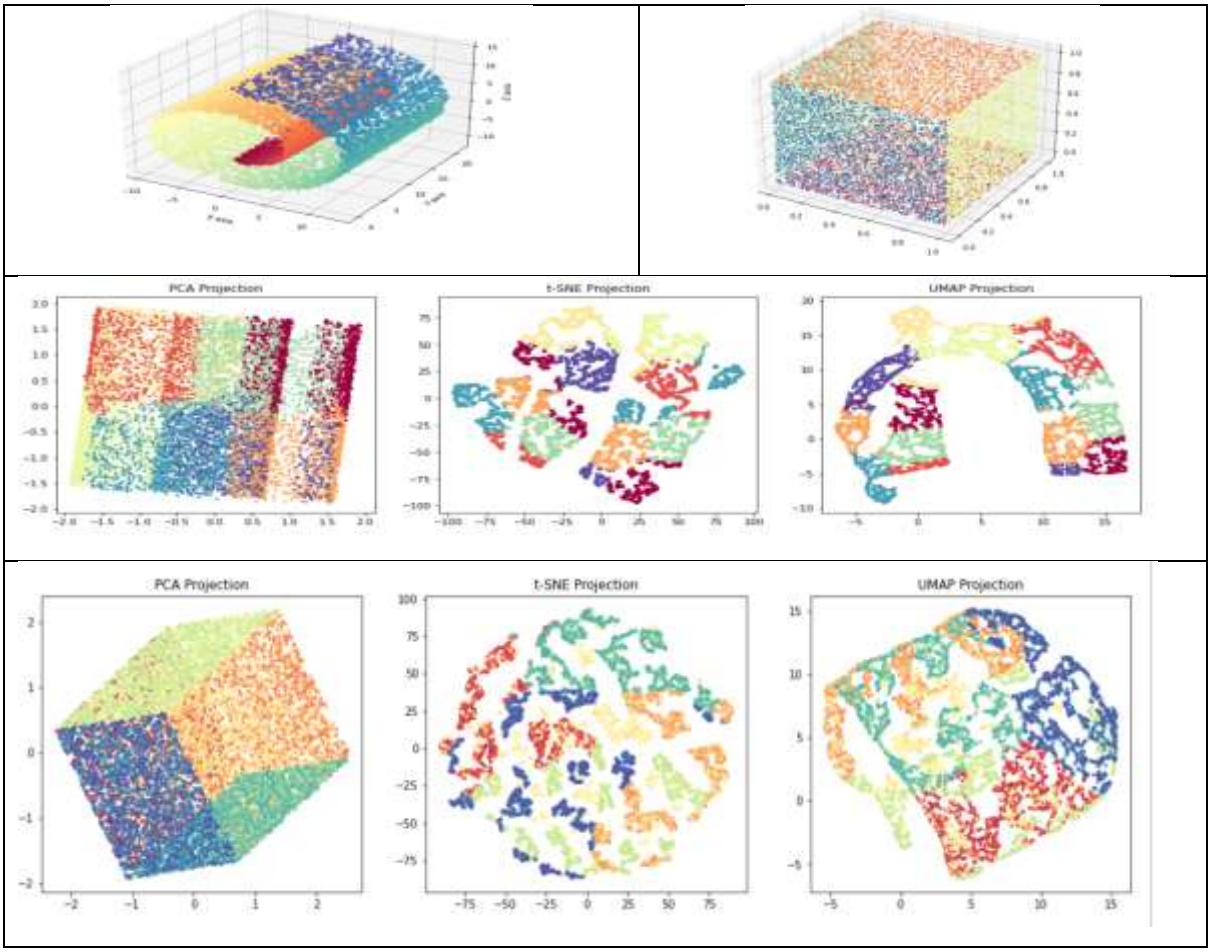

Figure 2. Swiss Roll Problem and Open Box problem projected into lower dimensional by using PCA, tSNE and UMAP

Various datasets from Python's sklearn library are used to showcase how dimensionality reduction can aid data analysis and visualization in structured and unstructured data contexts. Both structured and unstructured datasets from Python's sklearn library, highlight the unique behaviors of each. For structured data, the Breast Cancer Dataset includes 569 samples and 30 features derived from cell nuclei images, such as radius and texture, supporting predictive modeling for tumor malignancy (Malignant = 0, Benign = 1). The Diabetes Dataset features 768 samples with 8 health metrics like BMI and age, aiming to analyze disease progression through continuous target scores; higher values indicate more severe progression. Both datasets provide insight into how dimensionality reduction can improve data analysis and visualization in medical applications. For unstructured data, the Handwritten Digits Dataset includes 1,700 8x8 pixel images of digits (0-9), ideal for exploring image classification and high-dimensional data visualization. For big data, (mnist_784', version=1), contains 70,000 samples in total. This includes 60,000 training images and 10,000 testing images of handwritten digits are used alternatively to ensure some of the visualization results. These datasets demonstrate dimensionality reduction's utility in refining analysis and visualization for diverse data types.

(a) Cancer and Diabetics datasets (structured data)

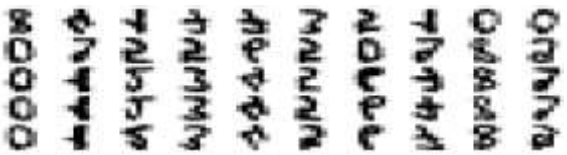

(b) Hand-written Digital Image Dataset (unstructured data)

Figure 3. Diverse Datasets for structured and unstructured data

Analysis of datasets for PCA, tSNE, UMAP

The Cancer Dataset has two groups i.e. benign and serious. When visualized in a scatter plot, it is already clear. However, the steadily increased silhouette score on PCA, tSNE, and UMAP shows that the clustering ability increases with each method even without the hyperparameter tuning. Baseline cancer dataset has low silhouette score and the relationship between clusters could not be seen clearly. However, after applying dimensional reduction, the data points in lower dimension show better silhouette score (between somewhat good) in all three cases even without the expensive parameter tuning.

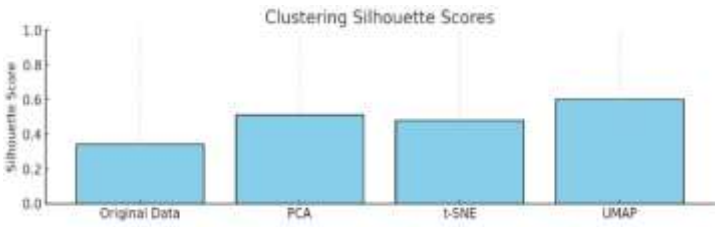

(a) Silhouette Scores for original data projection and dimensionality reduction methods

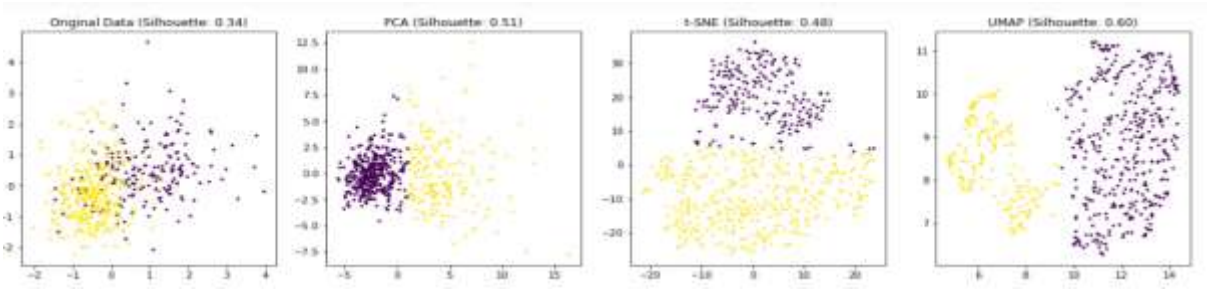

(b) Scatter plot visualization for original data projection and dimensionality reduction methods

Figure 4. Cancer Dataset with PCA, tSNE, and UMAP

The Diabetes Dataset has continuous values and is used for regression. When visualized in a scatter plot, the data points are unable to reveal any patterns in PCA. However, tSNE and UMAP with default values show two possible clusters.

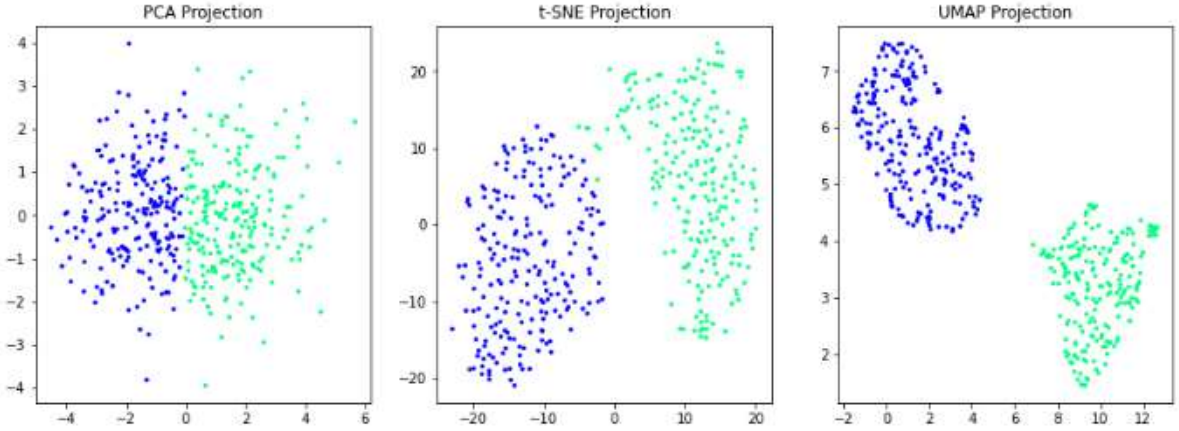

Figure 5. PCA, tSNE, and UMAP for Diabetes Dataset

The most prominent result comes in the unstructured image dataset MINST. PCA is unable to distinguish between clusters. However, both tSNE and UMAP show clear clusters in lower dimensions which greatly helped in further analysis processes.

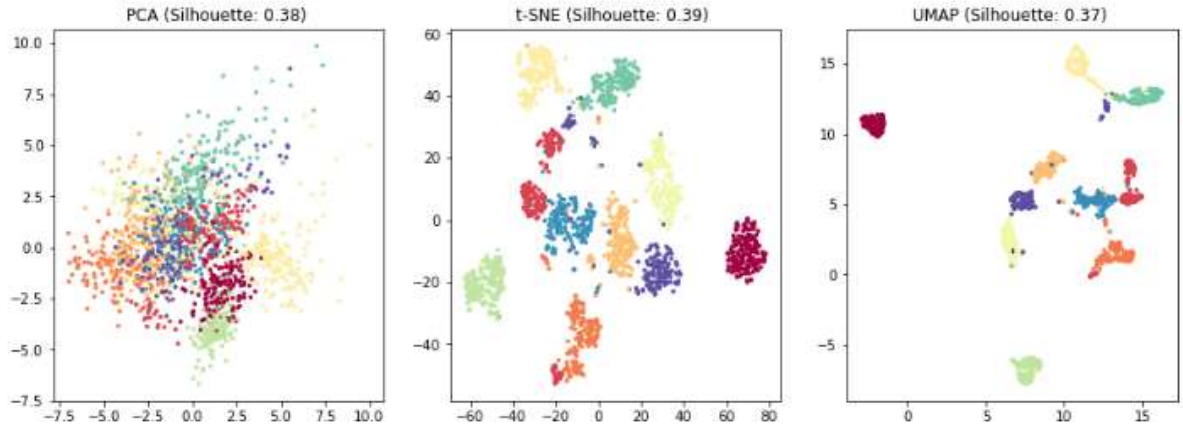

Figure 6. PCA, tSNE and UMAP on digit dataset

The other problem encountered is the volatile nature of tSNE. Based on the perplexity parameter, it generates different data at different parameter values. The silhouette scores vary in other methods such as UMAP but their visualization did not change much in lower dimensional

space showing that they are in stable condition. However, tSNE had an additional problem in unstability in the analysis process making them used only for visualization to understand patterns in only specified parameter values.

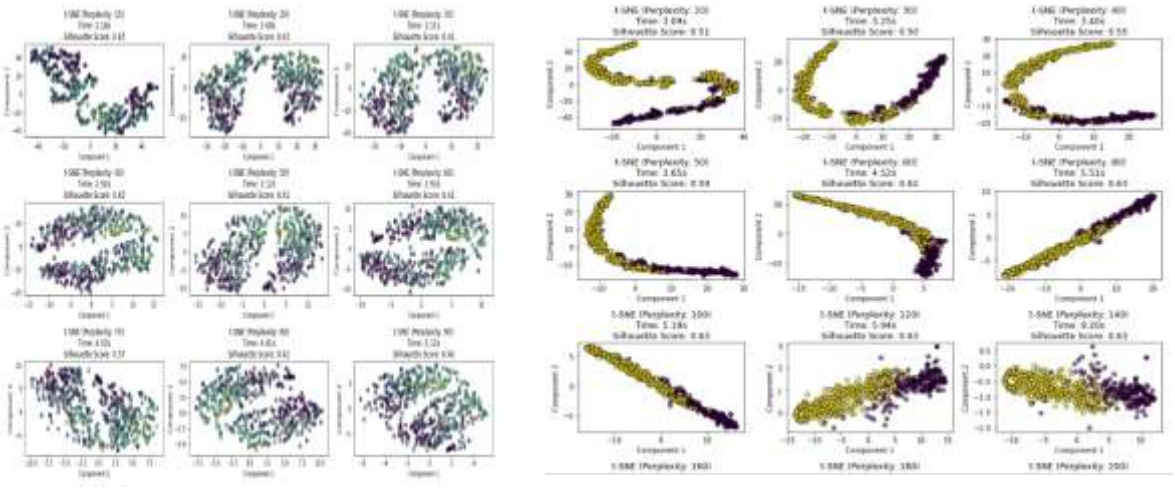

Figure 7. Volatile structure of diabetes dataset (left) and cancer dataset (right) using tSNE, leading to erroneous interpretation

In digit datasets, it creates false clusters when different parameter values are used as shown in the figure. Instead of 10 clusters, they create smaller erroneous clusters in visualization.

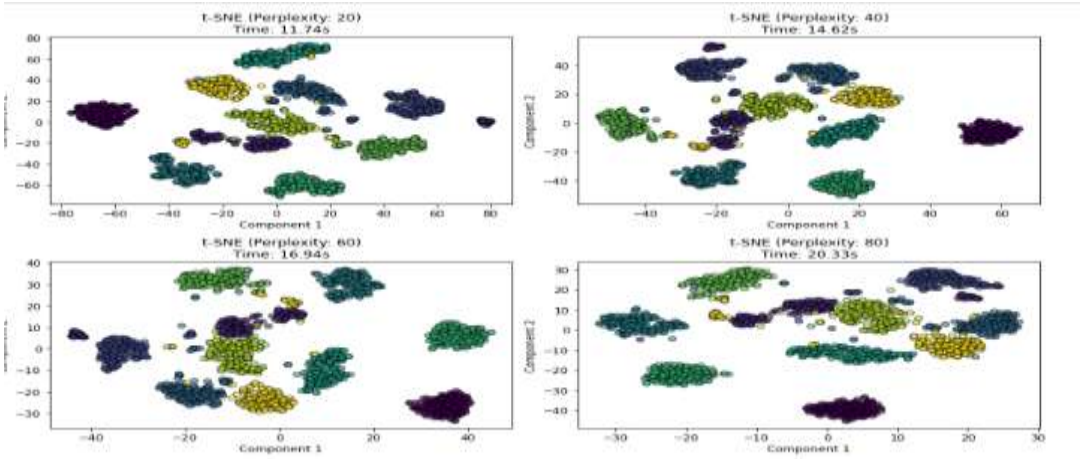

Figure 8. t-SNE creates false clusters in the digit dataset. Clusters are generated correctly or incorrectly based on different parameter values.

Result and Discussion

This paper explores the dimensionality reduction techniques on structured and unstructured data for preprocessing of machine learning datasets. Dimensionality reduction techniques such as PCA, t-SNE, and UMAP are crucial for visualizing high-dimensional data and facilitating subsequent analyses. Each method has unique characteristics, and their effectiveness requires specific evaluation metrics.

The "eye-rolling" approach is commonly adopted, where practitioners visually inspect various visualizations especially 2D or 3D scatter plots of the first two or three principal components. This qualitative evaluation allows researchers to identify patterns, clusters, or outliers without the need for formal quantitative metrics. Although traditional evaluation metrics

like silhouette scores are not typically employed with PCA, insights can still be drawn from the resulting data representations.t-SNE is a non-linear dimensionality reduction method specifically designed for visualizing high-dimensional data. Its effectiveness is often evaluated using quantitative metrics, with the silhouette score being a primary option. This score measures how similar an object is to its cluster compared to other clusters, ranging from -1 to 1, where higher values indicate better clustering. Similarly, UMAP is a non-linear technique that excels in preserving both local and global data structures, making it particularly effective for complex datasets. Evaluation metrics for UMAP include silhouette scores and other clustering metrics, such as the Davies-Bouldin index and adjusted Rand index. Silhouette score is used to have more understanding of data. For the Cancer Dataset, which consists of benign and malignant groups, scatter plot visualizations reveal clear separations. Notably, the silhouette scores steadily increase across PCA, t-SNE, and UMAP, indicating enhanced clustering ability with each method, even without hyperparameter tuning. In contrast, the Diabetes Dataset, characterized by continuous values and primarily used for regression, presents chal lenges in visualizing patterns. PCA visualizations fail to reveal any discernible patterns among data points. However, t-SNE and UMAP, using default parameters, uncover two potential clusters, demonstrating their capability to identify underlying structures within the data. In addition to structured datasets, t-SNE, and UMAP excel in analyzing unstructured image data, such as the MINST dataset. Here, PCA struggles to distinguish between clusters, while both t-SNE and UMAP effectively reveal clear clusters in lower dimensions, significantly aiding subsequent analytical processes.

Table 1. Comparison Analysis for PCA, tSNE, and UMAP

Properties	PCA	t-SNE	UMAP
Incremental Learning	Incremental PCA available	Stochastic Gradient Descent, Randomized	Can handle well in its own
Outlier Handling	Result affected	Handles well	Handles well
Computational Complexity	$O(d^2n+d^3)$	$O(n^2)$	O(n log n)
Data Restoration	Yes	No	Somewhat
Hyperparameter	-	Perplexity (neighbors within a cluster)	Number of Neighbors, Min Distance
Structured Data	Maintains global structure	Often loses global structure	Preserves both local and global structure (to an extent)

PCA is one of the most robust techniques used in dimensionality reduction. PCA reduces the dataset to two principal components while retaining as much variance as possible. As they maintain the data structure, it is easier to reconstruct data, therefore, PCA is good at the restoration of original data. TSNE is very volatile as the visualization changed with each perplexity score for breast cancer, diabetes, and digit dataset. It even creates false clusters in digits. t-SNE optimizes the dataset's structure in lower dimensions using probability distributions, allowing for clear clustering, especially useful in high-dimensional data. However, their volatile nature makes them unsuitable for the reconstruction of original data. UMAP somehow maintains both local and global structures, making it effective for visualizing datasets

with complex structures. Dimensionality Reduction is a necessary tool which could be often in machine learning procedures before data are exported for machine learning algorithms or when machine learning algorithms are required to reduce dimension to increase their accuracy in classification or make them more defined in clustering. To perform effective analytics. DM methods will be required to apply as necessary in any machine learning process pipelines. Different Dimensionality Reduction Techniques are applied for heterogenous data – PCA, tSNE, and UMAP on structured data (breast cancer, diabetics) and (handwritten digit).

By employing these dimensionality reduction techniques, researchers can enhance their understanding of data structures and improve the robustness and reliability of their findings in various analytical scenarios. Overall, the choice of evaluation metrics should align with the specific objectives of the analysis and the characteristics of the dataset.

Conclusion and Future Work

Dimensionality reduction techniques are essential for feature extraction, data analysis, and visualization, simplifying high-dimensional datasets into manageable representations. This transformation reveals hidden patterns, enhances model interpretability, and boosts overall performance. As data scales in volume and complexity, effective dimensionality reduction becomes increasingly critical for efficient analysis. Future research will prioritize deep learning-based dimensionality reduction, particularly through autoencoders, which enable learning complex data representations useful for tasks like anomaly detection, classification, and generative modeling. Applying these techniques to big data will also streamline processing and facilitate the extraction of valuable insights from large-scale datasets. Advances in dimensionality reduction are anticipated to drive progress across machine learning, AI, and data science. This research examines dimensionality reduction challenges across diverse datasets, promoting a deeper understanding of methods for handling complex data structures in real-world contexts.

Acknowledgments

I would like to thank my supervisor Dr. Thet Thet Hlaing (Professor), Dr. Soe Mya Mya Aye (Professor and Head), Department of Computer Studies, University of Yangon for their valuable guidelines in my research. I also would like to extend my gratitude to Dr. Wint Pa Pa Kyaw (Professor), and Dr. Khin Sandar Myint (Associate Professor), Department of Computer Studies, University of Yangon for their help given to me in the research.

References

Bingham, E.& Mannila, H. (2001). *Random projection in dimensionality reduction*. Proceedings of the seventh ACM SIGKDD international conference on Knowledge discovery and data mining – KDD '01. p. 245. doi:10.1145/502512.502546. ISBN 978-1581133912. S2CID 1854295

Hinton, G. & Roweis, S. (2002). *Stochastic neighbor embedding*. Neural Information Processing Systems.

Jolliffe, I.T. & Cadima, J. (2016), *Principal component analysis: a review and recent developments*. Philosophical Transactions of the Royal Society A: Mathematical, Physical and Engineering Sciences. 374 (2065): 20150202. Bibcode: 2016RSPTA.37450202J. doi:10.1098/ rsta.2015. 0202. PMC 4792409. PMID 26953178

Lespinats, S., Colange, B., & Dutykh, D. (2022). Nonlinear dimensionality reduction techniques: A data structure preservation approach. ISBN: 978-3-030-81025-2.

Maaten, L.V.D. & Hinton, G. (2008), *Visualizing Data Using t-SNE*. Journal of Machine Learning Research. 9: 2579–2605

McInnes, L., Healy, J. & Melville, J. (2018), *Uniform manifold approximation and projection for dimension reduction*. arXiv:1802.03426

ACCURACY ANALYSIS OF BMI PREDICTION USING REGRESSION ALGORITHMS

Thin Ei Zar[1], Khin Sandar Myint[2], Soe Mya Mya Aye[3]

Abstract

This study conducts an accuracy analysis of BMI prediction using regression algorithms, specifically decision tree and random forest regression. A dataset used in this paper was collected from the Kaggle data repository site. The dataset is split into training and testing sets to predict BMI, BMR and calories needed to maintain weight based on gender, age, weight, height, and activity level using decision tree and random forest regression algorithms. The performance accuracy of the proposed algorithms is evaluated using Root Mean Squared Error, Mean Absolute Error, R-squared, Mean Absolute Percentage Error and accuracy. The goal and content of this research are to study the prediction accuracy of decision tree and random forest regression machine learning algorithms in prediction. Analyzing BMI will be specifically focused on suggesting the daily calories to maintain weight to the user to get a healthy life that leads to a happy life.

Keywords: BMI Prediction, Regression Algorithm, Analysis of BMI, Prediction Accuracy

Introduction

Body Mass Index (BMI) is a commonly used measure that classifies individuals according to body weight and height, helping to identify if a person is underweight, normal weight, overweight, or obese. Body Mass Index (BMI), Basal Metabolic Rate (BMR), and caloric needs are essential metrics in assessing an individual's health status. BMR represents the number of calories required to maintain basic physiological functions. Understanding BMR is crucial for calculating daily caloric needs. Accurate prediction of BMI, BMR, and caloric needs is increasingly important for healthcare professionals and researchers to address various health-related issues.

This study aims to compare BMI prediction accuracy using regression algorithms, specifically decision tree and random forest regression. These algorithms are chosen for their ability to handle complex, non-linear relationships between variables and their robustness in prediction tasks. The dataset for the research consists of 10,726 records with attributes such as age, weight, height, gender, BMI, BMR, activity level and calories required to maintain weight. The dataset is split into training and testing sets, allowing for a systematic approach to predicting BMI, BMR and maintenance calories based on gender, age, weight, height and activity level. Using Python's Jupyter Notebook for data visualization and analysis, the study employs decision tree and random forest regression algorithms for the prediction process.

This comparative analysis offers valuable insights into the effectiveness of decision tree and random forest regression algorithms in predicting BMI. The findings have significant implications for health and a better understanding of the strengths and limitations of these algorithms in BMI prediction tasks. Moreover, the study emphasizes choosing the right algorithm for accurate health predictions, which can directly impact personalized healthcare.

[1] Department of Computer Studies, University of Yangon
[2] Department of Computer Studies, University of Yangon
[3] Department of Computer Studies, University of Yangon

Methods of Machine Learning Algorithms for BMI Prediction

A machine learning algorithm is a set of rules or processes used by an AI system to conduct tasks, most often to discover new data insights and patterns, or to predict output values from a given set of input variables. Machine learning algorithms can be categorized into four types: supervised, unsupervised, semi-supervised and reinforcement learning. This research will use a regression algorithm in supervised learning. Supervised learning is a form of machine learning in which the algorithm is trained on labeled data to make predictions or decisions based on the data inputs. Supervised learning can be further classified into classification and regression.

Classification is a two-step process such as learning (model development) and prediction, suitable for problems with discrete output labels such as email filtering (spam or not spam) and weather categorization (sunny, cloudy, rainy). Regression is predicting continuous values based on input such as housing price prediction.

Regression algorithms are appropriate in the context of BMI and BMR prediction in this research because they predict continuous values rather than discrete categories. Regression will be used for predicting values like BMI, BMR and calories needed to maintain weight based on continuous input variables such as age, height, weight, gender and activity level.

There are many different types of regression algorithms such as Linear Regression, Polynomial Regression, Support Vector Regression (SVR), Decision Tree Regression and Random Forest Regression. Among them, decision tree regression and random forest regression are chosen for their simplicity and accuracy in these predictions.

The implementation process of the research

To develop this research, the dataset collection is the basic step of the process. The dataset used in this research is collected from the Kaggle data repository site and the dataset includes 10726 records with suitable attributes for this research. The prediction process for BMI, BMR and calories needed to maintain weight based on age, height, weight, gender and activity level will be implemented in the Python Jupyter Notebook. After collecting the dataset, the stages of methodology and implementation process have seven stages as shown in Figure 1 as a flow diagram.

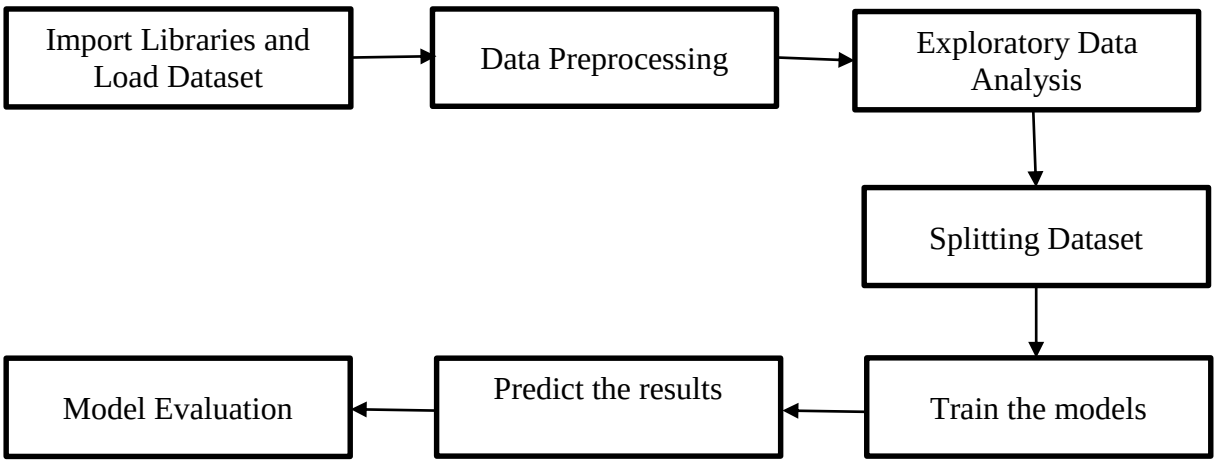

Figure 1 Flow diagram of the research for BMI prediction using regression algorithms

Import Libraries and Load Data

This step involves importing the necessary libraries such as pandas for data manipulation, scikit-learn for machine learning algorithms and seaborn and matplotlib for plotting. With pandas, data from various file formats (e.g., CSV, Excel) can be read, handle missing data and perform complex data transformations. Scikit-learn (sklearn) is a comprehensive library for machine learning in Python. Seaborn is built on top of Matplotlib and provides a high-level interface for drawing attractive and informative statistical graphics. Matplotlib is a widely-used plotting library that offers plots and charts such as line graphs, scatter plots, and more to visually explore and present data.

In the load data step, the dataset is loaded into the environment. The data can be from various sources like CSV files, databases or other formats. The dataset used in this research is a CSV file. It is essential to understand the structure and content of the dataset for effective analysis. Figure 2 shows the code for importing the libraries and loading the dataset into the Jupyter Notebook.

```
import pandas as pd
import matplotlib.pyplot as plt
import seaborn as sns
from sklearn import tree
from sklearn.metrics import accuracy_score
mydata = pd.read_csv('C:/Users/User/Downloads/BMIDataset.csv')
melbourne_data = mydata.dropna(axis=0)
result_data = melbourne_data.dropna(axis=0)

mydata.describe().round(decimals = 2)
```

Figure 2 Importing Python Libraries and Loading the Dataset

Data Preprocessing

Data preprocessing is an essential step that involves handling missing values, encoding categorical features, scaling numerical features and possibly other transformations. This step ensures the data is clean and suitable for model training. Data preprocessing can be performed to ensure the shape of the dataset, no duplicated and null data in the dataset, and the detailed information of the dataset and to drop or remove unnecessary attributes for the dataset.

The info () function is utilized to present the number of columns, their respective labels, data kinds and the count of non-null cells within each column. Kene, et.al, (2023) according to the data presented in Figure 3(a), there is a lack of empty values within the dataset.

```
mydata.isnull().any()

age                          False
weight(kg)                   False
height(m)                    False
gender                       False
BMI                          False
BMR                          False
activity_level               False
calories_to_maintain_weight  False
BMI_tags                     False
Label                        False
dtype: bool
```

Figure 3(a) No null data

```
mydata.info()

<class 'pandas.core.frame.DataFrame'>
RangeIndex: 10726 entries, 0 to 10725
Data columns (total 10 columns):
 #   Column                       Non-Null Count  Dtype
---  ------                       --------------  -----
 0   age                          10726 non-null  int64
 1   weight(kg)                   10726 non-null  float64
 2   height(m)                    10726 non-null  float64
 3   gender                       10726 non-null  object
 4   BMI                          10726 non-null  float64
 5   BMR                          10726 non-null  float64
 6   activity_level               10726 non-null  float64
 7   calories_to_maintain_weight  10726 non-null  float64
 8   BMI_tags                     10726 non-null  int64
 9   Label                        10726 non-null  int64
dtypes: float64(6), int64(3), object(1)
memory usage: 838.1+ KB
```

Figure 3(b) Information of the dataset

Figure 3(b) shows the information of the dataset that the dataset has 10726 entries, 0 to 10725, and 10 data columns (age, weight(kg), height(m), gender, BMI, BMR, activity-level, calories to maintain weight, BMI_tags, Label.

```
mydata.shape

(10726, 10)

mydata.duplicated()

0        False
1        False
2        False
3        False
4        False
        ...
10721    False
10722    False
10723    False
10724    False
10725    False
Length: 10726, dtype: bool
```

Figure 4(a) Shape of data and No Duplicated data in the dataset

```
Dropping Unwanted attributes

analysis= mydata.drop(['BMI_tags','Label'],axis = 1)

analysis.shape

(10726, 8)

pd.DataFrame(analysis[:6]).round(decimals = 2)
```

	age	weight(kg)	height(m)	gender	BMI	BMR	activity_level	calories_to_maintain_weight
0	2	16.10	0.93	Female	18.53	958.58	1.2	1150.30
1	4	14.62	0.92	Female	17.40	932.38	1.7	1585.05
2	4	17.90	1.00	Female	18.00	977.58	1.9	1857.40
3	3	13.53	1.02	Female	12.94	944.69	1.9	1794.91
4	4	17.04	1.05	Male	15.34	799.23	1.9	1518.54
5	3	12.03	1.08	Female	10.34	939.78	1.9	1785.58

Figure 4(b) Dropping unwanted columns

Figure 4(a) describes the shape of the dataset and the data contains 10726 rows, 10 attributes, and no duplicated data in the dataset. Figure 4(b) shows that dropping unnecessary columns for the machine learning process. In this research, the predictive modeling with decision tree and random forest regression will need only 8 columns without 2 columns (BMI_tags, Label). So, during this data pre-processing stage, unwanted columns need to drop for the improvement of the prediction accuracy.

In data preprocessing**,** data exploration is exploring the dataset using Exploratory Data Analysis (EDA) to understand the data before applying machine learning algorithms. EDA identifies data patterns and correlations, preparing the dataset for analysis.

Exploratory Data Analysis (EDA)

Exploratory Data Analysis (EDA) helps understand the data before applying machine learning algorithms. EDA identifies data patterns and correlations, preparing the dataset for analysis. Visualization is a crucial part of EDA. By analyzing the dataset based on the gender attributes, the data set involves the number of females 5572 and males 5154.

```
people = analysis['gender'].value_counts()
print(type(people))
people.head()

<class 'pandas.core.series.Series'>
gender
Female    5572
Male      5154
Name: count, dtype: int64

fig, ax= plt.subplots( figsize=(3,4))
sns.countplot(x='gender',  data=analysis)
```

Figure 5(a) Data count for Gender

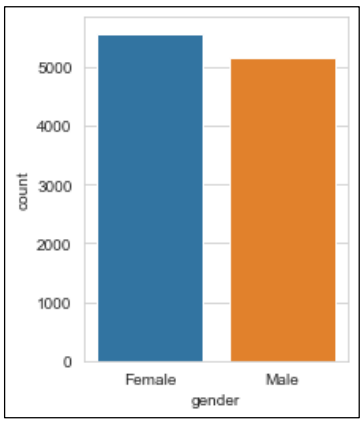

Figure 5(b) Count plot for Gender

Figure 5(a) shows the code for counting data based on the gender attribute of the dataset. Output can be seen in Figure 5(b) as a count plot.

Splitting Dataset

The dataset is divided into training and testing sets. The training set is used to train the model, while the testing set is used to evaluate its performance. For the prediction of the training and testing data of the dataset using the regression algorithm, X and Y must be defined first from the dataset. In this regression analysis, the dependent variable (outcome variable) is denoted "Y" and the independent variables(predictors) are denoted "X".

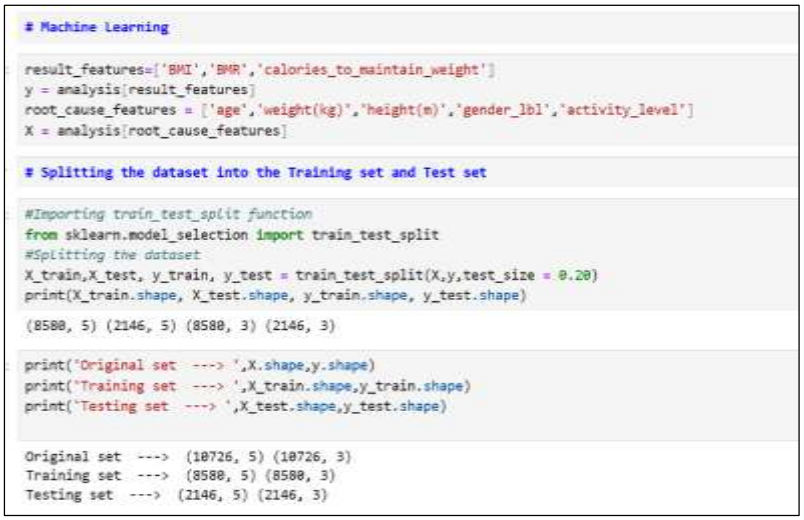

```
# Machine Learning

result_features=['BMI','BMR','calories_to_maintain_weight']
y = analysis[result_features]
root_cause_features = ['age','weight(kg)','height(m)','gender_lbl','activity_level']
X = analysis[root_cause_features]

# Splitting the dataset into the Training set and Test set

#Importing train_test_split function
from sklearn.model_selection import train_test_split
#Splitting the dataset
X_train,X_test, y_train, y_test = train_test_split(X,y,test_size = 0.20)
print(X_train.shape, X_test.shape, y_train.shape, y_test.shape)

(8580, 5) (2146, 5) (8580, 3) (2146, 3)

print('Original set  ---> ',X.shape,y.shape)
print('Training set  ---> ',X_train.shape,y_train.shape)
print('Testing set  ---> ',X_test.shape,y_test.shape)

Original set  --->  (10726, 5) (10726, 3)
Training set  --->  (8580, 5) (8580, 3)
Testing set  --->  (2146, 5) (2146, 3)
```

Figure 6 The code and output for splitting the dataset

Figure 6 shows the code for defining X and Y and splitting the dataset for training and testing data. For the prediction process, 5 attributes (age, gender, weight(kg), height(m), and activity level) from data will be used as input and will be defined as X. 3 attributes (BMI, BMR, and calories to maintain weight) are defined as Y, will be calculated and predicted as an output result based on X.

The split ratio of 80:20 means that t*he 20% testing data set is represented by the test_size= 0.20 at the end. The output of is original dataset is 10726 records. Training 80% is 8580 and testing 20% is 2146 for each attribute.*

Train the models

In this step, the Decision Tree and Random Forest Regressors are imported and fit the model for the prediction process using the training and testing dataset. These models learn the patterns and relationships within the data to make accurate predictions.

For the training and testing process using a decision tree, need to build and train the model by importing the scikit-learn DecisionTreeRegressor with the following code.

Code for importing the DecisionTree Regressor:

```
from sklearn.tree import DecisionTreeRegressor
X_train, X_test, y_train, y_test = train_test_split(X, y, test_size=0.20)
y_dt=DecisionTreeRegressor ().fit(X_train, y_train)
```

Decision tree regression will be used to predict y (BMI, BMR and calories_to _maintain _weight) based on X (height(m), weight(kg), gender_lbl, age, activity_level) for the training dataset.

Random forest regression will be used to predict y (BMI, BMR and calories_to _maintain _weight) based on X (height(m), weight(kg), gender_lbl, age, activity_level). To use random forest regression, the regressor must be imported by the following code.

Code for Importing the Random Forest Regressor:

```
from sklearn.ensemble import RandomForestRegressor
model = RandomForestRegressor(n_estimators = 30, random_state = 30)
X_train, X_test, y_train, y_test = train_test_split(X, y, test_size=0.20)
y_rf=model.fit(X_train, y_train)
```

The above code fits the decision tree and random forest regression model with training and testing data.

Predict the results

The trained models are used to make predictions on the training and testing data. The predictions on the training and testing dataset using decision tree regression are processed and predict the results of Y (BMI, BMR, and calories_to_maintain_weight) based on X (age, weight(kg), height(m), gender_lbl, and activity_level will be processed by the following code.

Code for prediction on the training dataset using decision tree regression:

```
ytrain_pred_tree= y_dt.predict(X_train)
pd.DataFrame(ytrain_pred_tree,columns=["BMI","BMR","calories_to_maintain_wei
ght"].round (decimals = 2)
```

Code for prediction on the testing dataset using decision tree regression:

```
ytest_pred_tree = y_dt.predict(X_test)
pd.DataFrame(ytest_pred_tree,columns=["BMI",  "BMR",  "calories_to_maintain_
weight"] ). round (decimals = 2)
```

The predictions on the training and testing dataset using random forest regression are processed and the results by the following code.

Code for prediction on the training dataset using random forest regression:

```
ytrain_pred_forest= y_rf.predict(X_train)
pd.DataFrame(ytrain_pred_forest,columns=["BMI","BMR","calories_to_maintain_w
eight"]).round (decimals = 2)
```

Code for prediction on the testing dataset using random forest regression:

```
ytest_pred_forest = y_rf.predict(X_test)
pd.DataFrame(ytest_pred_forest,columns=["BMI","BMR","calories_to_maintain_we
ight"] ).round (decimals = 2)
```

The predicted results for training and testing using decision tree regression and random forest regression are checked to evaluate the accuracy or performance of the model.

Model Evaluation

The models' performance is evaluated using metrics such as R-squared, Root Mean Squared Error (RMSE), Mean Absolute Error(MAE), Mean Absolute Percentage Error(MAPE), and Accuracy (%). These metrics provide insights into the accuracy and effectiveness of the models.

Results

Evaluation for Training and Testing Data using Decision Tree Regression

This study evaluates the performance of Decision Tree and Random Forest Regression models using several standard metrics: Mean Squared Error (MSE), Mean Absolute Error (MAE), R-squared (R^2), and Mean Absolute Percentage Error (MAPE) and Accuracy (%). These metrics are applied to assess the models' training and testing phases. The mathematical formulas for these metrics are provided below, while the corresponding Python code for the implementation can be run in the Python Jupyter Notebook environment.

Root Mean Squared Error (RMSE): $\text{RMSE} = \sqrt{\sum_{i=1}^{n} \frac{(\hat{y}_i - y_i)^2}{n}}$

Mean Absolute Error (MAE): $\text{MAE} = \frac{1}{N} \sum_{i=1}^{N} |y_i - \hat{y}_i|$

R-squared (R^2) Coefficient of determination: $R^2 = 1 - \frac{\sum_{i=1}^{n} (\hat{y}_i - y_i)^2}{\sum_{i=1}^{n} (y_i - \hat{y}_i)^2}$

Mean Absolute Percentage Error (MAPE): $\text{MAPE} = \frac{1}{n} \sum_{i=1}^{n} \left| \frac{\hat{y}_i - y_i}{y_i} \right| \times 100$

y = actual value of y, $\hat{y}_i$= predicted value of y, n = number of data points

Accuracy (%): Accuracy (%)=100%−MAPE

The metrics for the training dataset of the Decision Tree regression models are computed using Python within a Jupyter Notebook, without the need for manually applying mathematical formulas. An example of Python code for RMSE is shown in Figure 7.

```
Metric Evaluation for prediction of training data using decision tree regression

from sklearn.metrics import mean_absolute_error, mean_squared_error,r2_score

#The RMSE
import numpy as np
print("The RMSE is:", np.sqrt(mean_squared_error(y_train,ytrain_pred_tree)))

The RMSE is: 0.0
```

Figure 7 Examples of Python code for RMSE

The results of metric evaluation for the decision tree and random forest are summarized in Table 1 below.

Table 1: **Performance of Decision Tree and Random Forest on Training and Testing Datasets**

Model Evaluation Metrics	Decision Tree Training	Decision Tree Testing	Random Forest Training	Random Forest Testing
RMSE	0.00	8.06	2.14	5.53
MAE	0.00	3.18	0.95	2.42
R^2	1.00	1.00	1.00	1.00
MAPE	0.00 %	0.49 %	0.13 %	0.30 %
Accuracy(%)	100.00 %	99.51 %	99.87 %	99.70 %

Table 1 compares the Decision Tree and Random Forest models using various evaluation metrics: RMSE, MAE, R^2, MAPE, and Accuracy (%). The metrics are evaluated for both training and testing datasets, providing insights into model performance and its ability to handle new data.

Root Mean Squared Error (RMSE): The metric, representing the square root of the average squared differences between actual and predicted values, shows that the Decision Tree model achieves a training RMSE of 0.00 but a testing RMSE of 8.06, indicating a significant error increase on unseen data. In contrast, the Random Forest model has a training RMSE of 2.14 and a testing RMSE of 5.53, reflecting a more moderate error increase on the test set.

Mean Absolute Error (MAE): MAE represents the average absolute differences between predicted and actual values. The Decision Tree model achieves an MAE of 0.00 during training and 3.18 during testing, reflecting a noticeable rise in error on the test data. The Random Forest model has an MAE of 0.95 for training and 2.42 for testing, demonstrating more robust performance and less variation in error between training and testing datasets.

R-squared (R^2): This statistic indicates the proportion of variance in the target variable that is predictable from the independent variables. Both models achieve an R^2 of 1.00 in training and testing, suggesting a perfect fit. However, such high R^2 values could indicate potential overfitting, particularly when combined with higher error metrics in testing for the Decision Tree model.

Mean Absolute Percentage Error (MAPE): MAPE measures the model's performance as a percentage, with lower values indicating better performance. The Decision Tree model achieves a MAPE of 0.0 in training and 0.49 in testing, while the Random Forest model shows a MAPE of 0.13 in training and 0.30 in testing. The slightly higher MAPE values for the Random Forest in training and testing suggest a more realistic measure of prediction error than those of the Decision Tree.

Accuracy (%): The Decision Tree model has a training accuracy of 100% and a testing accuracy of 99.51%. The Random Forest model has a training accuracy of 99.87% and a testing accuracy of 99.70%.

Overall, the Decision Tree model demonstrates excellent performance in training but suffers from significant performance degradation in testing, potentially indicating overfitting. The Random Forest model, on the other hand, shows more consistent performance across training and testing, suggesting better generalizability.

Comparison of Accuracy (%) for Decision Tree and Random Forest Regression

The comparison between Decision Tree Regression and Random Forest Regression reveals that both models perform exceptionally well in predicting outcomes. However, the Random Forest model demonstrates a slight edge in accuracy and robustness, particularly in handling more complex datasets.

Table 2. Comparison of accuracy (%) for Decision Tree and Random Forest Regression

Model	Training Accuracy (%)	Testing Accuracy (%)
Decision Tree Regression	100.00 %	99.51 %
Random Forest Regression	99.87 %	99.70 %

Table 2 compares the training and testing accuracies of Decision Tree and Random Forest regression models. Both models show high accuracy, with the Decision Tree achieving

perfect accuracy in training (100%) and slightly lower in testing (99.51%). Random Forest performs nearly as well, with a slight drop in training (99.87%) and testing (99.70%) accuracies.

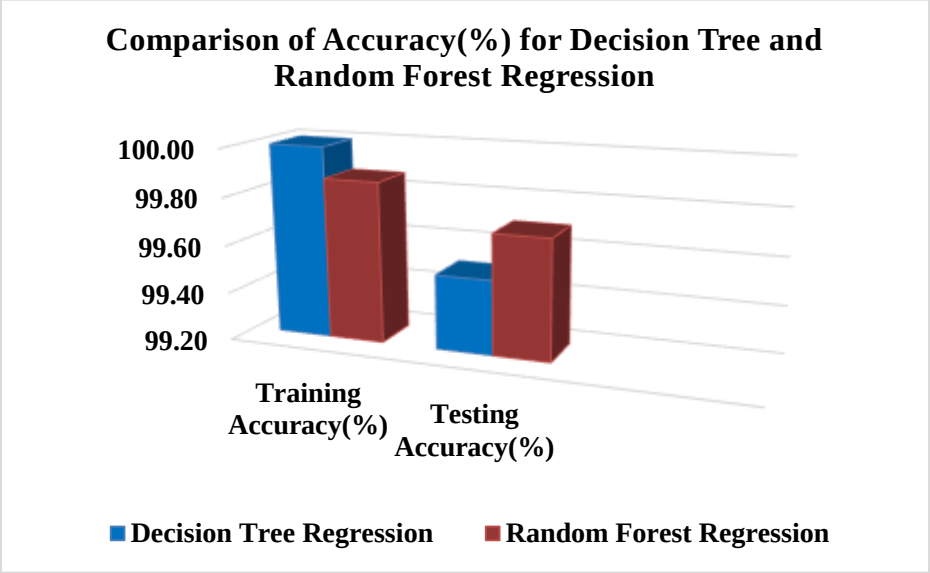

Figure 8 Comparison of Accuracy (%) between the two models

Figure 8 illustrates the performance of Decision Tree and Random Forest models mainly in accuracy (%). While Decision Tree performs slightly better in training accuracy, Random Forest exhibits a slight advantage in testing accuracy. The chart underscores the competitive nature of both models in predictive tasks.

Discussion

The performance comparison between decision tree regression and random forest regression reveals that the training accuracy is higher than the testing accuracy for both models. Decision tree regression shows perfect accuracy on the training data (100%) but a slight drop in testing accuracy (99.51%), suggesting that while the model captures the training data well, it may slightly overfit, leading to a minor reduction in generalization to new data.

Random forest regression achieves nearly perfect accuracy on both training (99.87%) and testing data (99.70%), indicating that this model generalizes slightly better to unseen data compared to the decision tree model. The high testing accuracy demonstrates its robustness and effectiveness in making accurate predictions across different data sets.

The random forest regression model achieves better accuracy (99.70%) compared to the decision tree regression model (99.51%) on the testing dataset. This superior performance can be attributed to the ensemble nature of the random forest, which reduces overfitting and improves generalization by aggregating the predictions of multiple decision trees.

This study predicts three attributes BMI, BMR and the calories needed to maintain weight based on age, weight, height, gender and activity level. Decision Tree Regression is simple to understand and interpret but can have high variance and may overfit the training data. On the other hand, Random Forest Regression, which combines multiple decision trees, delivers improved predictive accuracy and robustness. Both models show high accuracy in predictions, but Random Forest Regression generally offers more reliable results for new data due to its enhanced generalization ability. This reliability makes Random Forest a preferred option for applications that require consistent performance across varied datasets.

Conclusion

This study shows that random forest regression is more accurate and reliable than decision tree regression in predicting BMI, BMR and daily calorie needs based on age, weight, height, gender and activity level. The random forest model handles the complexity of predicting multiple outcomes at once and is less likely to make errors. This research highlights the value of machine learning in improving health assessments and creating personalized dietary recommendations. These advancements can benefit everyone, especially in areas where access to regular healthcare is limited. By making accurate health predictions more accessible, this study supports better health management and healthier lifestyles in our society. Future research could explore more machine learning methods to further improve these predictive systems.

Acknowledgement

I would like to express my profound gratitude to Dr. Soe Mya Mya Aye, Professor and Head of the Department of Computer Studies, University of Yangon, for her kind permission, encouragement, and valuable suggestions to carry out this research. I also would like to thank my supervisor Dr. Khin Sandar Myint, Associate Professor, Department of Computer Studies, University of Yangon, for her close supervision, invaluable suggestions and kind guidance. I wish to thank all who help and give me advice on this research.

References

B. Manoj Kumar, et al., (2022) “Accuracy Analysis of Heart Disease Prediction using Logistic Regression in Comparison with the Linear Regression Algorithm”, Journal of Pharmaceutical Negative Results, Volume 13, Special Issue 4.

F. Ferdowsy, K.S.A. Rahi, Md.I. Jabiullah et al., (2021) “A machine learning approach for obesity risk prediction”, DOI: https://doi.org/10.1016/j.crbeha.2021.100053.

Joy, Jodder, (2020) “An Effective Recommendation System to Forecast the Best Educational Program Using Machine Learning Classification Algorithms”, Journal of IIETA, Vol. 25, No. 5, pp. 559-568

Kamble Rita R (2014) “A Comparison of Decision Tree Algorithms on Healthy Eating System”, International Journal of Innovative Research in Engineering & Management (IJIREM) Volume-1, Issue-3.

K.T. Anyachebelu, M. U. Abdullahi, M. Abdullahi (2023) "Comparative Analysis of Machine Learning Algorithms for Breast Cancer Prediction", Dutse Journal of Pure and Applied Sciences (DUJOPAS), Vol. 9 No. 4b, https://dx.doi.org/10.4314/dujopas.v9i4b.8.

Ms. Madhuvanthi, et.al, (2024) "Comparative Analysis of Diabetic Prediction Using Machine Learning Algorithms", Journal of Advanced Zoology, ISSN: 0253-7214, Volume 45, Page 465-477

https://towardsdatascience.com

https://www.geeksforgeeks.org/regression-in-machine-learning/

https://www.ibm.com/topics/machine-learning-algorithms

https://www.kaggle.com

INSTRUCTIONS TO AUTHORS

Presentation: Manuscripts (MS) should be typed on one side of **quarto or A4 size paper**. Typing should be single spaced, with a one-inch margin all around. A CD of the paper should be submitted together with two print-outs. In general, the text should be organized according to the following outline:

(i) Title
(ii) Abstract
(iii) Materials & Methods/ Premises / Hypotheses
(iv) Results / Findings
(v) Discussion
(vi) Summary/ Conclusion
(vii) Acknowledgements
(viii) References

The body of the text should be printed in **font size 12**, and those of the Abstract, Acknowledgement and References should be printed in **font size 10.** The relative importance of the **headings** in the text should be indicated as follows:

First Order	-	CENTRE HEADING, All Capitals
Second Order	-	Centre Heading, Capitals & lower case
Side Heading	-	Capitals & lower case, not indented (bold – faced)
Run-in heading	-	Capitals & lower case, indented (bold-faced)

Title. The title should describe the contents of the article adequately and concisely and should be typed in **font size 14.**

Author's name. Capital & lower case. The designation of the first author and email (where the number of authors is more than two) and the name of the institution where the work was carried out should be given at the bottom of the title page; but academic degree of the author is not necessary.

Abstract. The main points of the paper, including its findings and conclusions, should be highlighted in the abstract; it should not contain more than 300 words. Add email address for making further contact with the author; evaluation of the paper should be typed in **font size 10**.

Keywords: Between 3-7 keywords highlighting the main points should be listed below the abstract.

References. References should be presented in alphabetical order, beginning with the surname first for the senior author and surname last for the other authors, followed by the year of publication. Examples of references are given below:

To a paper: Rabinowitz, A., Than Myint, email, Tun Khaing, and S. Rabinowitz, (1999)"Description of the Leaf Deer (*Muntiacus Putaoensis),* a New Species of Muntjac from Northern Myanmar" *Journal of Zoology,* London, vol.249, pp.427-435.

To a book: Corbet, G.B., & J.E. Hill, (1992) *The mammals of the Indomalayan Region.* Oxford, Oxford University Press.

To a thesis: May Soe Thu (1995) *Taxonomy of Offshore Fishes Caught by Bottom Trawl Operations in Myanmar Waters.* M.Sc. Thesis Zoology Department, Yangon University (Unpublished).

N.B. If the manuscript submitted is from a thesis, its format should be revised to conform to the instructions of the Myanmar Journal of Arts & Science presented here. **Pagination** should commence from the title page except when they are used to identify the affiliated instructions, and cite unpublished material. **Footnotes** should be avoided wherever possible. The MS, including illustrations and references, should not exceed **15 pages** for Arts and related subjects and **10 pages** for Science in length. Please kindly follow this limit in your final manuscript.

MYANMAR ACADEMY OF ARTS AND SCIENCE
EXECUTIVE COMMITTEE

President : Dr Thet Lwin

Vice-Presidents : Dr Maung Kyaw, Dr U Win

Secretary : Dr Win Tun

Joint Secretaries: Dr Tin Maung Tun, Dr Aye Aye Khaing, Dr Tin Tin Htwe

Executive Members

Dr Myo Thant Tyn
Dr Tin Nyo
Dr Khin Than Oo
Dr Hla Pe
Dr Maung Thin
Dr Daw Than Nwe
Daw Carole Ann Chit Tha
Daw Khin Lat

Publication Committee

Dr Thet Lwin	(Chairman)	Dr Maung Kyaw	(Vice-Chairman)
Dr Tin Nyo	(member)	Daw Carole Ann Chit Tha	(member)
Daw Khin Lat	(member)	Dr Hla Pe	(member)
Dr U Win	(member)	Dr Maung Thin	(member)
Dr Daw Than Nwe	(member)	Dr Khin Than Oo	(Joint Secretary)
Dr Myo Thant Tyn	(Secretary)		

Editorial Board

Dr Maung Kyaw	(Chairman)	Dr Daw Than Nwe	(member)
Dr Myo Thant Tyn	(member)	Dr Khin Than Oo	(member)
Dr Tin Nyo	(member)	Dr Hla Pe	(member)
Daw Khin Lat	(member)	Dr Aye Aye Khaing	(member)
Dr Maung Thin	(member)	Daw Carole Ann Chit Tha	(Joint Secretary)
Dr U Win	(Secretary)		

Coordinators for International Academies

Daw Carole Ann Chit Tha
Dr Myo Thant Tyn
Dr Tin Nyo
Dr Tin Tin Htwe
Dr Maung Kyaw
Dr Daw Than Nwe
Dr Tin Maung Tun